Couplage cristallisation-foisonnement au sein d'un échangeur de chaleur à surface raclée lors de la production de sorbet

Oscar Hernández Parra

agreenium
l'institut agronomique, vétérinaire & forestier de France

AgroParisTech

NNT: 2018IAVF0018

THESE DE DOCTORAT

préparée à l'Institut des sciences et industries du vivant et de l'environnement (AgroParisTech)

pour obtenir le grade de

Docteur de l'Institut agronomique vétérinaire et forestier de France

Spécialité : Génie des aliments

École doctorale n°581
Agriculture, alimentation, biologie, environnement et santé (ABIES)

par

Oscar Dario HERNANDEZ PARRA

Couplage cristallisation-foisonnement au sein d'un échangeur de chaleur à surface raclée lors de la production de sorbet

Directrice de thèse : **Graciela ALVAREZ**
Co-Directeur de thèse : **Denis FLICK**

Thèse présentée et soutenue à Paris, le 13 novembre 2018

Composition du jury :

Mme Martine ESTEBAN DECLOUX, Professeur, AgroParisTech	Présidente
M. Guillaume DELAPLACE, Directeur de recherche, INRA	Rapporteur
Mme Francine FAYOLLE, Professeur, ONIRIS	Rapporteur
Mme Laurence FOURNAISON, Directrice de recherche, IRSTEA	Examinatrice
Mme Graciela ALVAREZ, Directrice de recherche, IRSTEA	Directrice de thèse
M. Denis FLICK, Professeur, AgroParisTech	Co-Directeur de thèse
Mme Fatou-Toutie NDOYE, Ingénieur de recherche, IRSTEA	Invitée
Mme Hayat BENKHELIFA, Maître de conférences, AgroParisTech	Invitée

UR FRISE
IRSTEA 1 rue Pierre Gilles de Gennes
92751 ANTONY cedex

Denn der tiefere Grund meiner wissenschaftlichen Unfähigkeit scheint mir ein Instinkt und wahrlich kein schlechter Instinkt zu sein. […] Es war der Instinkt, der mich vielleicht gerade um der Wissenschaft willen, aber einer anderen Wissenschaft, als sie heute geübt wird, einer allerletzten Wissenschaft, die Freiheit höher schätzen ließ als alles andere. Die Freiheit! Freilich die Freiheit, wie sie heute möglich ist, ein kümmerliches Gewächs. Aber immerhin Freiheit, immerhin ein Besitz

Forschungen eines Hundes
Franz Kafka, 1922

TABLE OF CONTENTS

LIST OF FIGURES

LIST OF TABLES

INTRODUCTION

1. Introduction

1.1 Importance de la cristallisation et du foisonnement lors de la production d'un sorbet ou d'une crème glacée

Du point de vue de sa structure, une crème glacée est un arrangement complexe de différentes phases avec des éléments de différentes tailles. A l'échelle microscopique on distingue quatre phases : une phase liquide aqueuse, une phase solide constituée des cristaux de glace, une phase gaz représentant les bulles d'air et une phase lipidique constituée de globules et d'agrégats (clusters). Un sorbet à une structure légèrement plus simple car on n'y trouve quasiment pas de matière grasse. Une vue schématique est représentée sur la Figure 1 :

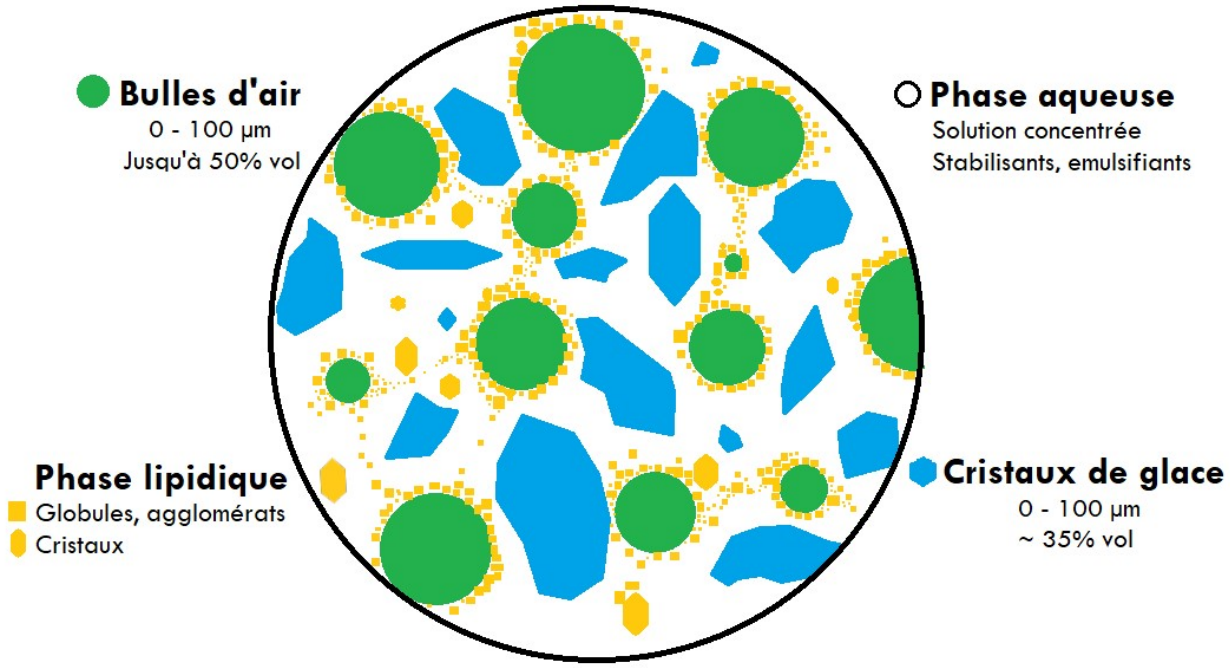

Figure 1. Vue schématique de la microstructure d'une crème glacée.

Les cristaux de glace sont obtenus par cristallisation de l'eau contenue dans la phase liquide. La quantité de cristaux et leur distribution de tailles déterminent de nombreux attributs du produit fini : cuillerabilité (*spoonability*), dureté/onctuosité (*hardness/smoothness*), effet rafraichissant (*cooling effect*), vitesse de fonte

(*meltdown rates*) qui font qu'un produit est apprécié ou non des consommateurs. Le plus souvent, les cristaux ont une taille comprise entre 1 et 100 µm et occupent environ 30% du volume d'une crème glacée. Par ailleurs, les bulles sont de formes quasiment sphériques et sont finement dispersées dans le milieu. Leur taille va de quelques microns à plus de 100 microns avec une moyenne souvent comprise entre 20 et 25 microns dans le produit fini. Comme dans beaucoup d'aliments, les bulles d'air sont introduites avant tout pour favoriser une texture légère mais elles peuvent affecter également d'autres propriétés. Les propriétés rhéologiques qui, d'une part, traduisent la texture en bouche et, d'autre part, conditionnent les écoulements dans les équipements dépendent directement des fractions volumiques de solide et de gaz ainsi que de la distribution granulométrique de ces phases dispersées.

Cette étude s'intéresse plus particulièrement aux **sorbets**. Ils contiennent au moins 25% de fruit et une forte concentration en sucre. Ils peuvent être stabilisés par du blanc d'œuf, de la pectine ou des 'gommes'. Il faut noter que si de faibles concentrations de stabilisant sont utilisées, comme on ne bénéficie pas des effets structurants des protéines laitières et de la matière grasse, la fraction volumique d'air incorporé ne dépasse souvent pas 20% alors qu'elle peut facilement atteindre 50% dans une crème glacée.

Le procédé de fabrication de crèmes glacées ou de sorbets comprend plusieurs opérations unitaires (Figure 2). En général, après le mélange des différents ingrédients (eau, sucre, lait, jus de fruits, stabilisants, émulsifiants et matière grasse pour la crème glacée) qui forment un « mix » de crème glacée ou de sorbet, celui-ci est pasteurisé, homogénéisé puis refroidi pour maturation pendant plusieurs heures. Après maturation, le mix est introduit, avec de l'air, dans un échangeur de chaleur à surface raclée (ECSR) où il est alors congelé et foisonné. A la sortie de l'ECSR (à une température comprise entre -4 et -6°C), le produit formé est stocké à basse température (environ -23°C) pour durcissement. Le schéma représenté sur la Figure 2 montre les différentes étapes d'un procédé de fabrication. Dans cette étude nous nous focaliserons sur l'étape de précongélation/foisonnement (*freezing/foaming*). C'est dans cette étape que les cristaux de glace et les bulles sont formés. Dans les étapes ultérieures (conditionnement, durcissement, stockage), on ne crée en général pas de nouveaux cristaux ou de nouvelles bulles. Les bulles peuvent éventuellement coalescer et les cristaux continuent de croître pendant la congélation finale (augmentation de la fraction de glace lorsque la température diminue) et lors du stockage (augmentation de la taille des cristaux par murissement d'Ostwald à fraction de glace constante).

La finesse des cristaux et des bulles dépend donc principalement de l'étape de précongélation/foisonnement qui constitue le cœur du procédé, c'est le seul endroit où de nouveaux cristaux sont formés et où la phase gazeuse est dispersée. Dans les procédés industriels cette étape se déroule en continu dans des échangeurs de chaleur à surface raclée.

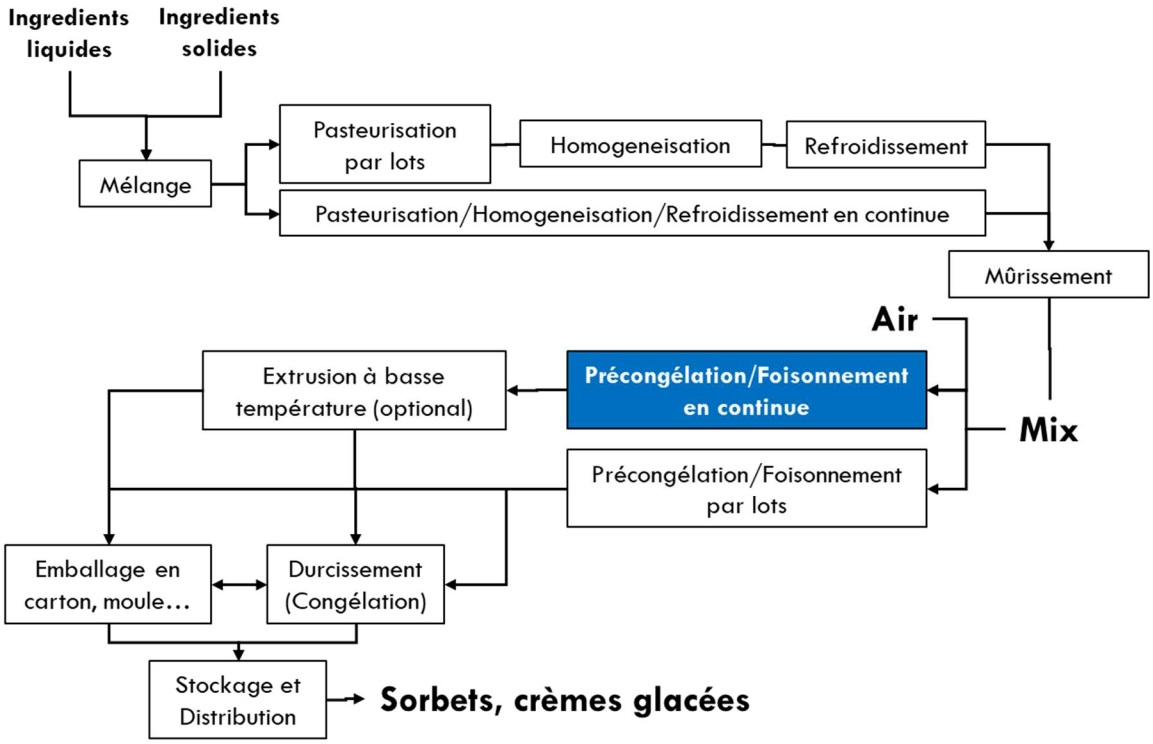

Figure 2. Schéma de production d'une crème glacée. L'étape sur laquelle se focalise cette étude est surlignée en bleu.

1.2 Etudes de la cristallisation de l'eau et du foisonnement dans des échangeurs de chaleur à surface raclée.

La Figure 3a présente un schéma d'échangeur de chaleur à surface raclée ECSR (en anglais : *scraped surface heat exchanger, SSHE*) utilisé pendant la précongélation des sorbets. Il comprend un tube cylindrique, refroidi par un frigorigène évaporant dans une double enveloppe, dans lequel tourne un rotor (*dasher*). Ce rotor porte un certain nombre de lames (*blades*) qui raclent constamment la surface d'échange. Le rotor peut prendre plusieurs formes (Figure 3b) ; il peut être plein ou creux. Sa forme impacte fortement le fractionnement des bulles et donc la texture du produit final.

Les échangeurs de chaleur à surface raclée sont utilisés depuis les années 1970 pour produire des sorbets et des crèmes glacées, mais ils sont également utilisés pour produire des coulis de glace à des fins énergétiques, pour cuire et pasteuriser des produits alimentaires liquides ou pâteux (crèmes dessert, soupes…). Ils sont également utilisés dans l'industrie chimique et cosmétique. Ils ont été l'objet de nombreuses études (voir la section 2) mais il y en a relativement peu dans le domaine de la production de sorbets et quasiment aucune étude ne porte sur la combinaison de la cristallisation et du foisonnement.

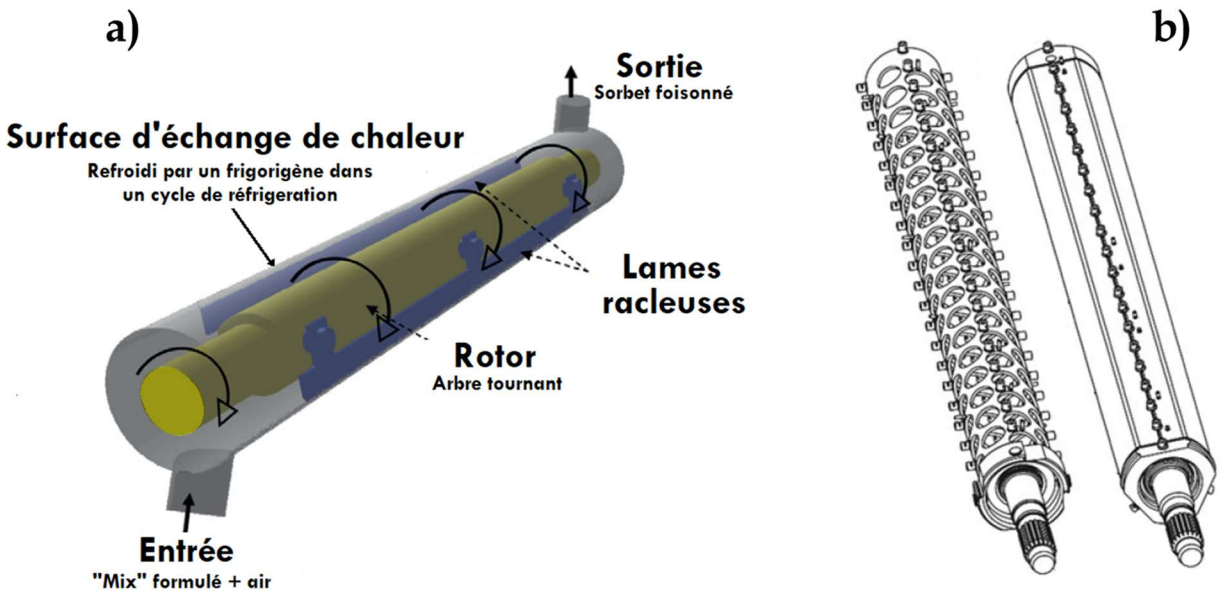

Figure 3. a) Schéma d'un échangeur de chaleur à surface raclée utilisé dans la production des sorbets (Adaptée de Yataghene and Legrand (2013), b) exemple des différents types de rotor : à gauche rotor creux, à droite rotor solide (Adaptée de Goff and Hartel (2013b))

1.3 Contexte et objectif de l'étude

D'un point de vue scientifique, l'étude de la production d'un sorbet foisonné au sein d'un échangeur à surface raclée offre l'opportunité d'explorer un procédé multiphasique dans lequel les phénomènes simultanés d'écoulement et de transfert thermique conduisent directement à la création d'une microstructure observable. La phase gazeuse est incorporée (*whipped*) dans le milieu par la rotation du rotor et des lames, fragmentant et dispersant les bulles initiales. Simultanément, les cristaux de glace sont produits sur la surface d'échange à partir de la phase liquide, ils sont ensuite arrachés par les lames et mélangés au reste du produit. L'interaction entre les 3 phases et l'évolution drastique des propriétés du mélange lors de la congélation rendent l'étude du système à la fois complexe et très riche en potentialités.

Cette étude s'inscrit dans la continuité d'études antérieures menées dans l'unité de recherché Génie des procédés frigorifiques (GPAN) d'IRSTEA (Institut national de recherche en sciences et technologies pour l'environnement et l'agriculture) pour mieux comprendre et maîtriser les phénomènes ayant lieu lors de la production de sorbets (et coulis de glace) dans des échangeurs à surface raclée et leurs influences sur la microstructure des aliments.

- Arellano, M. (2012). « Caractérisation expérimentale et modélisation de systèmes multiphasiques au cours du procédé de congélation à l'échelle pilote. Application à la fabrication de sorbets dans des échangeurs à surface raclée ». AgroParisTech. Paris, France.
- Gonzalez, J.E. (2012). « Contribution au contrôle par la modélisation d'un procédé de cristallisation en continu ». AgroParisTech, France
- Cerecero, Rosalia (2003). " Etude des écoulements et des transferts thermiques lors de la fabrication d'un sorbet à l'échelle du pilot et du laboratoire". Institut National Agronomique Paris Grignon, France.

Ces travaux portaient uniquement sur le cas de produits non foisonnés. La principale avancée attendue de cette étude est de voir l'influence des conditions opératoires en présence d'une injection d'air sur les écoulements, les transferts, la cristallisation et le foisonnement.

Les **questions scientifiques** auxquelles cette étude cherche à répondre sont les suivantes :

Question relative aux écoulements :

- Quelle est l'influence des conditions opératoires, notamment du débit d'air, sur la distribution des temps de séjour ?

Questions relatives aux transferts thermiques :

- Quelle est l'influence des conditions opératoires, notamment du débit d'air, sur l'intensité des transferts (relation entre température de sortie et température d'évaporation du fluide frigorigène) ?
- Peut-on modéliser le couplage écoulement/transfert/cristallisation au sein d'un ECSR en tenant compte de l'évolution drastique des propriétés physiques (notamment rhéologiques) lors de la congélation du sorbet ?

Questions relatives à la cristallisation :

- Est-il possible de mesurer de façon reproductible la distribution de taille des cristaux dans un sorbet foisonné à la sortie d'un ECSR ?
- Quelle est l'influence des conditions opératoires, notamment du débit d'air, sur la distribution granulométrique des cristaux ?
- Quels sont les paramètres les plus influents sur la granulométrie des cristaux ?

Questions relatives au foisonnement :

- Est-il possible de mesurer de façon reproductible la distribution de taille des bulles dans un sorbet foisonné à la sortie d'un ECSR ?
- Comment la distribution de taille des bulles est-elle influencée par les conditions opératoires durant le foisonnement combiné à la cristallisation ?
- Comment peut-on prédire la fragmentation des bulles d'après l'allure des écoulements : taux de cisaillement et d'élongation (issus des champs des vitesses simulées par CFD).

Le mémoire de thèse est structuré de la façon suivante : d'abord une synthèse bibliographique sera exposée en anglais, ensuite il sera présenté (en français) les principaux matériels et méthodes utilisés, puis le mémoire reprend trois articles et une communication (en anglais) afin de présenter les différents résultats obtenus et de les discuter, enfin une conclusion générale reviendra sur les questions scientifiques posées et proposera quelques perspectives.

Les résultats et leur analyse ont fait l'objet de trois articles rédigés en anglais et d'une communication dans un congrès international :

- Hernandez-Parra O., Plana-Fattori A., Alvarez G., Ndoye F.T., Benkhelifa H., Flick D. Modeling flow and heat transfer in a scraped surface heat exchanger during the production of sorbet. Journal of Food Engineering, Volume 221, March 2018, Pages 54-69
- Fatou Toutie Ndoye, Oscar Hernandez-Parra, Hayat Benkhelifa, Graciela Alvarez, Denis Flick. Influence of operating conditions on residence time distributions in a scraped surface heat exchanger during aerated sorbet production. Journal of Food Engineering, Volume 222, April 2018, Pages 126-138
- Oscar Darío Hernández Parra, Fatou-Toutie Ndoye, Hayat Benkhelifa, Denis Flick, Graciela Alvarez. Effect of process parameters on ice crystals and air bubbles size distributions of sorbets in a scraped surface heat exchanger. Soumis à International Journal of Refrigeration, accepted manuscript, Available online 6 April 2018
- Hernandez-Parra O.D., Plana-Fattori A., Alvarez G., Ndoye F.T., Benkhelifa H., Flick D. 2017 Prediction of bubble fragmentation during sorbet production in a scraped surface heat exchanger. International Conference on Food and Biosystems engineering (FABE). 14-17,6, 2017, Rhodes island, Greece.

Ce travail a fait l'objet de 3 communications supplémentaires au sein de congrès internationaux :

- Hernandez O.D., Ndoye F.T., Benkhelifa H., Flick D., Alvarez G. (2015) A low temperature microscopy technique for the measurement of ice crystals and air bubbles size distribution in sorbets. International Congress of Engineering and Food (ICEF). 14-18/6/15, Quebec, Canada. (oral presentation)
- Hernandez O.D., Ndoye F.T., Benkhelifa H., Flick D., Alvarez G. (2015) A discriminating microscopy technique for the measurement of ice crystals and air bubbles size distribution in sorbets. International Congress of Refrigeration. 16-22/8/15, Yokohama. Japan. (oral presentation)
- Hernandez-Parra O., Alvarez G., Flick D., Ndoye F.T., Benkhelifa H. (2015) Influencing the microstructure of aerated sorbets during continuous production in scraped surface heat exchangers. International Symposium on Delivery of Functionality in Complex Food Systems (DOF). 14-17/7/15. Paris

J'ai encadré trois stagiaires durant mon travail de thèse :

- Guillaume Laguerre : étudiant de l'Institut National des Sciences Appliquées – Strasbourg. (1 mois)
- Silvia Cometta. Étudiant en génie chimique à l'Universidad Nacional de Colombia – sede Bogotá, dans le cadre d'un programme d'échange avec l'Institut National de Physique, Matériaux et Electronique de Grenoble (6 mois).
- Kelly Sipewou : étudiant en Master Ingénierie des produits et des procédés à AgroParisTech (6 mois)

Ce travail de thèse a bénéficié du support financier du **Departamento Administrativo de Ciencia, Tecnología e Innovación (COLCIENCIAS)** du gouvernement de la République de Colombie par le bais du programme "**Generación del bicentenario, 2012**".

Références

Goff, H.D., Hartel, R.W., (2013). *Ice Cream*. Springer US.

Yataghene, M., Legrand, J., (2013). A 3D-CFD model thermal analysis within a scraped surface heat exchanger. Computers & Fluids 71, 380-399.

SYNTHESE BIBLIOGRAPHIQUE

2. Synthèse bibliographique

Ce chapitre vient en complément des parties bibliographiques des articles présentés ultérieurement, il a été rédigé en anglais et porte sur les points suivants :

- Ecoulements au sein des échangeurs à surface raclée
    - Ecoulements de liquides monophasiques
    - Ecoulements de mélanges gaz/liquide
    - Etudes de distribution des temps de séjour
- Cristallisation au sein d'échangeurs à surface raclée
- Foisonnement
    - Classification des mousses
    - Equipement de foisonnements
    - Caractérisation des mousses
    - Paramètres opératoires influençant le foisonnement
    - Théorie de la déformation et de la rupture des bulles
    - Influence de la formulation
- Modélisation de la cristallisation en échangeur de chaleur à surface raclée
    - Modélisation de la cristallisation par bilan de population
    - Application aux crèmes glacées et sorbets

Transport phenomena in scraped surface heat exchangers

2.1 Hydrodynamics within SSHEs

2.1.1 Single liquid phase flow patterns

(Abichandani et al., 1986a); Abichandani et al. (1986b); Härröd (1986a) have reviewed studies dealing with the flow pattern in SSHEs. And from these reviews and other works it is clear that a common approach to describe the flow phenomena of a single phase within a SSHE is to consider it as a superposition of an axial flow and a rotational flow, with possibly Taylor-Couette vortices according to the flow regime. This type of hydrodynamic has been reviewed in numerous works although not necessarily associated with SSHE (e.g. Fénot et al. (2011); Vedantam and Joshi (2006)). Therefore, only a general overview is given here on the subject.

The axial component corresponds to the flow through the annular space between the dasher and the internal heat exchanger wall and it has been treated as a classical Poiseuille flow, characterized by a Reynolds number:

$$Re_{ax} = \frac{\rho v^{2-n} D_h^2}{K} \tag{2.1}$$

The rotational component corresponds to the action of the rotating dasher and the scraping blades. However, the blades contribution when the ratio of diameters is between 0.5 to 0.9 has been shown to be negligible (Härröd, 1986a). Then, this component has been described as a Taylor-Couette flow (i.e. the flow between concentric cylinders in which one or the two are subjected to rotation) characterized by the Taylor number:

$$Ta = \sqrt{\frac{R_s - R_r}{R_r}} \frac{\rho D_h^n}{2^n} \frac{\left(\Omega R_r\right)^{2-n}}{K} \tag{2.2}$$

The existence of critical Taylor numbers, from which perturbations or instabilities appear forming patterns with characteristic vortex structures, has been shown experimentally and theoretically. In Figure 4a-c the different vortex structures presented in the literature are described.

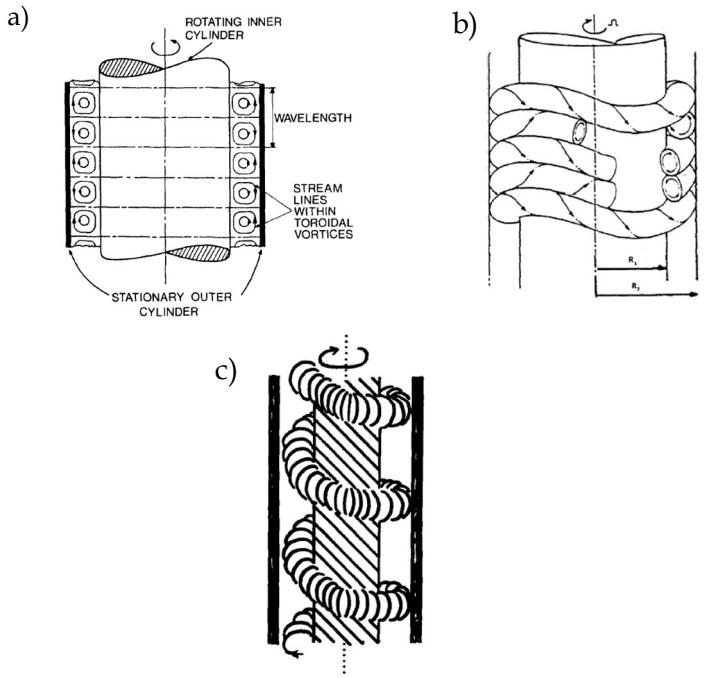

Figure 4. Flow patterns in Couette-Taylor and Taylor-Couette-Poiseuille flows with vortex characteristics: a) toroidal arrangement of vortex that comes in pairs with counter-rotation called Taylor vortex flows as presented by Härröd (1986a), b) azimuthal waves imposed on the Taylor vortices yielding the so called "wavy vortex" flow taken from Fénot et al. (2011) and c) "Spiral flow" pattern obtained when the axial flow stretches a Taylor vortex flow as presented by Härröd (1986a).

Once the two effects are combined, the axial flow displaces the instabilities yielding a variety of observable patterns depending on both Taylor and Reynolds numbers. A characteristic scheme is given in Figure 5. In general, under low axial Reynolds numbers the Taylor vortices move in the axial direction imitating a plug flow. Increasing Re_z, the toroidal arrangement of Taylor vortices is stretched to a spiral vortex flow (Figure 4c).

The critical values of *Ta* and *Re* at which regimes change have been extensively reviewed by Vedantam and Joshi (2006). It is noteworthy that critical values vary according to geometrical parameters like the size of the gap and the length of the cylinder.

As mentioned before, the classical approach consider the blades to have a negligible effect on the flow patterns observed (Härröd, 1986a), however several studies have found differences in the velocity profiles, critical values and wall shear rates between the Taylor-Couette-Poiseuille flow and SSHE. For instance, Wang et al. (1999) compared the angular velocity profiles of an analytical solution in laminar flow and experimental data obtained using a magnetic resonance imaging (MRI) technique for Newtonian and non-Newtonian fluids. They concluded that the blades have a non-negligible effect on flow patterns and

attributed this effect to a pressure gradient in the angular direction caused by the blades. (Dumont et al., 2000b; Mabit et al., 2003) investigated also the flow regimes and wall shear rates with an electrochemical technique. They concluded that hydrodynamics in SSHE and Taylor-Couette flows are not comparable since critical values, the formation and instability of vortices formed, and the high effect in wall shear rates due to the blades do not correspond. Using particle image velocimetry (PIV), Yataghene et al. (2011) investigated the flow patterns and velocity profiles in a transparent scaled SSHE with a zone sheared by the action of blades and another zone that was not. These authors observed a complete change of flow patterns between the two. Particularly, these authors established that tangential velocities changed because of a destruction of the hydrodynamic layer in the case of passage of the blade. Also, a reverse flow in axial velocity and radial velocity components in the exit and entrance zones were observed depending on operating conditions, although normally favored by increasing the rotation speed.

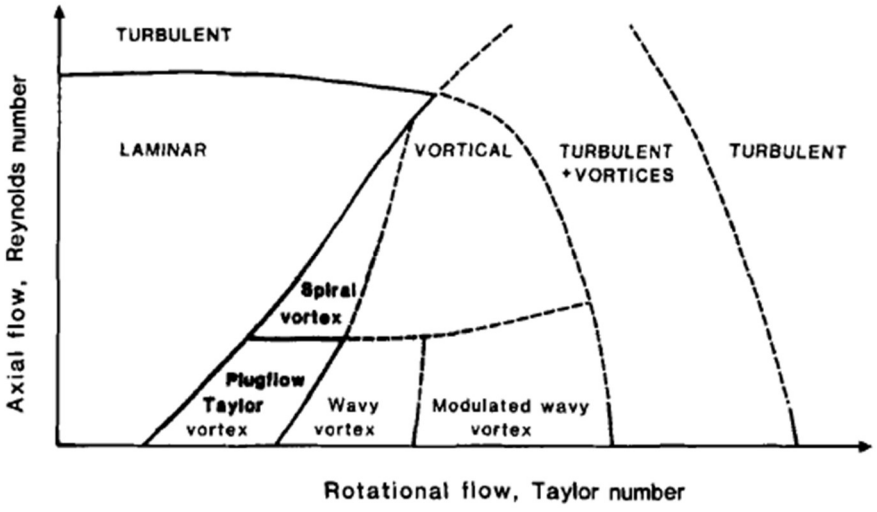

Figure 5. Schematic classification of single-phase flow patterns in SSHEs according to the axial flow represented by the Reynolds number and the rotational flow represented by the Taylor number. Taken from Härröd (1986a)

2.1.2 Two-phase gas/liquid flow

Literature concerning flow pattern in two-phase liquid/gas flow related to SSHEs is scarce. Only few studies were found in the literature consulted dealing with the flow patterns in Taylor-Couette flows. Particularly, Shiomi et al. (1993); (1995) described the air bubble/water flow in a vertical upward Taylor-Couette flow with internal cylinder rotation. They observed the flow patterns and described them according to the apparent shapes followed by the bubbles as dispersed bubbly, ring-form, single spiral, double spiral, triple spiral and transitional flows. Also, the authors described their observations using flow

regime maps showing that the liquid and bubble velocity as well as the inner cylinder rotation speed affect the pattern observed.

Djéridi et al. (2002) also studied the two-phase air/water upward flow in concentric cylinders with internal cylinder rotation. The authors compared the patterns observed with the corresponding value of transition between regimes in single-phase flows. The patterns observed followed the same shapes and descriptions shown in single phase flows presented above.

Hubacz and Wroński (2004) used a transparent Plexiglas horizontal concentric cylinder system with internal cylinder rotation to observe the flow patterns in nitrogen/water or nitrogen/glycerin flows. The authors observed several flow patterns which can be seen in Figure 6. The authors found that the flow regime was dependent on the ratio of internal and external diameter in the annulus, the power input per unit volume for the two-phase system and the ratio of gas-to-liquid volumetric flowrates.

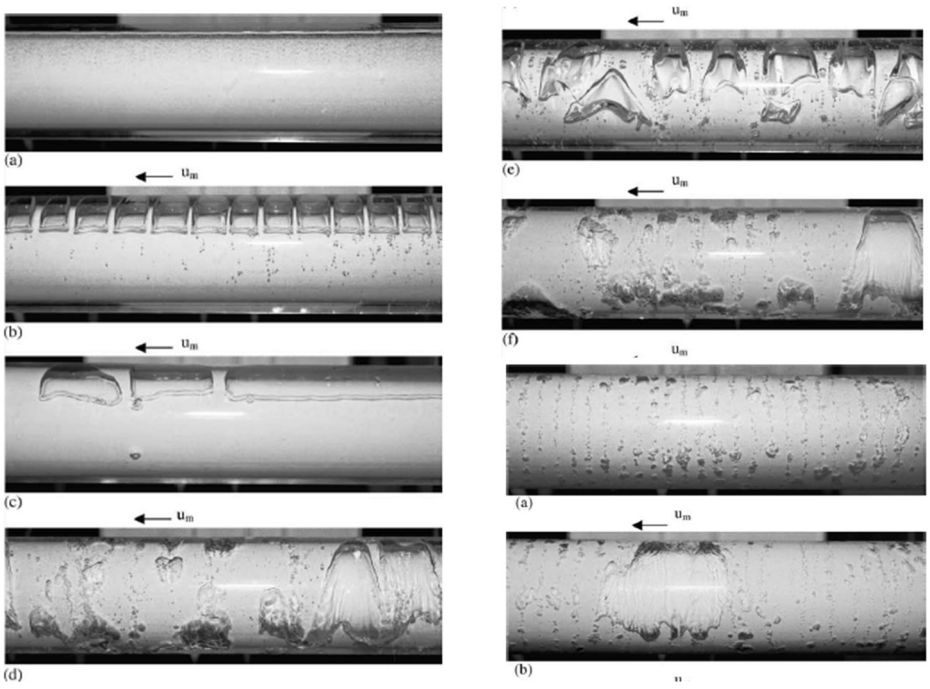

Figure 6. Taylor-Couette flow patterns observed by Hubacz and Wroński (2004): a) stratified flow, b) slug flow, c) first transition regime flow, d) periodic flow, e) disturbed slug flow, f) second transition regime, g) ring flow, and h) irregular ring flow.

2.1.3 Residence time distribution studies

The *residence time* concept was originally introduced by Danckwerts (1953) as a method for analysis and scale-up of continuous flow chemical reactors. Since its introduction it has been extended to include all sort

of continuous processing equipment, including heat exchangers, in applications relating to scale-up or design. It is based on the idea of following a small volume of material along the path traversed through the equipment studied and registering the time that takes for this volume to exit. The technique is usually based on the injection of a pulse of *tracer* (i.e. a substance that is incorporated in the streamlines of the flow) so that its concentration is measured at the exit of the equipment in time. This generates a distribution of times that tracer volumes reside inside the equipment studied (*residence time distribution*, RTD), such that it has the characteristics of a statistical probability distribution function that comes handy for analysis. Particularly, the first and second moments of this distribution (i.e. its mean or *normalized mean residence time* and its variance) become a reference that gives indications on how the flow develops inside the equipment analyzed.

Extensive reviews on RTDs in SSHEs have been presented already by (Arellano et al. (2013c); Rao and Hartel (2006)) and therefore, a brief account on the subject highlighting the most important aspects will be given here. For liquid flows passing through the exchanger it is clear that flow rate, rheology, dasher speed, number of blades, orientation of the exchanger (vertical or horizontal), isothermal, cooling or heating conditions, geometrical parameters such as length-to-diameter ratio and the diameters ratio influence the shape and values of the residence time distribution. Particularly, the shear thinning behavior represented in the flow index behavior in non-Newtonian fluids like ice cream mixes passing through the SSHE has been shown to be more important than the apparent viscosity for explaining the RTD results (Russell et al., 1997). On the other hand, the effect of all other operating conditions is not consistent among the different studies given that the variety of designs and properties used does not allow a thoroughly comparison. This was particularly highlighted by Arellano et al. (2013c) using a comparison of increasing effects shown in Table 1.

It is noteworthy that in cases of two-phase liquid/solid particle flows, it is necessary to differentiate the residence time distribution of the liquid from that of the particles (Alhamdan and Sastry, 1997; Chen and Ramaswamy, 2000; E.R.Alcairo and C.A.Zuritz, 1990; Ramaswamy et al., 1995a; Ramaswamy et al., 1995b), adding variables such as the particle size distribution, solid phase concentration or solid density to the conditions that determine the distribution observed. Also, Rao and Hartel (2006) remarked that when working with multiphase complex systems such as ice creams, since the product properties are dynamic and dependent on the time of processing, it is necessary to empirically determine the RTDs and verify them once a formulation has changed in order to improve the consistency of the data.

Table 1. Comparison of effects of increase in operating conditions on RTD distributions in SSHEs for non-Newtonian fluids. Adapted from Arellano et al. (2013c)

Reference	Fluid	Rotation speed effect	Product flow rate effect	Apparent viscosity effect
RTD studies under isothermal conditions				
Benezech and Maingonnat (1989)	Aqueous solutions of guar gum, CMC and sodium alginate	Broadened RTD	No effect on RTD	No effect on RTD
E.R.Alcairo and C.A.Zuritz (1990)	Single sphere suspended in CMC aqueous solution	Narrowed RTD	Narrowed RTD	No effect on RTD
Lee and Singh (1993)	Potato cubes with aqueous solutions	No effect on RTD	Narrowed RTD	Broadened RTD
Russell et al. (1997)	Carbopol	Broadened RTD	-	-
RTD studies under cooling conditions				
Russell et al. (1997)	Carbopol and ice cream mix	-	-	Broadened RTD
Belhamri et al. (2009)	Ice cream	Narrowed RTD	Narrowed RTD	-

Of special relevance for this work is the extensive review of RTD studies presented by Arellano et al. (2013c) which was developed within the group GPAN at IRSTEA. The authors obtained the RTD in an SSHE during sorbet production without foaming. They found that a reduction in product temperature leads to a broadening of the RTD curve and therefore an increase in the axial dispersion. This was explained by the fact that the radial temperature gradients affect greatly the viscosity of the product, and subsequently, the axial velocity increase. Also, with higher product flow rates the mean residence time decrease and the RTD curve narrows indicating a lower axial dispersion. Additionally, an increase in the rotation speed had no significant effect on the mean residence time; however, it broadens the RTD curve increasing the axial dispersion.

Under this perspective the work presented by Fayolle et al. (2013) becomes an interesting approach. In this work, RTDs for ice cream production using an SSHE were studied by coupling a proposed mathematical model with experimental measurements. The authors proposed that the flow could be modelled as a system of parallel plug flows with axial dispersion. The first one represents the zone near the stator wall where the ice crystallization taking place increase significantly the apparent viscosity by a higher ice fraction and lower temperatures and reduces the axial velocity. The second one represents the zone near the rotor. Both are connected through a radial mixing term that expresses the possible mass exchanges influenced by possible Taylor vortices and the blades action. Several resulting parameters were varied in the model to adjust the experimental data finding a good approximation of both approaches. Another interesting fact of this study is that it is the only one in the literature consulted for this review that deals with RTDs in SSHE using a flow that contains a gas even if the foaming conditions were held always constant and no effect of the foaming was considered.

Other systems in which air is included in liquids during a RTD study deal with agitated tanks or gas liquid mixers (e.g. Keshav et al. (2008); Madhuranthakam et al. (2009); Thijert et al. (1992)). It is remarkable from this studies that, as well as in the case on liquid/particle flows, it is necessary to differentiate the RTD of the liquid from that of the gas, and therefore other considerations are needed. For instance, Keshav et al. (2008) analyzed the liquid RTD in a Kenics static mixer and expressed the axial dispersion in terms of Reynolds, Froude and Galileo dimensionless numbers, which included a dependency on air volume fraction, consistency and flow index of the liquid phase, densities of both phases and gas phase velocity.

Crystallization in SSHEs

Crystallization in SSHE for production of ice cream has been studied extensively and is described in Figure 7. Cook and Hartel (2010) grouped previous studies into a proposed mechanism of crystallization for ice cream production:

1. Because of a strong temperature difference, an ice layer forms on the wall, and the scraper blade removes the ice layer into the bulk. Depending on how well the scraper blade removes ice from the wall, there may be a little residual ice left behind, if only in microscopic crevices, to seed the next round of crystal nucleation, or there may be a relatively thick layer of ice left behind that would simply keep growing.
2. Between the pass of scraping blades, the cold wall-zone temperatures cause the existing ice to grow at an accelerated rate, possibly in a dendritic fashion parallel to the freezing surface.
3. The ice layer (probably some form of slush containing also concentrated mix) scraped off is dispersed by the scraper blade into the warmer bulk medium, which causes this layer to melt into many disc-shaped crystals. Toward the freezer entrance, much of the ice dispersed into the warmer bulk fluid is likely to melt and bring down the bulk temperature. Farther along the length of the freezer, more ice would survive. By the freezer exit, the bulk ice crystals would be much larger than the new crystals being transported from the wall.
4. Those surviving crystals go into a ripening stage of crystals that would give rise to the final crystal size distribution. This wider crystal size distribution would accelerate ripening and encourage the large crystals to grow at the expense of the small crystals. Energy input from the dasher, due to friction at the wall and viscous dissipation, also can contribute significantly to crystal melting and ripening

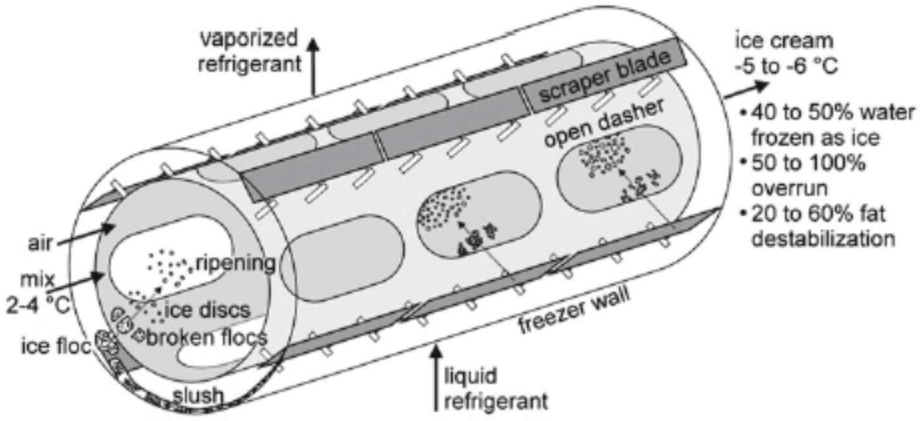

Figure 7. Mechanism of ice crystallization during ice cream production in a SSHE as given by Cook and Hartel (2010)

Foaming

2.2 Foams. Classification and basic characteristics

Foams are dispersions of gas into a continuous liquid, solid or semi-solid phase. They appear in a large number of consumer products and foods are not the exception. Although there exist solid foams, all foams are produced using an initial liquid continuous phase (Germain and Aguilera, 2014). The gas phase in foams arrange in bubbles with particular two- or three-dimensional structures with the continuous liquid phase acting as the *lamellae* between them. Usually these lamellae have small thickness, however, depending on the amount of liquid present, the shapes of bubbles can range from spherical in foams with larger liquid contents (varying from *bubbly liquids* to *wet foams*) to special polyhedral shapes in foams with very low liquid content (*dry foams*) (see Figure 8). It is noteworthy that, as pointed out by Campbell and Mougeot (1999), most aerated foods contain low amounts of air incorporated to the continuous phase such that it is common that bubbles inside food foams tend to be spherical rather than polyhedral forms.

Particularly, aerated sorbets and ice creams are examples of aerated foods with spherical bubbles, though a non-negligible amount of air is introduced into their structure (up to 50% volume). All foams consist of a mixture of immiscible phases with different densities, and therefore they are inherently thermodynamically unstable (Cantat et al., 2013) and as a consequence they tend to disintegrate separating the constituent phases.

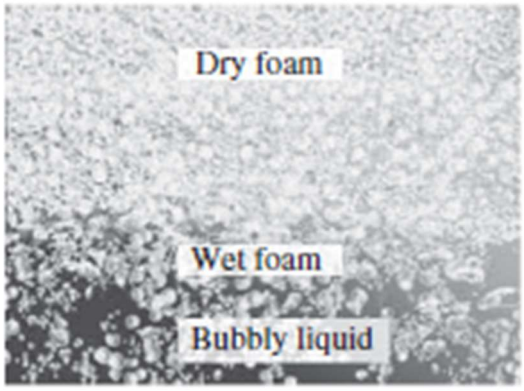

Figure 8. Classification of foams according to the amount of liquid in the interface between the gas phase. Picture taken from Cantat et al. (2013)

2.3 Foaming equipments

Foaming is defined here as a unit operation in which a foam is generated. The inherent instability of foams causes the foaming operation to be consisted on two steps carried out sequentially or simultaneously: the dispersion of gas in the liquid phase, and a stabilization procedure for delaying the destruction of the foam generated by the dispersion. The mechanisms of stabilization/destabilization of foams occur on a microscopical scale, and therefore, the equipment used for foaming is defined on the basis of the dispersion step.

The foaming equipment is also defined by the size of the operation. For low-volume operations, food foaming is done almost exclusively by the action of an impeller entraining air from a free surface or dispersing it from a sparger beneath the impeller (e.g. fermentation, carbonated drinks). It is a common practice for foods to use wire whips, that range from manually agitated whiskers (i.e. standard kitchen utensils) to planetary mixers or semi-industrial mixing vessels equipped with motor-driven whiskers with a variety of designs available (see Figure 8). In this type of equipment, the energy introduced by the impeller beating the liquid system provides the necessary energy to disperse the air in the headspace creating the foam. Also, in such equipment the liquid amount is limited and fixed while the air supply is as large as desired. The air volume fraction and the bubble size distribution on the foam will evolve depending on the balance between the entrainment and disengagement of air between the head space and the foam.

On the other hand, for large volume operation (normally operating continuously) it is common practice to use dented rotor-stator devices and scraped surface heat exchangers, the latter specially used when it is necessary to combine the foaming process with heat transfer as is the case of ice cream and sorbet production.

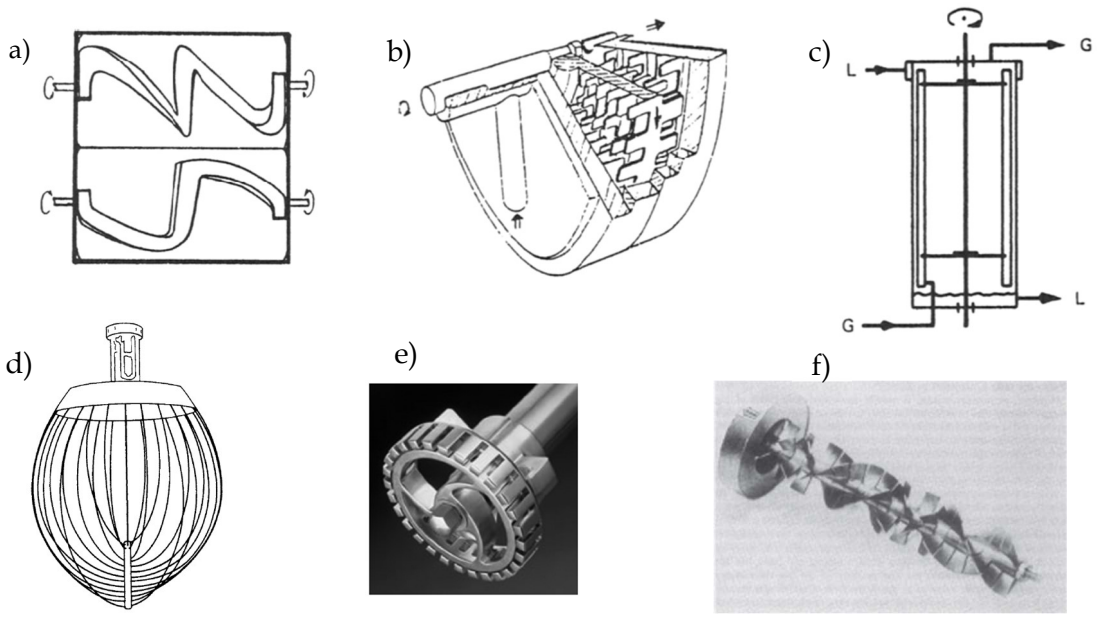

Figure 9. Gas/liquid mixing equipment commonly used for highly viscous liquids: a) dough mixer, b) dynamic in-line or rotor-stator mixer, c) scraped film contactors, d) wire whip for use with planetary mixers, e) rotor-stator impeller, f) static mixer. Images a), b) and c) are taken from Middleton (1997), d) from Green and Perry (2007), e) and f) from Chhabra and Richardson (2011)

2.4 Foam characterization

Regarding the characteristics of foams from a processing point of view, some macroscopical properties are used as control parameters for evaluating the quality of products and operation. Campbell and Mougeot (1999) grouped them in air content, bubble size distribution, rheology, texture, foam stability, and foamability of the liquid phase. Foam rheology and texture are dependent on the air content and the bubble size distribution. The foamability of the liquid phase is a function of the composition and the presence of surfactants and will be analyzed later. Therefore, here we consider three parameters as the most important: air volume fraction, bubble size distribution, and foam stability.

2.4.1 Air volume fraction

Perhaps the main control parameter is the air content of the obtained foam. Since the first observable effect upon foaming is an increase in volume due to the inclusion of the low gas density into the liquid. A basic characterization is the volume fraction occupied by the gas within the foam (ϕ_{air}):

$$\phi_{air} = \frac{V_{air}}{V_{total}} \tag{2.3}$$

In the particular case of ice cream related products, it is common to define another parameter, the *overrun* (*OR*). Overrun is defined as the volume of gas added per unit of liquid volume added to the foaming operation and can be calculated in several ways (Goff and Hartel, 2013a):

$$OR = \frac{\rho_{liquid}}{\rho_{air}} - 1 \tag{2.4}$$

For liquid foams overrun is related to air volume fraction by:

$$OR = \frac{\phi_{air}}{1 - \phi_{air}} \tag{2.5}$$

In the case of ice cream and aerated sorbets, care must be taken since the ice fraction present in the product has a lower density than the original liquid mix. From a mass balance around the product it can be shown that:

$$\phi_{air} = 1 - \rho_{sorb}\left(\frac{w_i}{\rho_i} + \frac{1 - w_i}{\rho_{mix}}\right) \tag{2.6}$$

2.4.2 Bubble size distributions (BSD)

Foams that contain bubbles of equal size (*monodisperse foams*) are not common on food materials (*polydisperse foams*). Also, bubble in different foams can present variable shapes and change during and after processing. Hence, there is not one bubble size but distributions of bubble sizes. Even in the case of spherical bubbles (i.e. aerated sorbets and ice cream), these distributions influence rheology and textural perceptions of food foams and therefore, the measurement and characterization of the distribution is a key parameter (Campbell and Mougeot, 1999).

A wide range of experimental techniques have been developed depending on the mean bubble size and the characteristics of the food product. These include (i) light microscopy techniques (e.g. Labbafi et al.

(2007); Fu and Ishii (2003)), (ii) scanning electron microscopy (SEM) (e.g. Chang and Hartel (2002b)), (iii) transmission electron microscopy (TEM) (e.g. Chang and Hartel (2002b)), (iv) confocal microscopy (e.g. Caillet et al. (2003)), (v) magnetic resonance imaging (MRI) (e.g. Simoneau et al. (1993)), (vi) acoustic probes, (vii) ultrasound (Scanlon et al., 2008), (viii) X-ray tomography (Barigou and Douaire, 2013).

Particularly for ice creams, light microscopy has been used because bubble sizes range from 1 – 100 μm (Goff and Hartel, 2013a). Necessary adaptations have been implemented in order to control temperature and preserve the structure from mechanical stresses such as refrigerated glove boxes (Chang and Hartel, 2002b), or special visualization cells (Labbafi et al., 2007). Caillet et al. (2003) used an optical microscope equipped with an optical fiber to provide an episcopic coaxial lighting on the sample to observe the structure in ice cream samples previously immersed in liquid nitrogen and polished.

To characterize a BSD in most practical cases it is common practice to use arithmetic means or Sauter mean diameters:

$$\overline{d} = \frac{\sum_{i=1}^{n_{bin}} n_i d_i}{\sum_{i=1}^{n_{bins}} n_i} \tag{2.7}$$

$$\overline{d}_{3,2} = \frac{\sum_{i=1}^{n_{bin}} n_i d_i^3}{\sum_{i=1}^{n_{bins}} n_i d^2} \tag{2.8}$$

In some cases, especially for modelling purposes (e.g. Azizi and Al Taweel (2007)), the distribution is characterized using assigned probability distribution functions (ψ) (i.e. gamma, normal, lognormal, etc).

For instance, Fradette et al. (2006) reviewed the prediction of bubble Sauter mean diameter in gas/liquid dispersions produced using static mixers in laminar regime. The author found that correlations are usually based on Reynolds number defined for such kind of equipment, as well as Weber numbers based on the bubble size. It can be extracted from this work and the correlations obtained that the mean diameters depend on properties such as densities of both phases, surface tension and rheology of the liquid however in a complex way.

Djelveh et al. (1994) found that Sauter mean diameter of model foams is independent of operating conditions in columns operating in a similar way to vertical scraped surface contactors, while Thakur et al.

(2003b) found that Sauter mean diameter of bubbles in foams exhibits a small tendency on diminish with an increase in the rotor volume and is mainly a function of the intensity of shear forces.

Thakur et al. (2003a); (2003b) noticed that an increase in rotational speed in continuously agitated columns and tanks had an effect on bubble Sauter diameter and apparent viscosity that followed a qualitatively general diminishing tendency; however, their values are different from each formulation prepared. Besides, the Sauter mean diameter effect is reduced as rotation speed surpasses some value that depends on the formulation. Oppositely, the viscosity effect increases once this rotation speed value is surpassed apparently because of a counterbalance effect of the diminished bubble size on the shear-thinning serum behavior. Therefore, from this work it can be extracted that there is an optimal rotation speed range that allows an effective power use and avoid the decrease in foam stability.

Mary et al. (2013) applied a dimensional analysis approach to model the bubble mean diameter in a rotor-stator mixer. Although the authors found that seven dimensionless numbers influence the behavior of the Sauter mean bubble diameter, also a good correlation using only the capillary number was found, even if the full correlation is better. The authors proposed that the final bubble size distribution obtained after a foaming process is a result of a dynamic equilibrium between bubble breakage and bubble–bubble coalescence.

2.5 Foam stability

Foam stability is a very important control parameter since it is expected that the foam food keeps stable at least until consumption, however it is only possible to evaluate once the foam is already formed. The phenomena involved in the foam destabilization mechanism in static foams have been classified as (1) disproportionation, (2) creaming, (3) drainage and (4) coalescence (Aguilera and Lillford, 2008).

1. *Disproportionation***.** For a bubble to exist surrounded within a liquid and not to be crushed, it is necessary that a balance between the forces exerted by the internal bubble pressure, the surrounding liquid pressure and the interfacial tension be stablished. It can be shown that, for an isolated spherical bubble in thermodynamical equilibrium (Cantat et al., 2013; Tester and Modell, 1997):

$$\Delta P = P_{bubble} - P_{liquid} = \frac{4\sigma}{d} \tag{2.9}$$

Therefore, the pressure within an internal bubble must be higher than that of the liquid. However, this positive pressure difference (also called *Laplace pressure*) and the fact that

the gas phase is partially soluble on the liquid phase, provoke a difference in the chemical potentials of air in the bubble and the liquid, and the subsequent establishment of air mass transfer from the bubble to the liquid. Also, it can be seen from equation (9) that the larger the bubble the lower this internal pressure.

Under this perspective, when bubbles of different sizes are present, pressure differences vary for different bubble sizes, as well as their internal pressures. Since the solubility of gases in liquids increases with pressure, the concentration of air at interfaces on larger bubbles are lower than those of small ones, promoting the air mass transfer to go from the smallest bubbles to the large ones. This effect, however, further increases the size of larger bubbles making their pressure even lower. In gross, an enlargement of larger bubbles at expense of disappearance of small ones is observed. This phenomenon is called *disproportionation* and is the gas version of the *Ostwald ripening* observed in crystals.

2. *Drainage and creaming*. Another phenomenon of interest in the destabilization of foams is the flow caused by the imbalance between capillarity, viscosity and gravity forces in the liquid lamellae. Its main result is the retreat of liquid downwards leaving the bubbles displaced upwards. As a consequence of this flow, lamellae are thinned and eventually could be ruptured which leads to further destabilization. Also, the upper part of the foam reduces its liquid volume fraction and even bubbles could change their spherical form to rearrange as dry foams. This phenomenon is called *drainage* and has been recently reviewed by Kruglyakov et al. (2008) for static foams. According to the authors, the studies on drainage in foams can be carried out using (i) determining the liquid flow through the foam, (ii) determining the liquid velocity that exits the foam, (iii) measuring the foam syneresis after applying different pressure drops, (iv) free drainage and (v) forced drainage (adding a wet foam over an already dry foam). *Creaming* is basically the same phenomenon but originated on the buoyancy of the bubbles pushing upwards, which displaces the liquid down. It has been analyzed classically using sedimentation theory, and hence, commonly described using the Stokes equation of terminal velocity of spheres in stagnant Newtonian liquids as the rising velocity of bubbles:

$$v = \frac{d^2 g\left(\rho_{liquid} - \rho_{gas}\right)}{18\mu} \tag{2.10}$$

Recently, Narsimhan (2010) proposed a model for simulation of monodisperse foams formation and creaming using a coupled CFD-population balance approach with bubbles

approximated as deformable spheres. This was later extended by Sattar et al. (2013) including variable volume characteristics in the foam layer. Their results were expressed in forms of foam phase diagrams showing the transition from bubbly liquids to foams

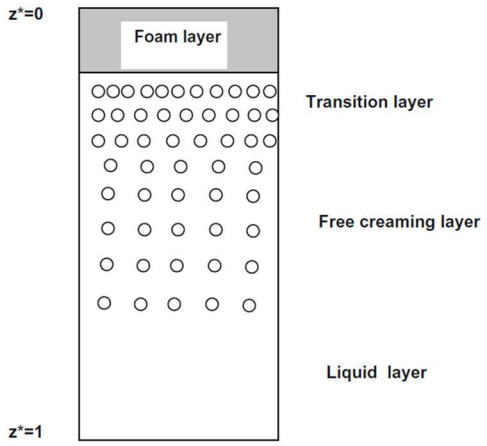

Figure 10. Zones formed during creaming of static foams. The movements on the liquid films and the rising bubbles create layers differentiated by the density of bubbles, from the bubble-free liquid layer at the bottom, a free creaming or bubbly liquid with bubbles not interacting among them up to a semi-dry or dry foam layer on top. Taken from Narsimhan (2010).

3. *Coalescence*. Drainage and creaming contribute to the loss of thickness in the foams lamellae but they do not imply the destruction of the foam. It has been shown that the final rupture is based on the increased probability of reaching a critical thickness. This probability variation is caused by the imbalance of forces present on those thinned lamellae. In food foams it has extensively been shown that equilibrium and dynamical properties of the interfaces, particularly influenced by the inclusion of macromolecules with surfactant properties like proteins or carbohydrates, affect not only the critical thickness value but the probability of film rupture (Xu et al., 2003). Once food foams coalesce there is a loss in textural and organoleptic qualities with a subsequent decrease of appreciation by the consumers.

2.6 Influential operating conditions on foaming

From an operational point of view, it is not only important to relate the air content and the BSD parameters to the operating conditions, but also to the energy cost of the operation. Again, in this matter, the air dispersion step holds the key influencing parameters.

The energy consumption is usually evaluated through the power ($\dot{W}$) or the power per unit volume of mixture. In the case of liquid mixing, this operation is commonly carried out in vessels agitated by an impeller of a determined design. Then, the evaluation of the power used is accomplished defining a dimensionless number called the *power number, Po*, or *Newton number*, *Ne* (Green and Perry, 2007):

$$Po = Ne = \frac{\dot{W}}{\rho_{liquid} N^3 D^5} \tag{2.11}$$

In this definition, D is the impeller diameter. The power number is then correlated to different geometric ratios within the vessel and to the Reynolds number based on the impeller diameter:

$$Re = \frac{\rho N D^2}{\mu} \tag{2.12}$$

An example of such correlation is given in Figure 11. For low Reynolds it can be observed an inverse proportionality in the relation between the power number and the Reynolds number, which is an indicative of the prevalence of the viscous forces over the inertial. In general, at high Reynolds numbers the power number tends to stabilize. The proportionality constant is shown to be dependent on the tank and impeller designs.

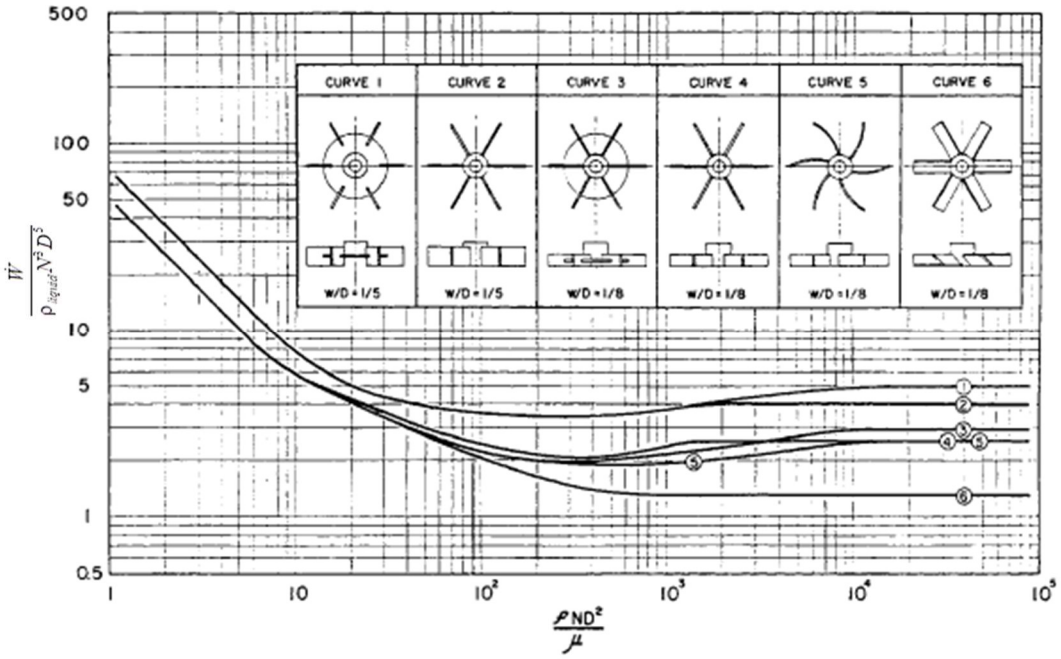

Figure 11. Example of Po as a function of Re for liquids mixed in stirred tanks with different impeller configurations. Taken from Green and Perry (2007)

Studies on gas/liquid mixing in stirred tanks follow this tendency; however, the observed power number is different from the degased power number. A power number, commonly written as Po_g indicating that the power used in the definition is related to a system with aeration, is used in opposition to the *Po* used for unaerated liquid mixing. Additionally, the effect of the introduction of a gas flow and the inertial force of the impellers is indicated by a new parameter called *the gas flow number*, Fl_G, or *aeration number*, N_{ae}:

$$Fl_G = N_{ae} = \frac{\dot{V}_g}{ND^3} \tag{2.13}$$

where $\dot{V}_g$ is the gas volume flowrate introduced. Then, again, depending on the configuration and geometric ratios a curve or correlation is produced. An example is shown in Figure 12.

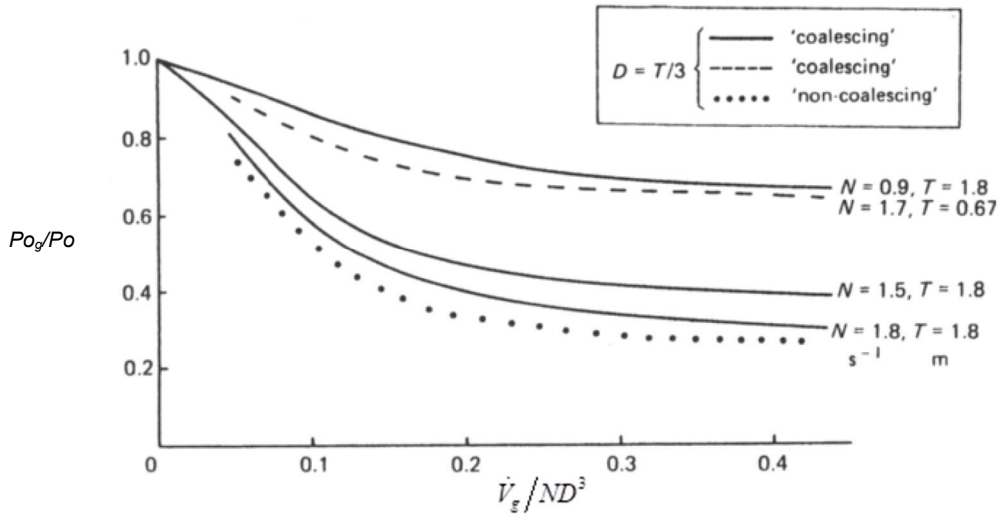

Figure 12. Example of Po_g/Po vs N_{ae} for a gas/liquid mixing in agitated vessels using Rushton turbines. Taken from Middleton (1997)

Also, in agitated-tanks gas/liquid mixing has been evaluated using the Froude number ($Fr = \dot{N}^2D/g$). For instance, for a six-blade Rushton turbine and six-blade Smith turbine impellers, the following correlation has been presented (Green and Perry, 2007):

$$\frac{Po_g}{Po} = \left[1 - \left(b - a\mu\right)\right] Fr^d \tanh\left(cN_{ae}\right) \tag{2.14}$$

In this expression *a, b, c* and *d* are adjustable constants dependent on the geometrical parameters of the impeller. When dealing with non-Newtonian liquids, aeration and foaming has been described using generalized Reynolds numbers. Particularly, Cheng and Carreau (1994) analyzed the aeration of a power-law liquid (consistency index *k* and flow index *n*) using a mixer equipped with helical ribbon impellers. For their analyses, a generalization of Reynolds number was proposed using an effective viscosity from an approximation by Metzner and Otto (1957) which continuous to be used nowadays. If the effective shear rate is supposed to be proportional to the impeller rotation speed with constant K_S, then the Reynolds number can be expressed as:

$$Re_g = \frac{\rho_{liquid}\dot{N}^{2-n}D^2}{kK_S^{n-1}} \tag{2.15}$$

An example of the relationship between the ratio of aerated-to-non-aerated power number and the Reynolds number is shown in Figure 13.

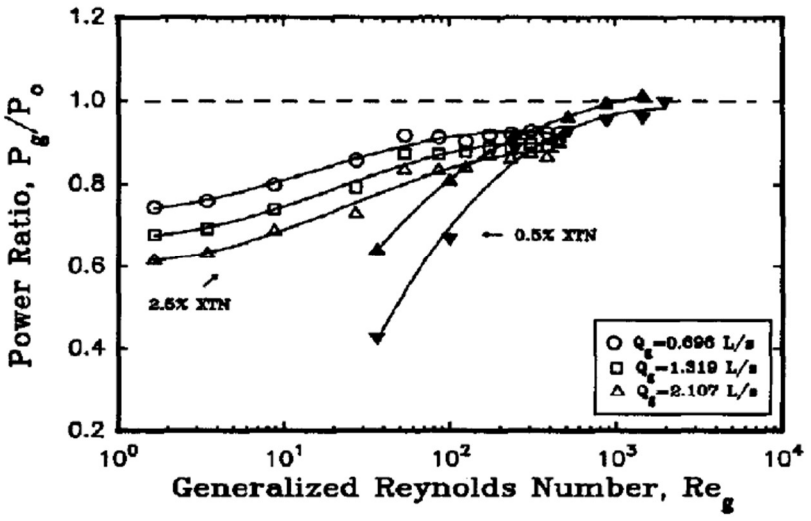

Figure 13. Effect of *Re* on the power ratio Po_g/Po for aeration of xanthan aqueous solutions using helical ribbon impellers at three air flowrates. Taken from Cheng and Carreau (1994)

Djelveh et al. (1994) evaluated the aeration of a model food in a vertical column equipped with internal paddles simulating a SSHE (the more internal paddles, the more similar to SSHE). In their equipment a gas sparger introduces the air in the system. The authors found that the foam density diminishes with increasing rotor speed and the number of paddles. This effect is attributed to the mixing occurring close to the paddles.

Indrawati et al. (2008) used a batch configuration consisting of a conical cup equipped with a mechanical whipper. They adjusted impellers of different diameters to make foams from buffered solutions of sodium caseinate and whey protein. They found that increasing the impeller rotation speed made foams with higher stability; lower apparent viscosity and that most of the energy input was expended as viscous dissipation.

2.7 Theory of deformation and rupture of bubbles

The mechanism for a bubble break up clearly depends on the hydrodynamic conditions around it, as well as the possible inherent instabilities between the bubble and the surrounding media. Liao and Lucas (2009) have classified the purposed mechanisms into four categories: (1) viscous shear stress; (2) turbulent shearing; (3) erosive breakup; and (4) interfacial instability. Also, simple empirical approaches have also been used for modelling in systems with bubble breakup

2.7.1 Viscous shear stress

Since the work of Taylor (1934) it is known that, even in a laminar flow, bubbles and drops can be subjected to deformation by a viscous stress to a point that interfacial forces cannot hold the bubble together and ruptures. The force balance in these situations is expressed in terms of the Capillary number defined by the ratio between viscous and surface tension forces.

$$Ca = \frac{\mu\dot{\gamma}}{\sigma} r_{bubble} \tag{2.16}$$

A critical Capillary number, Ca_{cr}, must be surpassed for a viscous stress shear to break a bubble. Grace (1982) showed that this value depends on the ratio of the viscosity the fluids involved ($p = \mu_g/\mu_l$) and on the type of flow the bubble is subjected to (i.e. rotational, extensional, etc.). A number of works later have attempted to find a correlation describing how the critical capillarity number changes in different flow configurations. A review of some expressions found in the literature is given in Table 2.

Table 2. Proposed correlations for Ca_{cr} for different flow configurations

Reference	Equation	Range of p	Type of flow	Comments
Acrivos and Lo (1978)	$Ca_{cr} = 0{,}145p^{-1/6}$	-	Pure elongation	-
Hinch and Acrivos (1980)	$Ca_{cr} = 0{,}0541p^{-2/3}$	-	Simple shear	-
Bentley and Leal (1986)	$Ca_{cr} = 0{,}145p^{-1/6}\alpha^{-1/2}$	-	Mixed to pure elongated	α is a parameter defined to quantify the relative deformation character of flows
Müller-Fischer et al. (2008)	$Ca_{cr} = 2{,}465p^{-0{,}171}$	$\sim 3{,}09\times10^{-7}$	Simple shear	-

For pure extensional flows in Newtonian liquids, Liao and Lucas (2009) have summarized the experimental results and the modes of breakup occurring on bubbles and droplets in a plot of the critical Capillary number vs the viscosity ratio (see Figure 14a). When the capillary number is increased suddenly well above the critical value, the bubble is rapidly elongated into a thin cylindrical form with a wavy surface that collapses giving birth to several smaller bubbles. On the contrary, close to the critical value, the bubble breaks by necking until division into two equal big fragments and much smaller surrounding bubbles.

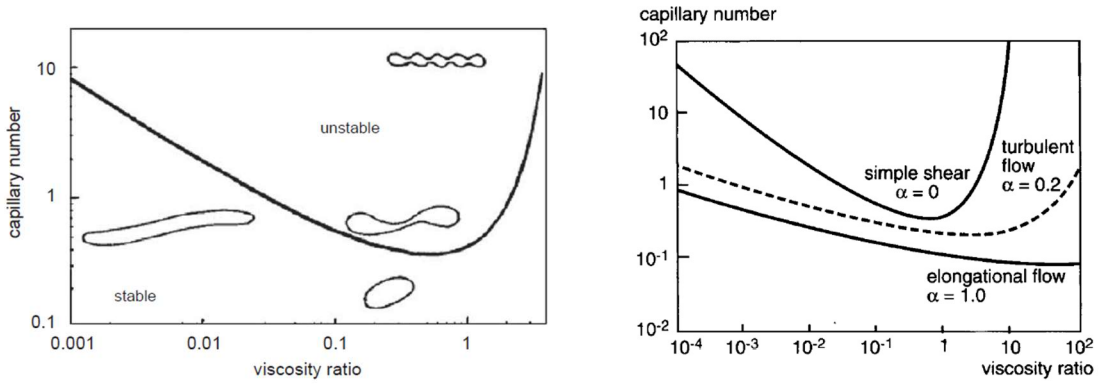

Figure 14. Critical capillary number as a function of the viscosity ratio: a) For pure extensional flow (Liao and Lucas, 2009) and b) for different kind of flows (Groeneweg et al., 1994)

Although the critical condition must be accomplished, the breakup of the bubble is not instantaneous. The viscous shear must be applied a certain amount of time for the bubble to break. The time required is a function again of the ratio of viscosities and has been expressed as (Liao and Lucas, 2009):

$$t_{breakup} = \frac{\mu_{liquid} d}{2\sigma} f(p) \tag{2.17}$$

Where $f(p) = c_1 p^{c_2}$ or $f(p) = c_1 + c_2 \log(p^{c_3}) + c_4 \log^2(p^{c_3})$. In these equations each constant c_i correspond to adjustable constants depending on experimental data used in every application desired.

In practical cases bubbles are not subjected to pure extensional or pure elongational flows but to intermediate and dynamical situations. As seen in Table 2, Bentley and Leal (1986) proposed a correlation with a factor, α, that takes into account the type of flow surrounding the bubble. Yang and Manas-Zloczower (1992) proposed for describing the type of flow, the dispersive mixing index λ_{MZ} defined as

$$\lambda_{MZ} = \frac{|\mathbf{D}|}{|\mathbf{D}| + |\mathbf{\Omega}|} \tag{2.18}$$

where **D** and **Ω** are the rate of deformation and vorticity tensors within the flow. Using this parameter, Vyakaranam and Kokini (2012) used the correlation by Bentley and Leal (1986) and this parameter to calculate a critical value after a CFD simulation in a twin-screw extruder to find a correlation for the critical capillary number in air bubbles disperse in honey (viscosity ratio = $1{,}42\times10^{-7}$):

$$Ca_{cr} = 1{,}9174\lambda_{MZ}^{-1{,}555} \tag{2.19}$$

2.7.2 Turbulent shearing

In turbulent flows, the pressure or velocity fluctuations around the bubble interface or a hitting eddy present in the continuous phase can interact with the bubble and get to deform it to a point that ends up dividing it into two or more new bubbles. This interaction does not exclude the effect of viscous shear forces on breakage of bubbles, however the viscous shear effect is often considered negligible compared to the turbulent effect. Hinze (1955) expressed the balance of inertial forces acting at the interface of the bubble and the interfacial tension as the Weber number, *We*, in such a way that a critical value determines the breakup criteria.

$$We = \frac{\rho v^2 d}{\sigma} \tag{2.20}$$

The critical value, as well as the rate at which bubbles breakup occurs, has been the subject of numerous works in the literature. Models of how this turbulent breakup occurs propose different quantities that are required to reach a critical value. After some mathematical work all can be translated into critical Weber numbers and rate of deformations. (Liao and Lucas, 2009) have classified the models into those who propose as critical values:

1. A greater turbulent kinetic energy of the particle
2. A greater velocity fluctuation around that particle surface
3. A greater turbulent kinetic energy of the hitting eddy
4. An inertial force of hitting eddy greater than the interfacial force of the smallest daughter bubble
5. Combination of criteria 3 and 4.

Some examples and equations for critical bubble number are given in Table 3.

Table 3. Examples of critical Weber number for turbulent shearing breakup of bubbles and drops according to their proposed models (Liao and Lucas, 2009).

Criteria	We_{cr}
1	$We_{cr} = \frac{\rho \varepsilon^{2/3} d^{5/3}}{\sigma} \geq C$
2	$We_{cr} = \frac{\rho v_\lambda^2 d}{\sigma} \geq 12\left(2^{1/3} - 1\right)$
3	$We_{cr} = \frac{\rho \varepsilon^{2/3} d^{5/3}}{\sigma} \geq \frac{12 C_1}{C_2 \left(\frac{\lambda}{d}\right)^{11/3}}$
4	$We_{cr} = \frac{\rho \varepsilon^{2/3} d^{5/3}}{\sigma} \geq \frac{12}{C_1}$
5	$We_{cr} = \frac{\rho v_\lambda^2 d_{smallest\ daughter}}{\sigma} \geq 4$

2.7.3 Shearing-off and interfacial instabilities

When bubble sizes increase, other breakup mechanisms can appear or become more visible. For instance, one mechanism called *shearing-off* or *erosive breakup* was observed and described by Fu and Ishii (2003). These authors observed that in a vertical air-water flow in slug regime, when the difference between the bubble and the liquid velocities at the interface is large enough, the lower interface of the slug bubble became instable and the bubble eroded giving birth to a rim of smaller bubbles. This was explained by the internal gas velocity profile entering into the liquid film creating the new bubbles. Also, phenomena like Rayleigh-Taylor or Kelvin-Helmholtz instabilities (i.e. instabilities produced from acceleration of a lighter fluid into a heavier one) can appear in bubbles, foams and froths (Stewart et al., 2013).

2.8 Influence of the formulation

As said before, the composition and formulation of the liquid from which foams are being made are important to understand the different mechanisms underlying its stability. In food foams several substances act in a way that promotes the increase or decrease of surface tension and rheological properties, and the mechanisms and time scales at which these changes occur. In Figure 15 a schematic of the relationships of these different additives is presented.

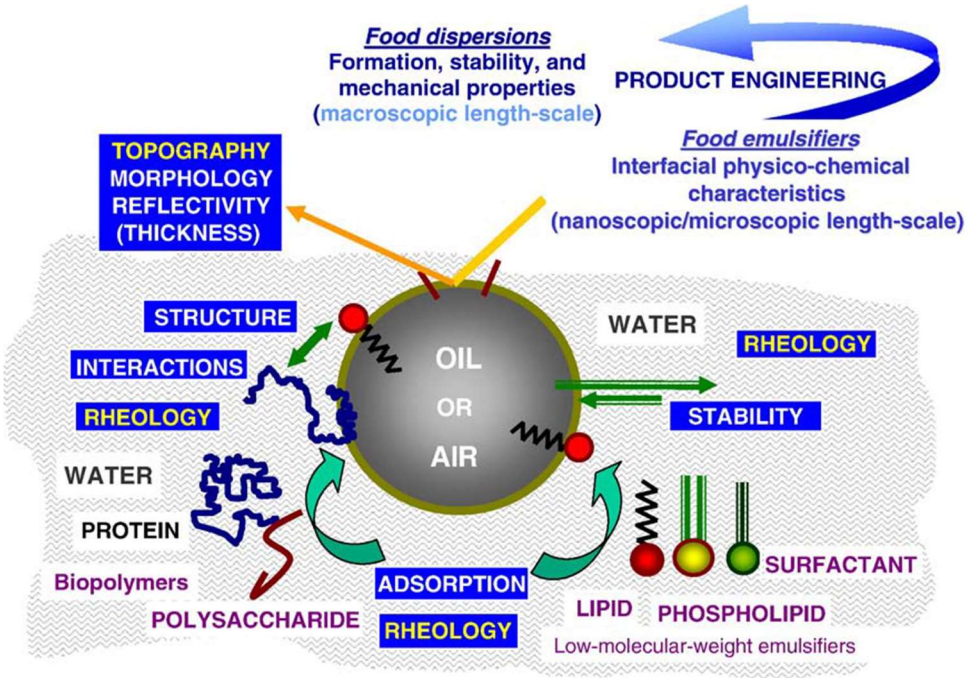

Figure 15. Interfacial physico-chemical characteristics of food additives at a fluid interface in foams or oil-in-water emulsions. Image taken from Balerin et al. (2007)

Stabilizers, emulsifiers and additives. Several of these substances are surfactants. Surfactants are molecules that have one side with greater affinity for oily phases (*lipophilic group*), while the other side of the molecule has more affinity for the water phases (*hydrophilic group*). Therefore, these molecules tend to be adsorbed in the interface between the two. Usually the hydrophobic part of the molecule (having higher affinity with oily phases) consists of an alkyl chain; the hydrophilic part (having higher affinity with an aqueous phase) can be a nonionic chain, such as an ethylene oxide chain or a chain consisting of glucose units, or a chain containing charged groups (such as a sulphonate group). For instance, Thakur et al. (2005) analyzed the influence of formulation combined with operating conditions in foams produced in a jacketed column equipped with a three stage impeller using two emulsifier blends consisting on mixtures of mono- and diglycerides with different unsaturated fatty acid contents.

Proteins. Proteins are macromolecular structures present in nature that affect all living organisms with a great variety of functions. In their most basic form, they are biopolymers created by enchaining a number of natural amino acids through a covalent bond between the carboxyl group of the acid and the amine group of another, thus forming a fundamental backbone (*primary structure*). These amino acid residues could present hydrogen bonding locations in their molecular structure, enabling the linear sequence of a protein to fold itself locally giving place to helical and planar structures characteristic of a particular protein (*secondary structure*). Also, interactions can give rise to global macromolecular folding processes creating special particular three-dimensional structures (*tertiary structures*). In some cases, associations of macromolecules can occur to form protein complexes (*quaternary structure*).

The process of a protein intervention in the air/liquid interface in foams has been recently reviewed by Germain and Aguilera (2014) and is schematically presented in Figure 16. A protein must diffuse to the interface, adsorb on it, unfold its structure to re-accommodate in the new balance of forces and this will make it interact with neighboring proteins and other substances. At equilibrium this process leads to an increase in surface pressure up to a certain threshold from which remains constant even if the thickness of layer increases.

The work by Thakur et al. (2005) is an example of the importance of the proteins on formulations. The authors used different liquid serums formulated using whey protein concentrate, skim milk powder, two commercial grade fats with different unsaturated fatty acid content and solid fat content. Even small

changes in protein content at the fat interface due to a change in emulsifier or fat type may drastically affect the foaming ability of the serum, and therefore the bubble Sauter diameter, because of the interactions proteins/emulsifiers and proteins/fat that affect rheological parameters.

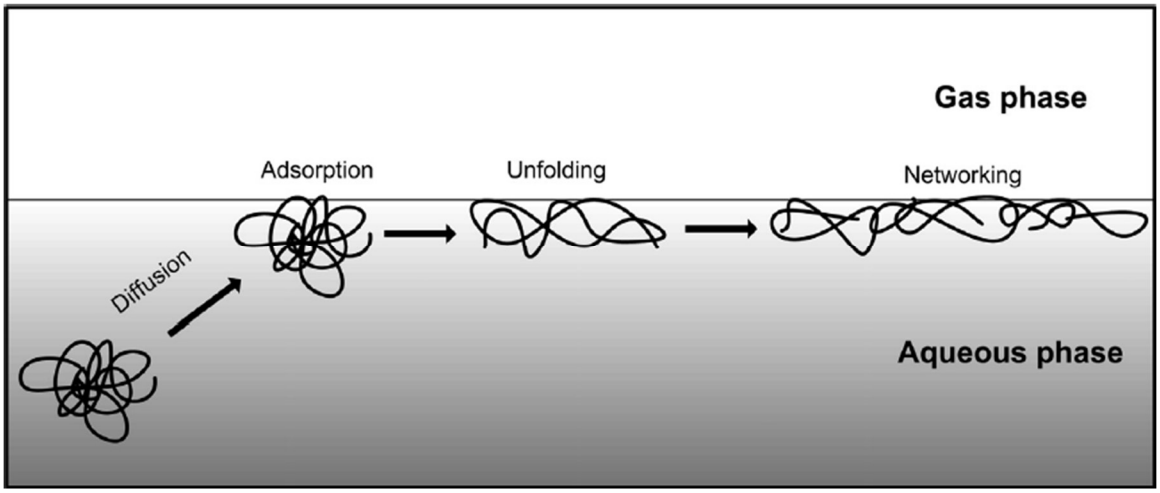

Figure 16. Protein adsorption process at air/liquid interfaces. Taken from Germain and Aguilera (2014)

Protein adsorption also has other effects. For instance, the migration of protein towards the interface makes the film interface viscoelastic and the compression and expansion suffered during foaming becomes an important parameter of analysis for foam stability. Also, the presence of protein in the films can have an effect of the disproportionation since proteins can act as a barrier to the mass transfer.

Modelling crystallization in SSHEs

2.9 Ice crystallization modelling. Population balance approach

Crystallization is an extensively studied unit operation with a plethora of applications in chemical, pharmaceutical, food and other process industries, and as such, extensive amounts of information available. Recently, several papers have presented excellent reviews regarding the modelling of crystallization operations (e.g. Casenave et al. (2014a); Costa et al. (2007); Nagy et al. (2013)). Therefore,

only the most relevant elements around modelling are presented here with an emphasis on systems dedicated to ice cream related products. One first noticeable fact on crystallization modelling is that it is dominated by the formalism of a balance around the statistical distribution function of the population of countable entities, generally called *population balance*. This approach will be presented briefly in this section, using the formality of a remarkable reference book by Ramkrishna (2000b).

Let us consider a system in which a continuous phase flows and, within this phase, several countable entities (for example solid particles, liquid drops or bubbles) also flow and interact with other of these countable entities and the continuous phase. Let us suppose that these entities can be described with n attributes (for example a drop size or sizes, volume or surface area) assembled into a vector, $\boldsymbol{l} = (l_1, l_2, \ldots, l_n)^T$, called the *internal coordinates*. Of course, all entities are flowing in space such that we have a set of three *external coordinates* $\mathbf{r} = (r_1, r_2, r_3)^T$. At some determined time t and some point in space, $\mathbf{r}$, we can count the number of entities that have a determined value of attributes, $\boldsymbol{l}$, such that we define the number $n(\boldsymbol{l},\mathbf{r},t)$ and a *density function* as the number of entities per unit volume, $\psi(\boldsymbol{l},\mathbf{r},t)$.

On the other hand, the continuous phase is also characterized by its own set of attributes (for example its temperature, velocity field, or concentrations) so that they vary with space and time. Let us assemble them in a m-dimensional vector $\mathbf{Y}(\mathbf{r},t) = (y_1, y_2, \ldots, y_m)^T$.

As interaction between the entities themselves and with the continuous phase develops, the attributes of the particles and the continuous phase can change with time and space. For example water molecules in a liquid surrounding a crystal can freeze on its surface increasing its size, or the velocity fields in a gas phase are affected by the wakes left for a particle during its movement. This change in the value of attributes, as seen in the examples before, can also be dependent on the current attributes of particles and the continuous phase, so let us define a vector of rates of change (usually a growth rate), $\mathbf{G}(\boldsymbol{l},\mathbf{r},\mathbf{Y},t)$, and the velocity field $\mathbf{v}(\boldsymbol{l},\mathbf{r},\mathbf{Y},t)$ as functions of all attributes, time and space.

The density function can also be altered by changing directly the number of entities with determined values of attributes, for example, two or more bubbles can coalesce or aggregate into one bubble with a larger size or one solid particle can break up and create several particles of lesser size. In fact, events such as those can produce new entities with attributes that did not exist before. Let us then define a volumetric rate of particles generation or disappearance with a determined set of attributes at a time t in a position $\mathbf{r}$ in space as $S(\boldsymbol{l},\mathbf{r},\mathbf{Y},t)$

Therefore, the density function changes according to the equation (Ramkrishna, 2000a; Yeoh et al., 2014):

$$\frac{\partial \psi(\boldsymbol{l},\mathbf{r},t)}{\partial t} + \nabla \cdot \left[\mathbf{v}(\boldsymbol{l},\mathbf{r},\mathbf{Y},t)\psi(\boldsymbol{l},\mathbf{r},t) \right] + \nabla_l \cdot \left[\mathbf{G}(\boldsymbol{l},\mathbf{r},\mathbf{Y},t)\psi(\boldsymbol{l},\mathbf{r},t) \right] = S(\boldsymbol{l},\mathbf{r},\mathbf{Y},t) \quad (2.21)$$

In the left hand side of this equation the first two components represent the regular substantial derivative (inherent changes with time and position), while the third one stands for the change on the density because of the changes in the entities attributes.

In terms of applications, normally the events associated with generation and disappearance of entities can be classified as: breakage/break up, $S_B(\boldsymbol{l},\mathbf{r},\mathbf{Y},t)$, and coalescence/aggregation $S_C(\boldsymbol{l},\mathbf{r},\mathbf{Y},t)$. Then the equation transforms into:

$$\frac{\partial \psi(\boldsymbol{l},\mathbf{r},t)}{\partial t} + \nabla \cdot \left[\mathbf{v}(\boldsymbol{l},\mathbf{r},\mathbf{Y},t)\psi(\boldsymbol{l},\mathbf{r},t) \right] + \nabla_l \cdot \left[\mathbf{G}(\boldsymbol{l},\mathbf{r},\mathbf{Y},t)\psi(\boldsymbol{l},\mathbf{r},t) \right] = S_B(\boldsymbol{l},\mathbf{r},\mathbf{Y},t) + S_C(\boldsymbol{l},\mathbf{r},\mathbf{Y},t) \quad (2.22)$$

In the sake of simplicity, we abbreviate the notation by not describing the functionalities in all the parameters involved so that the equation can be rewritten as:

$$\frac{\partial \psi}{\partial t} + \nabla \cdot \left[\mathbf{v}\psi \right] + \nabla_l \cdot \left[\mathbf{G}\psi \right] = S_B + S_C \quad (2.23)$$

This equation is not useful unless some simplifications are made. In fact, one of the most common assumptions is that only one attribute is enough to account for the features to be observed on the entities. The decision among what parameter to take is based mainly on what is possible to follow experimentally for the system. On a few cases where it is possible to have analytical solutions, the feasibility on the solution becomes the deciding factor. However, when used for real applications that is not the most common case. If only one attribute, l, is enough to describe the entities, the equation reads as:

$$\frac{\partial \psi}{\partial t} + \nabla \cdot \left[\mathbf{v}\psi \right] + \frac{\partial}{\partial l}\left(G\psi \right) = S_B + S_C \quad (2.24)$$

In case that the changes in the density function with position within the system are negligible (for example a well-mixed stirred tank), the second term on the left becomes zero:

$$\frac{\partial \psi}{\partial t} + \frac{\partial}{\partial l}\left[G\psi \right] = S_B + S_C \quad (2.25)$$

Sometimes the growth rate is not dependent on the attributes followed in the particle so that:

$$\frac{\partial \psi}{\partial t} + G\frac{\partial \psi}{\partial l} = S_B + S_C \tag{2.26}$$

Breakage and coalescence are generally considered as instantaneous. They are characterized by different parameters such as breakage rate (depending on particle size and local shear for example), the number of daughters and their size, the coalescence rate (depending on the particle sizes, local shear, interface stability) etc.

2.9.1 Highlighted applications relevant to ice cream or sorbet production

Lian et al. (2006) have used a CFD – PB model for simulating the crystallization of a 25% aqueous sucrose solution in a scraped surface heat exchanger. Their model was solved assuming steady state conditions in different points along the axis of the exchanger and superimposing these different flow fields in dynamic simulations on the transverse planes at these points. The calculated particle density was compared to experimental data taken at the outlet of the equipment. The model overpredicted the density of low size particles and underpredicted the larger particles values. The authors attributed this discrepancy to an unknown effect of the particles that are not detectable experimentally (sizes < 5 μm) on the size distribution, the assumptions made to simplify flow conditions and crystal growth and birth rates, and the assumption of sphericity for the crystals. Furthermore, the authors suggest that the effect of ice crystallization in the physicochemical properties must be included to enhance the prediction capability of the model.

Arellano et al. (2013b); Casenave et al. (2014a); González Ramírez et al. (2012) presented studies carried out under the GPAN research unit at IRSTEA dealing with sorbet and ice cream production and are of foremost interest to this thesis. The authors developed a model consisting of coupling an experimental RTD model and a heat transfer model based on ordinary differential equations with a population balance approach to model the production of non-aerated sorbet in a SSHE. The authors found a good agreement between experimental and predicted data for crystal chord length distribution data and product temperature.

Conclusions

Les principales conclusions de cette analyse bibliographique par rapport à nos objectifs sont les suivantes :

Il existe une abondante littérature sur les échangeurs de chaleur à surface raclée (ECSR) ; elle porte surtout sur les écoulements monophasiques de fluides newtoniens ou non-newtoniens, du point de vue expérimental et/ou numérique. Peu de travaux portent sur la cristallisation au sein des ECSR et aucun à notre connaissance sur la combinaison de la cristallisation et du foisonnement.

De même, il existe une abondante littérature sur les mousses, mais très peu sur les sorbets foisonnés. La déformation et la rupture des bulles ont été étudiées de façon expérimentale et théorique souvent pour des bulles isolées et presque toujours pour un milieu monophasique et toujours newtonien environnant la (les) bulle(s). Or dans le cas qui nous intéresse, la fraction de gaz atteint environ 20% (nombreuses bulles en interaction) et le milieu environnant est lui-même un milieu diphasique : solution concentrée de sucre contenant des cristaux de glace d'une dizaine de microns.

Il en ressort que les études suivantes, envisagées pour notre travail, constituent une avancée dans les connaissances

- Etude expérimentale de l'influence des paramètres opératoires lors de la production d'un sorbet aéré
    - sur les écoulements et les transferts thermiques
    - sur la granulométrie des cristaux et des bulles

- Modélisation et simulation numérique du couplage entre écoulement, transfert, cristallisation et foisonnement.

Lors de ces études nous pourrons nous inspirer des nombreux travaux de la littérature pour les techniques expérimentales, les corrélations proposées et les méthodes numériques même si notre cas d'étude est un peu éloigné des travaux publiés.

Nomenclature

Ca	Capillary number (-)
d	diameter (m)
$\bar{d}$	arithmetic mean diameter (m)
$\bar{d}_{3.2}$	Sauter mean diameter (m)
d_i	mean diameter in the class size i (m)
D	impeller diameter (m)
$\mathbf{D}$	rate of deformation tensor (s^{-1})
D_h	hydraulic diameter (m)
Fl_G	gas flow number (-)
Fr	Froude number (-)
g	gravitational force (= 9.81 m s^{-2})
$\mathbf{G}$	growth rate (m s^{-1} K^{-1})
K	consistency index for power law fluids (Pa s^n)
l	particle size (m)
$\dot{m}$	mass flowrate (kg h^{-1})
n	flow behaviour index for power law fluids (-)
n_i	frequency number in the class size i (-)
N	rotor's rotational speed (rev s^{-1})
N_{ae}	aeration number (-)
Ne	Newton number (-)
OR	overrun (-)
P	pressure (Pa)
Po	power number (-)
r	crystal or bubble radius (m)
R	heat exchanger radius (m)
Re	Reynolds number (-)
S	generation or disappearance rate of particles (m s^{-1} K^{-1})
t	time (s)
T	temperature (°C)
Ta	Taylor number (-)
T_R	refrigerant fluid evaporating temperature (°C)
v	fluid velocity (m s^{-1})
V	volume (m^3)

$\dot{V}_g$	gas volume flowrate ($m^3\ s^{-1}$)
w	mass fraction (-)
$\dot{W}$	energy consumption rate in foaming operation ($W\ m^{-3}$)
We	Weber number (-)

Greek letters

ϕ	volume fraction (-)
$\dot{\gamma}$	shear rate (s^{-1})
λ_{MZ}	dispersive mixing index (-)
μ	dynamic viscosity (Pa s)
π	constant pi (= 3.1416)
ρ	density ($kg\ m^{-3}$)
σ	surface tension ($N\ m^{-1}$)
Ω	rotor's rotational speed ($rad\ s^{-1}$)
$\mathbf{\Omega}$	vorticity tensors (s^{-1})
Ψ	number density function of ice crystals (m^{-4})

Subscripts

air	air
ax	axial
B	breakage
breakup	breakup of bubbles
bubble	bubble
C	coalescence
cr	critical
gas	gas
i	ice
liquid	liquid
mix	mix
r	rotor
rot	rotational
s	stator
sorb	sorbet
total	total

Abbreviations

RTD	residence time distribution
SSHE	scraped surface heat exchanger

References

Abichandani, H., Sarma, S.C., Heldman, D.R., (1986). Hydrodynamics and heat transfer in thin film scraped surface heat exchangers — A review. Journal of Food Process Engineering 9(2), 143-172.

Acrivos, A., Lo, T.S., (1978). Deformation and breakup of a single slender drop in an extensional flow. Journal of Fluid Mechanics 86(04), 641-672.

Aguilera, J.M., Lillford, P.J., (2008). *Food Materials Science. Principles and Practice*. Springer.

Alhamdan, A., Sastry, S., (1997). Residence time distribution of food and simulated particles in a holding tube. Journal of Food Engineering 34(3), 271-292.

Arellano, M., Benkhelifa, H., Alvarez, G., Flick, D., (2013a). Coupling population balance and residence time distribution for the ice crystallization modeling in a scraped surface heat exchanger. Chemical Engineering Science 102(0), 502-513.

Arellano, M., Benkhelifa, H., Alvarez, G., Flick, D., (2013b). Experimental study and modelling of the residence time distribution in a scraped surface heat exchanger during sorbet freezing. Journal of Food Engineering 117(1), 14-25.

Azizi, F., Al Taweel, A.M., (2007). Population balance simulation of gas–liquid contacting. Chemical Engineering Science 62(24), 7436-7445.

Balerin, C., Aymard, P., Ducept, F., Vaslin, S., Cuvelier, G., (2007). Effect of formulation and processing factors on the properties of liquid food foams. Journal of Food Engineering 78(3), 802-809.

Barigou, M., Douaire, M., (2013). 9 - X-ray micro-computed tomography for resolving food microstructures, in: Morris, V.J., Groves, K. (Eds.), *Food Microstructures*. Woodhead Publishing, pp. 246-272.

Belhamri, R., Fayolle, F., Flick, D. (2009). Simplified flow pattern model in SSHE during crystallization process In *Proceedings of the Conference Name|*, Conference Location|.

Benezech, T., Maingonnat, J.F., (1989). Etude de la distribution des temps de séjour dans des échangeurs à surface raclée traitant des fluides non-Newtoniens. Entropie 151, 37 - 46.

Bentley, B.J., Leal, L.G., (1986). A computer-controlled four-roll mill for investigations of particle and drop dynamics in two-dimensional linear shear flows. Journal of Fluid Mechanics 167, 219-240.

Caillet, A., Cogné, C., Andrieu, J., Laurent, P., Rivoire, A., (2003). Characterization of ice cream structure by direct optical microscopy. Influence of freezing parameters. LWT - Food Science and Technology 36(8), 743-749.

Campbell, G.M., Mougeot, E., (1999). Creation and characterisation of aerated food products. Trends in Food Science & Technology 10(9), 283-296.

Cantat, I., Cohen-Addad, S., Elias, F., Graner, F., Höhler, R., Pitois, O., Rouyer, F., Saint-Jalmes, A., (2013). *Foams: Structure and Dynamics*. Oxford University Press.

Casenave, C., Dochain, D., Alvarez, G., Arellano, M., Benkhelifa, H., Leducq, D., (2014). Model identification and reduction for the control of an ice cream crystallization process. Chemical Engineering Science 119(0), 274-287.

Cook, K.L.K., Hartel, R.W., (2010). Mechanisms of Ice Crystallization in Ice Cream Production. Comprehensive Reviews in Food Science and Food Safety 9(2), 213-222.

Costa, C.B.B., Maciel, M.R.W., Filho, R.M., (2007). Considerations on the crystallization modeling: Population balance solution. Computers & Chemical Engineering 31(3), 206-218.

Chang, Y., Hartel, R.W., (2002). Measurement of air cell distributions in dairy foams. International Dairy Journal 12(5), 463-472.

Chen, C.R., Ramaswamy, H.S., (2000). A neuro-computing approach for modeling of residence time distribution (RTD) of carrot cubes in a vertical scraped surface heat exchanger (SSHE). Food Research International 33(7), 549-556.

Cheng, J., Carreau, P.J., (1994). Aerated mixing of viscoelastic fluids with helical ribbons impellers. Chemical Engineering Science 49(12), 1965-1972.

Chhabra, R.P., Richardson, J.F., (2011). *Non-Newtonian Flow and Applied Rheology: Engineering Applications*. Elsevier Science.

Danckwerts, P.V., (1953). Continuous flow systems: Distribution of residence times. Chemical Engineering Science 2(1), 1-13.

Djelveh, G., Bacati, O., Gros, J.B., (1994). Mechanical aspects of gas dispersion in continuous foaming food processes using scraped surface heat exchangers. Journal of Food Engineering 23(2), 213-223.

Djéridi, H., Gabillet, C., Billard, J.-Y., (2002). Écoulement de Couette Taylor diphasique. Comptes Rendus Mécanique 330(2), 113-119.

Dumont, E., Fayolle, F., Legrand, J., (2000). Flow regimes and wall shear rates determination within a scraped surface heat exchanger. Journal of Food Engineering 45(4), 195-207.

E.R.Alcairo, C.A.Zuritz, (1990). Residence time distributions of spherical particles suspended in non-Newtonian flow in a scraped-surface heat exchanger. 33(5).

Fayolle, F., Belhamri, R., Flick, D., (2013). Residence time distribution measurements and simulation of the flow pattern in a scraped surface heat exchanger during crystallisation of ice cream. Journal of Food Engineering 116(2), 390-397.

Fénot, M., Bertin, Y., Dorignac, E., Lalizel, G., (2011). A review of heat transfer between concentric rotating cylinders with or without axial flow. International Journal of Thermal Sciences 50(7), 1138-1155.

Fradette, L., Li, H.-Z., Choplin, L., Tanguy, P., (2006). Gas/liquid dispersions with a SMX static mixer in the laminar regime. Chemical Engineering Science 61(11), 3506-3518.

Fu, X.Y., Ishii, M., (2003). Two-group interfacial area transport in vertical air–water flow: I. Mechanistic model. Nuclear Engineering and Design 219(2), 143-168.

Germain, J.C., Aguilera, J.M., (2014). Multi-scale properties of protein-stabilized foams. Food Structure 1(1), 55-70.

Goff, H.D., Hartel, R., (2013). Freezing and Refrigeration, *Ice Cream*. Springer US, pp. 193-248.

González Ramírez, J.E., Leducq, D., Arellano, M., Alvarez, G. (2013). Modelo de un proceso de cristalización continua de un sorbete por medio de la metodología de momentos. Revista Internacional de Métodos Numéricos para Cálculo y Diseño en Ingeniería.

Grace, H.P., (1982). Dispersion phenomena in high viscosity inmiscible fluid systems and application of static mixers as dispersion devices in such systems. Chemical Engineering Communications 14(3-6), 225-277.

Green, D., Perry, R., (2007). *Perry's Chemical Engineers' Handbook, Eighth Edition*. McGraw-Hill Education.

Groeneweg, F., van Dieren, F., Agterof, W.G.M., (1994). Droplet break-up in a stirred water-in-oil emulsion in the presence of emulsifiers. Colloids and Surfaces A: Physicochemical and Engineering Aspects 91(0), 207-214.

Härröd, M., (1986). Scraped surface heat exchangers. Journal of Food Process Engineering 9(1), 1-62.

Hinch, E.J., Acrivos, A., (1980). Long slender drops in a simple shear flow. Journal of Fluid Mechanics 98(02), 305-328.

Hinze, J.O., (1955). Fundamentals of the hydrodynamic mechanism of splitting in dispersion processes. AIChE Journal 1(3), 289-295.

Hubacz, R., Wroński, S., (2004). Horizontal Couette–Taylor flow in a two-phase gas–liquid system: flow patterns. Experimental Thermal and Fluid Science 28(5), 457-466.

Indrawati, L., Wang, Z., Narsimhan, G., Gonzalez, J., (2008). Effect of processing parameters on foam formation using a continuous system with a mechanical whipper. Journal of Food Engineering 88(1), 65-74.

Keshav, T.R., Somaraju, P., Kalyan, K., Saroha, A.K., Nigam, K.D.P., (2008). Liquid phase residence time distribution for gas–liquid flow in Kenics static mixer. Chemical Engineering and Processing: Process Intensification 47(12), 2275-2280.

Kruglyakov, P.M., Karakashev, S.I., Nguyen, A.V., Vilkova, N.G., (2008). Foam drainage. Current Opinion in Colloid & Interface Science 13(3), 163-170.

Labbafi, M., Thakur, R.K., Vial, C., Djelveh, G., (2007). Development of an on-line optical method for assessment of the bubble size and morphology in aerated food products. Food Chemistry 102(2), 454-465.

Lee, J.H., Singh, R.K., (1993). Residence time distribution characteristics of particle flow in a vertical scraped surface heat exchanger. Journal of Food Engineering 18(4), 413-424.

Lian, G., Moore, S., Heeney, L., (2006). Population balance and computational fluid dynamics modelling of ice crystallisation in a scraped surface freezer. Chemical Engineering Science 61(23), 7819-7826.

Liao, Y., Lucas, D., (2009). A literature review of theoretical models for drop and bubble breakup in turbulent dispersions. Chemical Engineering Science 64(15), 3389-3406.

Mabit, J., Fayolle, F., Legrand, J., (2003). Shear rates investigation in a scraped surface heat exchanger. Chemical Engineering Science 58(20), 4667-4679.

Madhuranthakam, C.M.R., Pan, Q., Rempel, G.L., (2009). Residence time distribution and liquid holdup in Kenics® KMX static mixer with hydrogenated nitrile butadiene rubber solution and hydrogen gas system. Chemical Engineering Science 64(14), 3320-3328.

Mary, G., Mezdour, S., Delaplace, G., Lauhon, R., Cuvelier, G., Ducept, F., (2013). Modelling of the continuous foaming operation by dimensional analysis. Chemical Engineering Research and Design 91(12), 2579-2586.

Metzner, A.B., Otto, R.E., (1957). Agitation of non-Newtonian fluids. AIChE Journal 3(1), 3-10.

Middleton, J.C., (1997). Gas-liquid dispersion and mixing, in: Harnby, N., Edwards, M.F., Nienow, A.W. (Eds.), *Mixing in the Process Industries*. Butterworth-Heinemann, Oxford, pp. 322-363.

Müller-Fischer, N., Tobler, P., Dressler, M., Fischer, P., Windhab, E., (2008). Single bubble deformation and breakup in simple shear flow. Experiments in Fluids 45(5), 917-926.

Nagy, Z.K., Fevotte, G., Kramer, H., Simon, L.L., (2013). Recent advances in the monitoring, modelling and control of crystallization systems. Chemical Engineering Research and Design 91(10), 1903-1922.

Narsimhan, G., (2010). Analysis of creaming and formation of foam layer in aerated liquid. Journal of Colloid and Interface Science 345(2), 566-572.

Ramaswamy, H.S., Abdelrahim, K.A., Marcotte, M., Clavier, P., (1995a). Residence time distribution (RTD) characteristics of meat and carrot cubes in starch solutions in a vertical scraped surface heat exchanger (SSHE). Food Research International 28(4), 331-342.

Ramaswamy, H.S., Abdelrahim, K.A., Simpson, B.K., Smith, J.P., (1995b). Residence time distribution (RTD) in aseptic processing of particulate foods: a review. Food Research International 28(3), 291-310.

Ramkrishna, D., (2000a). Chapter 2 - The Framework of Population Balance, in: Ramkrishna, D. (Ed.), *Population Balances*. Academic Press, San Diego, pp. 7-45.

Ramkrishna, D., (2000b). *Population Balances: Theory and Applications to Particulate Systems in Engineering*. Elsevier Science.

Rao, C.S., Hartel, R.W., (2006). Scraped Surface Heat Exchangers. Critical Reviews in Food Science and Nutrition 46(3), 207-219.

Russell, A.B., Burmester, S.S.H., Winch, P.J., (1997). Characterization of Shear Thinning Flow Within a Scraped Surface Heat Exchanger. Food and Bioproducts Processing 75(3), 191-197.

Sattar, M.A., Naser, J., Brooks, G., (2013). Numerical simulation of creaming and foam formation in aerated liquid with population balance modeling. Chemical Engineering Science 94(0), 69-78.

Scanlon, M.G., Campbell, G.M., Pyle, D.L., Chemists, A.A.o.C., (2008). *Bubbles in Food 2: Novelty, Health and Luxury*. Egan Press [for the American Association of Cereal Chemists].

Shiomi, Y., Kutsuna, H., Akagawa, K., Ozawa, M., (1993). Two-phase flow in an annulus with a rotating inner cylinder (flow pattern in bubbly flow region). Nuclear Engineering and Design 141(1–2), 27-34.

Shiomi, Y., Kutsuna, H., Akagawa, K., Ozawa, M., (1995). Bubble and Particle Behavior in Taylor- and Spiral-Vortex Flows, in: Serizawa, A., Fukano, T., Bataille, J. (Eds.), *Multiphase Flow 1995*. Elsevier, Amsterdam, pp. 17-26.

Simoneau, C., McCarthy, M.J., German, J.B., (1993). Magnetic resonance imaging and spectroscopy for food systems. Food Research International 26(5), 387-398.

Stewart, P.S., Davis, S.H., Hilgenfeldt, S., (2013). Viscous Rayleigh–Taylor instability in aqueous foams. Colloids and Surfaces A: Physicochemical and Engineering Aspects 436(0), 898-905.

Taylor, G.I., (1934). The Formation of Emulsions in Definable Fields of Flow. Proceedings of the Royal Society of London. Series A 146(858), 501-523.

Tester, J.W., Modell, M., (1997). *Thermodynamics and Its Applications*. Prentice Hall PTR.

Thakur, R.K., Vial, C., Djelveh, G., (2003a). Foaming of Commercial Grade Food Products in a Continuous Stirred Column. Chemical Engineering Research and Design 81(9), 1083-1089.

Thakur, R.K., Vial, C., Djelveh, G., (2003b). Influence of operating conditions and impeller design on the continuous manufacturing of food foams. Journal of Food Engineering 60(1), 9-20.

Thakur, R.K., Vial, C., Djelveh, G., (2005). Combined effects of process parameters and composition on foaming of dairy emulsions at low temperature in an agitated column. Journal of Food Engineering 68(3), 335-347.

Thijert, M.P.G., Oyevaar, M.H., Kuper, W.J., Westerterp, K.R., (1992). Residence time distribution of the gas phase in a mechanically agitated gas-liquid reactor. Chemical Engineering Science 47(13–14), 3339-3346.

Vedantam, S., Joshi, J.B., (2006). Annular Centrifugal Contactors—A Review. Chemical Engineering Research and Design 84(7), 522-542.

Vyakaranam, K.V., Kokini, J.L., (2012). Prediction of air bubble dispersion in a viscous fluid in a twin-screw continuous mixer using FEM simulations of dispersive mixing. Chemical Engineering Science 84(0), 303-314.

Wang, W.E.I., Walton, J.H., McCarthy, K.L., (1999). Flow profiles of power-law fluids in scraped surface heat exchanger geometry using MRI. Journal of Food Process Engineering 22(1), 11-27.

Xu, W., Nikolov, A., Wasan, D.T., Gonsalves, A., Borwankar, R.P., (2003). Foam film rheology and thickness stability of foam-based food products. Colloids and Surfaces A: Physicochemical and Engineering Aspects 214(1–3), 13-21.

Yang, H.-H., Manas-Zloczower, I., (1992). 3D Flow field analysis of a Banbury mixer, in: Moldenaers, P., Keunings, R. (Eds.), *Theoretical and Applied Rheology*. Elsevier, Amsterdam, pp. 408-410.

Yataghene, M., Francine, F., Jack, L., (2011). Flow patterns analysis using experimental PIV technique inside scraped surface heat exchanger in continuous flow condition. Applied Thermal Engineering 31(14–15), 2855-2868.

Yeoh, G.H., Cheung, C.P., Tu, J., (2014). Chapter 3 - Population Balance Approach—A Generic Framework, in: Yeoh, G.H., Cheung, C.P., Tu, J. (Eds.), *Multiphase Flow Analysis Using Population Balance Modeling*. Butterworth-Heinemann, Oxford, pp. 69-90.

MATERIELS ET METHODES

3. Matériels et méthodes

3.1 Mix de sorbet

Pour l'ensemble des résultats présentés, le produit utilisé pour la cristallisation/foisonnement est un mix commercial de sorbet pasteurisé parfum citron (fournisseur : Laiterie Montaigu - Montaigu, France). Quelques propriétés sont présentées dans le Tableau 1.

Tableau 1. Propriétés physiques du mix du sorbet

Propriété	**Valeur**
Composition	% m/m
Eau	76,8
Saccharose	14,6
Jus de citron concentré 60°Brix	3,0
Fructose	8,0
Dextrose	0,09
Stabilisant : gomme de xanthane/gomme de guar/hypromellose	0,5
Concentration des solides solubles	25°Brix
Masse volumique à 25°C	1098 kg m^{-3}
Température de congélation commençante*, T_{if}	-2,72°C

*Extrapolée des mesures rapportées par González (2012)

D'autres propriétés physiques du mix du sorbet sont d'intérêt dans cette thèse, d'un côté la courbe d'équilibre thermodynamique de saturation pendant la congélation (aussi appelé *courbe de liquidus*) et de l'autre son comportement rhéologique.

La courbe de liquidus relie la température de congélation commençante du sorbet à la concentration de solutés dans la phase continue. González (2012) a mesuré par calorimétrie différentielle les températures de congélation commençantes du mix utilisé dans cette thèse à cinq concentrations en matières solubles obtenues en évaporant de l'eau sous vide. Dans ce travail ces résultats expérimentaux ont été utilisés dans une approche thermodynamique du phénomène de congélation afin d'obtenir l'équation (3.1). Les données et la courbe sont présentées dans la Figure 17.

$$w_s^*\left(T_{if}\right) = 0.7316\frac{1-x_w^*\left(T_{if}\right)}{1-0.9476x_w^*\left(T_{if}\right)} \tag{3.1}$$

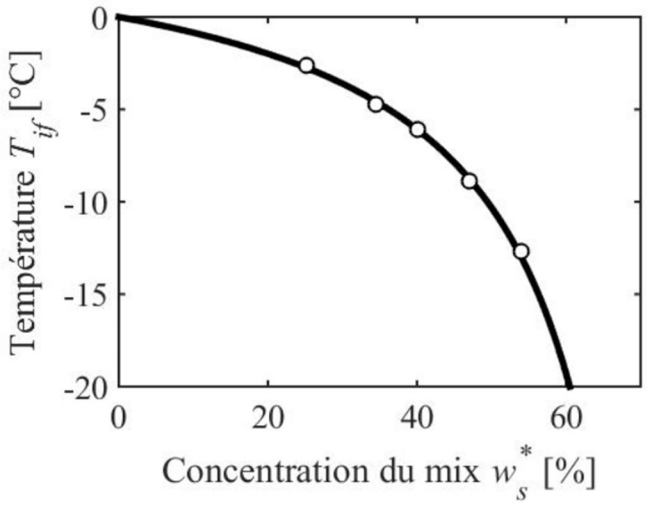

Figure 17. Courbe de liquidus du mix du sorbet : (O) données expérimentales mesurés par González (2012); (—) données extrapolées à partir de l'équation (3.1)

González (2012) a également caractérisé le comportement rhéologique du mix à des concentrations en solides solubles entre 25.2 et 52.5°Brix et à des températures allant de -2 jusqu'à +13°C. Les résultats ont montré que le mix suit un comportement de fluide non-Newtonien suivant la loi de puissance avec un indice de consistance (K_{mix}) qui dépend de la température et d'un indice d'écoulement (n_{mix}) selon les équations suivantes :

$$K_{mix}\left[\text{Pa s}^{n_{mix}}\right] = 39\times10^{-9}\left(100w_s^*\right)^{2.557}\exp\left(2248/T\right), \quad n_{mix} = 0.553 \tag{3.2}$$

3.2 Pilote de production de sorbet

L'équipement pilote de production de sorbet utilisé est un freezer de type Freezer Technohogy WCB® Model MF 50 d'une capacité de production comprise entre 25 et 75 kg/h (Figure 18). Le freezer utilise le R22 (chlorodifluorométhane) comme fluide frigorigène dans un cycle à détente directe avec une température d'évaporation pouvant être réglée entre -20 et -10°C. Le freezer est muni d'un ECSR horizontal dont le rotor est plein et équipé de deux lames racleuses (Figure 18B) occupe environ 45% du volume du cylindre intérieur (Figure 18 ; Tableau 2). La vitesse de rotation des lames racleuses pouvait être variée entre 250 et 1000 tr/min.

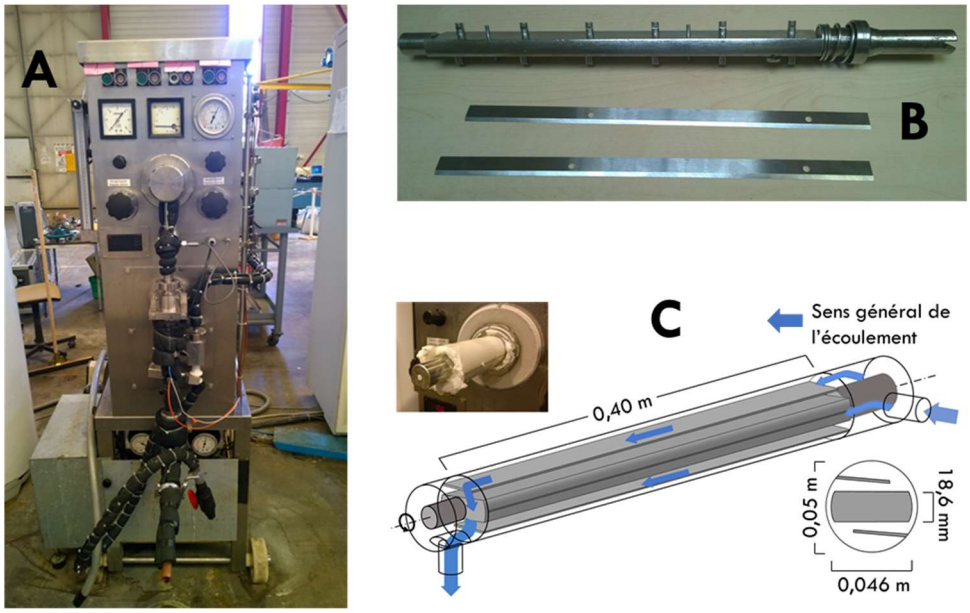

Figure 18. Equipement pilote de production de sorbet- Freezer Technology MF 50 : **A**. Photographie de l'équipement ; **B**. Rotor de l'ECSR avec ses lames ; **C**. Dimensions du rotor et des lames

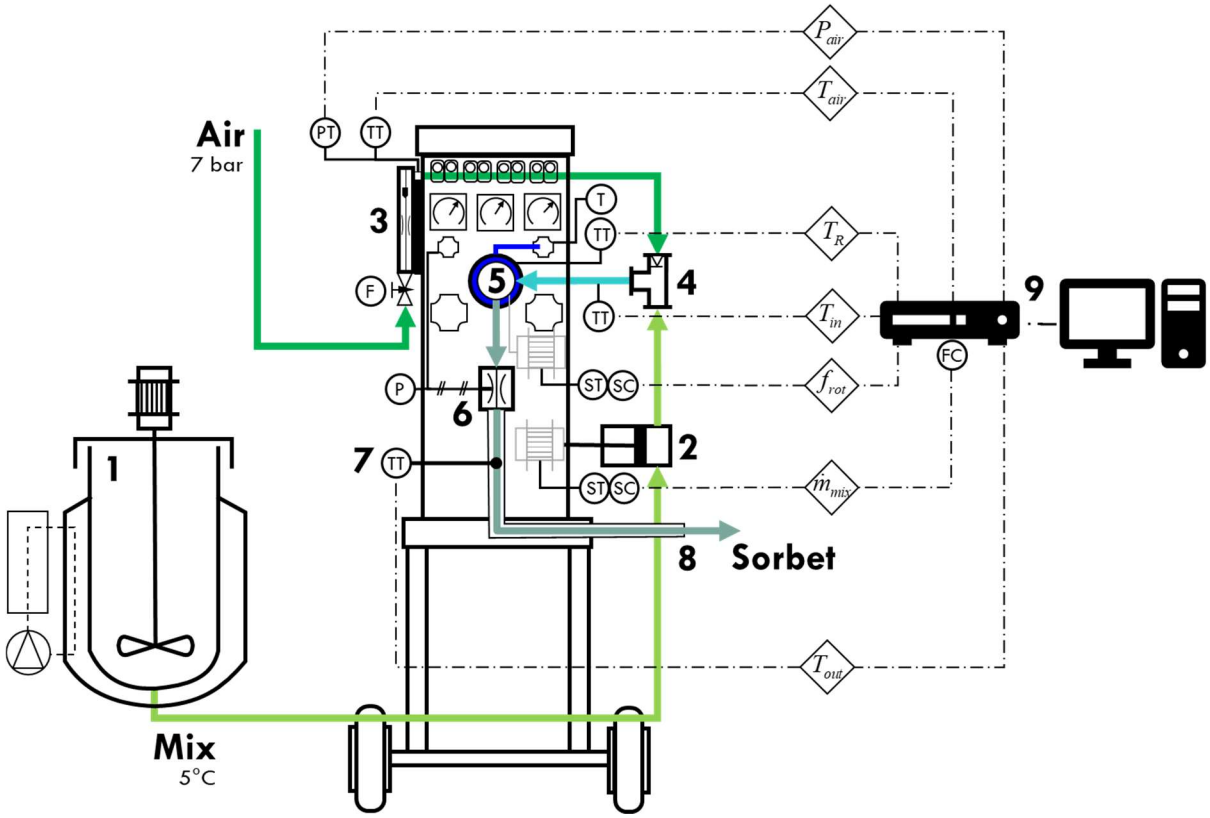

Figure 19. Représentation schématique du dispositif expérimental : 1. Réservoir de stockage du mix. 2. Pompe d'alimentation. 3. Entrée d'air. 4. Mélange mix et d'air. 5. ECSR. 6. Vanne de contrepression. 7. Mesure de température du sorbet. 8. Sortie du sorbet. 9. Central d'acquisition de données. 10. Ordinateur de control

Tableau 2. Dimension géométrique de l'ECSR WCB® Model MF 50.

Diamètre du cylindre échangeur de chaleur (D_c)	0,05 m
Longueur du cylindre échangeur de chaleur (L_{SSHE})	0,40 m
Diamètre maximale du rotor (D_r)	0,046 m
Rayon (D_r/D_c)	0,92
Surface d'échange de chaleur (A_{wall})	0,0628 m²

Le dispositif expérimental est schématisé sur la Figure 19. Il est composé d'un réservoir réfrigéré à 5°C par un bain thermostaté (**élément 1** de la figure), d'une capacité de 200 L, qui sert au stockage du mix. Ce dernier est acheminé par une pompe volumétrique à piston (**élément 2**) vers l'intérieur du freezer. Le débit de mix qui circule est réglé à l'aide d'un variateur de fréquence AC Drives (Series 650 Parker®) branché au moteur de la pompe et d'un tachymètre photoélectrique (Ahlborn®, type FUA9192, précision : 1 tr/min) qui mesure la vitesse de rotation du moteur. Une boucle de contrôle installée relie la variation de la fréquence et la variation du débit entre 0.007 et 0.021 kg s^{-1} (25 – 75 kg h^{-1}) avec une précision de ± 9.2 10^{-5} kg s^{-1}.

L'air est introduit dans le système grâce à une vanne régulatrice de pression à partir du réseau d'air comprimé local (7 bars). Le débit d'air introduit est contrôlé manuellement (**élément 3**) grâce à un rotamètre (Brooks, gamme Sho-Rate modèle GT1357 R2-25-A, précision : ±10%). Un thermocouple (type T, précision : ±0.5 K) et un capteur de pression (Baumer Boudon-Haenni® modèle E912, précision : ±0,2%) sont installés à la sortie du rotamètre afin d'obtenir une correspondance entre la hauteur de la bille (H mesurée en mm) dans le rotamètre et le débit d'air selon l'équation suivante :

$$\dot{m}_{air}\left[\frac{\text{kg}}{\text{h}}\right] = 1.2\left(c_5 H^5 + c_4 H^4 + c_3 H^3 + c_2 H^2 + c_1 H\right)\sqrt{\frac{T_{air}\left[\text{K}\right]}{294}\frac{1.013}{P_{air}\left[\text{atm}\right]}} \tag{3.3}$$

Avec c_1 = 0,041811, c_2 = -6,3464×10^{-4}, c_3 = 1,1264×10^{-5}, c_4 = -5,1024×10^{-8}, c_5 = 7,4698×10^{-11}.

L'air est incorporé à l'écoulement de mix dans un raccord en T avec une vanne antiretour (**élément 4**). La sortie latérale du raccord dirige l'écoulement vers l'ECSR (**élément 5**) où l'air est incorporé au mix en congélation grâce à la rotation des lames racleuses. L'arbre de ce rotor est actionné par un moteur pour lequel un variateur de fréquence AC Drives (Series 650 Parker®) et un tachymètre photoélectrique (Ahlborn®, type FUA9192, précision : 1 tr/min) permettent le contrôle de la vitesse de rotation entre 250 – 1000 tr/min. Le froid est apporté par le fluide frigorigène en évaporation circulant dans l'enveloppe de l'ECSR et sa pression est variée manuellement par une vanne, ce qui permet le réglage rapide de la température du frigorigène. Un thermocouple (type T, précision : ±0.2°C) collé à la surface extérieure de l'enveloppe par un ruban adhésif conducteur en aluminium permet de mesurer la température du

réfrigérant. La pression à l'intérieur de l'ECSR est réglée manuellement par une vanne de contrepression pneumatique et mesuré à l'aide d'un manomètre connecté à l'ECSR (**élément 6**). La température à l'entrée de l'ECSR est également mesurée à l'aide un thermocouple (type T, précision : ±0.2°C).

Le sorbet ainsi obtenu par cristallisation et foisonnement emprunte alors la conduite de sortie où la température est mesurée à l'aide d'une sonde Pt100 (Baumer®, précision : ± 0.1°C) (**élément 7**). Au cours de chaque essai, une fois le régime permanent établi, 4 échantillons sont récupérés dans des pots en sortie finale du dispositif pilote (**élément 8**) puis immédiatement placées dans un congélateur réglé à la température de sortie ou analysées directement dans la boite à gants réfrigérées (cf. section Microscopie en ambiance contrôlée). Ces échantillons ont servi à déterminer la taille des bulles et des cristaux de glace par analyse au microscope et traitement d'image.

Les différents paramètres du procédé mesurés sont recueillis au moyen de centrales d'acquisition Agilent HP (Model 34970 A) connectées à un ordinateur (**élément 9**) et sont enregistrés grâce à un programme d'acquisition sous Labview®. Ce programme d'acquisition permet également de commander la vitesse de rotation des lames racleuses et le débit du mix.

3.3 Microscopie en ambiance contrôlée

3.3.1 Conception d'une boîte à gants réfrigérée

Une fois le produit sorti du freezer, il est impératif de maintenir l'échantillon à une température la plus proche possible de celle de sortie de freezer. En effet, la température modifie l'équilibre entre les cristaux de glace et leur phase environnante, pouvant ainsi mener à une fonte partielle des cristaux en cas d'une hausse de la température ou à une croissance des cristaux en cas d'une diminution. Ceci nous a conduit à concevoir une enceinte réfrigérée à température et humidité contrôlée à l'intérieur de laquelle il est possible de mesurer les tailles de bulles d'air et de cristaux de glace. Il a ainsi été entrepris (en collaboration étroite avec l'équipe technique) la mise au point d'une « boite à gants » sur le modèle de celle déjà présentée dans la littérature par l'équipe de Richard Hartel de l'Université du Wisconsin (USA). Cette équipe a utilisé cette approche pour l'obtention de distributions de tailles de cristaux et de bulles dans des échantillons de crème glacée (Donhowe et al., 1991a; Sofjan and Hartel, 2004).

Le schéma de la « boîte à gants » est présenté sur la Figure 20. Il s'agit d'une armoire congélateur modifiée de manière à pouvoir contrôler la température et le taux d'humidité. L'intérieur de l'armoire est divisé en deux parties de volume égal à l'aide d'une paroi placée au centre. La partie gauche de l'armoire constitue

l'espace d'analyse. Une étagère à hauteur réglable y est installée pour accueillir le matériel d'analyse. La porte gauche de l'armoire est modifiée de sorte à y ajouter une fenêtre de visualisation ainsi que deux orifices munis de gants pour permettre la manipulation et la visualisation des échantillons. En plus de l'évaporateur du système frigorifique, une résistance chauffante et un ventilateur sont installés dans la partie droite de l'armoire afin de réguler la température dans la totalité de l'enceinte.

L'air brassé par le ventilateur traverse l'évaporateur situé dans la partie supérieure droite puis un nid d'abeille vertical pour atteindre la partie gauche de l'armoire. Il passe alors à travers un lit de silica gel placé sur un nid d'abeille horizontal installé en haut de la partie supérieure gauche de l'armoire pour rejoindre la zone d'analyse. Un circuit d'air à température et taux d'humidité contrôlée est ainsi établi au sein de l'armoire.

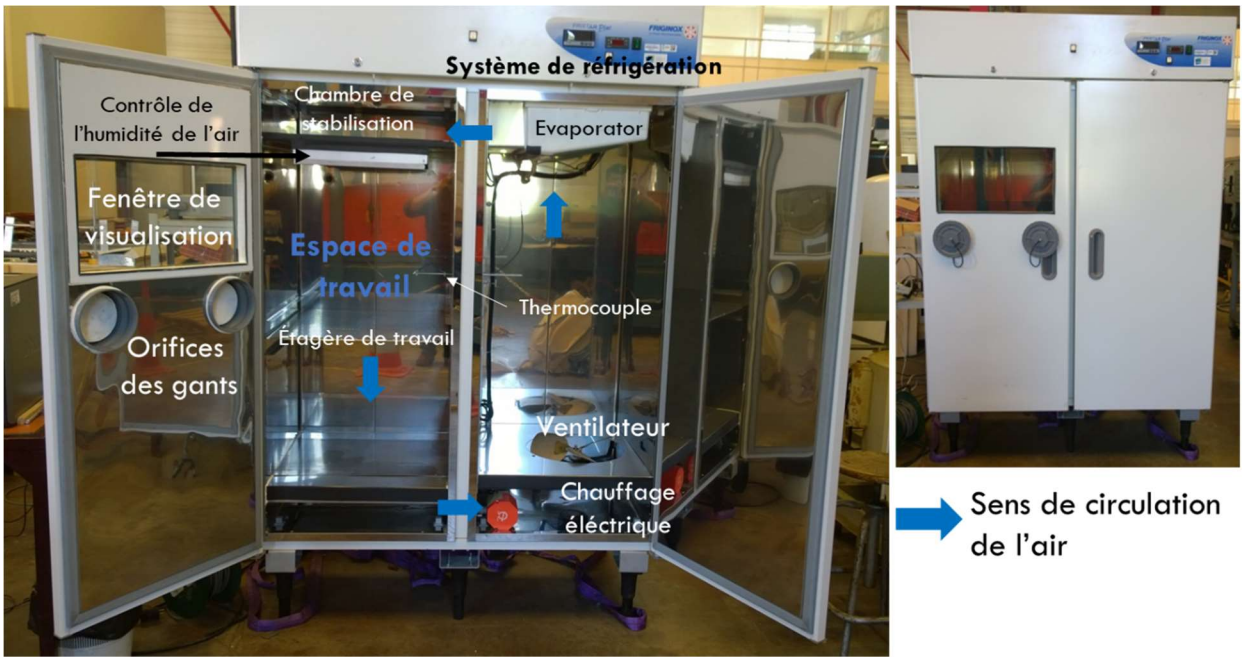

Figure 20. Schéma de la « boîte-à-gants » pour les observations microscopiques à température et humidités contrôlées

3.3.2 Prise des images microscopiques du sorbet et analyse

Un microscope optique (OMAX LED 40X – 2000X) muni d'une caméra a été utilisé pour la visualisation et la quantification de la taille des bulles et cristaux de glace. Le microscope, ainsi que l'ensemble des outils nécessaires pour son usage (lame, lamelles, spatules, etc.) étaient placés préalablement à température adéquate.

De manière conventionnelle, pour réaliser une observation au microscope, un échantillon est placé sur une lame puis est recouvert avec une lamelle pour complètement enfermer l'échantillon entre les deux. Cette procédure n'est pas recommandée pour un échantillon de sorbet ou de crème glacée vu que l'écrasement entre la lame et la lamelle peut casser les cristaux et provoquer une agglomération rapide des bulles déformant la structure qui devrait être observée (Figure 21). Pour cette raison une modification était nécessaire pour mieux préserver la structure à observer. La modification a consisté à coller un morceau de lamelle (d'une épaisseur moyenne de 256 µm) à chaque extrémité d'une lame créant ainsi un volume pour placer l'échantillon à observer (Figure 22). De cette façon, la lamelle risque moins d'écraser l'échantillon et celui-ci se répand légèrement sur la lame sans que sa structure ne soit modifiée. Dans tous les cas, la préparation de l'échantillon sur la lame doit être faite avec délicatesse afin d'éviter toute altération de l'échantillon à analyser. Une fois que l'échantillon est placé et répandu correctement, l'observation peut démarrer.

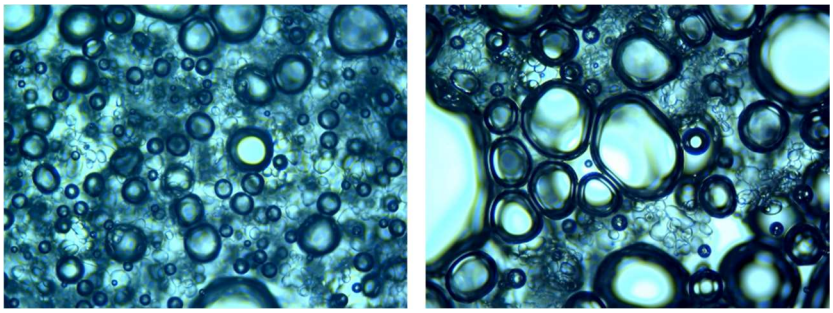

Figure 21. Exemples d'images avec peu ou pas de bulles coalescées (gauche) et avec des bulles coalescées (droite)

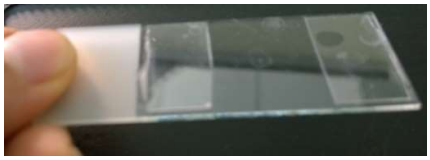

Figure 22. Lame avec lamelles collées aux extrémités pour l'observation microscopique

L'acquisition des images a été faite à l'aide de la caméra couplée au microscope. Pour un échantillon donné, de nombreuses images (typiquement 20 images) avec des bulles et des cristaux ont pu être obtenus en balayant toute l'étendue de l'échantillon sur la lame. Les bulles sont caractérisées par leur forme ronde, plutôt circulaire avec un contour obscur et épais (Figure 23A). En revanche, les cristaux n'ont pas une forme régulière et leur contour est visiblement moins épais que celui des bulles (Figure 23B). En plus, pour une image donnée, il est possible d'observer plusieurs plans de bulles et de cristaux vu l'épaisseur de l'échantillon. L'analyse des images a été faite à l'aide du logiciel ImageJ®.

Comme premier pas dans l'analyse, il fallait déterminer l'échelle correspondant à une distance réelle dans les images à l'aide d'une échelle calibrée. Avec des images de résolution maximale de la caméra du microscope on a pu constater que 228 pixels correspondent à une longueur en ligne droite de 100 µm. La forme circulaire d'une bulle a permis de déterminer son diamètre en utilisant deux points sur le contour et en les reliant en passant par le centre de la bulle (Figure 23A). En revanche, la mesure des caractéristiques de taille d'un cristal a été faite en utilisant un polygone pour représenter son contour (Figure 23B). Le nombre de sommets de chaque polygone varie selon la forme du cristal observé, en moyenne, il était nécessaire d'utiliser des polygones de quatre à dix sommets pour mieux représenter le cristal. Le logiciel ImageJ® a permis alors de calculer les caractéristiques suivantes : d'une part le diamètre pour les bulles d_i, et d'autre part la surface projetée a_i, le périmètre p_i et le **diamètre de Feret maximal*** $l_i \mid_F$ pour les cristaux.

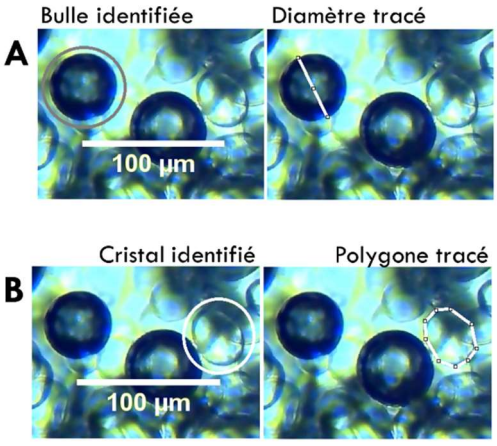

Figure 23. Différentiation et mesure de taille à partir des images obtenues au microscope (**A**) des bulles d'air et (**B**) des cristaux de glace

*Le **diamètre de Feret maximal** est le diamètre le plus grand possible mesuré en utilisant un pied-à-coulisse sur le polygone tracé

3.3.3 Traitement des données

Les informations du logiciel sont recueillies pour un nombre représentatif de cristaux et de bulles (au moins 200 éléments pour une distribution) puis utilisées pour établir la distribution de tailles. Comme les images des bulles ainsi que leurs diamètres ont été obtenus à pression ambiante ; une correction sa été appliquée pour avoir chaque diamètre à la pression interne de l'ECSR :

$$d_i = d_i\big|_{1\text{ atm}} \left(\frac{P}{1\text{ atm}} \right)^{-\frac{1}{3}} \tag{3.4}$$

Trois définitions de diamètres ont été utilisées pour caractériser la taille de cristaux l_i : le diamètre Feret maximale ($l_i|_F$), le diamètre de cercle équivalent à la surface du polygone tracée ($l_i|_a$) et le diamètre d'un cercle équivalent au périmètre tracé ($l_i|_p$) :

$$l_i\big|_a = \sqrt{\frac{4a_i}{\pi}} \tag{3.5}$$

$$l_i\big|_p = \frac{p_i}{\pi} \tag{3.6}$$

Une fois les diamètres calculés, les distributions de tailles ont été représentées par des histogrammes et des distributions cumulées avec des intervalles de classes de 5 µm. La Figure 24a) représente un exemple d'image prise au microscope avec le comptage séparé des bulles d'air et cristaux de glace. Les distributions respectives obtenues (à partir de plusieurs images du même échantillon) sont également représentées sur les Figure 24b) et c). Ce résultat montre que l'observation directe sous microscope optique a permis l'identification et la discrimination des bulles d'air et des cristaux de glace. Le principal inconvénient de cette technique est sa lourdeur en termes de temps et de quantité de données à analyser pour chaque essai. Plusieurs procédés de segmentation ont été testés pour automatiser la discrimination entre les bulles d'air et les cristaux de glace, mais sans succès. Cette différentiation s'est donc faite manuellement.

Les résultats des distributions de taille des cristaux montrent qu'il n'y a pas de différence significative selon le choix du diamètre équivalent utilisé. Dans cette thèse le diamètre équivalent à la surface a été choisi comme représentatif de la taille des cristaux.

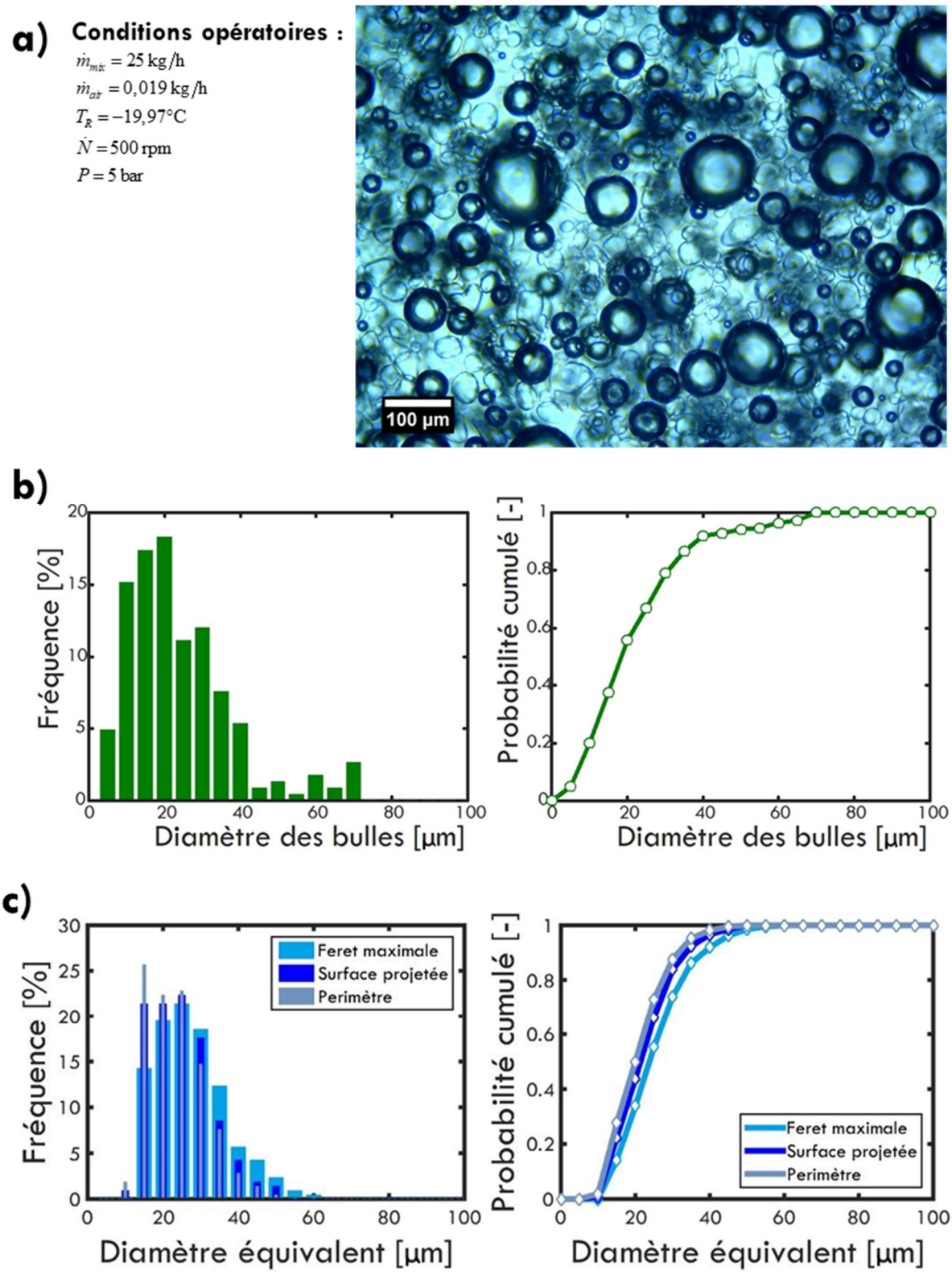

Figure 24. Analyse et traitement des données : a) Exemple d'image obtenue au microscope ; b) distribution de tailles de bulles d'air en fréquence (gauche) et cumulé (droite) ; c) distribution de taille de cristaux de glace en fréquence (gauche) et cumulé (droite)

La répétabilité des techniques de mesure et de traitement des données a été évaluée en comparant les résultats obtenus à partir de différents échantillons d'un même essai. La Figure 25 montre les distributions cumulées de taille des bulles d'air obtenus à partir de quatre échantillons. On peut remarquer que les résultats obtenus sont très proches.

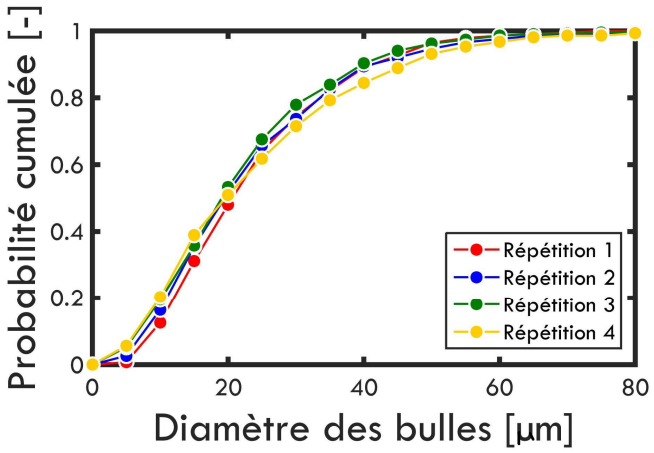

Figure 25. Répétabilité des distributions de taille de bulles obtenus

3.4 Mesure de la distribution des temps de séjour de la phase liquide

Le concept de distribution des temps de séjour (DTS) a été proposé par Danckwerts (1953) comme une méthode pour caractériser l'écoulement dans un réacteur pour des besoins d'analyse des performances ou de dimensionnement. Ce concept a ensuite été étendu à d'autres types d'équipements continus tels que les échangeurs de chaleur, comme moyen de caractérisation des écoulements au sein des équipements. Cette méthode considère, en régime permanent, un flux de matière comme étant composé de différentes fractions entrant en même temps dans le réacteur mais ne franchissent pas la section de sortie au même instant. De ce fait, le temps passé par les différentes fractions à l'intérieur du réacteur est variable. Ce phénomène peut être représenté par une distribution statistique des temps de séjour (Fogler, 1999).

La DTS est déterminée expérimentalement par un traceur qui marquera les fractions de fluide entrant dans le réacteur, et suivra leur histoire jusqu'à la sortie. Pour cela, on utilise un traceur qui peut être un traceur radioactif, un colorant, un sel ou toute substance de mêmes propriétés hydrodynamiques que le fluide, mais décelable par une propriété physique caractéristique telle que la conductivité électrique, ou l'absorbance. On applique, à l'aide du traceur, un certain signal à l'entrée du réacteur (typiquement une impulsion de type Dirac), de manière à ne pas perturber le régime d'écoulement, et on examine sa réponse à la sortie en continu sous la forme d'historique de concentration $C(t)$. On en déduit des informations sur

le comportement interne du fluide. La Figure 26 représente le schéma de principe de détermination de la DTS dans un système quelconque avec un fluide en écoulement

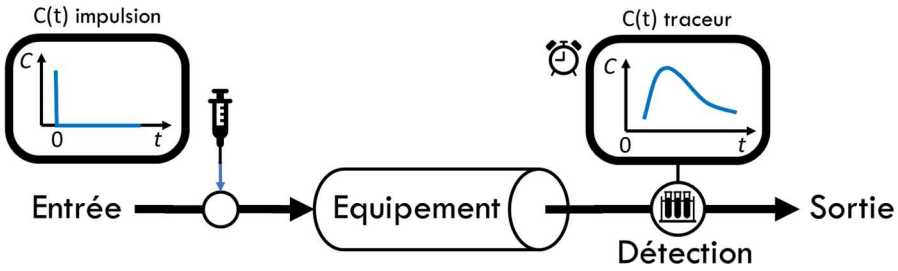

Figure 26. Principe de mesure de la DTS

Si l'entrée est une impulsion, alors la DTS est obtenue par la relation suivante (Villermaux, 1993) :

$$E(t) = \frac{C(t)}{\int_0^\infty C(t)\,dt} \tag{3.7}$$

$E(t)\,dt$ représente la fraction de fluide ayant séjourné dans le système étudié pendant un temps compris entre t et $t + dt$.

Pour appliquer le signal à l'entrée du réacteur, il convient de choisir un traceur capable de suivre le même parcours que le mix dans l'ECSR sans perturber l'écoulement dans l'échangeur. Ce traceur doit aussi avoir les caractéristiques suivantes :

- Utilisable en petites quantités
- Mesure et détection faciles
- Possibilité de réaliser la mesure en continu
- Neutralité vis-à-vis des réactions dans le système
- Pas de toxicité

Le bleu de méthylène (BM) remplit toutes ces conditions et il a été utilisé pour les études de DTS précédentes réalisées avec l'ECSR (Arellano et al., 2013c), il a donc été choisi pour ces travaux.

Le BM est facilement détectable par spectrophotométrie dans des solutions de mix avec une concentration minimale de l'ordre de 0,000025% (m/m) et a un maximum d'absorption à une longueur d'onde de 672 nm. L'absorbance des échantillons a été mesuré à l'aide d'un spectrophotomètre Beckman Coulter DU® 730. De façon préalable aux expériences de mesure de DTS, un étalonnage a été effectué en utilisant des

solutions de mix de sorbet citron colorées à différentes concentrations connues de BM (entre 0 et 0.0004% m/m). Les résultats obtenus sont représentés dans le Tableau 3, ils constituent la moyenne de 3 répétitions. A partir de ces mesures, il a été construit une droite d'étalonnage représentée sur la Figure 27, qui relie la concentration en BM (% m/m) à l'absorbance du milieu en Unité d'absorbance (UA).

Tableau 3.Valeurs moyennes d'absorbances de solutions de mix de sorbet colorés au BM.

Concentration×10⁶ % (m/m)	25	50	100	200	400
Absorbance (UA)	0,061 ± 0,001	0,097 ± 0,002	0,184 ± 0,005	0,326 ± 0,003	0,648 ± 0,003

La corrélation ainsi obtenue permet de connaitre la concentration de BM dans une solution à travers la mesure de son absorbance. Le coefficient de corrélation R^2 de 0.9995 nous permet d'affirmer que pour ce domaine des concentrations la Loi de Beer Lambert est vérifiée.

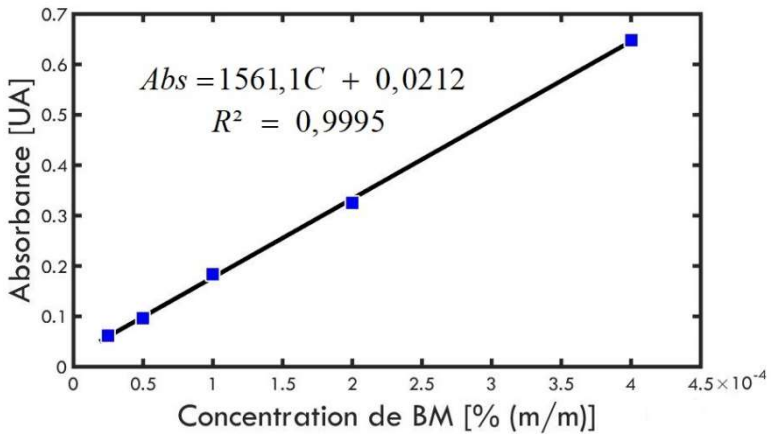

Figure 27. Corrélation entre absorbance et concentration du BM des solutions de mix de sorbet.

3.4.1 Plan d'expériences pour la DTS

Le Tableau 4 ci-dessous présente le plan d'expériences ; 6 conditions expérimentales ont été explorées correspondant à la variation de différents paramètres opératoires : débit d'air, débit de mix et température de réfrigération. Deux expérimentations complètes ont été menées pour chaque point du plan d'expérience, donnant ainsi deux répétitions.

Tableau 4.Plan d'expériences DTS. Les variables variées sont encadrées.

Expérience	$\dot{m}_{air}$ (kg/h)	$\dot{m}_{mix}$ (kg/h)	T_R (°C)	f_{rot} (rpm)	Pressure (bar)
1	0,0375	50	-15,5	500	3
2	0,0014	50	-15,5	500	3
3	0,0125	50	-15,5	500	3
4	0,0125	25	-15,5	500	3
5	0,0125	25	-12	500	3
6	0,0125	25	-10	500	3

3.4.2 Mis en place du système d'injection dans le freezer

Un système d'injection du traceur a été conçu et mis en place à l'entrée de l'échangeur. Le freezer possède un raccord en croix près de l'entrée de l'ECSR et qui constitue le point de mélange des alimentations en mix et en air. Cette pièce a été modifiée afin de permettre l'injection du traceur (voir Figure 28). Ainsi un tube en acier inox (inséré dans le raccord en croix) conduit le mix coloré directement jusqu'à l'entrée de l'échangeur. Ce tube est connecté à une vanne et à une seringue en verre de 20 ml qui contient initialement le mix coloré : un volume de 13 mL de mix additionné de BM à une concentration de 0,008% (m/m). Le système a permis d'avoir une injection de type impulsion avec un temps d'injection étant très bref par rapport au temps de séjour moyen (toujours moins de 1,5 s pour injection par rapport à 2 min de temps de séjour en moyenne). En sortie de l'ECSR, des échantillons ont été prélevés en continu à faibles intervalles de temps et analysés par spectrophotométrie.

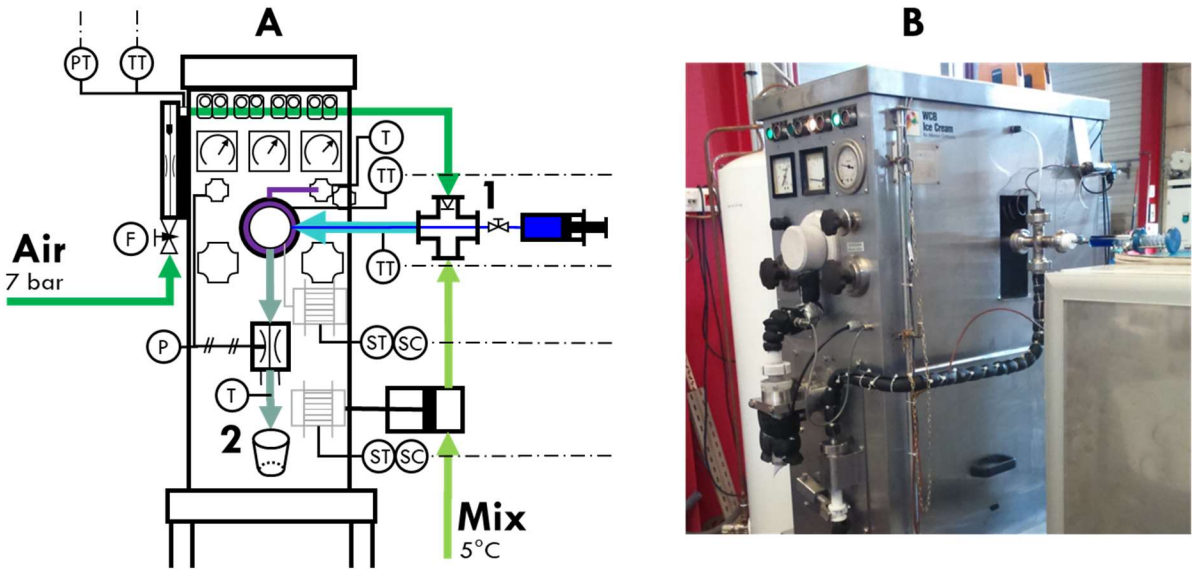

Figure 28. Modification du freezer pour la mesure de DTS. A. Schéma du freezer adapté : 1) le système d'injection installé ; 2) récolte de produit en sortie. B. Image du système réel mis en place

3.4.3 Méthodologie d'obtention de la DTS

La méthodologie suivie pour obtenir une DTS est présentée dans la Figure 29. Une expérience type de fabrication de sorbet au freezer débute tout d'abord par un nettoyage de la machine en faisant passer de l'eau chaude au moins 10 minutes à l'aide de la pompe d'alimentation du système. Ensuite on verse le mix de sorbet dans un réservoir possédant une double enveloppe où il sera amené à une température de 5°C, puis le mix est introduit dans l'ECSR à l'aide de la pompe. On allume le système de réfrigération du freezer et ensuite le racleur, quand le mix commence à sortir congelé, on ouvre la vanne d'air et on règle son débit à l'aide du rotamètre. On attend, environ 30 minutes, que le système atteigne le régime permanent (débit de mix et d'air, vitesse de raclage, température d'évaporation et température de sortie du sorbet stables).

A l'aide de la seringue on injecte d'abord 4 ml de mix coloré (BM à 0,008%) dans le tube reliant la seringue à l'entrée de l'échangeur pour le remplir entièrement. Puis, après plusieurs minutes, on fait l'injection des 13 ml du traceur pour mesurer la DTS, cette injection est chronométrée de manière à s'assurer d'une injection de type impulsion (durée d'injection inférieure à 2% du temps de passage théorique). Immédiatement après l'injection, on commence à prélever le sorbet en sortie de l'ECSR (**élément 1** de la Figure 29). Le prélèvement se fait de manière continue à l'aide de flacons translucides en polyéthylène préalablement tarés et numérotés. Le prélèvement s'effectue jusqu' à ce qu'on ne distingue plus la coloration bleue sur le sorbet en sortie de l'ECSR.

Par la suite, tous les prélèvements sont pesés afin d'obtenir la masse d'échantillon récupéré dans chaque flacon (par différence avec la tare du flacon vide) (**élément 2**). Cette opération nous permet de connaître les durées d'échantillonnage individuelles (pour chaque flacon) et totale (pour l'ensemble de l'essai), connaissant la masse volumique du mix et le débit traversant le système (**élément 6**). Les pots sont ensuite stockés dans un réfrigérateur à 5°C pendant 24 h afin que tous les cristaux de glace puissent fondre et que les bulles d'air puissent être libérées aidés par centrifugation des échantillons si besoin (**élément 3**).

Après la fonte du sorbet dans les différents flacons, les cuves de spectrophotométrie (3 pour chaque échantillon) sont préparées (**élément 4**). Les échantillons sont ensuite analysés au spectrophotomètre à une longueur d'onde fixe de 672 nm et on détermine l'absorbance moyenne pour chaque boîte d'échantillon (**élément 5**). On traduit les absorbances obtenues en concentrations de BM à l'aide de la courbe d'étalonnage préalablement établie et ensuite on établit la correspondance temps et concentration. Puis on obtient les fonctions de DTS, le temps de séjour moyen, sa variance et la fonction de DTS normalisé (**élément 7**). En fin, on procède à la construction des graphiques de DTS (**élément 8**).

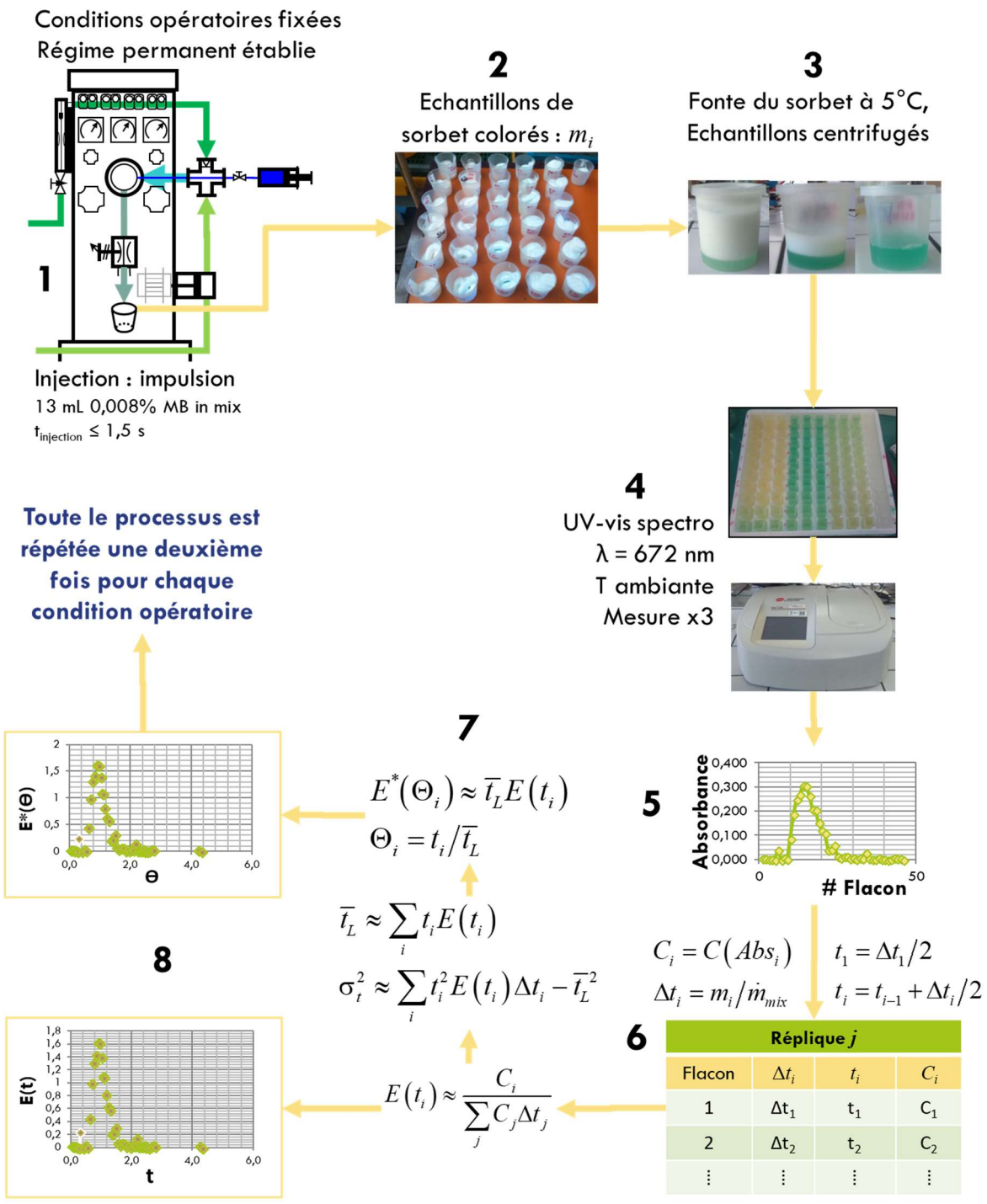

Figure 29.Methodologie d'obtention de la DTS. Voir le texte pour détails

Tout le procédé décrit est refait pour avoir une répétition de la DTS obtenue à chaque ensemble de conditions opératoires.

3.4.4 Ajustement de paramètres des modèles de DTS aux données expérimentales

Quelques modèles de DTS (modèle de dispersion axiale, des réacteurs en cascades et modèle gamma) ont été calés aux résultats expérimentaux par ajustement paramétrique. Le calage s'est effectué par minimisation de la somme des carrés des écarts entre les résultats expérimentaux et les résultats théoriques. Les calculs ont été effectués sur Matlab à l'aide de la fonction *fminsearch* qui utilise l'algorithme du simplexe Nelder-Mead détaillé dans Lagarias et al. (1998).

Nomenclature

a_i	surface projetée d'une bulle dans la classe i (m^2)
Abs	absorbance (UA)
c_1, c_2, c_3, c_4, c_5	constantes pour le calcul du débit massique d'air
$C(t), C$	concentration en traceur pour la DTS (kg m^{-3})
d_i	diamètre des bulles dans la classe i (m)
$E(t); E$	fonction de la DTS (s^{-1})
$E^*(\theta)$	fonction adimensionnelle de la DTS (-)
H	hauteur de la bille dans le rotamètre (mm)
K	indice de consistence pour la loi de puissance (Pa s^n)
$l_i \mid_F$	diamètre maximal de Feret des cristaux dans la classe i (m)
$\dot{m}$	débit massique (kg h^{-1})
m_i	masse de l'échantillon de sorbet dans le flacon i (kg)
n	Indice d'écoulement pour la loi de puissance (-)
$\dot{N}$	vitesse de rotation du rotor (tr s^{-1})
p_i	périmètre d'une bulle dans la classe i (m)
P	Pression (Pa)
t	temps (s)
$t_{injection}$	durée d'injection (s)
t_L	temps de séjour moyen (s)
Δt_i	durée d'échantillonnage de sorbet dans le flacon i (s)
T	température (K)
T_R	température d'évaporation du fluide réfrigérant (K)
w	fraction massique (-)
x	fraction molaire (-)

Greek letters

θ	temps adimensionnel (-)
σ^2	variance (s^2)

Subscripts

air	air
if	congelation commençante
mix	mix
s	soluté
w	eau

Superscripts

*	in the liquidus curve

Abbreviations

DTS	distribution des temps de séjour

Références

Arellano, M., Benkhelifa, H., Alvarez, G., Flick, D., (2013). Experimental study and modelling of the residence time distribution in a scraped surface heat exchanger during sorbet freezing. Journal of Food Engineering 117(1), 14-25.

Danckwerts, P.V., (1953). Continuous flow systems: Distribution of residence times. Chemical Engineering Science 2(1), 1-13.

Donhowe, D.P., Hartel, R.W., Bradley Jr, R.L., (1991). Determination of Ice Crystal Size Distributions in Frozen Desserts. Journal of Dairy Science 74(10), 3334-3344.

Fogler, H.S., (1999). *Elements of Chemical Reaction Engineering*. Prentice Hall PTR.

González, J.E., (2012). Contribution au contrôle par la modélisation d'un procédé de cristallisation en continu. AgroParisTech.

Lagarias, J.C., Reeds, J.A., Wright, M.H., Wright, P.E., (1998). Convergence Properties of the Nelder--Mead Simplex Method in Low Dimensions. SIAM Journal on Optimization 9(1), 112-147.

Sofjan, R.P., Hartel, R.W., (2004). Effects of overrun on structural and physical characteristics of ice cream. International Dairy Journal 14(3), 255-262.

Villermaux, J., (1993). *Génie de la réaction chimique - Conception et fonctionnement des réacteurs* (2nde ed). Tec & Doc - Lavoisier, Paris.

RESULTATS ET DISCUSSION

4. Effect of process parameters on ice crystals and air bubbles size distributions of sorbets in a scraped surface heat exchanger

Accepted manuscript in International Journal of Refrigeration, in press. Available online 6 April 2018. https://doi.org/10.1016/j.ijrefrig.2018.02.013

Abstract

Ice crystals and bubbles size distributions were characterized for aerated sorbets produced during a crystallization-foaming process in a scraped surface heat exchanger. Size measurements were performed immediately at the exit of the heat exchanger by means of a low-temperature microscopy method especially developed in order to discriminate between ice crystals and bubbles and to make possible to measure both sizes simultaneously. The influence of process parameters such as refrigerant fluid evaporating temperature and air flowrate on both size distributions was investigated. Larger ice crystals were obtained when refrigerant fluid temperature increased, but this effect was minimized by the presence of air which retards crystal growth by insulation and hindrance effect. Low refrigerant fluid temperature led to small air bubbles size because of the enhancement of bubbles breakup by shear forces. Ice crystals size was reduced when air flowrate was increased, even if the effect was less pronounced at the lower refrigerant fluid temperature. Variations on air flowrate had a very small effect on air bubbles size.

Keywords

Sorbet, Ice crystal size, Bubble size, Air flowrate, Low-temperature microscopy, Scraped surface heat exchanger

Highlights

- A low-temperature microscopy method was developed for crystals and bubbles size measurement
- The influences of refrigerant fluid temperature and air flowrate were investigated
- Lowering refrigerant fluid temperature decreased ice crystals and air bubbles sizes
- Increasing air flowrate reduces ice crystals size
- Changes in air flowrate have a slight impact on air bubbles size

4.1 Introduction

Industrial manufacture of ice creams and sorbets is commonly carried out in continuous units equipped with scraped surface heat exchangers (SSHEs). The latter are fed with a formulated liquid (mix) whose water is frozen on the walls of the exchanger and the ice is scraped into the product by the SSHE rotating blades. Also, during production, air is incorporated to the mix flow before entering the SSHE and whipped into the product by the blades making the ice cream or sorbet production an interesting coupled crystallization/foaming process. In ice cream production, fat and dairy proteins present in the mix play a complex role along with the processing conditions (i.e. formulations, flowrates, overrun, etc.) on the development of the microstructure. Consequently, they influence the bubble (BSD) and crystal size distributions (CSD) in the product obtained at the exit of the SSHE (Cook and Hartel, 2010; Goff et al., 1999). However, for sorbets, the absence of fat or dairy ingredients is to be compensated by the sole effect of operating conditions. In all cases, immediately after freezing, the soft product undergoes a storage step during some time at low temperature for hardening. During this step, Ostwald ripening is observed on crystals leading to overall crystal growth (Russell et al., 1999) and changes in the air cells size occur by disproportionation, coalescence and channeling (Chang and Hartel, 2002c) depending on the hardening conditions and the size distributions at the freezer exit.

To follow the effect of operating conditions during freezing or hardening, it is necessary to obtain the CSD and BSD in the product. Several analysis methodologies have been proposed in the literature for that aim. One of the first and most commonly used consist of the technique of optical microscopy in a cold environment (e.g. Chang and Hartel (2002b); Donhowe et al. (1991b); Inoue et al. (2008)), with the help of special lighting like episcopic coaxial lighting (e.g. Caillet et al. (2003); Faydi et al. (2001)), or fluorescence (e.g. Regand and Goff (2003)). Scanning (e.g. Goff et al. (1999); Inoue et al. (2008); Miller-Livney and Hartel (1997); Russell et al. (1999)) or transmission electron microscopy (e.g. Goff et al. (1999)) in cryogenic conditions have also been proposed. Most of these methods have been only used after hardening and can alter or destroy the microstructure of samples (e.g. immersion in liquid nitrogen, use of solvents for obtaining one or both size distributions, sublimation, etc.). A successful implementation of a laser focused beam reflectance method (FBRM) for on-line measurement of ice crystals during the freezing of non-aerated sorbet in continuous freezers (Arellano et al., 2012b) have been reported. The FBRM has also been successfully used to study recrystallization phenomena during storage of commercial ice creams (Hernandez et al., 2015), as well as to measure micro bubbles generated during fermentation (Druzinec et al., 2015). This methodology has the advantage of being a non-destructive online measurement system

suitable to be placed on the conduct at the exit of the freezer. However, it yields distributions in terms of chord lengths that prove difficult to compare with other image-based microscopy information since chord length distributions can only be exactly related to diameters for a suspension of spheres. Additionally, the fact that bubbles and crystals in ice creams and sorbets are expected to be of similar sizes, makes this methodology inadequate for simultaneous measurement of both distributions.

Regarding the CSD, the mechanisms of ice crystallization in SSHEs during ice cream production have been thoroughly described (Cook and Hartel, 2010). In summary, the key phenomena that describe the evolution of crystals are nucleation near or at the wall and crystal growth and ripening throughout the barrel. The last two are the most influential on the observed CSD at the freezer exit (Cook and Hartel, 2011; Russell et al., 1999). For instance, decreasing mix flowrates have been reported to increase crystal sizes in ice creams (Drewett and Hartel, 2007; Inoue et al., 2008; Russell et al., 1999), and sucrose solutions (Haddad Amamou et al., 2010) since crystal growth and ripening are favored by long residence times. However, for non-aerated sorbets no significant effect have been observed (Arellano et al., 2012b) due to an opposing effect of lower temperature caused by longer residence times, with a subsequent strong effect on viscosity and shear stress, that could lead to attrition of ice crystals. Also, an increased air content led to decrease ice crystal sizes in ice creams since bubbles could act as a barrier for water diffusion and consequently for crystal growth (Caillet et al., 2003; Flores and Goff, 1999; Sofjan and Hartel, 2004). Larger crystals have been observed in ice creams at higher refrigerant fluid evaporating temperatures in ice creams (Russell et al., 1999) and non-aerated sorbets (Arellano et al., 2012b).

On the other hand, considering the elevated viscosity variations at low temperatures in concentrated ice cream mixes (Bolliger et al., 2000) and concentrated sorbet mixes (González-Ramírez, 2012), it is likely that a viscous stress mechanism is responsible for the bubble breakup, as with other food processes with air whipping (Mary et al., 2013; Müller-Fischer and Windhab, 2005). This mechanism has been reviewed elsewhere (Liao and Lucas, 2009). In summary, breakup of a particular air cell is conditioned (i) on surpassing a critical Capillary number (i.e. the ratio between viscous stress applied to interfacial tension) that depends on the viscosity ratio (μ_{air}/μ_{fluid}) and the type of stress applied, (ii) and on maintaining it longer than the required breakup time (which also depends on the viscosity ratio). Consequently, it is not surprising that, for ice creams, draw temperature had been reported to have the most significant effect on mean air bubbles size in ice cream production (Inoue et al., 2008) and that lower draw temperatures resulted in smaller air bubbles in continuous freezers (Caillet et al., 2003; Inoue et al., 2008), continuous

freezers coupled with low-temperature extruders (Eisner et al., 2005) and batch freezers (Chang and Hartel, 2002a).

As mentioned above, in most of the works reported in the literature, CSD and BSD of products were measured after hardening where crystal growth could occur, and bubble size could be modified after storage. There is relatively little work in literature about the characterization of the microstructure just at the freezer outlet which would be very valuable information on the effect of the process on crystals and bubbles distributions. Under this perspective, the aim of this work is to develop an experimental protocol based on a low-temperature microscopy technique to measure at the same time both BSD and CSD immediately after the exit of a continuous freezer (SSHE). The methodology will be used to study the effect of operating conditions, such as the refrigerant fluid evaporating temperature and the air flowrate, on the aerated sorbet.

4.2 Materials and methods

4.2.1 Sorbet production

A commercial ultra-high temperature pasteurized lemon sorbet mix of 25 Brix from Laiterie de Montaigu (Montaigu, France) was employed in this work for sorbet production. It is composed of 14.6% w/w sucrose, 8% w/w fructose, 0.09% w/w dextrose, 3% w/w lemon juice concentrate, 0.5% w/w locust bean gum/guar gum/ hypromellose stabilizer blend. The initial freezing temperature of the mix was -2.6°C and the density was 1100 kg m^{-3} at 5°C. The sorbet mix was kept at 5°C for at least 24 h before freezing.

A scheme of the continuous freezing equipment is presented in Figure 30. Sorbet mix was stored in a jacketed feeding tank (**1**) that is connected to a thermostatic bath set to maintain the mix temperature at 5°C during the experimental runs. Freezing of the mix was carried out in an instrumented pilot-scale continuous freezer (WCB® Model MF 50) equipped with an SSHE. A piston pump in the system (**2**), allowed the sorbet mix to flow at a controlled flowrate of 0.0069 ± 0.0001 kg s^{-1} (25.0 ± 0.4 kg h^{-1}). Air flowrates ranging from 0 to 1.04×10^{-5} kg s^{-1} (0.05 kg h^{-1}) ±10% were introduced to the equipment from the available local facility through a rotameter (**3**) (Sho-Rate GT 1357, Brook Instruments, Crawley UK) equipped with a needle valve. Both mix and air flowrates were directed into a T-joint (**4**) where a non-return check valve allowed the incorporation of air into the liquid flow before freezing.

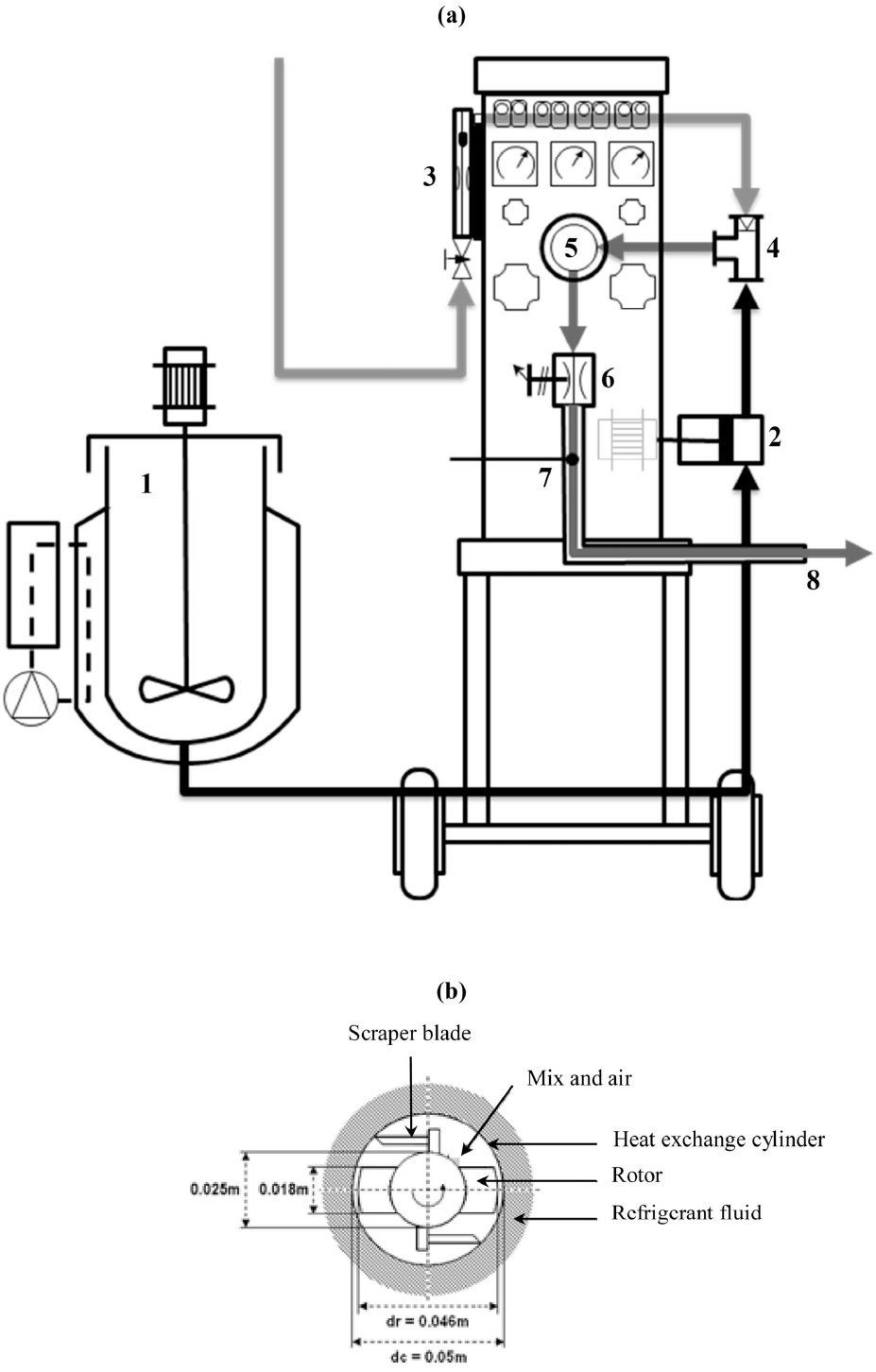

Figure 30. **(a)** Schematic representation of the freezer used in this work. **1**. Refrigerated feeding tank, **2.** Piston pump connected to a variable speed drive, **3.** Air flow measurement with attached pressure and thermocouple system, **4.** Air dispersion into the mix flow through a non-return valve, **5.** Scraped surface heat exchanger, **6.** Backflow valve for internal pressure control, **7.** Draw temperature measurement point, **8.** Sample recovery point. **(b)** Schematic representation of the cross section of the SSHE.

The SSHE (**5**) was a double pipe heat exchanger whose inner pipe (0.05 m inner diameter, 0.40 m long) contains a solid flattened cylindrical rotor (dasher: 0.018 - 0.044 m diameter, 0.40 m long) equipped with

two scraper blades placed at opposite positions and occupying approximately 46% of the volume of the inner pipe. The total volume of the SSHE available to the working fluid was 6.7×10^{-4} m^3, which includes the volume available within the heat exchange cylinder, the inlet and outlet bowls, as well as the outlet pipe. The outlet pipe of the SSHE represents 20% of the total available volume to the fluid. The rotor was connected to a motor with variable rotational frequencies in the range of 21 to 105 rad s^{-1} (200 to 1000 ± 1 rpm), In the jacket, evaporating R22 refrigerating fluid provided freezing. The temperature of the refrigerant fluid was adjusted manually within the range of -10 to -20°C through a valve releasing pressure and registered using a calibrated type T (copper - constantan) thermocouple (accuracy: ± 0.2°C) fixed on the surface wall of the jacket. At the outlet of the SSHE, the sorbet was directed towards the exit where a manual pneumatic back pressure membrane valve (**6**) allows the control of the pressure inside the cylinder. The pressure was measured by a manometer connected to the inner pipe. Also, the draw temperature of the product was measured online by a calibrated Pt100 probe (Baumer®, accuracy: ± 0.1°C) inserted into the outlet pipe (**7**) just before the sampling point (**8**). All piping, from the feeding tank to the outlet was covered with insulation foam. Programs written on LabVIEW® allowed control of variables and collected all operating conditions by means of two data-loggers Agilent HP (Model 34970 A) and two Switch Units Agilent HP (Model 34901 A) connected to a PC. The acquisition of data was performed every 5 s.

Once the freezer operation was started and the desired operating conditions were set up, stationary state was reached after no longer change in temperatures during 30 min of operation.

4.2.2 CSD and BSD measurement

The refrigerated glove-box

Once the freezer attained stationary operation, the exiting product was recovered by filling carefully 125 mL carton boxes. Each carton box was placed in a refrigerated glove box built for this work and the microscope observation was performed immediately after sampling. The refrigerated glove box was inspired by a previously published method (Donhowe et al., 1991b) and presented in Figure 31. It was built adapting a laboratory cold cabinet that was divided vertically into two zones (right and left-hand sides) with upper and lower conducts for connecting both. A fan (**1**) installed in the right-hand side delivered an internal circulation air flow of approximately 2×10^{-3} m^3 s^{-1} throughout the system. The air was cooled by a refrigerating machine (**2**) working with R404a. The airflow passed through a chamber for dehydration and stabilization (**3**). A honeycomb mesh directed the air flow towards the workspace chamber (**4**) for microscopy analysis. The door of this side has been embedded with a triple-glass insulation window to provide internal view during microscopy manipulations. The workspace chamber was equipped with a thermocouple (**5**) placed as close as possible to the microscope stage. Two orifices in the door were positioned to place insulated gloves (**6**) that allowed quickly removal and placement during operation.

Also, a small orifice allowed connection of the microscope placed in the workspace to an external computer (**7**). Under the fan, an electrical heating resistance (**8**) was installed at the lower intersection of both sides in order to provide heating on the air flow. Both, the refrigeration system on top and the heating system on the bottom served as an automated control system for the temperature in the workspace chamber through the aid of a programmable PLC within a range of -25 to 25°C ± 0.1°C. The temperatures homogeneity in the glovebox was controlled and measured.

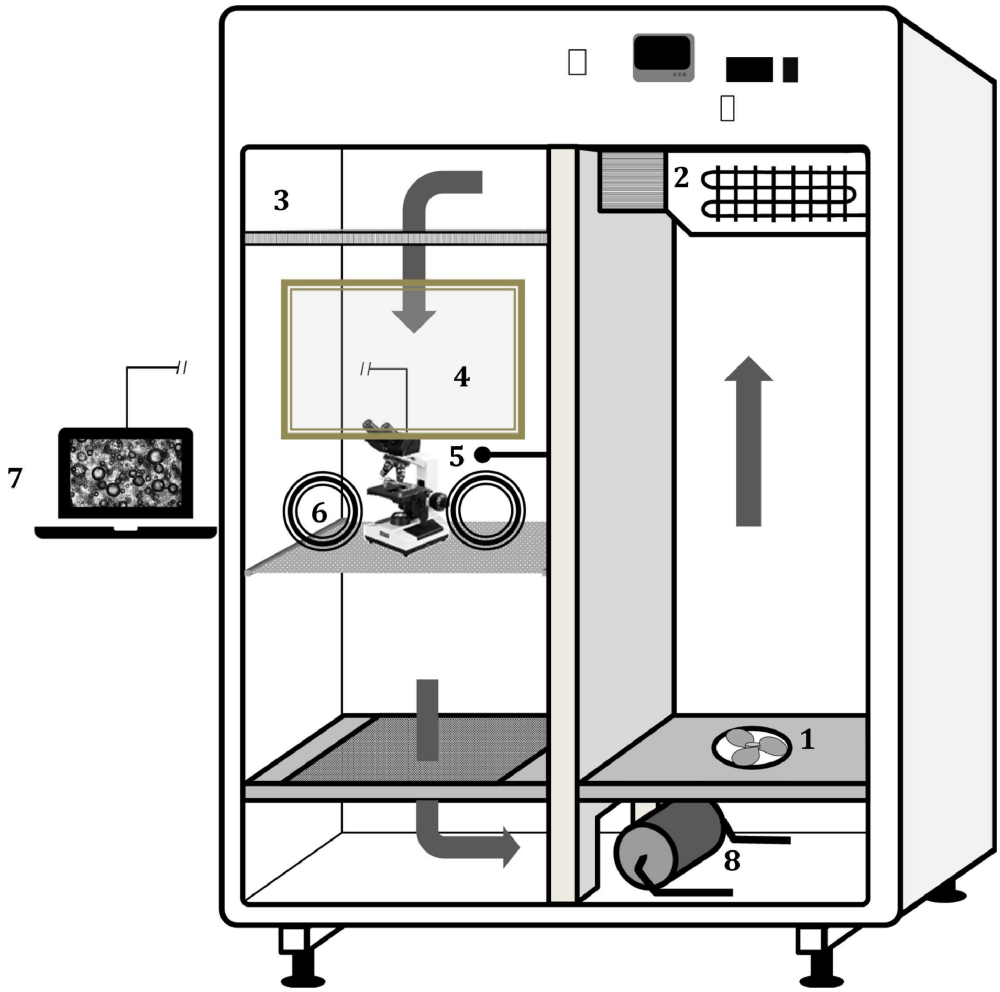

Figure 31. Schematic representation of the refrigerated glove box used in this work. See text for details.

Microscopy analysis

Preliminary temperatures measurements were performed in order to evaluate the local heating due to the light microscope. A local temperature of -6°C was found close to the observation point when the glove box temperature is set at -10°C. As -6°C corresponds to an average SSHE exit sorbet temperature, -10°C was

selected as setting temperature of the glove box. Before any observation, the microscope and all materials (except the sorbet sample) were placed inside the glove box set at -10°C and allowed to cool down overnight. The microscope observation was carried out immediately (within 1 minute) after sampling from the freezer exit according to the protocol described in the diagram shown in Figure 32. Small sample (typically less than 10 mg) was extracted from the center of the sorbet container and gently spread at the middle of a modified slide (with a pair of pieces of slips glued at both extremes providing a space with a thickness of about 240 μm between the covering slips and the slide for sorbet sample – Figure 33a). Observations were done using an optical microscope (OMAX) at 10X magnification equipped with a camera connected to a computer. Several pictures on different random zones of the visualization field were taken and used for image analysis of which an example is presented in Figure 33b. The temperature close to the observation point is continuously recorded during images acquisition and was found to be around -6°C (for a set temperature of -10°C). The whole analysis is carried out within a short time (≈ 2 minutes), making sure that there was no melting of the sorbet sample. Otherwise, the ratio between the ice crystal size measured inside the glove box at -6°C (d_{meas}) and the ice crystal size at the outlet temperature T_{outlet} ($d_{Toutlet}$) can be calculated using the following expression: $d_{meas}/d_{Toutlet} = (w_{i,-6°C}/w_{i,Toutlet})^{1/3}$ where and w_i is the ice mass fraction at a given temperature. In the outlet temperature range of -7.2 to -5.1°C, this ratio varies from 0.97 to 1.12, meaning very little variation in the ice crystal sizes.

The image analysis of the photographs was carried out using software ImageJ®. The bubbles in the pictures were easily identified by their characteristic circular form with a thick dark boundary and background with a bright center as shown in Figure 33c. For every identified bubble, the diameter was carefully traced and the software provided the equivalent length. Since the samples and the microscope observation are carried out outside the exchanger (i.e. at P_{atm} = 101,3 kPa), all measured diameters were corrected to SSHE pressure, assuming that air in the bubble follows ideal gas behavior, i.e. multiplying by $(P/P_{atm})^{1/3}$. This allows to compare crystals and bubbles sizes inside the SSHE. At least 200 diameters were measured from photographs coming from every set of operating conditions, and with them, the BSD was obtained through counting the elements contained in classes of 5 μm wide. For this, several pictures (up to 20) were required for each set of operating conditions. On the other hand, crystals were identified by the thin dark boundary with a transparent or semitransparent background as shown in Figure 32c. The shape of every crystal was obtained by carefully drawing its projection on the image. The software allowed the calculation of its area and the size was expressed in terms of the circle diameter having the same area as the projected crystal shape. Similarly, at least 200 crystals sizes were obtained from the photographs coming from a unique set of operating conditions and the CSD was obtained counting the elements contained in bins of 5 μm wide.

CSD and BSD were expressed in cumulative fractions (Figure 33d) or frequencies (Figure 33e) within each class.

It should be pointed out that this microscopy method was especially developed in this work and that it has the advantage to make possible to measure simultaneously both ice crystals and bubbles sizes.

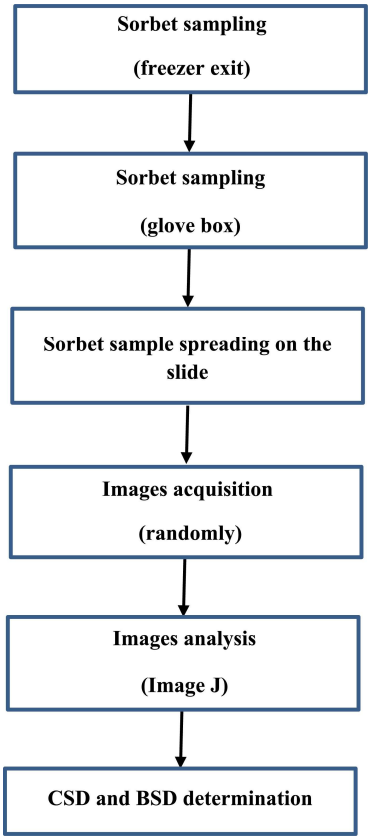

Figure 32. Diagram of the microscopy analysis steps.

(a)

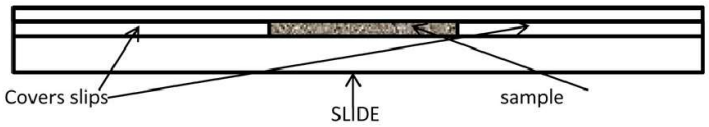

(b)

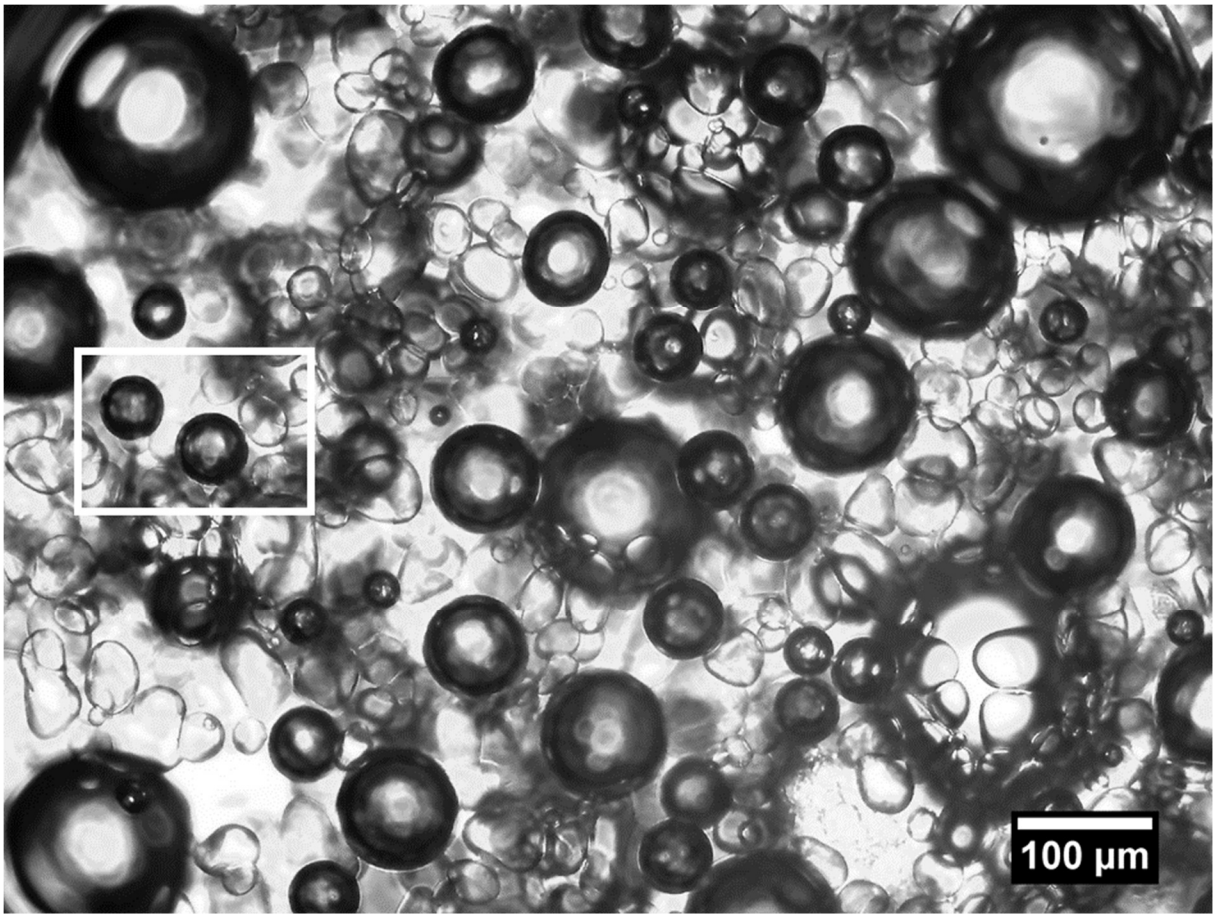

Figure 33. Example of sorbet CSD and BSD measurement procedure obtained at $\dot{m}_{air}$ = 0.0116 kg h^{-1}, T_R = -19.3°C, f_{rot} = 500 rpm and P = 5 bar. (a) Slides with two glued slips pieces; (b) Sample of image; (c) illustration of bubble and crystal measurement, top: bubble identification and diameter outline, bottom: crystal identification and drawing; (d) cumulative distributions; (e) frequency plot.

(c)

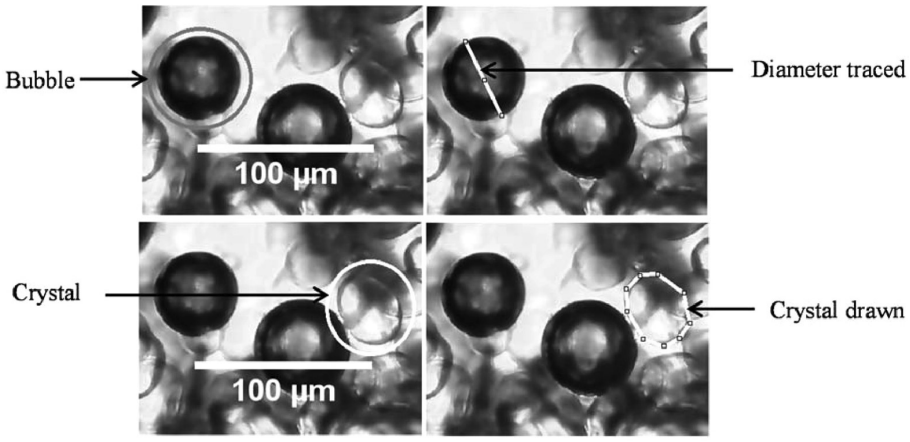

(d)

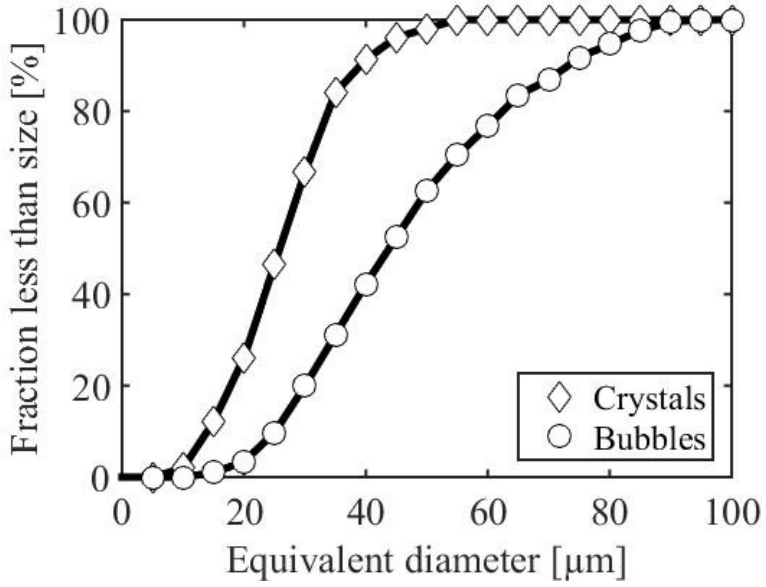

Figure 33. Continuation

(e)

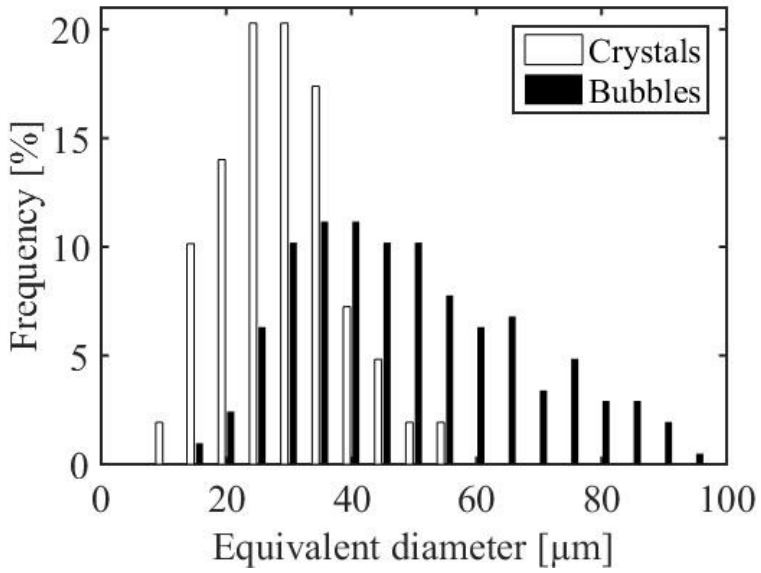

Figure 33. Continuation

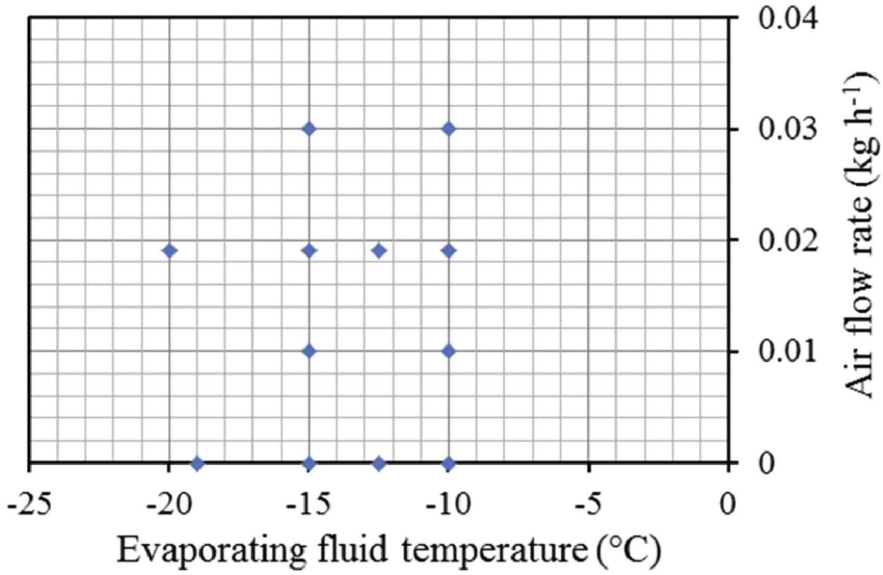

Figure 34. Experimental design.

4.2.3 Operating process parameters

In this work, the effects of two operating parameters were explored: the refrigerant fluid evaporating temperature (T_R) and the air flowrate. The mix flowrate ($\dot{m}_{mix}$), the dasher rotation frequency (f_{rot}) and the cylinder pressure (P) were kept constant at 25 kg h^{-1}, 500 rpm and 3 ± 0.1 bar respectively. The set of operating conditions used are presented in Figure 34. For each operating condition, the freezing procedure with the microscopy observation and determination of CSD and BSD was carried out by at least two replicates.

4.3 Results and discussion

4.3.1 Repeatability of the experimental measurement

In order to evaluate the repeatability of the measurement of CSD and BSD, three replications of sorbet freezing runs at $\dot{m}_{air}$ = 0.019 kg h^{-1} (overrun of 67%), T_R = -15.0°C, f_{rot} = 500 rpm and P = 3.0 bar were carried out and the results are shown in Figure 35. This figure shows that for the same operating conditions, CSD and BSD show a good repeatability. Low variability was found corresponding to low coefficients of variation: 3.6% and 6.2% for CSD and for BSD respectively.

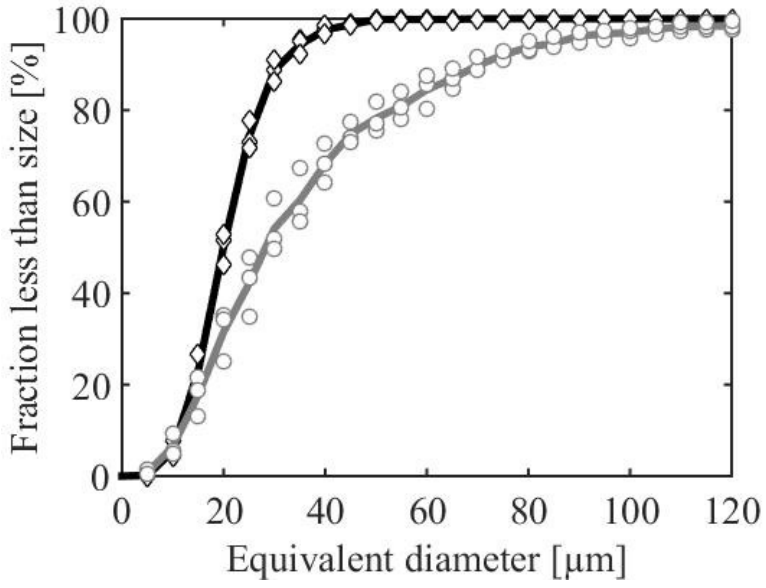

Figure 35. Reproducibility of the BSD and CSD measurement at $\dot{m}_{air}$ = 0.019 kg h^{-1}, T_R = -15.0°C, f_{rot} = 500 rpm and P = 3 bar: (—) average CSD; (◊) experimental replications of CSD; (—) average BSD; (○) experimental replications of BSD.

4.3.2 Effect of refrigerant temperature on the CSD and BSD

Effect of refrigerant fluid evaporating temperature on the CSD

The effect of refrigerant fluid evaporating temperature on the CSD of sorbets was studied with and without air incorporation. Experimental results obtained without air and at an air flowrate of 0.019 kg h^{-1} (overrun of 67%) are presented in Figure 36a and b, respectively. In both cases, a decrease in the evaporation temperature of the refrigerant fluid resulted in CSDs with smaller ice crystals. At T_R = -10°C without air incorporation, only 5% of the population of ice crystals are in the size range between 0 and 40 µm. This fraction increased sharply to reach 93%, 98% and 99% at -12.5, -15 and -19°C respectively. CSDs obtained at -15°C and -19 /-20°C exhibit very similar behaviors, both with and without air incorporation. This result can be explained by the fact that at a lower refrigerating fluid temperature, nucleation is the main mechanism occurring and a large amount of nuclei are formed at the SSHE's wall. Crystal growth mechanism takes place at a smaller extent, resulting in a large amount of small crystals. Moreover, the high viscosity obtained at those temperatures makes water molecules diffusion difficult, resulting in less crystal growth and ripening. In contrast, at a higher refrigerating fluid temperature, the growth of crystals is easier and nucleation more limited, hence producing less crystals but with larger sizes. These results agree with those reported in a similar range of refrigerant fluid temperatures for non-aerated sorbets (Arellano et al., 2012b), and for ice cream (Russell et al., 1999).

On comparing CSDs with and without air, it can be seen in Figure 36 that the air incorporation significantly changes the CSD at the higher refrigerant fluid temperature values. Indeed, at T_R = -10°C, the presence of air leads to a large decrease of the crystals size which passes from an average of 72 ± 2 µm without air to 35.6 ± 1.0 µm with air (Table 4). Only slight decreases were obtained at -12.5°C with ice crystals size passing from an average of 29.8 ± 0.3 µm without air to 28.3 ± 0.8 µm with air, and at -15°C with 25.1 ± 0.1 µm and 23.4 ± 0.7 µm without and with air respectively. For the lower temperature (T_R = -20°C), no significant change was observed on average crystals sizes with (25.4 ± 1.1 µm) and without air (24.9 ± 1.0 µm). These results show that at high temperature, air bubbles play a very important role on the crystal growth mechanism. The effect may be related to a less efficient heat transfer between the SSHE's wall and the heat exchanger bulk volume, due to the presence of air which may act as an insulator, thus limiting the ice crystal growth. Air bubbles may also reduce water mobility through steric hindrance, retarding crystal growth. At low refrigerant fluid temperature, ice is mainly produced by nucleation at the wall, the insulation and hindrance effects of air cells in the bulk has therefore a limited effect on CSD. This could explain the slight influence of the presence of air on CSDs at -15 and -20°C. Similar findings were reported in previous studies about ice cream (Caillet et al., 2003; Inoue et al., 2008; Sofjan and Hartel, 2004). It should

be pointed out that mean crystals sizes obtained in this work are often (except at T_R = -10°C) in the size range recommended for a good acceptability of consumers (< 50µm).

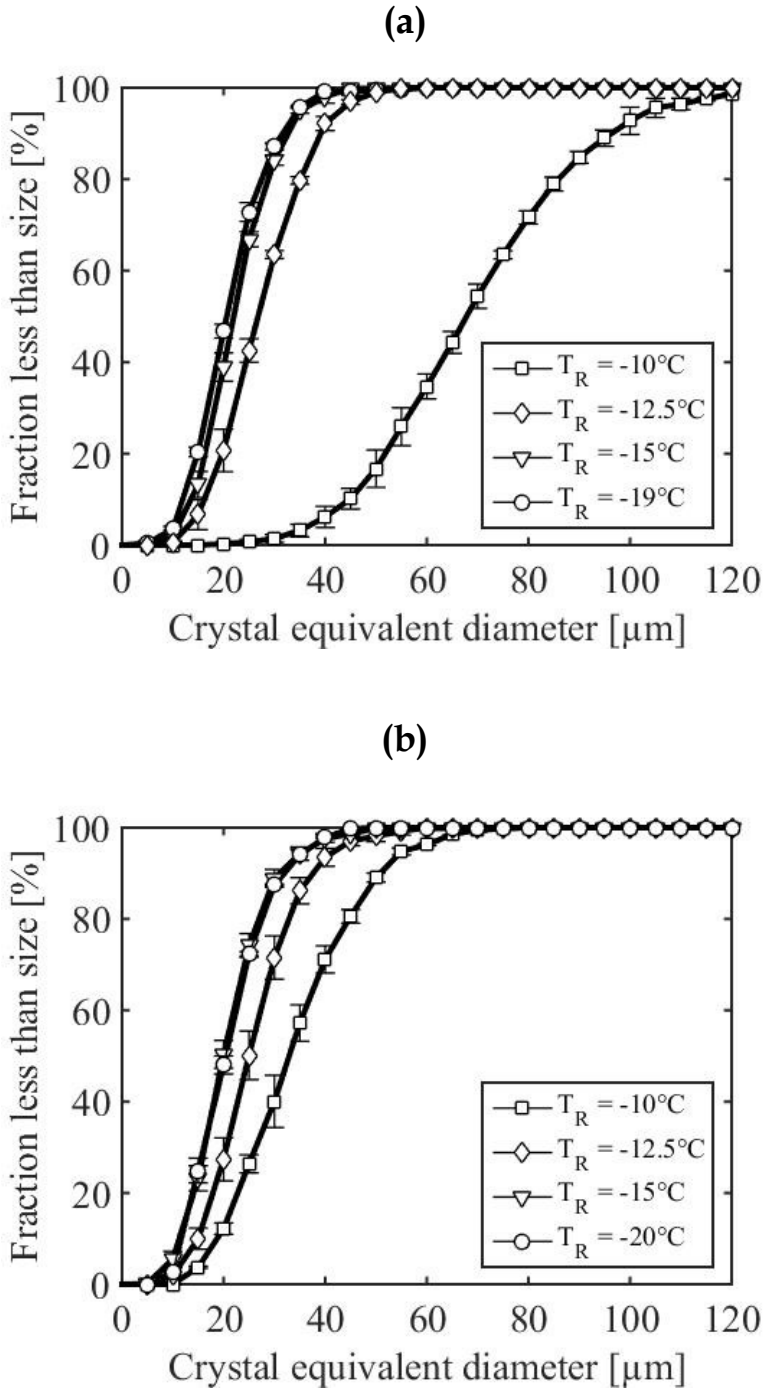

Figure 36. Effect of refrigerant temperature on the CSD obtained in sorbets using f_{rot} = 500 rpm and P = 3 bar: a) without air and b) with air supplied at 0.019 kg h^{-1}.

Table 4. Effect of refrigerating fluid evaporating temperature on mean ice crystals and bubbles sizes

$\dot{m}_{air}$ (kg h^{-1})	0				0.019			
Overrun (%)	0				67			
T_R (°C)	-10.3	-12.5	-15.5	-18.7	-10.0	-12.6	-15.1	-20.0
T_{outlet} (°C)	-3.8	-5.1	-6.5	-7.2	-3.2	-5.1	-5.8	-6.3
Ice volume fraction*	0.19	0.31	0.38	0.41	0.09	0.31	0.35	0.37
Crystals mean size (µm)	72.0 ± 2.0	29.8 ± 0.3	25.1 ± 0.1	25.4 ± 1.1	35.6 ± 1.0	28.3 ± 0.8	23.4 ± 0.7	24.9 ± 1.0
Bubbles mean size (µm)	-	-	-	-	49.7 ± 1.8	36.0 ± 0.4	27.5 ± 0.23	14.3 ± 1.3

Mix flowrate = 25kg h^{-1}; Rotational speed = 500 rpm; Pressure = 3 bar
*Calculated from Arellano et al (2013a)

Effect of refrigerant fluid temperature on the BSD

Figure 37 shows the effect of the evaporation temperature of the refrigerant fluid on BSD obtained at constant air flowrate (0.019 kg h^{-1}), rotation frequency (500 rpm) and pressure (3.0 bar). Smaller bubbles sizes were obtained with lower refrigerant fluid temperatures. Mean sizes ranging from 49.7 ± 1.8 to 14.3 ± 1.3 µm were obtained at refrigerant fluid temperature varied between -10 and -20°C respectively (Table 4). The maximum air bubble size was lowered from about 150 to about 50 µm when the refrigerant fluid temperature was decreased from -10 to -20°C, resulting in narrower BSDs as shown in Figure 37. The bubbles sizes obtained in this study are in the size range already reported in the literature for ice cream (Caillet et al., 2003; Chang and Hartel, 2002a, b; Eisner et al., 2005; Sofjan and Hartel, 2004). Lower refrigerant temperatures are associated with lower fluid temperatures inside the exchanger and at the outlet (see T_{outlet} in Table 4). (Caillet et al., 2003) and (Eisner et al., 2005) also reported air cells size increasing with outlet temperatures. This ending may be attributed to changes in the viscosity of the liquid phase surrounding the bubbles. Lower refrigerant temperatures enhance the nucleation rate of ice on the internal wall, leading to an increase of ice fraction (Table 4) which further increases the apparent viscosity. Consequently, the shear forces which tend to deform and break-up the bubbles becomes higher, enhancing bubbles fragmentation. Moreover, the probability of coalescence, which involves two or more bubbles to form larges one, is reduced, leading to a population of small air bubbles.

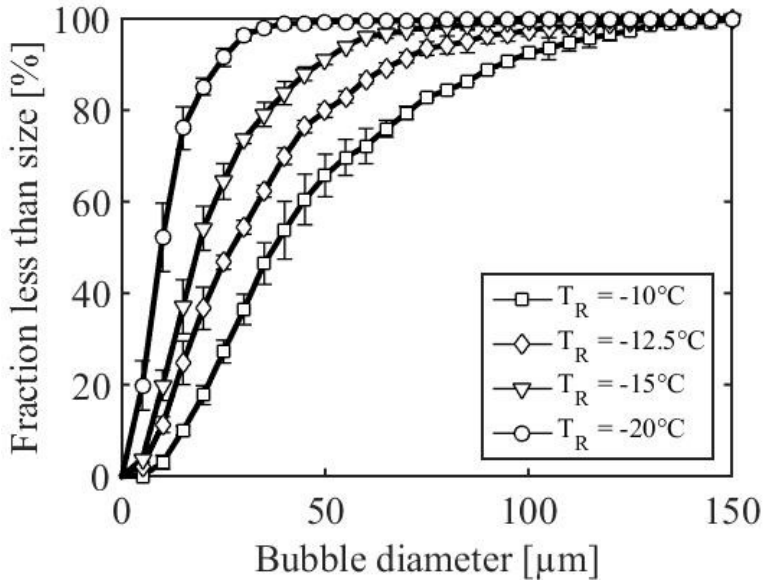

Figure 37. Effect of temperature refrigerant on the BSD in sorbets at $\dot{m}_{air}$ = 0.019 kg h^{-1}, f_{rot} = 500 rpm and P = 3 bar.

4.3.3 Effect of air flowrate on the CSD and BSD

Effect of air flowrate on the CSD in sorbets

The influence of air flowrate variation on the CSD of sorbets produced at a mix flowrate of 25 kg h^{-1}, a dasher rotation speed kept constant at 500 rpm and a cylinder pressure of 3 ± 0.1 bar is presented in Figure 38a and b for a refrigerant fluid evaporating temperature of -10°C and -15°C respectively. At T_R = -10°C, it is clearly shown in Figure 37a that the CSD is shifted towards the smaller sizes when the air flowrate is increased. The mean crystal size is lowered from 72.0 ± 2.0 µm in absence of air to 27.6 ± 1.6 µm at 0.03 kg h^{-1} of air flowrate as can be seen in Table 5. The results obtained in this work corroborate those reported by (Sofjan and Hartel, 2004) who investigated the effect of overrun (the percentage of increase in volume resulting from air addition) on ice crystal size in ice cream and showed that the size of crystals decreased with increasing overrun (meaning increasing the air flowrate).

On the other hand, Figure 38b show that CSDs have the same trends regardless of the air flowrate at T_R = -15°C. It is also shown in Table 5 that the air flowrate does not have a significant effect on the mean crystals size (taking into account the standard deviations) at T_R = -15°C. On the basis of these results, it appears that, at low refrigerating fluid temperature, the effect of temperature prevails over that of air on crystal growth mechanism, as previously stated about the effect of the refrigerant fluid evaporating temperature in presence of air (0.019 kg h^{-1}).

(a)

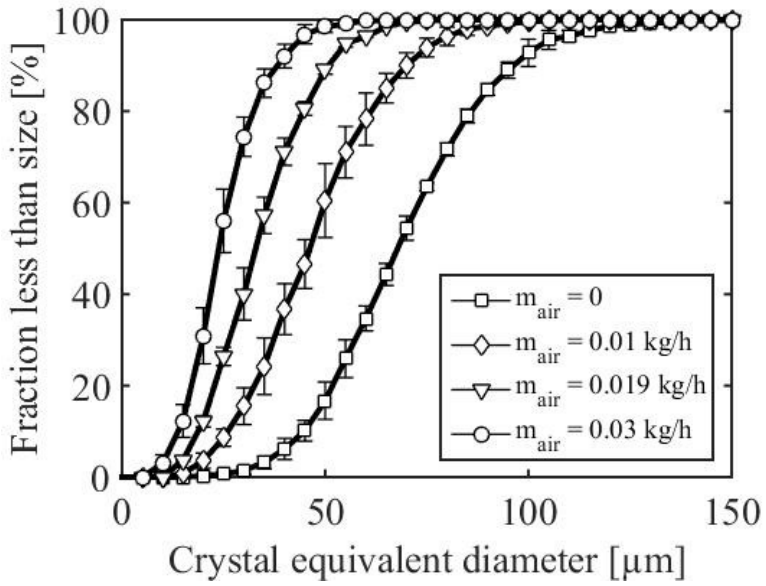

(b)

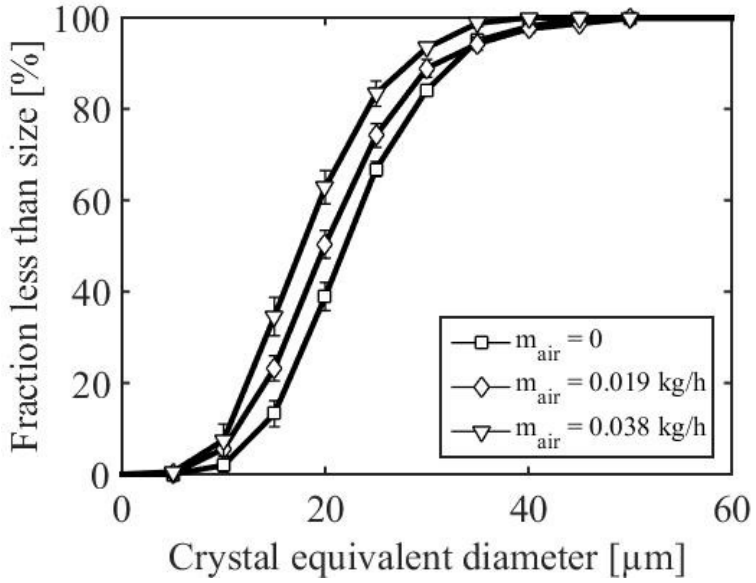

Figure 38. Effect of air flowrate on the CSD in sorbets at f_{rot} = 500 rpm and P = 3 bar using a temperature refrigerant of a) -10.0°C and b) -15.0°C.

Table 5. Effect of air flowrate on mean ice crystals and bubbles sizes.

T_R (°C)	-10.0				-15.0			
$\dot{m}_{air}$ (kg h^{-1})	0	0.01	0.019	0.03	0	0.01	0.019	0.03
Overrun (%)	0	35	67	106	0	35	67	106
T_{outlet} (°C)	-3.8	-3.6	-3.2	-3.1	-6.5	-6.3	-5.8	-4.7
Ice volume fraction*	0.19	0.16	0.09	0.07	0.38	0.37	0.35	0.28
Crystals mean size (µm)	72.0 ± 2.0	29.8 ± 0.3	35.6 ± 1.0	27.6 ± 1.6	25.1 ± 0.1	24.0 ± 0.0	23.4 ± 0.7	22.7 ± 1.0
Bubbles mean size (µm)	-	50.9 ± 0.4	49.7 ± 1.8	39.4 ± 0.3	-	30.4 ± 1.2	27.5 ± 0.3	27.8 ± 0.5

Mix flowrate = 25 kg h^{-1}; Rotational speed = 500 rpm; Pressure = 3 bar
*Calculated from Arellano et al. (2013)

Effect of air flowrate on the BSD in sorbets

Figure 39 show the BSDs obtained at various air flowrates and at two refrigerant fluid evaporating temperatures (-10°C / Figure 39a and -15°C / Figure 39b). Mix flowrate, dasher rotation speed and cylinder pressure were maintained at 25 kg h^{-1}, 500 rpm and 3 ± 0.1 bar respectively. At T_R = -10°C, Figure 39a shows similar behavior for BSDs obtained at the two lowest air flowrates investigated (0.01 and 0.019 kg h^{-1}). For the higher one (0.03 kg h^{-1}), the BSD shows smaller sizes. Mean sizes of 50.9 ± 0.4 and 49.7 ± 1.8 were found at 0.01 and 0.019 kg h^{-}1 of air flowrate respectively. This result means a non-significant effect of air flowrate at low air flowrate. On the other hand, a significantly smaller mean size (39.4 ± 0.3) was obtained at 0.03 kg h^{-1} of air flowrate, as shown in Table 5. At T_R = -15°C, Figure 39b shows that BSDs obtained are very close. Mean sizes presented in Table 5 show that the air flowrate has not a significant effect on bubbles size at this refrigerant fluid evaporating temperature. Sofjan and Hartel (2004) also reported a slight decrease of air bubbles size when increasing the overrun. They attributed the effect to the probable higher shear stresses exerted in the freezer barrel due to higher air content, which promotes the breakage of air bubbles and the production of smaller sizes. On the other hand, a recent study on the residence time distribution of the liquid phase during crystallization-foaming process inside the SSHE has revealed the presence of a nearly stagnant air pocket (Ndoye et al., 2018). This stagnant air volume was found to increase with the air flowrate. This tends to reduce the volume available for the liquid phase, thus increasing shear and finally bubble fragmentation.

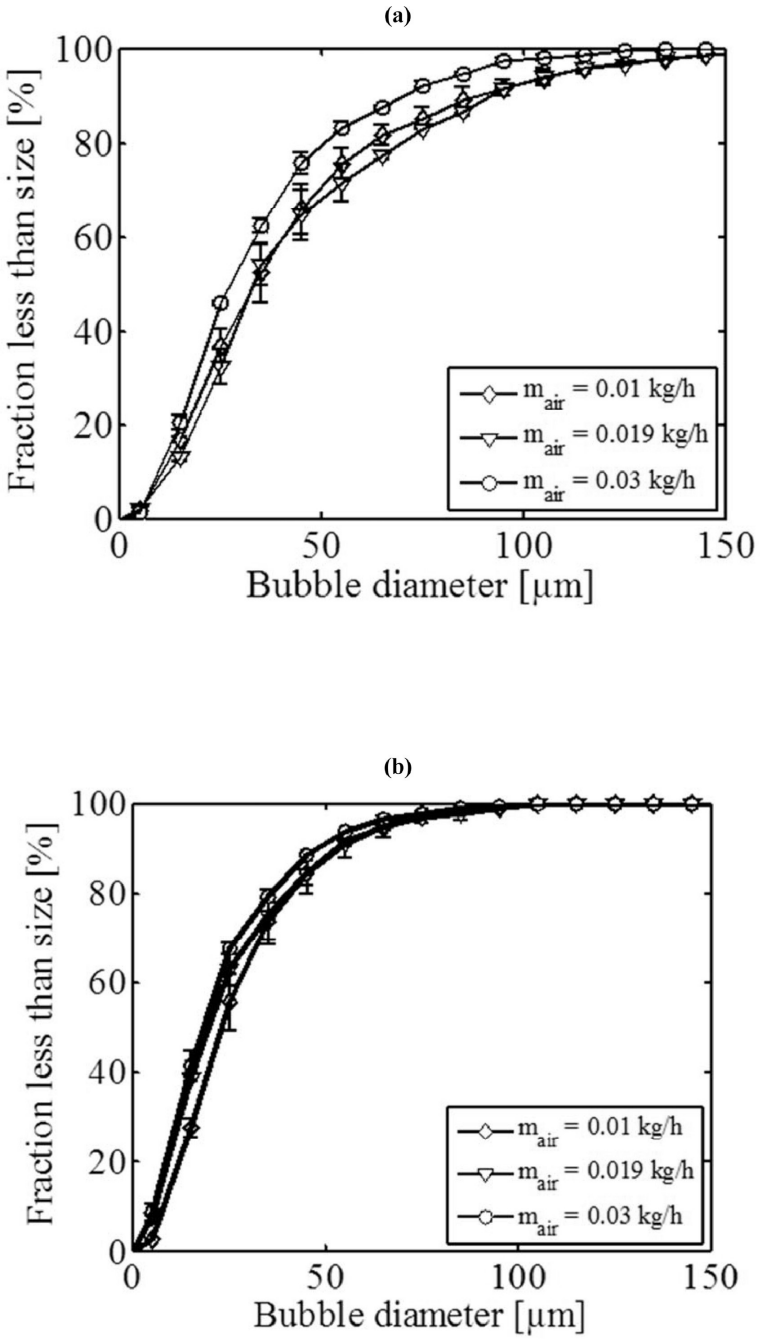

Figure 39. Effect of air flowrate on the BSD in sorbets produced at f_{rot} = 500 rpm and P = 3 bar using at refrigerant temperatures of a) -10.0°C and b) -15.0°C.

4.4 Conclusion

Variations in refrigerant fluid evaporating temperature and air flowrate generated significant effects on ice crystals and bubbles sizes of sorbets produced by crystallization-foaming process in a SSHE. Crystal's sizes were greater when refrigerant fluid evaporating temperatures were higher, both with and without air incorporation. But the influence was less pronounced when air was added due to insulation and hindrance effect of air, retarding crystal growth. Air cells sizes also decreased with refrigerant fluid evaporating temperatures because of the enhancement of the apparent viscosity which promotes bubbles breakup by shear forces and limits their coalescence.

The increase in air flowrate lowered the crystals sizes, especially at the higher refrigerant fluid evaporating temperatures (-10°C). The same trend was found for air bubbles sizes, even the effect was less at the high refrigerant fluid evaporating temperature (-10°C) and insignificant at the low refrigerant fluid evaporating temperature (-15°C).

Further investigations will be performed on the effects of the blades rotation speed and of the cylinder pressure on both CSD and BSD in order to have a complete characterization of the influence of process parameters on sorbet microstructure during crystallization-foaming process in SSHEs.

Nomenclature

d	ice crystal diameter (m)
f_{rot}	dasher rotation frequency (rpm)
$\dot{m}$	mass flowrate (kg h^{-1})
P	pressure (Pa)
T	temperature (°C)
T_R	refrigerant fluid evaporating temperature (°C)
w	ice fraction

Greek letter

μ	dynamic viscosity (Pa s)

Subscripts

air	air

atm	atmosphere
fluid	fluid
i	ice
meas	measured
mix	mix
outlet	outlet

Abbreviations

BSD	bubble size distribution
CSD	crystal size distribution
FBRM	focused beam reflectance method
SSHE	scraped surface heat exchanger

References

Arellano, M., Benkhelifa, H., Flick, D., Alvarez, G., (2012). Online ice crystal size measurements during sorbet freezing by means of the focused beam reflectance measurement (FBRM) technology. Influence of operating conditions. Journal of Food Engineering 113(2), 351-359.

Bolliger, S., Wildmoser, H., Goff, H.D., Tharp, B.W., (2000). Relationships between ice cream mix viscoelasticity and ice crystal growth in ice cream. International Dairy Journal 10(11), 791-797.

Caillet, A., Cogné, C., Andrieu, J., Laurent, P., Rivoire, A., (2003). Characterization of ice cream structure by direct optical microscopy. Influence of freezing parameters. LWT - Food Science and Technology 36(8), 743-749.

Cook, K.L.K., Hartel, R.W., (2010). Mechanisms of Ice Crystallization in Ice Cream Production. Comprehensive Reviews in Food Science and Food Safety 9(2), 213-222.

Cook, K.L.K., Hartel, R.W., (2011). Effect of freezing temperature and warming rate on dendrite break-up when freezing ice cream mix. International Dairy Journal 21(6), 447-453.

Chang, Y., Hartel, R.W., (2002a). Development of air cells in a batch ice cream freezer. Journal of Food Engineering 55(1), 71-78.

Chang, Y., Hartel, R.W., (2002b). Measurement of air cell distributions in dairy foams. International Dairy Journal 12(5), 463-472.

Chang, Y., Hartel, R.W., (2002c). Stability of air cells in ice cream during hardening and storage. Journal of Food Engineering 55(1), 59-70.

Donhowe, D.P., Hartel, R.W., Bradley, R.L., Jr., (1991). Determination of Ice Crystal Size Distributions in Frozen Desserts. Journal of Dairy Science 74(10), 3334-3344.

Drewett, E.M., Hartel, R.W., (2007). Ice crystallization in a scraped surface freezer. Journal of Food Engineering 78(3), 1060-1066.

Druzinec, D., Salzig, D., Kraume, M., Czermak, P., (2015). Micro-bubble aeration in turbulent stirred bioreactors: Coalescence behavior in Pluronic F68 containing cell culture media. Chemical Engineering Science 126, 160-168.

Eisner, M.D., Wildmoser, H., Windhab, E.J., (2005). Air cell microstructuring in a high viscous ice cream matrix. Colloids and Surfaces A: Physicochemical and Engineering Aspects 263(1–3), 390-399.

Faydi, E., Andrieu, J., Laurent, P., (2001). Experimental study and modelling of the ice crystal morphology of model standard ice cream. Part I: Direct characterization method and experimental data. Journal of Food Engineering 48(4), 283-291.

Flores, A.A., Goff, H.D., (1999). Ice Crystal Size Distributions in Dynamically Frozen Model Solutions and Ice Cream as Affected by Stabilizers. Journal of Dairy Science 82(7), 1399-1407.

Goff, H.D., Verespej, E., Smith, A.K., (1999). A study of fat and air structures in ice cream. International Dairy Journal 9(11), 817-829.

González-Ramírez, J.E., (2012). Contribution au contrôle par la modélisation d'un procédé de cristallisation en continu. AgroParisTech.

Haddad Amamou, A., Benkhelifa, H., Alvarez, G., Flick, D., (2010). Study of crystal size evolution by focused-beam reflectance measurement during the freezing of sucrose/water solutions in a scraped-surface heat exchanger. Process Biochemistry 45(11), 1821-1825.

Inoue, K., Ochi, H., Taketsuka, M., Saito, H., Sakurai, K., Ichihashi, N., Iwatsuki, K., Kokubo, S., (2008). Modeling of the Effect of Freezer Conditions on the Principal Constituent Parameters of Ice Cream by Using Response Surface Methodology. Journal of Dairy Science 91(5), 1722-1732.

Liao, Y., Lucas, D., (2009). A literature review of theoretical models for drop and bubble breakup in turbulent dispersions. Chemical Engineering Science 64(15), 3389-3406.

Mary, G., Mezdour, S., Delaplace, G., Lauhon, R., Cuvelier, G., Ducept, F., (2013). Modelling of the continuous foaming operation by dimensional analysis. Chemical Engineering Research and Design 91(12), 2579-2586.

Miller-Livney, T., Hartel, R.W., (1997). Ice Recrystallization in Ice Cream: Interactions Between Sweeteners and Stabilizers. Journal of Dairy Science 80(3), 447-456.

Müller-Fischer, N., Windhab, E.J., (2005). Influence of process parameters on microstructure of food foam whipped in a rotor–stator device within a wide static pressure range. Colloids and Surfaces A: Physicochemical and Engineering Aspects 263(1–3), 353-362.

Ndoye, F.T., Alvarez, G., (2015). Characterization of ice recrystallization in ice cream during storage using the focused beam reflectance measurement. Journal of Food Engineering 148, 24-34.

Ndoye, F.T., Hernandez-Parra, O., Benkhelifa, H., Alvarez, G., Flick, D., (2018). Influence of operating conditions on residence time distributions in a scraped surface heat exchanger during aerated sorbet production. Journal of Food Engineering 222, 126-138.

Regand, A., Goff, H.D., (2003). Structure and ice recrystallization in frozen stabilized ice cream model systems. Food Hydrocolloids 17(1), 95-102.

Russell, A.B., Cheney, P.E., Wantling, S.D., (1999). Influence of freezing conditions on ice crystallisation in ice cream. Journal of Food Engineering 39(2), 179-191.

Sofjan, R.P., Hartel, R.W., (2004). Effects of overrun on structural and physical characteristics of ice cream. International Dairy Journal 14(3), 255-262.

5. Influence of operating conditions on residence time distributions in a scraped surface heat exchanger during aerated sorbet production

Published in Journal of Food Engineering, volume 222, April 2018, Pages 126-138

Abstract

The residence time distribution (RTD) inside a scraped surface heat exchanger (SSHE) during simultaneous crystallization-foaming process for continuous production of an aerated sorbet was studied. The effect of mix flowrate, air flowrate and refrigerant temperature on the unfrozen liquid/ice crystals phase RTD was investigated using a dye tracer method. The experimental results revealed that both mix and air flowrates increase leads to a lessening of the minimum and of the mean residence time inside the SSHE. Flow diagnosis showed the presence of a nearly stagnant air pocket which volume increase with the air flowrate increase, resulting in an augmentation of the liquid phase velocity. More axial dispersion was observed at higher air flowrates and at lower refrigerant temperature due to greater radial temperature and axial velocity gradients. These conclusions were confirmed by the parameters of the fitted flow models (axial dispersion, tank-in-series and gamma distribution models) even if only the gamma distribution model succeeded to well describe the flow patterns observed. The findings of this pioneering work in the field of gas-liquid flow in SSHEs might be useful for several applications involving multiphasic flow in SSHEs.

Keywords

Residence time distribution, SSHE, Crystallization, Foaming, Gas-liquid phase, Sorbet

5.1 Introduction

Scraped surface heat exchanger (SSHE) is a tubular heat exchanger composed of two concentric cylinders acting like a rotor-stator device: a stationary external cylinder in contact with the heating or cooling fluid (the thermal transfer surface) and a rotating internal cylinder (opened or closed dasher) that is equipped with scraping blades. Since they allow efficient heat transfer, SSHEs are extensively used in processing of complex fluid undergoing structural transformations that induce high viscosities or non-Newtonian behavior during heating or cooling. In food industries, SSHE are used for heating and freezing applications. Sorbet production is one of the main freezing applications.

Sorbet is a complex multiphasic system composed of a dispersion of ice crystal and air bubbles inside a concentrated liquid matrix. The manufacturing process of sorbet is carried out in several unit operations ranging from the ingredients homogenization (liquid mix production) to the hardening of the crystallized product, via the crystallization step which occurs in a SSHE. In addition to the mix, air is also incorporated into the sorbet mix flow inside the SSHE, leading to a combined crystallization-foaming operation. The microstructure of the sorbet product is defined inside the SSHE where ice crystals nucleate and grow, and air bubbles are formed. The functional properties and quality attributes of the finished product are essentially related to both ice crystal and bubble size distributions. These latter are strongly dependent on operating conditions, especially on the coupled effect of heat transfer, phase change and flow phenomena. Phase change occurring during crystallization induces an increase of ice crystal volume fraction and of apparent viscosity. It has also been demonstrated that the air incorporation increases the apparent viscosity (Arellano et al., 2012a). An increase in apparent viscosity leads to a modification of the fluid flow pattern and of the velocity profile. Consequently, the time-temperature-shear rate history inside the SSHE is changed and that considerably affects the size distributions of both ice crystals and bubbles (Fayolle et al., 2013; Fayolle et al., 2005; Yataghene et al., 2008). Therefore, knowledge of the fluid flow behaviour within the SSHE is crucial for the optimization of the crystallization-foaming process and the induced finished product functionalities.

The flow behavior in SSHE for a single-phase fluid is described as a superposition of an axial and a rotational flow, with possibly Taylor vortices, above a critical value of the rotating cylinder angular velocity (Trommelen and Beek, 1971; Wang et al., 1999). The axial component corresponds to the classical Poiseuille flow (characterized by the axial Reynolds number – Reax) through the annular space between the dasher and the external wall. The rotational flow results from the combined actions of the rotating dasher and the scraping blades. This component has been assimilated to a Taylor-Couette (TC) flow characterized by the Taylor number. The combination of these two flows yields to helicoidal flows with a variety of observable patterns depending on both axial Reynolds and Taylor (Fayolle et al., 2005; Härröd, 1986b; Yataghene et al., 2011). These flow regimes may be modified in case of two-phase systems, especially for gas/liquid flow. There has been no investigation about the hydrodynamics of gas/liquid or gas/liquid/solid in SSHE. Only few studies dealing with gas/liquid TC flows (without scraping blades) were found in the literature. Shiomi et al. (1993) described the air bubble/water flow in a vertical upward TC flow with internal cylinder rotation, in turbulent regime. They identified different flow patterns according to the mean velocity values of the two phases and the inner cylinder rotation speed: dispersed bubbly, ring-form, spiral and transitional flows. Later, Djéridi et al. (1999) also studied the two-phase air/water upward flow in concentric cylinders with internal cylinder rotation, but for low Taylor numbers corresponding to the first instabilities. The authors showed that air bubbles are captured in flow structures generated in single phase flows (helicoidal

flow) and migrate from the bottom to the top following the organized flow pattern. Recently, Hubacz and Wroński (2004) investigated flow regimes in a horizontal TC using nitrogen/water and nitrogen/glycerin fluids, as a function of rotational speed, both liquid and gas volumetric flowrates and rotor diameters. They described 6 different flow patterns and constructed flow regimes maps according to the different parameters studied. In particular, the authors identified ring flow of the bubbles for high rotational speed and showed that increasing the liquid viscosity improved the stability of the gas rings. Afterwards, this flow regimes map was extended in a more generalized form taking into account more geometries and larger liquid phase physical properties such as density, viscosity and surface tension (Hubacz, 2015). These authors (Hubacz, 2015; Hubacz and Wroński, 2004) showed that gas/liquid flow behavior in horizontal TC systems are different to that observed in vertical ones, except in the case of high rotational speed.

In such complex flow dynamic systems, the residence time distribution (RTD) can be used as a simple and effective method to describe the fluid flow behaviour within the heat exchanger. By definition, RTD represents the fluid age dispersion, describing the different path and length of time a fluid element can spend between the inlet and the outlet of the exchanger. RTD is related to the global motion of the flow, but provides additional information about mixing, dispersion, recycling and flow anomalies such as dead zone and bypass. RTD studies on SSHEs have been already presented by several authors and have been reviewed extensively (Alcairo and Zuritz, 1990; Arellano et al., 2013c; Benezech and Maingonnat, 1993; Fayolle et al., 2013; Rao and Hartel, 2006; Russell et al., 1997). One can highlight the work of Arellano et al. (2013c) which is the only one dealing with sorbet production in SSHE, but without foaming. Authors (Arellano et al., 2013c) found that a reduction in product temperature leads to a broadening of the RTD curve and therefore to an increase of the axial dispersion. This finding was explained by the modification of the radial temperature gradients which greatly increase the viscosity gradient between the wall and the center of the exchanger and, subsequently, the axial velocities. Moreover, mean residence time decreases and RTD curve narrows when product flow rates increases, indicating a lower axial dispersion. Additionally, an increase in the rotational speed has no significant effect on the mean residence time; however it broadens the RTD curve meaning an increase in the axial dispersion. It appears that the effect of process variables such as product flowrate, dasher rotational speed and apparent viscosity is not consistent among the different studies depending on the variety of designs and fluid properties used. Moreover, it should be pointed out that almost all these works deal with either a single-phase flow (Benezech and Maingonnat, 1993) or a two-phase solid/liquid flow (Alcairo and Zuritz, 1990; Arellano et al., 2013c; Russell et al., 1997). The RTD description of the two phase gas/liquid flow or three-phase gas/liquid/solid flow inside SSHE is still scarce. Fayolle et al. (2013) worked on ice cream which is a multiphasic fluid (gas/liquid/solid), but the gas quantity was maintained always constant during the RTD measurement, hence the effect of the gas fraction was not investigated.

Modelling is often necessary for optimization, process and product development, or process control purposes. Hence, in order to complete the RTD study, experimental results have to be fitted to a one or multiple parameter-model for a better understanding and prediction purposes. RTD models representing ideal flow regimes such as plug flow, mixed flow and laminar flow often fail to represent real systems in which flow patterns deviate from the ideal ones. So, non-ideal models, usually derived by combining ideal ones, are developed in order to take into account the deviations. For small deviation from plug flow, the well-known axial dispersion model (ADM) and tank-in-series model can give good representations (Levenspiel, 1999; Villermaux, 1993). Compartment models combining simple models in series or in parallel and taking into account dead zone and bypass or recycle flows can be found in the literature (Fillaudeau et al., 2009; Levenspiel, 1999; Ndoye et al., 2012; Wen and Fan, 1975). More complex models have been developed on the basis of hydrodynamic and mass balance equations (Nauman and Nigam, 2004; Zhang et al., 2005) or using semi-empirical methods (Ham and Platzer, 2004). Stochastic models such as the gamma distribution model (GDM) have also been used to describe non-ideal flows in several systems (Arellano et al., 2013c; Wen and Fan, 1975).

At the current time, the literature regarding experimental measurements and modelling of RTD during crystallization-foaming processes in SSHEs is missing. In response to this lack of knowledge and in continuity with the work of Arellano et al. (2013c), the present paper presents a RTD study to characterize the hydrodynamics in a laboratory scale SSHE during aerated sorbet production. The aerated sorbet is a triphasic system composed of liquid (unfrozen mix), solids (ice crystals) and gas (Alcairo and Zuritz, 1990). The RTD study was focused on the liquid and solid phases which were considered to be a single and homogeneous phase, assuming that unfrozen mix and ice crystals flow at the same velocity. Thus, RTD of the gas phase was not investigated but the effect of its presence in liquid-solid phase flow patterns inside the SSHE was especially studied. Model fitting was used to represent the experimental RTD data by a flow model that could explain satisfactorily the liquid-solid phase dispersion of time inside the SSHE.

5.2 Materials and methods

5.2.1 The crystallization-foaming process equipment

The experimental setup (Figure 40) is a laboratory scale continuous pilot freezer (MF 50 Freezer, Freezer Technology WCB®, Aarhus, Denmark). This system includes a SSHE (Figure 41) whose detailed description can be found in Arellano et al. (2013c). The heat exchange cylinder (stator) had a length of 0.40 m and an exchange surface of 0.0628 m^2. The experimental device works with a nominal capacity of 0.007–0.021 kg s^{-1} of mix, which is fed into the SSHE with an inlet temperature of 5 °C. Mix crystallization takes place into the SSHE thanks to a chlorodifluoromethane (R22) refrigerant which allows to cool the heat exchanger cylinder

with evaporation temperatures ($T_{Refrigerant}$) ranging from −20 to −10 °C. Ice crystals formed on the exchanger surface are continuously removed using two opposite floating scraper blades attached to the dasher which rotates at speeds varying from 21 to 105 rad s^{-1} (200–1000 rpm). Pressurized air (7 bars) is introduced into the system, simultaneously with the mix, through a non-return pressure regulating valve with a regulated pressure from 3 to 5 bars. Air flowrate is controlled using a rotameter (Shorate GT1357 R2-25-A, Brooks Instrument, Hatfield, USA). The pilot freezer is instrumented with calibrated thermocouples (type T; ±0.2 °C of accuracy) to measure the refrigerant evaporation and the sorbet outlet temperatures. All measurements were performed using data-loggers (34970 A, Agilent HP, Santa Clara, USA) and were recorded using an acquisition data program under LabVIEW®. This acquisition program also makes it possible to control the rotation speed of the scraper blades and the mix flowrate.

Residence time distributions were investigated in a total volume of 713 mL including the gap between the dasher and the heat exchange cylinder of the SSHE, the inlet and outlet bowls and the outlet pipe.

5.2.2 The working fluid

A commercial ultra-high temperature pasteurized lemon sorbet mix (Laiterie de Montaigu – Montaigu, France) was used. The exact composition of the mix and physical properties are given by Arellano et al. (2013c). The mix has a solid concentration of 25.8° Brix, an initial freezing temperature at −2.63 °C and a density of 1100 kg m^{-3} at 5 °C. Pressurized and filtered air was used for foaming purpose and was added to the mix flow using a nozzle. At the entrance of the SSHE cylinder, the inlet flow is already a two-phase fluid composed of air bubbles dispersed in a liquid mix.

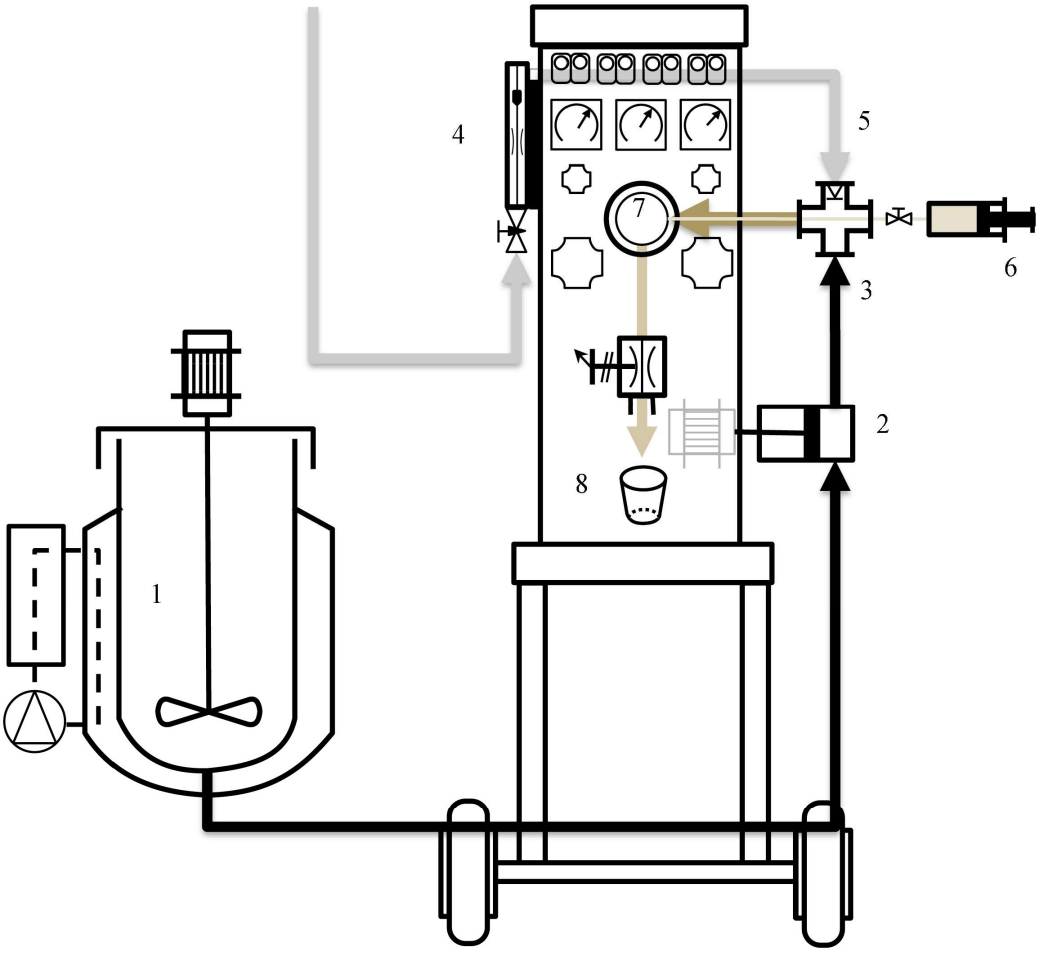

1 – Feeding tank of mix
2 – Feeding pump of mix
3 - Mix inlet
4 – Air flowmeter
5 – Air inlet
6 – MB syringe
7 – SSHE
8 – Cup sampling

Figure 40. Experimental set-up for RTD measurements

(a)

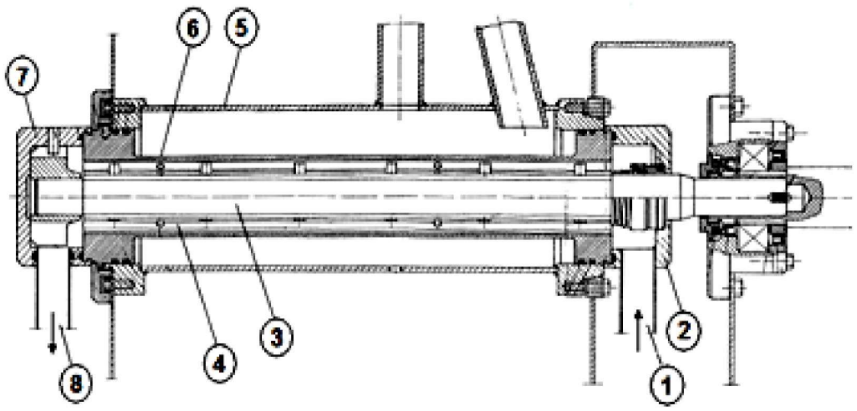

1 - Inlet connection for sorbet mix and air
2 - Inlet cover bowl
3 - Rotor
4 - Scraper blades
5 - Freezer jacket with vaporizing R22
6 - Heat exchange cylinder
7 - Outlet cover bowl
8 - Outlet pipe for sorbet

(b)

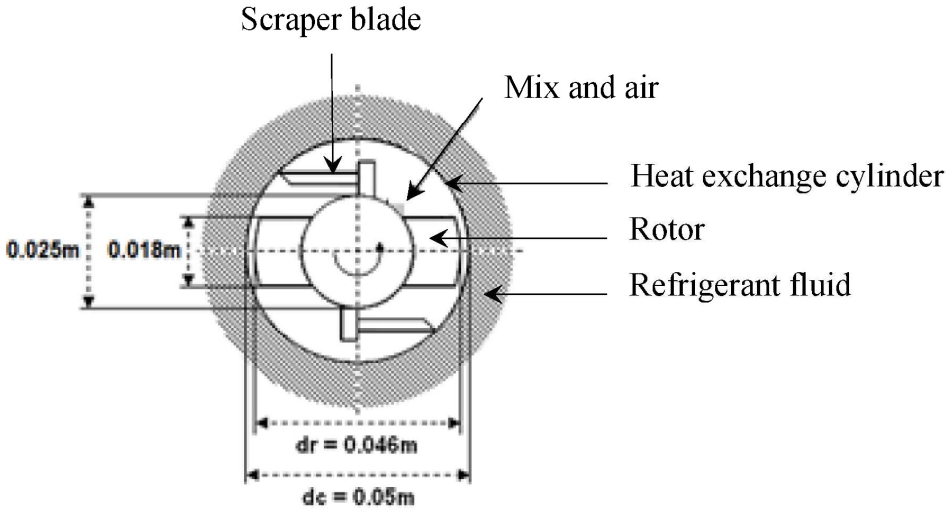

Figure 41. Schematic representation of the pilot Freezer WCB MF 50: (a) side view (b) cross section.

5.2.3 The working conditions

Process parameters such as mix flowrate, air flowrate and refrigerant temperature were varied. All experiments were performed at the same rotational speed (52 rad s^{-1}) and the same pressure inside the heat exchange cylinder (3 bars). The operating conditions and the calculated flow regime are given in Table 6. Axial Reynolds numbers (Re_{ax}), rotational Reynolds numbers (Re_{rot}) and Taylor numbers (Ta) were determined at the entrance and exit conditions of the SSHE. No rheological measurement was made during this work and no rheological data for aerated sorbet under the working conditions of this study is available in the literature. Thus, the flow parameters (Re_{ax}, Re_{rot} and Ta) were determined without taking into account the air incorporation. Nevertheless, the effect of the increase of ice volume fraction was taken into account by the use of rheological model previously established to predict parameters of the power law equation: consistency (K) and behavior (n) indexes (Arellano et al., 2012a). The flow parameters were calculated using the following equations:

$$Re_{ax} = \frac{\rho v^{2-n} D_h^2}{K} \tag{5.1}$$

$$Re_{rot} = \frac{\rho N^{2-n} D_h^2}{K} \tag{5.2}$$

$$Ta = \sqrt{\frac{R_s - R_r}{R_r}} \frac{\rho D_h^n}{2^n} \frac{\left(\Omega R_r\right)^{2-n}}{K} \tag{5.3}$$

For each run, experiments were carried out in duplicate.

Table 6. Investigated experimental conditions.

Run	$Q_{m,L}$ (kg h^{-1})	$Q_{m,G}$ (kg h^{-1})	$T_{refrigerant}$ (°C)	T_{outlet} (°C)	$w_{m,\,ice}$	Inlet at 5 °C			Outlet at T_{outlet}		
						Re_{ax}	Re_{rot}	Ta	Re_{ax}	Re_{rot}	Ta
1	25	0	−15.2	−5.1	0.27	0.43	0.84	30.54	0.0096	0.020	1.39
2	25	0.0014	−15.2	−5.1	0.27	0.43	0.84	30.54	0.0096	0.020	1.39
3	25	0.0125	−15.8	−5.2	0.28	0.43	0.84	30.54	0.0092	0.019	1.34
4	25	0.0375	−14.2	−5.0	0.26	0.43	0.84	30.54	0.0100	0.021	1.45
5	50	0.0014	−15.0	−4.7	0.25	1.16	0.84	30.54	0.035	0.024	1.64
6	50	0.0125	−15.4	−4.7	0.25	1.16	0.84	30.54	0.035	0.024	1.64
7	50	0.0375	−15.7	−3.8	0.16	1.16	0.84	30.54	0.061	0.042	2.67
8	25	0.0125	−9.9	−3.6	0.14	0.43	0.84	30.54	0.024	0.050	3.07
9	25	0.0125	−11.7	−4.5	0.23	0.43	0.84	30.54	0.013	0.027	1.80

Data are mean values of two replicates. Standard deviations are given in the text.

5.2.4 The RTD measurement

A colorimetric method was used to conduct RTD experiments. Methylene blue (Rhône Poulenc, 3.10957, Villers St Paul, France) was selected as dye tracer based on preliminary solubility and thermal stability tests (Arellano et al., 2013c). A cross-shaped junction located at the entrance of the SSHE and used for mix and air inlet was fitted with a syringe for tracer injection as described in Figure 40. The syringe is connected to a stainless-steel tube (internal volume of 4 mL) inserted into the cross-shaped junction and which goes directly at the entrance of the exchanger cylinder.

Once the steady state was reached, an injection of 13 mL of a MB dyed sorbet mix at 0.008% w/w was achieved in roughly 1 s. This injection time is very small compared to the minimum geometrical residence time τ = 46.4 s (about 2%) corresponding to the highest volume flowrate used, so that pulse injection can be assumed. It was also assumed that dispersions between the injection point and the exchanger entrance was negligible. Simultaneously to the injection, continuous cup sampling was made at the outlet of the SSHE using 40 pre-weighted transparent cups. They were immediately weighted in order to know the sampling times (total sampling time around 200 s). Samples were then stored at 5 °C in order to be thawed and to remove air. Subsequently, MB absorbance was measured in each cup by triplicate using a spectrophotometer (Beckman Coulter DU 730, Fullerton, USA) set at a wavelength of 672 nm (the maximum absorbance of MB). The first cup sample collected simultaneously with the injection of tracer was used as blank for spectrophotometric analysis. Outlet tracer concentrations were finally determined using a tracer calibration curve established preliminarily.

Inlet signal was not detected because of the difficulty to perform this measurement when sampling and off-line measurements are used.

5.2.5 Data treatment

The exit age distribution function curve or density function $E(t)$ (also called E-curve) is used to quantitatively analyse the RTD. The E-curve is obtained from the tracer outlet concentration $C(t)$ according to Eq. (5.4) (Levenspiel, 1999).

$$E(t) = \frac{C(t)}{\int_0^\infty C(t)\,dt} \tag{5.4}$$

The liquid phase mean residence time or average age is defined as the first moment of the distribution and is expressed in Eq. (5.5)

$$\overline{t}_L = \int_0^\infty tE(t)\,dt \tag{5.5}$$

In the following sections, the term "liquid phase" will be used to designate the fluid phase comprising both the ice crystals and the unfrozen liquid (unfrozen liquid and ice crystals are assumed to flow at the same velocity and to constitute a homogeneous phase).

The relative standard deviation of the RTD is defined by the coefficient of variation *CoV* as shown in Eq. (5.6)

$$CoV = \frac{\sigma}{\overline{t}_L} \tag{5.6}$$

where is the standard deviation calculated according the moment's method and $\tau_L = V_{tot}/Q_{v,L}$ is the "liquid geometrical residence time". The *CoV* measures the axial dispersion inside the vessel: the smaller the *CoV*, the narrower is the RTD and the closer is the distribution to the mean residence time.

The "sorbet geometrical residence time" τ is defined by Eq. (5.7) where the volumetric flow rate of the gas phase ($Q_{v,G}$) was calculated taking into account the pressure inside the cylinder.

$$\tau = \frac{V_{tot}}{Q_{v,L} + Q_{v,G}} \tag{5.7}$$

It would be equal to mean residence time in the ideal case in which gas and liquid have everywhere the same velocity in the SSHE and without dead zone.

The *E*-curve can be defined in a dimensionless form (5.8) using the dimensionless time $\theta = t/\overline{t}_L$

$$E^*(\theta) = \overline{t}_L E\left(t = \overline{t}_L \theta\right) \tag{5.8}$$

With the cup sampling method, only the mean concentration during the sampling time of a cup can be known, subsequently the *E*-curve is approximated as a step function. Therefore, the integrals calculated according to Eqs. (5.4) and (5.5) were estimated using the rectangle method. The sampling time Δt_i of cup *i* was deduced from the mass of the cup m_i and the mass flowrate of mix $Q_{m,L}$: $\Delta t_i = m_i/Q_{m,L}$.

5.3 Results and discussion

The geometrical residence time for liquid (τ_L) and for sorbet (τ), the experimental minimum residence time (t_{min}), the experimental mean residence time ($\bar{t}_L$) and the standard deviation (σ) obtained for the different investigated operating conditions are shown in Table 7 and Table 8. The reproducibility of experiments has been tested by realizing two replicates for each condition. The standard deviation of the dimensionless mean residence times ($\bar{t}_L/\tau_L$ and $\bar{t}_L/\tau$) varied from 0.01 to 0.09. The mass balance between the injected and the collected tracer ranged from 0.94 to 1.04 for all experiments performed. Experimental results displayed in Table 7 and Table 8 represent the average values of the two replicates carried out for each operating condition. Contrariwise, all graphs (Figure 42, Figure 45 and Figure 46) presented in the following sections represent only one of the two replicates of each experimental condition.

Table 7. Effect of mix and air flowrates on measured RTD - Experimental characteristic times and dispersion parameters

Mix flowrate	$Q_{m,L}$ **(kg h^{-1})**	**25**				**50**		
	$Q_{v,L}$ **(10^{-6} m^3 s^{-1})**	**6.31**				**12.63**		
Air flowrate	$Q_{m,G}$ **(kg h^{-1})**	**0**	**0.0014**	**0.0125**	**0.0375**	**0.0014**	**0.0125**	**0.0375**
	$Q_{v,G}$ **(10^{-6} m^3 s^{-1})**	**0**	**0.103**	**0.916**	**2.746**	**0.103**	**0.916**	**2.746**
Liquid geometrical residence time τ_L (s)		113.0				56.5		
Sorbet geometrical residence time τ(s)		113.0	111.2	98.6	78.6	56.1	52.7	46.4
Minimum residence time t_{min} (s)		51.0	41.4	31.3	15.3	21.4	11.5	5.0
t_{min}/τ_L		0.45	0.37	0.28	0.14	0.38	0.20	0.09
Liquid mean residence time $\bar{t}_L$(s)		105.5	89.1	71.3	47.6	51.2	36.8	26.5
$\bar{t}_L/\tau_L$		0.93	0.79	0.63	0.42	0.91	0.65	0.47
$\bar{t}_L/\tau$		0.93	0.80	0.72	0.61	0.91	0.70	0.57
Standard deviation σ (s)		28.5	26.6	26.7	21.0	17.3	16.2	14.3
$CoV = \sigma/\bar{t}_L$		0.27	0.29	0.37	0.44	0.34	0.44	0.54

Refrigerant temperature ≈ −15 °C; Rotational speed = 52 rad s^{-1}; Pressure = 3 bars.

Table 8. Effect of refrigerant temperature on measured RTD - Experimental characteristic times, dispersion and volume parameters

Refrigerant Temperature (°C)	−9.9	−11.7	−15.8
Liquid geometrical residence time τ_L (s)	113.0		
Sorbet geometrical residence time τ (s)	98.6		
Minimum residence time t_{min} (s)	49.7	33.2	31.3
t_{min}/τ_L	0.44	0.29	0.28
Liquid mean residence time $\bar{t}_L$(s)	80.3	75.1	71.3
$\bar{t}_L/\tau_L$	0.71	0.66	0.63
$\bar{t}_L/\tau$	0.81	0.76	0.72
Standard deviation σ (s)	20.2	25.0	26.7
$CoV = \sigma/\bar{t}_L$	0.25	0.33	0.37
$\frac{Q_{v,G}}{Q_{v,G}+Q_{v,L}}$	0.127		
$\frac{V_G}{V_G+V_L}$	0.239	0.288	0.324

Mix flowrate = 25 kg h^{-1}: Air flowrate = 0.0125 kg h^{-1}; Rotational speed = 52 rad s^{-1}; Pressure = 3 bars.

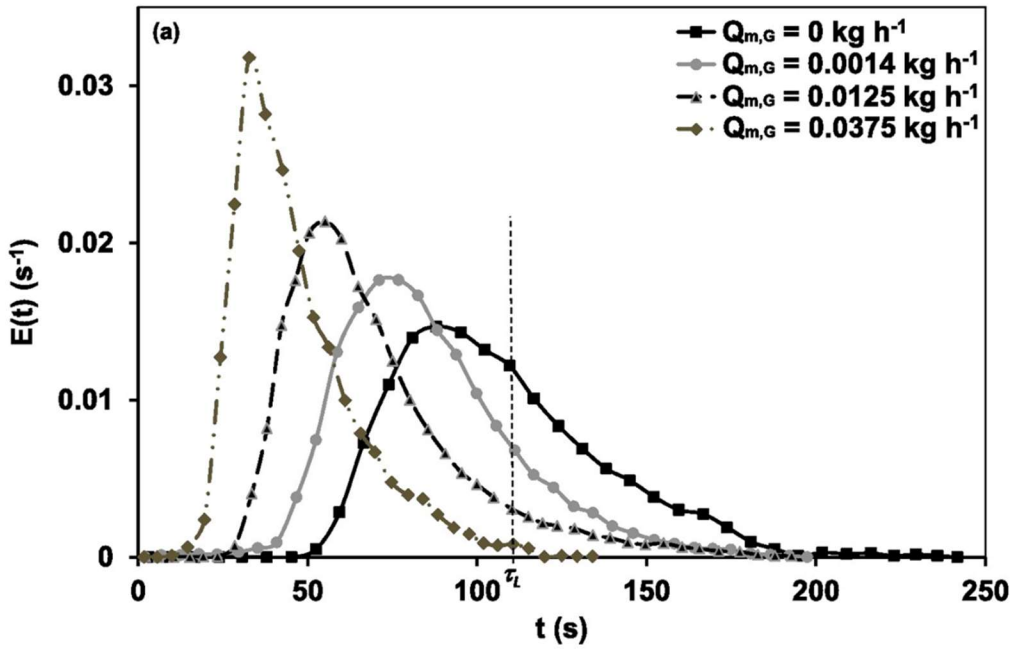
(a)
$Q_{m,G}$ = 0 kg h^{-1}
$Q_{m,G}$ = 0.0014 kg h^{-1}
$Q_{m,G}$ = 0.0125 kg h^{-1}
$Q_{m,G}$ = 0.0375 kg h^{-1}
E(t) (s^{-1})
0.03
0.02
0.01
0
0
50
100
150
200
250
τ_L
t (s)

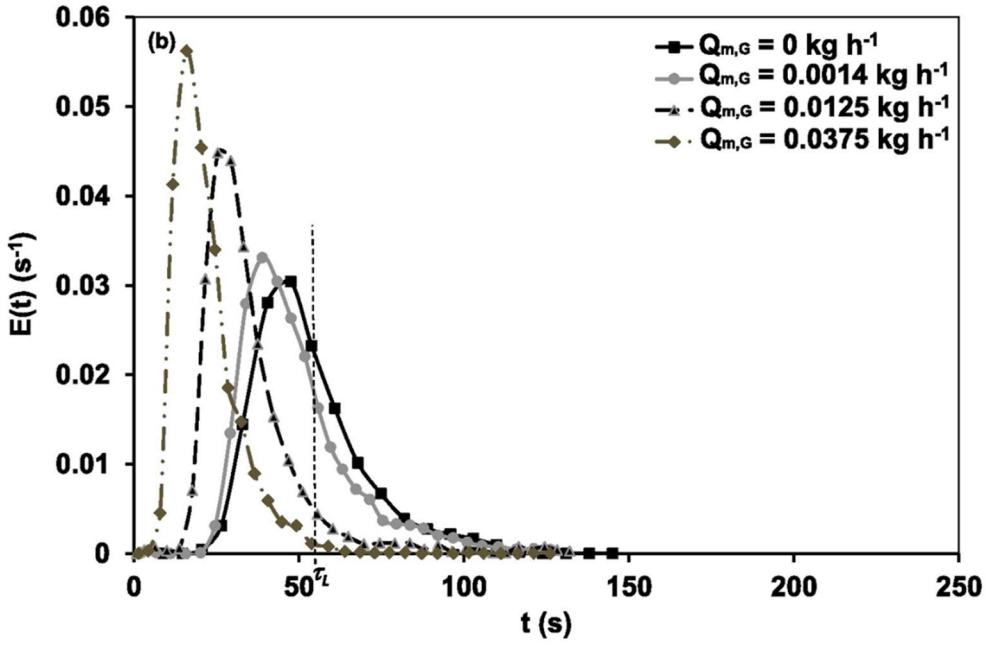
(b)
$Q_{m,G}$ = 0 kg h^{-1}
$Q_{m,G}$ = 0.0014 kg h^{-1}
$Q_{m,G}$ = 0.0125 kg h^{-1}
$Q_{m,G}$ = 0.0375 kg h^{-1}
E(t) (s^{-1})
0.06
0.05
0.04
0.03
0.02
0.01
0
0
50
100
150
200
250
τ_L
t (s)

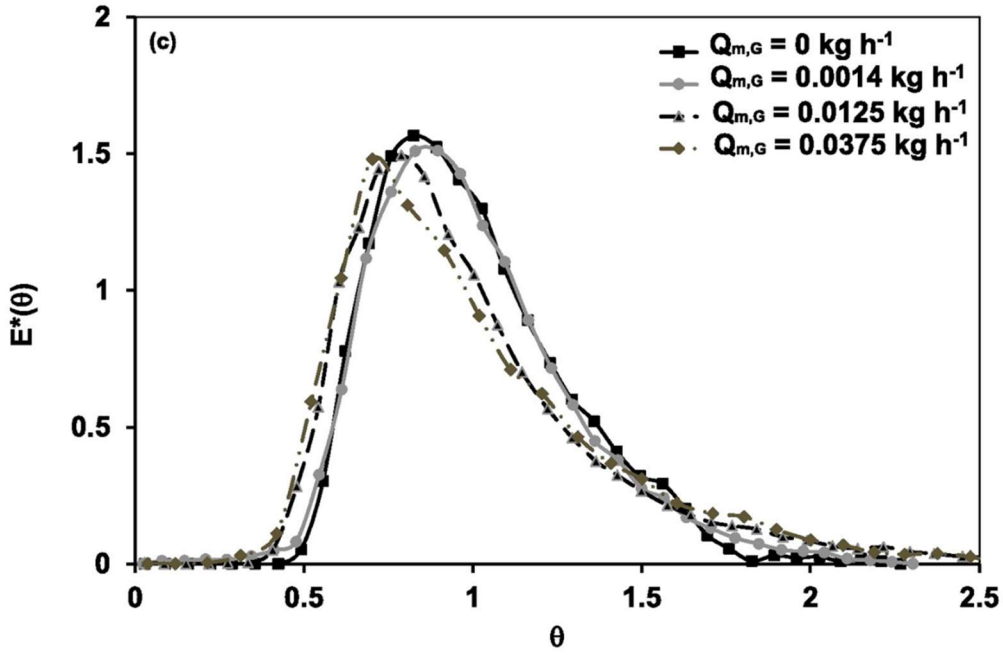

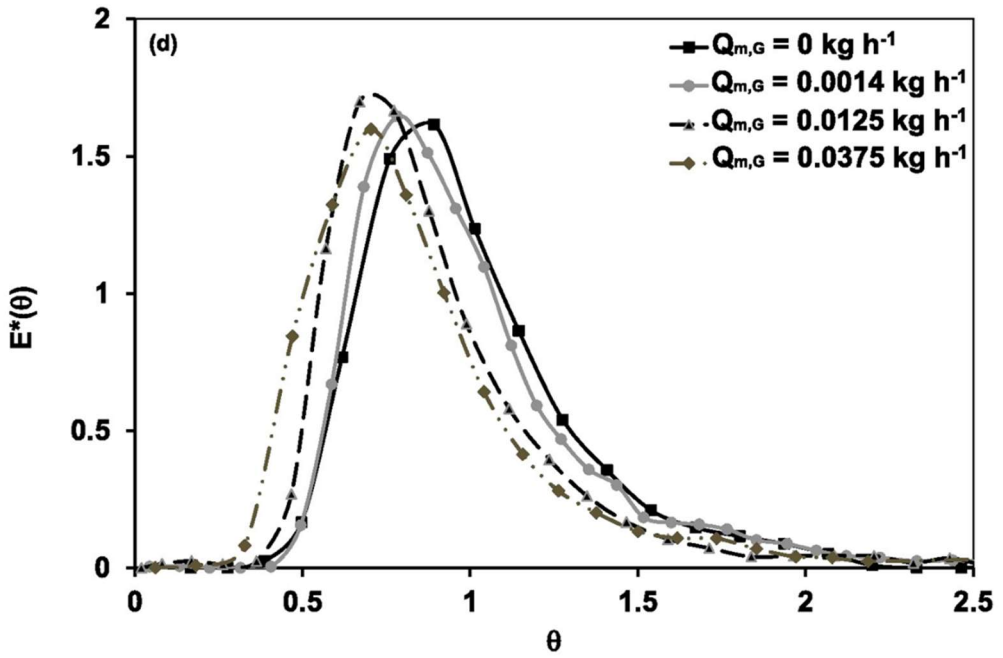

Figure 42. Effect of mix and air flowrate on the liquid phase RTD inside the SSHE – $T_{refrigerant} \approx -15$ °C: (a) 25 kg h^{-1} of mix; (b) 50 kg h^{-1} of mix; (c) Dimensionless *E*-curve for 25 kg h^{-1} of mix; (d) Dimensionless *E*-curve for 50 kg h^{-1}

5.3.1 Effect of mix and air flowrates on the liquid phase RTD

The trends of RTD curves as a function of air flowrate are shown in Figure 42a and b for 25 and 50 kg h^{-1} of mix flow rate respectively, a dasher rotation speed of 52 rad s^{-1} and a cylinder pressure of 3 bars. Corresponding characteristics times and dispersion parameters are displayed in Table 7. Figure 42a and b clearly show that RTD curves are significantly affected by the variations in mix and air flowrates. On comparing Figure 42a and b at a given air flowrate, it can be noticed that RTD curves are shifted towards the left-hand side when mix flowrates is increased meaning a reduction of the minimum and of the mean residence time, as can be seen in Table 7. On analyzing the effect of air flowrates, both Figure 42a and b also show a progressive left-hand side shifting of RTD curves when air flowrate is increased, for both mix flowrates. This result, as shown in Table 7, also means a decrease of the minimum and of the mean residence time of the liquid phase with the increase of the gas phase flowrate.

In condition without air incorporation, it can be seen in Table 7 that the liquid mean residence time ($\overline{t_L}$) is lower than the liquid geometrical residence time (τ_L) (a difference of 7% at 25 kg h^{-1}), meaning the presence of a dead volume or stagnant fluid inside the SSHE (V_d = 47.4 mL). Thereby, the total volume of the SSHE (V_{tot}) can be divided into a volume which is effectively swept by the liquid phase (V_L) and a dead volume (V_d) where the liquid is nearly stagnant. The experimental liquid mean residence time is related to the volume flow rate and the volume swept by the liquid as shown in Eq. (5.9):

$$\overline{t_L} = \frac{V_L}{Q_{v,L}} = \frac{V_{tot} - V_d}{Q_{v,L}} \tag{5.9}$$

As a first approach the volume of the liquid dead zone is assumed to remain the same when air is incorporated.

When air is injected, part of the SSHE's volume is also occupied by the gas phase (V_G) as schematized in Figure 43 and thus the total volume of the system is expressed as follows with Eq. (5.10).

$$V_{tot} = V_d + V_L + V_G \tag{5.10}$$

In this case, the RTD measurement still concerns the liquid phase but it can indirectly give information about the volume occupied by the gas as $\overline{t_L} = V_L / Q_{v,L}$ and $\overline{t_G} = V_G / Q_{v,G}$.

The volume occupied by the gas phase can be deduced from the experimental value of using Eq. (5.11)to calculate V_L at first, then using Eq. (5.10):

$$V_L = \left(V_{tot} - V_d\right)\left(1 - \frac{\bar{t}_L}{\tau_L}\right) \tag{5.11}$$

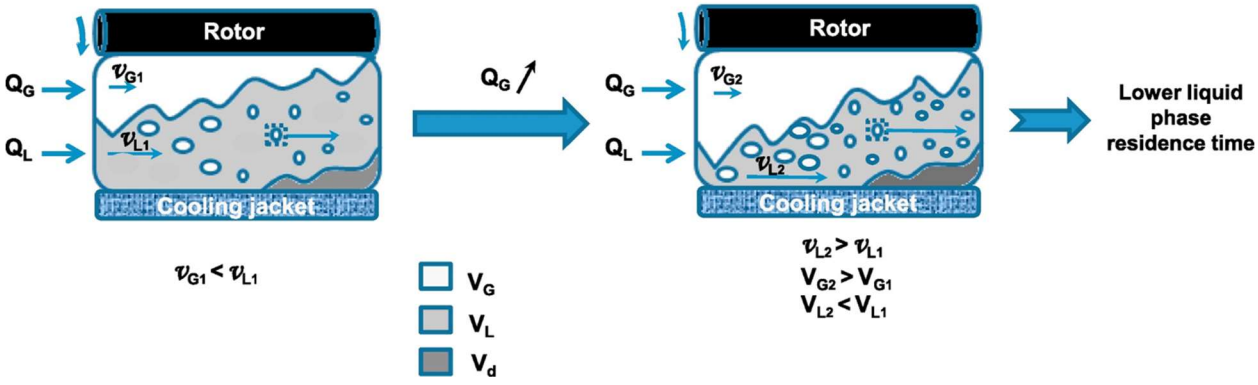

Figure 43. Schematic representation of the gas/liquid flow through the SSHE's annular space at different gas flowrates

If the gas velocity (v_G) is equal to the liquid velocity (v_L) in the whole SSHE's volume, the liquid mean residence time should be equal to the gas mean residence time ($\bar{t}_L = \bar{t}_G = (V_L+V_G)/(Q_{v,L}+Q_{v,G})$) and the gas holdup (fraction of the SSHE's volume occupied by the gas phase, excepted the dead volume) should be equal to the gas-to-liquid volumetric flowrate ratio ($V_G/(V_L+V_G) = Q_{v,G}/(Q_{v,L}+Q_{v,G})$). In order to test this hypothesis, the gas holdup is compared to the gas-to-liquid volumetric flowrate ratio in Figure 44. If gas and liquid phases were flowing at the same velocity, the experimental data shown in Figure 44 would be confounded with the parity line. Contrariwise, it can be seen that the gas holdup is systematically higher than the theoretical values (parity line) which assume that $v_G = v_L$ in the whole volume of the SSHE.

The previous reasoning and the results thereof leads to the conclusion that there are probably zones in the SSHE where the gas phase flows at a lower velocity than the liquid phase. Part of the volume occupied by the gas phase could be a nearly stagnant gas pocket where gas is trapped by means of centrifugal forces (liquid is submitted to a much higher centrifugal force by volume unit than gas), probably close to the rotor, as previously reported in TC systems (Hubacz, 2015; Hubacz and Wroński, 2004). This hypothesis is

confirmed by the fact than even for very low gas flowrate, the volume occupied by the gas phase (V_G) reaches about 20% of the SSHE's total volume as can be seen in Figure 44. The volume of the gas pocket increases with the gas phase flowrate increase. Beside this gas pocket, air bubbles are progressively incorporated into the liquid phase in the form of bubbles which become smaller throughout the SSHE (smaller than 100 µm) (Hernandez et al., 2015). These bubbles flow at the same velocity than the surrounding liquid phase and come to be more numerous when the air flowrate increases as schematized in Figure 43. All these phenomena result in an increase of the partial occupancy of the SSHE's available volume by gas phase. Consequently, the liquid phase flows in a smaller and smaller volume and gets out of the exchanger more quickly (Figure 43), resulting in lower minimum and mean residence times. A shorter mean residence time means less heat exchange between the flowing fluid and the cylinder wall. That leads to a reduction of the nucleation rate and of ice crystal growth. Moreover, the lessening in mean residence time implies that all the incorporated air has less time available to be entirely distributed into the liquid phase. That results to a final product exiting the SSHE with small ice crystals but at a few numbers, as few air bubbles, denoting a low quality final product, especially in terms of texture.

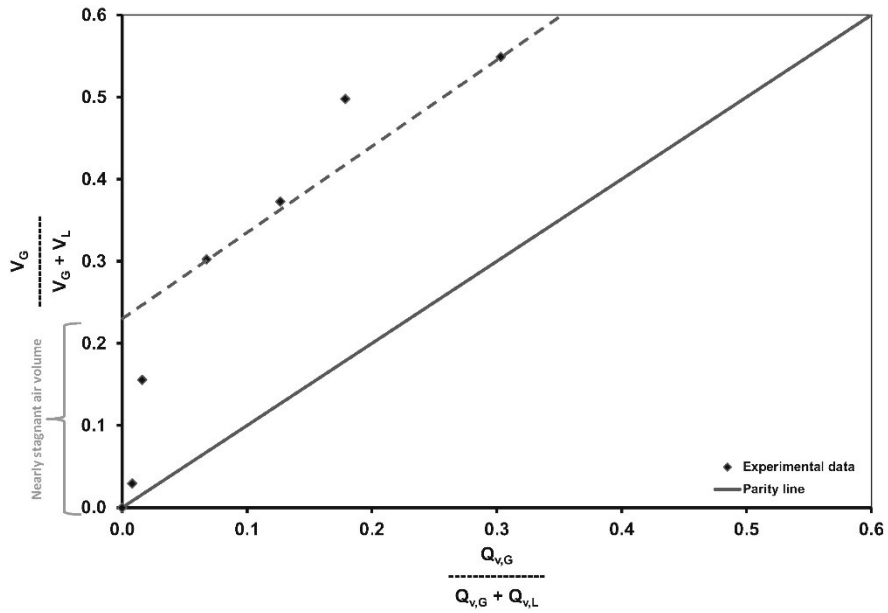

Figure 44. Comparison between gas holdup and gas-to-liquid volumetric flowrate ratio: evidence of a stagnant volume.

The dimensionless RTD curves as a function of air flowrate are represented in Figure 42c and d for 25 and 50 kg h^{-1} of mix flow rate respectively, a dasher rotation speed of 52 rad s^{-1} and a cylinder pressure of 3 bars. In conditions without air incorporation (0 kg h^{-1}) and low air flowrates (0.0014 kg h^{-1}), the

dimensionless *E*-curves are very close and seem to exhibit similar flow behavior, for both mix flowrates. This result means that there is no significant difference in the relative axial dispersion at low air flowrate, as shown by the values of the coefficient of variation which do not vary significantly. However, at higher air flowrates (0.0125 and 0.0375 kg h^{-1}), there is a more important tailing effect which can be associated to an enhancement of the relative axial dispersion inside the exchanger, as comforted by the CoV values (Table 7). This outcome, in our knowledge, has never been reported in the literature before, due to the lack of work on RTD for two phase gas-liquid flow in SSHE. Nevertheless, it can be compared to those of authors who have investigated RTD in two phase gas-liquid flow in pipes (Oriol et al., 2008; Saxena et al., 1996; Sharma et al., 2017). Saxena et al. (1996) studied liquid phase RTD of air-water flow through helical coiled tubes and reported more axial dispersion when gas flowrate is increased, at low Reynolds numbers, for a given liquid flowrate. Recently, Sharma et al. (2017) studied the liquid phase RTD of a two-phase (gas-liquid) flowing through a horizontal helical coil. As Saxena et al. (1996), they reported that at low liquid and gas velocities (low Reynolds numbers), there is an increase in axial dispersion with increasing gas velocity at a fixed liquid velocity. Authors (Sharma et al., 2017) attributed this effect to the enhancement of the velocity of liquid in the vicinity of gas while the rest of the liquid phase moves slower, causing flow to scatter and in turn axial dispersion to increase. Moreover, because of the lower temperature close to the cooling wall and thus the higher ice volume fraction at this location, the fraction of liquid flowing near the cooling wall has a higher apparent viscosity, with respect to the fluid near the rotor. Consequently, this difference in apparent viscosity contributes to modify the axial velocity profile, with a layer near the cooling wall flowing at low speed and another one at the centre moving at a higher velocity. This effect of apparent viscosity is intensified when air flowrate increases, knowing that increasing air fraction implies an augmentation of the apparent viscosity (Arellano et al., 2012a). An increase in axial dispersion could result in a final product with an ice crystal size distribution largely dispersed composed of small crystals coming from the centre of the SSHE (short residence time) and large crystals which grow close to the cylinder wall.

5.3.2 Effect of refrigerant fluid temperature on the liquid phase RTD

Figure 45 compares *E*-curves according to the refrigerant temperature at a mix flowrate of 25 kg h^{-1}, a gas flowrate of 0.0125 kg h^{-1}, a dasher rotation speed of 52 $rads^{-1}$ and a cylinder pressure of 3 bars. Table 8 presents the resultant parameters of time, dispersion and volume. It is shown in Table 8 a decrease of the mean residence time with the decrease of the cooling temperature. It can also be seen in Table 8 that, again, the gas phase holdup ($V_G/(V_L+V_G)$) is higher than the gas-to-liquid volumetric flowrates ratio ($Q_{v,G}/(Q_{v,L}+Q_{v,G})$), indicating the presence of a nearly stagnant air pocket inside the exchanger. In addition, this stagnant volume increases when the refrigerant temperature decreases as shown in Table 8. This may be a

consequence of the enhancement of the apparent viscosity. Indeed, it can be seen in Table 6 that a decrease in refrigerant fluid temperature reduces the sorbet outlet temperature and increases the ice mass fraction which leads to an enhancement of the apparent viscosity. This latter could result in less air incorporation in the liquid phase. Thereby, the stagnant gas volume would increase and the section available for liquid phase would reduce, resulting in shorter residence times. As mentioned above, a reduction in the mean residence time induces a product exiting the SSHE earlier with a microstructure incompletely defined, resulting in a final product with a low quality (few ice crystals and air bubbles).

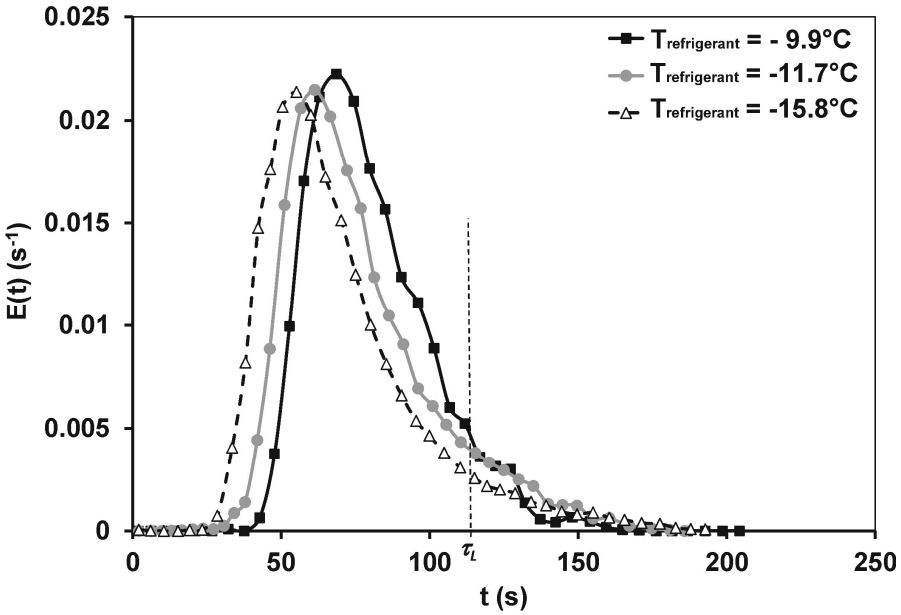

Figure 45. Influence of the refrigerant fluid temperature on the liquid phase RTD of the aerated sorbet inside the SSHE: mix flowrate = 25 kg h^{-1}; air flowrate = 0.0125 kg h^{-1}.

The graph in Figure 45 shows significant shifting to the left-hand side of liquid phase RTD curves when the refrigerant temperature is decreased. This shift corresponds to a lower minimum residence time with the refrigerant temperature decrease, as can be seen in Table 8. It is also shown in Table 8 that the *CoV* increased when the working temperature was lowered, indicating more relative axial dispersion. Such behaviors could be explained by the enhancement of the radial temperature gradient inside the exchanger. The ice crystallization is more important near the cooled outer cylinder wall, implying that both ice volume fraction and apparent viscosity locally increase more rapidly than near the rotor. The local viscosity enhancement leads to a decrease of the velocity close to the stator wall and to an increase near the dasher

at the centre of the SSHE. As a result, the velocity distribution is gradually modified as the aerated sorbet flows through the exchanger. Thereby, more ice crystallization reduces the minimum residence time and slows down the flow close to the cooling wall as indicated by the tailing effect on the RTD curves of Figure 45. Similar observations were made by Arellano et al. (2013c) using the same system with sorbet flowing as a single phase (without air incorporation). Radial gradients temperature may also be due to recirculation occurring in the vicinity of the blades ending as evidenced by several numerical studies of fluid flow in SSHEs (Baccar and Abid, 1997; Duffy et al., 2007).

5.4 RTD models fitting

5.4.1 Description of RTD models

RTD model must be selected based on the flow characteristics within the vessel. Table 6 showed axial Reynolds numbers (Re_{ax}), rotational Reynolds numbers (Re_{rot}) and Taylor numbers (Ta) calculated at the inlet and at the outlet of the SSHE. According to flow regimes criteria given by Härröd (1986b) for Re_{ax} and Re_{rot} (laminar regime: Re_{ax} <15,000 and Re_{rot} <250), calculated data indicate a laminar flow regime through the SSHE for all experiments performed. Ta number values are also below the critical Taylor number Ta_{cr} ($Ta_{cr} \approx 80$, with two blades), which indicates the transition between the laminar and the vortex flows in SSHEs as given by Dumont et al. (2000b). Thus, all experiments were carried out without apparition of Taylor vortices in the SSHE. As mentioned above, these values were calculated without taking into account the air due to the unavailability of rheological data at the working conditions of this study. Nevertheless, Arellano et al. (2012a) reported that an increase in air volume fraction resulted in the decrease of the flow behavior index n, which indicates that the aerated sorbet becomes more shear-thinning as more air is incorporated into the product. They also found that the higher the air fraction, the higher the consistency index K and therefore the higher the apparent viscosity of the product is. Based on this result, one can assume that Re_{ax}, Re_{rot} and Ta numbers calculated in aeration conditions would be lower than values showed in Table 6. Thereby, laminar regime and absence of Taylor vortices can be assumed within the investigated conditions in the present work (with air incorporation).

The laminar flow regime combined with the absence of Taylor vortices can allow to use RTD mathematical models which describe small deviations from ideal flow: the very common ADM and the TSM.

1. The ADM is the most widely applied model to describe RTD inside pipes during thermal processing (Torres and Oliveira, 1998). The model is characterized by the Peclet number Pe which represents the extent of the axial dispersion (Ekambara and Joshi, 2004). Eq. (5.12) which represents

the analytical solution of the axial dispersion differential equations with opened system boundary conditions is often used to approximate the ADM (Villermaux, 1993).

$$E_{ADM} = \sqrt{\frac{Pe}{4\pi\theta}} \exp\left(-\frac{Pe\left(1-\theta\right)^2}{4\theta} \right) \tag{5.12}$$

The ADM is able to represent large axial mixing but shows poor performance to describe RTD curve with long tail (Yuan et al., 2004).

2. With the TSM, the actual fluid flow within the device is schematically replaced by a series of consecutive, equal-sized and perfectly mixed tanks, which results in the same longitudinal mixing effect (Levenspiel, 1999). The larger the number of tanks N_T, the more the fluid behavior in the system approaches plug flow. The TSM is expressed as follows with Eq. (5.13).

$$E_{TSM} = \frac{N_T \left(N_T\theta\right)^{N_T-1}}{\left(N_T-1\right)!} \exp\left(-N_T\theta\right) \tag{5.13}$$

In a previous work, using the same experimental system but without incorporating air, Arellano et al. (2013c) fitted RTD measurements to both ADM and TSM, but found poor agreement between experimental and model behaviors. Contrariwise, they obtained a very accurate representation of experimental RTD using the GDM defined by Eq. (5.14):

$$E_{GDM} = \frac{p^p}{\left(1-\theta_0\right)^p \Gamma\left(p\right)} \left(\theta-\theta_0\right)^{p-1} \exp\left[-p\left(\frac{\theta-\theta_0}{1-\theta_0} \right) \right] \tag{5.14}$$

where p and θ_0 are the two parameters of the model and Γ is the gamma function expressed as

.

Even if the GDM has not any physical sense; the two parameters of the model offer more flexible fits compared to the single-parameter models. The GDM is able to represent different distributions from exponential decays up to normal distributions. The model has been successfully used to describe the RTD of several systems (Ji et al., 2010; Lee and Singh, 1993; Wen and Fan, 1975). The parameter p is related to the extension of fluid mixing in the axial flow direction. θ_0 is defined analogously to a breakthrough time, which is the ratio of the minimum residence time to the geometrical residence time. An increase of the *p*-

value denotes a reduction of the axial dispersion towards plug flow behavior. In a like manner, an increase of θ_0 indicates a flow pattern approaching the plug flow.

In the present work, ADM, TSM and GDM were compared for a better understanding of the gas/liquid-solid-phase fluid behavior within the SSHE.

5.4.2 RTD model adjustment

RTD experimental data were fitted to each of the previously described model using unknown parameters estimation by the minimization of the mean squared errors (MSE) computed from Eq. (5.15), E^*_{exp} being the experimental RTD, E^*_{th} the theoretical RTD and M the total number of experimental points.

$$MSE = \frac{1}{M}\sum_{1}^{M}\left(E^*_{exp}\left(\theta_i\right) - E^*_{th}\left(\theta_i\right)\right)^2 \tag{5.15}$$

Minimization of the MSE function was performed by the use of direct method (simplex) with the *fminsearch* function of MATLAB.

5.4.3 RTD modelling results

Experimental data were modelled using the ADM, the TSM and the GDM by means of fitting as described in section 5.3. Figure 46 exhibits an example of the adjustments of the different models at 25 kg h^{-1} of mix flowrate and 0.0014 kg h^{-1} of air flowrate. The adjusted parameters and respective MSEs are given in Table 9 for all investigated experimental conditions. On examining Figure 46, it can be seen that both ADM and TSM failed to fit correctly the general trend of the experimental RTD curve. The ADM gave the best fit of the breakthrough time (minimum residence time) but did not describe satisfactorily both the height and the tail of the experimental *E*-curve. Contrariwise, the TSM missed both the breakthrough time and the peak of the *E*-curve but gave a good fit of the tail. The use of GDM leads to the best global fit with a description of the trend of the experimental data with a good accuracy as can be seen in Figure 46 and Table 9 (very low MSEs ranging from 0.0019 to 0.0045), even if the breakthrough time is less well fitted compared to the ADM results. Arellano et al. (2013c) also obtained a best fit with the GDM compared to ADM and TSM for RTD of non-aerated sorbet produced in the SSHE used in this work.

Adjusted ADM Peclet numbers (Table 9) corroborates experimental results, which showed that axial dispersion is increased when air flowrates increased, but ADM cannot explain the dissymmetry observed in experimental *E*-curves. Occurrence of axial dispersion was also demonstrated by the *N*-values of the TSM and the *p*-values of the GDM. Indeed, both values decreased when air flowrates increased, indicating more axial dispersion.

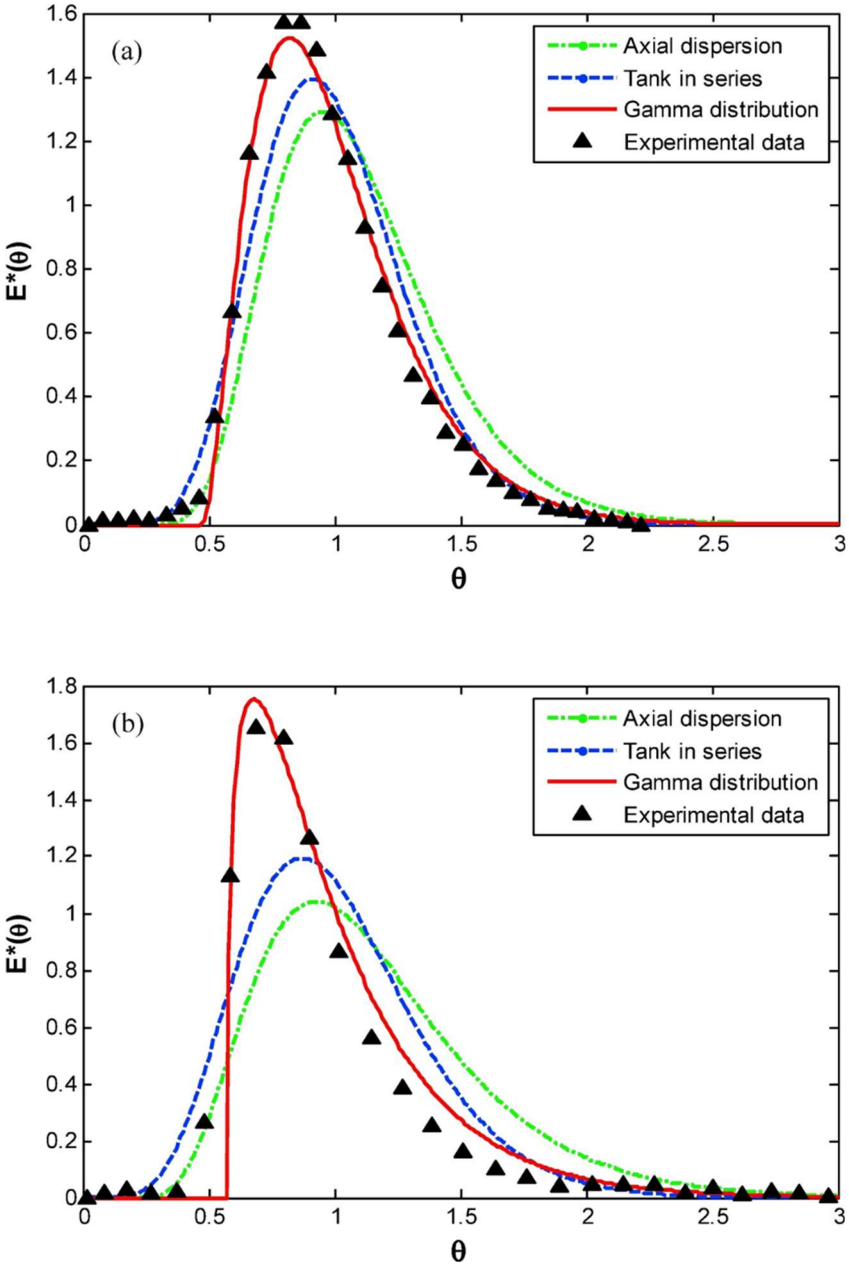

Figure 46. Examples of ADM, TSM and GDM adjustments with experimental RTD data - $T_{refrigerant} \approx -15$ °C: (a) $Q_{m,L}$ = 25 kg h^{-1} – $Q_{m,G}$ = 0.0014 kg h^{-1} – *MSE* = 0.0019; (b) $Q_{m,L}$ = 50 kg h^{-1} – $Q_{m,G}$ = 0.0125 kg h^{-1} – *MSE* = 0.0045.

Table 9. Adjusted model parameters and corresponding MSEs

Run	Q_{Mix} (kg h^{-1})	Q_{Air} (kg h^{-1})	$T_{refrigerant}$ (°C)	ADM		TSM		GDM		
				Pe	*MSE*	*N*	*MSE*	θ_0	*p*	*MSE*
1	25	0	−15.2	20.5	0.026	12	0.019	0.49	2.81	0.0038
2	25	0.0014	−15.2	20.5	0.044	11	0.015	0.47	2.96	0,0019
3	25	0.0125	−15.8	12.9	0.167	8	0.088	0.49	1.56	0.0028
4	25	0.0375	−14.2	11.4	0.047	7	0.020	0.48	1.80	0.0023
5	50	0.0014	−15.0	16.2	0.053	9	0.027	0.55	1.71	0.0032
6	50	0.0125	−15.4	13.1	0.056	8	0.030	0.58	1.32	0.0045
7	50	0.0375	−15.7	6.0	0.050	4	0.024	0.44	1.10	0.0034
8	25	0.0125	−9.9	17.1	0.164	10	0.099	0.57	1.41	0.0024
9	25	0.0125	−11.7	11.1	0.156	7	0.094	0.52	1.31	0.0022

5.5 Conclusion

The RTD of the liquid phase of an aerated sorbet was studied during production in a laboratory scale SSHE. The present work demonstrates that the presence of air induces significant modifications of the fluid age dispersion, in particular involving a stagnant air pocket inside the exchanger. Main results are a reduction of the mean residence time and more axial dispersion when the air flowrate is augmented, due to an increase of the stagnant air volume and of the liquid phase axial velocity. It was also shown that the presence of air leads to a greater radial temperature gradient between the cooled wall and the rotor. Consequently, higher viscosity and axial velocity gradients were obtained, leading to an increased axial dispersion. A shorter residence time and an increased axial dispersion ultimately end by a final product exiting the SSHE with less and small ice crystals (due to a reduction of the nucleation rate and of crystals growth) and less air bubbles (because they do not have enough time to be finely distributed into the liquid phase). Three RTD models were compared by means of fitting with the experimental data. The GDM was found to be the more accurate while the ADM and the TSM failed to describe the totality of the experimental behaviors of the sorbet inside the SSHE.

In a practical point of view, it is suggested to ensure a good mixing of the liquid and gas phases at the entrance of the exchanger in order to avoid or to reduce the occurrence of the gas pocket close to the dasher. This problem can also be solved by changing the geometry of the rotor (for example by the use of blades equipped with “teeth”) order to have a better mixing of the different fluid phases close to the rotor and close to the wall.

It should be pointed out that, in our knowledge, this study is pioneering in terms of description of a RTD for a two-phase gas/liquid flow in a SSHE. The results obtained might be valuable for several applications of gas-liquid flow in SSHE, especially during simultaneous crystallization-foaming process.

We are aware that many assumptions have been made to explain the experimental results observed in this work. Thereby, further investigations will be aimed at verifying these assumptions by studying: (i) the velocity profiles inside the SSHE (by CFD and X-ray visualization) in order to localize the air pocket; (ii) the effect of air addition on the apparent viscosity of the sorbet in order to establish a rheological model. Future works should also be devoted to the study of other operating parameters such as the freezing point depression, the rotor's speed and the pressure inside the SSHE's cylinder.

Nomenclature

$C(t)$	concentration of tracer (kg m^{-3})
CoV	coefficient of variation
$E(t)$; E	residence time distribution function, E-curve (s^{-1})
$E^*(\theta)$	dimensionless E-curve
K	consistency index for power law fluids (Pa s^n)
L	SSHE cylinder length (m)
m_i	mass of cup sample i (kg)
M	number of experimental data
MSE	mean squared error of the dimensionless E-curve
n	flow behaviour index for power law fluids
N	rotor's rotational speed (tr s^{-1})
N_T	number of tank for the TSM
p	GDM parameter
Pe	Peclet number
Q_m	mass flowrate (kg h^{-1})
Q_v	volumetric flowrate (m^3 s^{-1})
R	radius (m)
Re	Reynolds number
t	time (s)

$\bar{t}$	mean residence time (s)
t_{min}	minimum residence time (s)
t_{inj}	injection time (s)
Δt_i	sampling time for cup i (s)
$\Delta t_{sampling}$	total sampling time (s)
T	temperature (K)
Ta	Taylor number
v	mean velocity (m/s)
V	internal volume (m^3)

Greek letters

Γ	gamma function
μ	viscosity (Pa s)
θ	dimensionless time
θ_0	breakthrough time
π	constant pi ($\pi = 3.1416$)
ρ	density (kg/m^3)
σ	standard deviation
σ^2	variance
τ	geometrical residence time (s)
Ω	rotor's rotational speed ($rad\ s^{-1}$)

Subscripts

ax	axial
d	dead
exp	experimental
G	gas
L	liquid
r	rotor
rot	rotational
s	stator
th	theoretical
tot	total

Abbreviations

ADM	axial dispersion model
GDM	gamma distribution model
MB	methylene blue
RTD	residence time distribution
SSHE	scraped surface heat exchanger
TC	Taylor - Couette
TSM	tank in series model

References

Alcairo, E.R., Zuritz, C.A., (1990). Residence time distributions of spherical particles suspended in non-Newtonian flow in a scraped-surface heat exchanger. Transactions of the American Society of Agricultural Engineers 33(5), 1621-1628.

Arellano, M., Benkhelifa, H., Alvarez, G., Flick, D., (2013). Experimental study and modelling of the residence time distribution in a scraped surface heat exchanger during sorbet freezing. Journal of Food Engineering 117(1), 14-25.

Arellano, M., Benkhelifa, H., Flick, D., Alvarez, G., (2012). Online capillary rheometry of commercial sorbet, *16th IUFoST World Congress of Food Science and Technology*, Foz do Iguaçu - Brazil.

Baccar, M., Abid, M.S., (1997). Numerical analysis of three-dimensional flow and thermal behaviour in a scraped-surface heat exchanger. Revue Générale de Thermique 36(10), 782-790.

Benezech, T., Maingonnat, J.F., (1993). Study of residence-time distribution of non-Newtonian fluids in scraped-surface heat exchangers. International Chemical Engineering 33(2), 215-225.

Djéridi, H., Favé, J.F., Billard, J.Y., Fruman, D.H., (1999). Bubble capture and migration in Couette-Taylor flow. Experiments in Fluids 26(3), 233-239.

Duffy, B.R., Wilson, S.K., Lee, M.E.M., (2007). A mathematical model of fluid flow in a scraped-surface heat exchanger. Journal of Engineering Mathematics 57(4), 381-405.

Dumont, E., Fayolle, F., Legrand, J., (2000). Flow regimes and wall shear rates determination within a scraped surface heat exchanger. Journal of Food Engineering 45(4), 195-207.

Ekambara, K., Joshi, J.B., (2004). Axial mixing in laminar pipe flows. Chemical Engineering Science 59(18), 3929-3944.

Fayolle, F., Belhamri, R., Flick, D., (2013). Residence time distribution measurements and simulation of the flow pattern in a scraped surface heat exchanger during crystallisation of ice cream. Journal of Food Engineering 116(2), 390-397.

Fayolle, F., Mabit, J., Legrand, J., (2005). Determination of heterogeneities in a scraped surface heat exchanger using electrochemical sensors. Journal of Applied Electrochemistry 35(5), 487-498.

Fillaudeau, L., Le-Nguyen, K., André, C., (2009). Influence of flow regime and thermal power on residence time distribution in tubular Joule Effect Heaters. Journal of Food Engineering 95(3), 489-498.

Ham, J.H., Platzer, B., (2004). Semi-Empirical Equations for the Residence Time Distributions in Disperse Systems – Part 1: Continuous Phase. Chemical Engineering & Technology 27(11), 1172-1178.

Härröd, M., (1986). Scraped surface heat exchangers - a literature survey of flow patterns, mixing effects, residence time distribution, heat transfer and power requirements. Journal of Food Process Engineering 9(1), 1-62.

Hernandez, O., Ndoye, F., Benkhelifa, H., Flick, D., Alvarez, G., (2015). A discriminating microscopy technique for the measurement of ice crystals and air bubbles size distribution in sorbets, *24ième Congrès International du Froid ICR 2015*, Yokohama, Japan, p. 8 p.

Hubacz, R., (2015). Classification of flow regimes in gas-liquid horizontal Couette-Taylor flow using dimensionless criteria. Journal of Hydrodynamics, Ser. B 27(5), 773-781.

Hubacz, R., Wroński, S., (2004). Horizontal Couette–Taylor flow in a two-phase gas–liquid system: flow patterns. Experimental Thermal and Fluid Science 28(5), 457-466.

Ji, L., Wu, B., Chen, K., Zhu, J., (2010). Experimental study and modeling of residence time distribution in impinging stream reactor with GDB model. Journal of Industrial and Engineering Chemistry 16(4), 646-650.

Lee, J.H., Singh, R.K., (1993). Residence time distribution characteristics of particle flow in a vertical scraped surface heat exchanger. Journal of Food Engineering 18(4), 413-424.

Levenspiel, O., (1999). *Chemical Reaction Engineering* (3rd ed). John Wiley & Sons, New York.

Nauman, E.B., Nigam, A., (2004). On Axial Diffusion in Laminar-Flow Reactors. Industrial & Engineering Chemistry Research 44(14), 5031-5035.

Ndoye, F.T., Erabit, N., Alvarez, G., Flick, D., (2012). Influence of whey protein aggregation on the residence time distribution in a tubular heat exchanger and a helical holding tube during heat treatment process. Journal of Food Engineering 112(3), 158-167.

Oriol, J., Leclerc, J.P., Jallut, C., Tochon, P., Clement, P., (2008). Characterization of the two-phase flow regimes and liquid dispersion in horizontal and vertical tubes by using coloured tracer and non-intrusive optical detector. Chemical Engineering Science 63(1), 24-34.

Rao, C.S., Hartel, R.W., (2006). Scraped Surface Heat Exchangers. Critical Reviews in Food Science and Nutrition 46(3), 207-219.

Russell, A.B., Burmester, S.S.H., Winch, P.J., (1997). Characterization of Shear Thinning Flow Within a Scraped Surface Heat Exchanger. Food and Bioproducts Processing 75(3), 191-197.

Saxena, A.K., Nigam, K.D.P., Schumpe, A., Deckwer, W.D., (1996). Liquid phase residence time distribution for two phase flow in coiled tubes. The Canadian Journal of Chemical Engineering 74(6), 861-866.

Sharma, L., Nigam, K.D.P., Roy, S., (2017). Axial dispersion in single and multiphase flows in coiled geometries: Radioactive particle tracking experiments. Chemical Engineering Science 157, 116-126.

Shiomi, Y., Kutsuna, H., Akagawa, K., Ozawa, M., (1993). Two-phase flow in an annulus with a rotating inner cylinder (flow pattern in bubbly flow region). Nuclear Engineering and Design 141(1–2), 27-34.

Torres, A.P., Oliveira, F.A.R., (1998). Residence time distribution studies in continuous thermal processing of liquid foods: a review. Journal of Food Engineering 36(1), 1-30.

Trommelen, A.M., Beek, W.J., (1971). Flow phenomena in a scraped-surface heat exchanger ("Votator"-type). Chemical Engineering Science 26(11), 1933-1942.

Villermaux, J., (1993). *Génie de la réaction chimique - Conception et fonctionnement des réacteurs* (2nde ed). Tec & Doc - Lavoisier, Paris.

Wang, W.E.I., Walton, J.H., McCarthy, K.L., (1999). Flow Profiles of Power law Fluids in Scraped Surface Heat Exchanger Geometry Using MRI. Journal of Food Process Engineering 22(1), 11-27.

Wen, C.Y., Fan, L.T., (1975). *Models for flow systems and chemical reactors*. Marcel Dekker.

Yataghene, M., Francine, F., Jack, L., (2011). Flow patterns analysis using experimental PIV technique inside scraped surface heat exchanger in continuous flow condition. Applied Thermal Engineering 31(14–15), 2855-2868.

Yataghene, M., Pruvost, J., Fayolle, F., Legrand, J., (2008). CFD analysis of the flow pattern and local shear rate in a scraped surface heat exchanger. Chemical Engineering and Processing: Process Intensification 47(9–10), 1550-1561.

Yuan, Y., Han, M., Wang, D., Jin, Y., (2004). Liquid phase residence time distribution for a two-phase countercurrent flow in a packed column with a novel internal. Chemical Engineering and Processing: Process Intensification 43(12), 1469-1474.

Zhang, T., Wang, T., Wang, J., (2005). Mathematical modeling of the residence time distribution in loop reactors. Chemical Engineering and Processing: Process Intensification 44(11), 1221-1227.

6. Modeling flow and heat transfer in a scraped surface heat exchanger during the production of sorbet

Published in Journal of Food Engineering 221 (2018) 54–60

Abstract

A computational fluid dynamics model was implemented for studying the production of non-aerated sorbet in a scraped surface heat exchanger under different operating conditions. The coupled problem of fluid flow and heat transfer is solved by taking into account realistic values for the product physical properties as well as its complex rheology. The mathematical solution of the coupled problem represents a challenging task, among other reasons by the strong influence of temperature on product physical properties and rheology due to phase change. Fluid flow, heat transfer freezing and viscous dissipation phenomena are analyzed locally in the heat exchanger. The modeling approach is consistent, as indicated by comparisons between model predictions of the temperature profile along the heat exchanger and available experimental results.

Keywords

Scraped surface heat exchanger, sorbet production, sorbet rheology, computational fluid dynamics

6.1 Introduction

Scraped surface heat exchangers (SSHEs) are commonly found in the food industry as a way of controlling the heat transfer in products of high viscosity or that could lead to fouling on the internal walls. Many designs exist; they generally consist of a double pipe heat exchanger which contains a rotating element inside the inner pipe, where a number of blades are attached with purpose of scraping the inner cylinder at every rotation (Rao and Hartel, 2006). One application for SSHEs has been the industrial production of ice cream-like desserts (e.g. sorbets), where the purpose of the SSHE is to chill and freeze a formulated mix in order to crystallize the water present on the walls of the inner pipe (Goff and Hartel, 2013; Rao and Hartel, 2006). The blades also serve in this case as a dispersion system for the ice formed and a certain amount of air that could be introduced into the product. Air bubbles and ice crystals sizes are major quality parameters in sorbets, and their occurrence is closely related to the heat transfer mechanism and the flow characteristics in the SSHE. Actually, complicated heat transfer mechanisms and very complex flow profiles take place in the SSHE as a result of the presence of rotating elements, of the crystallization phenomena,

and of the product rheology (which is highly dependent on the ice fraction). The experimental analysis of flow characteristics and heat transfer mechanisms inside the SSHE, particularly during the production of frozen desserts, is onerous and technically difficult to carry out. This is a situation in which physics-based modeling can effectively be used as a tool for providing insight about relevant phenomena.

Flow through the inner pipe of SSHEs has been extensively studied experimentally for the single-phase Newtonian and non-Newtonian fluids (e.g. Dumont et al. (2000a, 2000b); Wang et al. (1999, 2000); Yataghene et al. (2011); see also the reviews by Abichandani et al. (1986); Härröd (1986); Rao and Hartel (2006)). In summary, the flow structure can be understood as an annular gap flow (i.e. Taylor-Couette) disturbed by the presence of rotor parts. Once a critical Taylor number value is reached, stable or wavy unstable forms of vortices begin to establish throughout the inner pipe. However, the flow patterns can be strongly affected by the rheological behavior of the fluid, the presence of blades in the system, their angle, and particularly, the gap (i.e. the clearance) between the tips and the inner wall. Large local shear rates are observed to appear in the clearance, as well as secondary vortexes in zones related to the blades. Modeling approaches have been developed to overcome the complex experimentation required, i.e. whether more precise investigation of flow phenomena or changes on the geometry of the blades make impractical the development of experimental facilities (e.g. Baccar and Abid (1997, 1999); Błasiak and Pietrowicz (2016); D'Addio et al. (2013); Duffy et al. (2007); Stranzinger et al. (2001); Yataghene et al. (2009); Yataghene et al. (2011); Yataghene et al. (2008)).

Numerous studies dealing with heat transfer phenomena in single-phase fluids in SSHEs have been reported (e.g. Härröd (1986); Rao and Hartel (2006)). Experimental studies usually rely on obtaining the average heat transfer coefficient in the inner pipe of the exchanger; results are often expressed in terms of Nusselt number correlations in function of axial and rotational Reynolds as well as the Prandtl number, the number of blades, and geometrical ratios of diameters and lengths (e.g. Abichandani et al. (1986); Boccardi et al. (2010); Skelland (1958); Trommelen et al. (1971)). Numerical approaches have also been used to complement or develop heat transfer correlations (e.g. Baccar and Abid (1997, 1999); Błasiak and Pietrowicz (2016); D'Addio et al. (2013); Dehkordi et al. (2015); Rainieri et al. (2014); Saraceno et al. (2011); Yataghene et al. (2009); Yataghene and Legrand (2013)).

It is noteworthy that few experimental works deal with heat transfer in freezing solutions in SSHEs (e.g. Lakhdar et al. (2005); Martínez et al. (2014); Qin et al. (2006); Qin et al. (2003)). In such cases, as freezing takes place, the apparent physical properties of the fluids change strongly and affect the heat transfer coefficient. For instance, Arellano et al. (2013c) have shown that the apparent viscosity of non-aerated sorbet can increase from 1 to 12 Pa s along its pathway in the SSHE. Lakhdar et al. (2005) included the influence of initial non-freezing substance concentration in their heat transfer coefficient during freezing of

milk and aqueous glycerol mixtures which include a correction term for the ice heat of fusion can be found in the literature (e.g. Qin et al. (2006); Qin et al. (2003)).

Mathematical models have also been developed specifically for SSHE ice cream production; we can identify classes of models associated with increasing degree of complexity about coupled phenomena. Bongers (2006) proposed a model considering the freezer barrel as a series of well mixed stages, taking into account four contributions to the energy balance: refrigeration, crystallization, dissipation of mechanical energy, and scraping friction of the blades on the ice layer. In a further development of this model, Dorneanu et al. (2009) have included conservation equations for selected dispersed phases (water, sugar, fat and remaining components); they considered an immobile frozen layer at the wall, and the plug-flow assumption for the mean axial flow. Lian et al. (2006) have combined a 2D computational fluid dynamics model and a population balance approach with the aim to predict he ice crystal size distribution in the final product.

Non-aerated lemon sorbet production has been studied in a series of articles by Arellano et al. (2013a, 2013b); Arellano et al. (2013c); Casenave et al. (2013, 2014); González-Ramírez et al. (2013); González Ramírez et al. (2013). Modeling efforts were devoted by those authors in predicting ice crystal size distributions. These models used residence time distributions and reduced heat transfer equations under transient operation with population balance approaches in order to predict crystal chord length distributions during steady-state operations. Particularly, the model developed by Arellano et al. (2013a) reached good agreement with experimental crystals mean chord lengths and temperature profiles along the exchanger. In such a goal, key parameters as global heat transfer coefficients, and crystal growth and nucleation rate constants, were adjusted in the model. Although the results how a good agreement, the reduced models cannot offer a full insight into the heat transfer mechanisms taking place inside the exchanger.

In the logical continuation of experimental and modeling efforts devoted by Arellano et al. (2013a, 2013b); Arellano et al. (2013c), this study presents a numerical model for predicting the non-aerated lemon sorbet production in a pilot-scale SSHE under different operating conditions. The main objectives were: firstly, to implement a 3D computational fluid dynamics (CFD) model for solving the coupled problem of fluid flow and heat transfer within the SSHE, while respecting the strong influence of temperature on key properties of the liquid food product; secondly, to analyze the 3D distributions of key variables throughout the SSHE, at scales beyond usual experiments, and lastly, to assess the performance of this model under different operating conditions, using as reference measurements conducted in those early contributions.

6.2 Development of the model

6.2.1 Physical problem description

Before developing the model equations, a short description of the physical problem is required. The modeling approach could be applied to the production of non-aerated sorbet in any SSHE freezer; here it was implemented for the pilot unit used by Arellano et al. (2013a, 2013b); Arellano et al. (2013c). Those authors carried out the freezing of a commercial UHT-pasteurized lemon sorbet mix (14.6% w/w sucrose, 8% w/w fructose, 0.09% w/w dextrose, 3% w/w lemon juice concentrate 60 Brix, 0.5% w/w locust bean gum/guar gum/Hypromellose stabilizer blend) in a laboratory scale continuous pilot freezer (WCB Model MF 50). Within the freezer, the SSHE consists of a double pipe heat exchanger whose inner pipe (0.05 m inner diameter, 0.40 m long) contains a solid flattened cylinder rotor equipped with two scraper blades placed at opposite positions. A scheme of the SSHE is presented in Figure 47.

Four wireless data loggers with built-in temperature sensors (Thermochron iButton DS1922 – Maxime; 16.3 mm diameter and 6.4 mm thick, calibrated to an accuracy of ±0.2°C within a range from -20 to 20°C) were placed at regular distances on the flat dasher surface as viewed in Figure 47B. Also, a calibrated type T thermocouple (accuracy of ± 0.2°C) was placed at the entrance of the heat exchanger, and a calibrated Pt100 probe (Baumer, accuracy of ±0.1°C) was placed at the outlet pipe of the exchanger. These probes allowed the measurement of temperature during steady-state operation of the freezer.

The processing unit has a nominal capacity of 25 – 75 kg/h (about 0.007 – 0.021 kg/s), with accuracy of $\pm 9\times10^{-5}$ kg/s. Refrigerant fluid was evaporating dichlorodifluoromethane (R22), which circulated through the cooling outer pipe of the SSHE at controlled temperature. This temperature was measured through a calibrated type-T thermocouple. This temperature was measured through a calibrated type-T thermocouple, with an accuracy of ±0.2°C, fixed with conductive aluminum tape on the external surface wall of the outer pipe. The rotational speed of the dasher and blades varied from 545 to 1000 rpm (about 9-17 rev/s), with accuracy of 1 rpm (about 0.017 rev/s).

Using this device, Arellano et al. (2013b) measured the fluid temperature at selected positions inside the SSHE under seven combinations of operating conditions, using three refrigerant temperatures (T_R = -10.6°C, -15.3°C and -20.1°C), three mass flow rates ($\dot{m}_{mix}$ = 25, 50 and 75 kg/h) and three dasher rotation frequencies (f_{rot} = 545, 750 and 1000 rpm). In all cases the sorbet mix inlet temperature was held constant at 5°C.

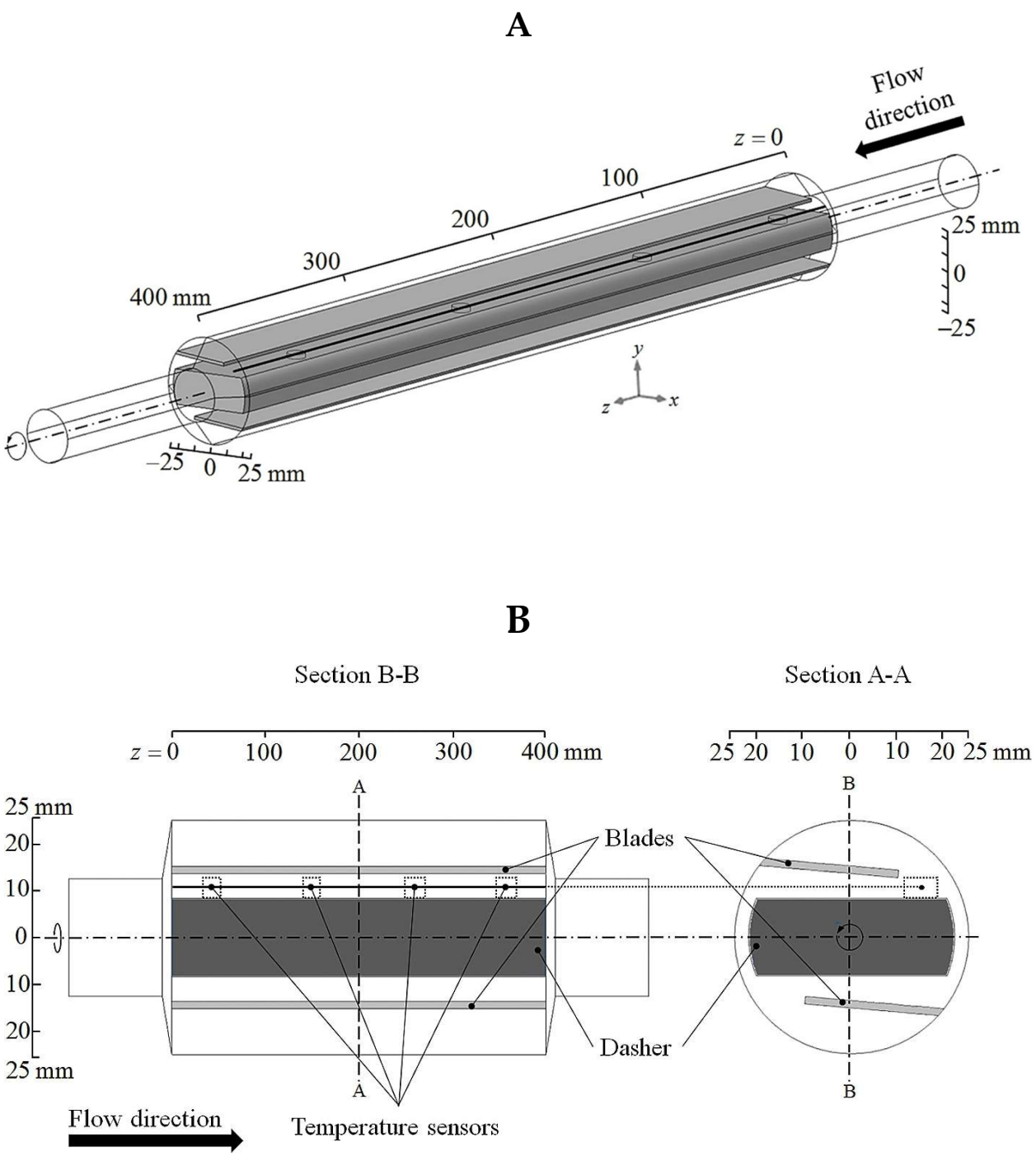

Figure 47. Schematic view of the SSHE pilot unit used for freezing lemon sorbet (Arellano et al., 2013a, b; Arellano et al., 2013c): **A)** 3D view of the SSHE as represented in the numerical model, and **B)** longitudinal (left) and cross-sectional (right) views of the SSHE as employed for displaying model predictions.

6.2.2 Governing equations

Although non-aerated sorbets are two-phase systems containing ice and concentrated liquid mix, in this work it is assumed that sorbet mix and freezing sorbet can be treated as a single-phase fluid with apparent physical properties varying with temperature; hence mass, momentum and energy conservation equations for single-phase fluids were used, following the approach proposed by Lakhdar et al. (2005). The inner cylinder and the rotating elements are the most relevant parts in the SSHE, and therefore, it is convenient to establish the governing equations using a reference frame rotating with them since that allows deal with a non-moving geometry. From this, a relative velocity in the moving frame, **v**, can be defined from the velocity in the Galilean frame, **u**, such that:

$$\mathbf{u} = \mathbf{v} + \boldsymbol{\Omega}_{rotor} \times \mathbf{r} \tag{6.1}$$

And the conservation equations or mass, momentum and energy can be expressed as:

$$\nabla \cdot \mathbf{v} = 0 \tag{6.2}$$

$$\rho\left(\mathbf{v} \cdot \nabla\right)\mathbf{v} = -\nabla \cdot \boldsymbol{\tau} - \nabla p - 2\rho\left(\boldsymbol{\Omega}_{rotor} \times \mathbf{v}\right) - 2\rho\left(\boldsymbol{\Omega}_{rotor} \times \boldsymbol{\Omega}_{rotor} \times \mathbf{r}\right) \tag{6.3}$$

$$\rho C_p \mathbf{v} \cdot \nabla T = \nabla \cdot \left(k \nabla T\right) - \left(\boldsymbol{\tau} : \nabla \mathbf{v}\right) \tag{6.4}$$

Where **v** is the velocity (magnitude in m/s), **τ** the viscous stress tensor obtained from a power-law model, p the pressure (Pa), and T the temperature (K); ρ is the product density (kg m^{-3}), C_p its specific heat capacity (J kg^{-1} K^{-1}), and k its thermal conductivity (W m^{-1} K^{-1}).

Since the internal dasher and the blades occupy a non-negligible portion of the volume inside the inner pipe in the heat exchanger, it is possible that heat conduction in the solids affects the temperature profiles in the fluid. In other works this has been sometimes neglected (Lian et al., 2006; Yataghene et al., 2009) or included (Yataghene and Legrand, 2013). In the present work, heat transfer across the dasher and blades were included while dasher and blade supports were neglected; the influence of heat conduction in the dasher and the blades is assessed through numerical simulation while that associated with their supports remains a matter of discussion (see section 6.5.2). Under the rotating reference frame, both elements (dasher and blades) appear static, and therefore, the following equation holds for the heat transfer:

$$\nabla \cdot \left(k \nabla T\right) = 0 \tag{6.5}$$

The following boundary conditions were considered for solving fluid flow equations:

a) Under the rotating reference frame: the inner wall of the internal cylinder, the inlet and outlet bowls and pipes were perceived o be rotating at the speed of the rotor on the opposite sense of rotation; hence the non-slip condition in these surfaces becomes $\mathbf{v} = -\boldsymbol{\Omega}_{rotor} \times \mathbf{r}$.

b) On the dasher and blades surfaces: $\mathbf{v} = 0$ (no-slips condition).

c) At the inlet boundary: laminar flow profile was imposed from the specified mass flow rate and the rheology of the sorbet mix:

$$v_x = \Omega_{rotor} y; \quad v_y = -\Omega_{rotor} x; \quad v_z = \frac{3n+1}{n+1} \frac{\dot{m}_{mix}}{\rho \pi r_{pipe}^2} \left(1 - \left(\frac{r}{r_{pipe}} \right)^{\frac{n+1}{n}} \right) \tag{6.6}$$

Where n is the flow behavior exponent.

d) At the outlet boundary, the same flow profile was imposed to insure mass conservation.

e) The relative pressure was set to be zero at the center point of the exit boundary.

The following boundary conditions were considered for solving the equation of conservation of energy:

a) The product was assumed to enter in the inlet pipe of the SSHE at a uniform temperature of 5°C.

b) At exit the outlet pipe of the SSHE, a null gradient was assumed for the product temperature.

c) The product was assumed to flow under adiabatic conditions in the inlet and outlet pipes as well as in the inlet and outlet bowls of the SSHE: these computational sub-domains were assumed to be delimited y thermally-insulated walls.

d) Inside the SSHE cylinder, the product flows confined between the wall, the dasher and the blades. Conduction is solved throughout these solid elements; at the interface between product and dasher or blades, continuity of temperature and heat flux was assumed.

e) At the internal wall of the SSHE inner cylinder, the heat flux density as expressed as the product of a global heat transfer coefficient (U) and the difference between the refrigerant evaporating temperature (T_R) and the liquid product temperature in contact with the wall ($T = T_{inside}$) (see Figure 48):

$$U\left(T_R - T\right) = k \nabla T \cdot \mathbf{n} \tag{6.7}$$

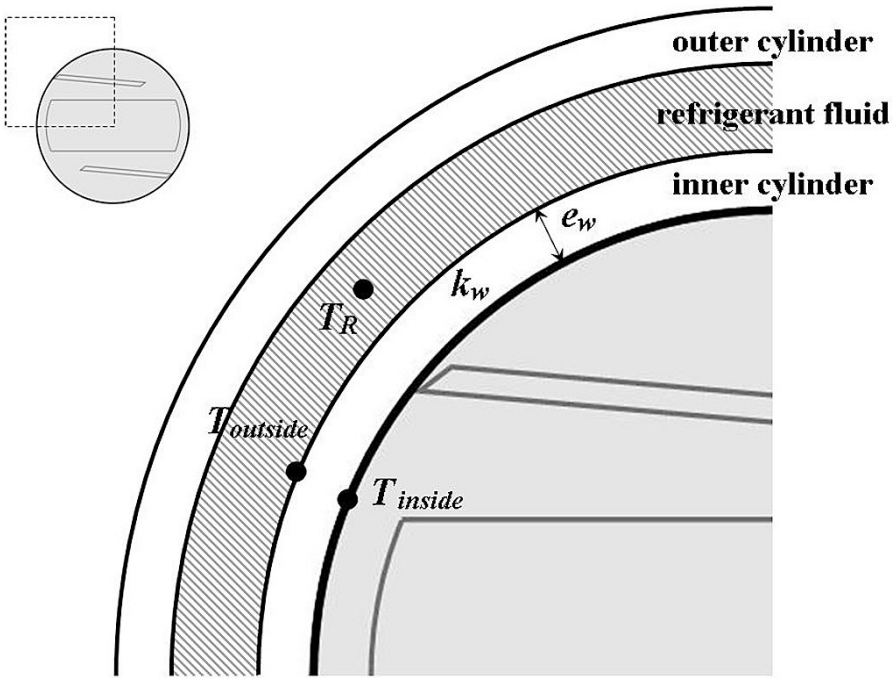

Figure 48. Cross-section view of the SSHE. The computation domain taken into account by the numerical model is pictured in grey (see the whole cross-section view at top-left). This domain is delimited by the thickest line, which corresponds to the internal wall of the SSHE inner cylinder. Other black lines delimitate the SSHE outer and inner cylinders. The wall of the inner cylinder is characterized by thickness e_w, thermal conductivity k_w, and the outside and inside temperatures ($T_{outside}$ and T_{inside} respectively). The dashed zone corresponds to the refrigerant fluid, characterized by evaporating temperature T_R

We applied the value U = 2500 W m^{-2} K^{-1} reported by Arellano et al. (2013a). This heat transfer coefficient is associated with a) convection between the refrigerant fluid and the external side of the SSHE inner cylinder, which is characterized by the outside convective heat transfer coefficient $h_{outside}$, and b) conduction through the stainless-steel wall which separates the refrigerant fluid and the product inside the SSHE inner cylinder; the wall is characterized by thickness e_w = 0.002 m and conductivity k_w = 15 W m^{-1} K^{-1}. This way, U can be expressed as:

$$U = \frac{1}{\frac{e_w}{k_w} + \frac{1}{h_{outside}}} \tag{6.8}$$

The SSHE inner cylinder was not included in the computational domain because, in the reference frame of the blades, it is in rotation; hence the problem would become unsteady. The heat transfer resistance of the wall (e_w/k_w) represents one third of the total resistance $1/U$. An upper limit for the global heat transfer coefficient in our problem would be $U = k_w/e_w \approx$ 7500 W m^{-2} K^{-2}, which can be estimated by neglecting the

convective heat transfer resistance between the external side of the SSHE inner cylinder and the refrigerant fluid ($1/h_{outside}$) in equation (6.8).

6.3 Product physical properties

Physical properties of sorbets were estimated from experimental measurements or from available information in the literature. Some approximations were performed in order to reduce the mathematical difficulty of solving the governing equations. Table 10 summarizes values and correlations assumed.

Table 10. Physical properties of the sorbet and sorbet mix used in this work

Property	Value or expression
Sorbet	
Density	1050 kg m^{-3}
Power-law flow index, n	0.5
Power-law consistency index, K	Equation (6.13)
Heat capacity, C_p	Equation (6.15)
Thermal conductivity, k	Equation (6.16)
Steel	
Thermal conductivity, k_w	15 W m^{-1} K^{-1}

6.3.1 Freezing point curve of concentrated lemon sorbet mix and sorbet ice fraction

Although non-aerated sorbets are two-phase systems containing ice and concentrated liquid mix, in this work it is assumed that the apparent physical properties can e approximated assuming that a local thermodynamical equilibrium is established at any point of the fluid inside the SSHE. This approach has been also used before in order to simulate similar systems e.g. ice crystallization from sugar solutions (Lakhdar et al., 2005) and ice cream properties estimation (Cogné et al., 2003). At equilibrium, the solute fraction (in the liquid surrounding the ice crystals) becomes that of the freezing point curve of concentrated sorbet mix at the local temperature.

Data of freezing point temperatures for the commercial lemon sorbet mix modeled in this work were obtained experimentally by González Ramírez (2012), who proposed a polynomial correlation restricted to the range from -13°C to 0°C whereas the sorbet temperature can be as low as -20°C. To improve the predictions, a correlation based on a thermodynamical approach was developed. To improve the predictions, a correlation based on a thermodynamical approach was developed. Freezing point depression curves of thermodynamically ideal binary solutions of a freezing solvent compound i.e. water) and a solute

(i.e. soluble solids) can be expressed; their molar fraction being a function of temperature, solvent, solid heat capacity solvent liquid and solid heat capacity as follows:

$$\ln x_w(T) = \frac{\Delta \hat{H}_{f,mp}}{R}\left(\frac{1}{T_{mp}} - \frac{1}{T}\right) - \frac{1}{R}\left(\int_{T_{mp}}^{T} \frac{c_{p,w} - c_{p,i}}{T} dT' - \int_{T_{mp}}^{T} \frac{c_{p,w} - c_{p,i}}{T'} dT'\right) \tag{6.9}$$

The solute mass fraction can be expressed in function of the water molar fraction:

$$w_s^*(T) = \frac{1 - x_w(T)}{1 - C x_w(T)} \tag{6.10}$$

Where $C = 1 - M_w/M_s$ could be regarded as a fitting parameter depending on the molar mass of water and of solute. In order to improve the quality of the fitting curve, a second constant was introduced, and the equation fitted was:

$$w_s^*(T) = C_1 \frac{1 - x_w(T)}{1 - C_2 x_w(T)} \tag{6.11}$$

In equation (6.9) the heat capacities of liquid water and ice were taken as functions of temperature according to Choi and Okos (1986). After fitting the experimental data to equation (6.11) the values obtained were C_1 = 0.7316 and C_2 = 0.9476. Figure 49 displays experimental data and corresponding results from equation (6.11) for two products: concentrated lemon sorbet mix and sucrose solution.

Once the equilibrium solute concentration is determined, a mass balance yields the ice mass fraction using the initial solute fraction in the mix, as indicated in equation (6.12). The estimated ice fractions at different temperatures are shown in Figure 50D.

$$w_i = 1 - \frac{w_{s0}}{w_s^*} \tag{6.12}$$

6.3.2 Density

The sorbet density was estimated from the ice mass fraction and the specific densities of ice and mix at temperatures ranging from -20 to 10°C using the approach recommended by Choi and Okos (1986). Estimated values of density vary slightly (less than 6%) and the constant value of 1050 kg m^{-3} was assumed for modeling purposes.

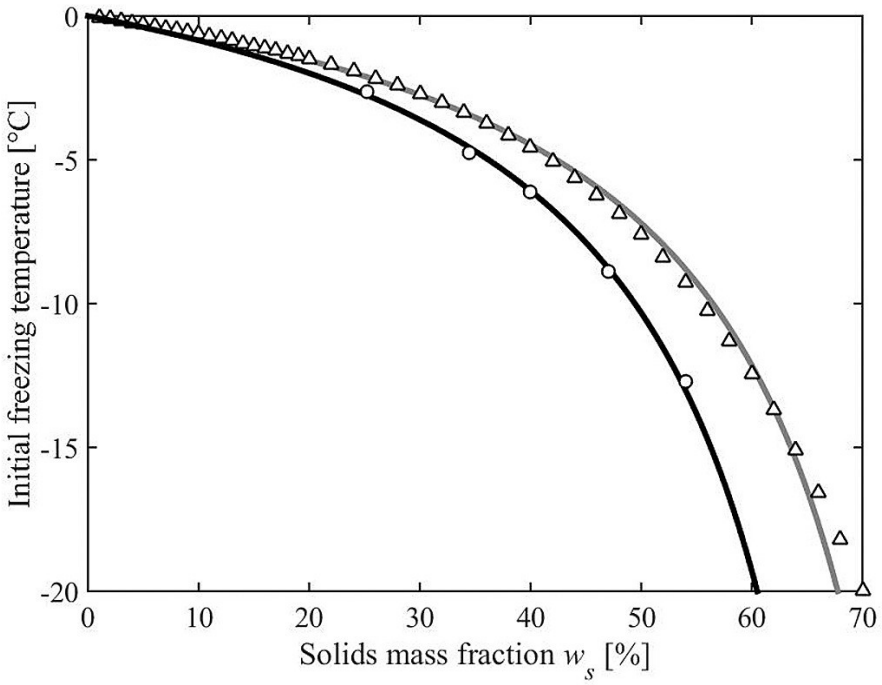

Figure 49. Freezing depression curve of concentrated lemon sorbet mix and sucrose solution : (O) obtained experimentally for lemon sorbet mix by González Ramírez (2012), (—) estimated for lemon sorbet mix using equation (6.11), (Δ) obtained experimentally for sucrose solutions by Reiser et al. (2012), and (—) estimated for sucrose using equation (6.11)

6.3.3 Rheological behavior of non-aerated lemon sorbet

Arellano et al. (2013c) have thoroughly investigated the influence of the temperature and thus of the ice volume fraction on the apparent viscosity of sorbet by using pipe rheometry measurements. Their main results can be summarized by an empirical rheological power-law model which predicts the consistency index and the flow behavior index as function of the ice volume fraction and the temperature, these two parameters being linked by the hypothesis of local equilibrium.

The difficulty to study the sorbet rheological behavior is put in evidence in Figure 2 of Arellano et al. (2013c): the range of shear rates permitting reliable observations decreases as the sorbet becomes colder and associated with higher ice volume fraction. Indeed, at -2.89°C (ice volume fraction of 5.8%), the observations were reliable for shear rates up to about 450 s^{-1}; at -5.68°C (ice volume fraction of 39%) the observations were reliable for shear rates up to 40 s^{-1} only. The rheological model proposed by those authors represents a synthesis over the whole dataset of operating conditions studied (mass sorbet flow rate and sorbet temperature). The following approximation was fitted to describe the consistency index (in units of Pa s^n) of both sorbet mix and sorbet:

$$K = 0.5838 \qquad \text{for} \quad T \geq T_{if}$$
$$K = 0.5838 + 10.16\left(T_{if} - T\right) \qquad \text{for} \quad T < T_{if} \tag{6.13}$$

Where T_{if} = -2.72°C is the initial freezing temperature. Figure 50A compares equation (6.13) with the consistency index estimated accordingly to Arellano et al. (2013c) at selected temperatures. Applying the local thermodynamical equilibrium assumption as discussed above between -20 and 10°C, the sorbet flow index (n) reported by Arellano et al. (2013c) ranges between 0.38 and 0.55. In this work a constant value of 0.5 was used for modeling purposes.

6.3.4 Apparent heat capacity

In order to include the effect of water freezing into the enthalpy of the sorbet, he apparent heat capacities of the sorbet mix and the frozen non-aerated sorbet were estimated using the approach proposed by Cogné et al. (2003) for ice cream and by Lakhdar et al. (2005) for crystallizing sugar solutions. It consists of a weighted average between the values for mix and ice, including a correction term for the change in the amount of ice according to the local thermodynamical equilibrium approximation:

$$C_p = C_{pi} w_i + C_{ps} w_s + C_{pw}\left(1 - w_i - w_s\right) - \Delta \hat{H}_f \frac{dw_i}{dT} \tag{6.14}$$

In order to simplify the heat capacity calculation, the following equation was fitted from estimation:

$$C_p = 3500 \qquad \text{for} \quad T \geq T_{if}$$
$$C_p = 3500 + 7.95 \times 10^4 \exp\left(0.543\left(T - T_{if}\right)\right) \qquad \text{for} \quad T \geq T_{if} \tag{6.15}$$

Figure 50B compares estimated values provided by equations (6.14) and (6.15).

6.3.5 Thermal conductivity

Non-aerated sorbet was represented as by Cogné et al. (2003) as a two-phase material, which consist of a solid phase ice crystals) dispersed in a continuous fluid phase made of dry matter and unfrozen water (Maxwell-Eucken model). The thermal conductivity of the continuous phase was estimated by using the intrinsic thermal conductivity values of each main component and their volume fractions estimated from their weight fraction and their density (Choi and Okos, 1986). In the present study, the solute mass fractions were obtained from equation (6.10). As before, a simpler equation was fitted:

$$k = 0.432 \qquad \text{for} \quad T \geq T_{if}$$
$$k = 0.432 + 0.303\left(1 - \exp\left(-0.367\left(T_{if} - T\right)\right)\right) \qquad \text{for} \quad T < T_{if} \tag{6.16}$$

A comparison between estimated values and equation (6.16) is shown in Figure 50C

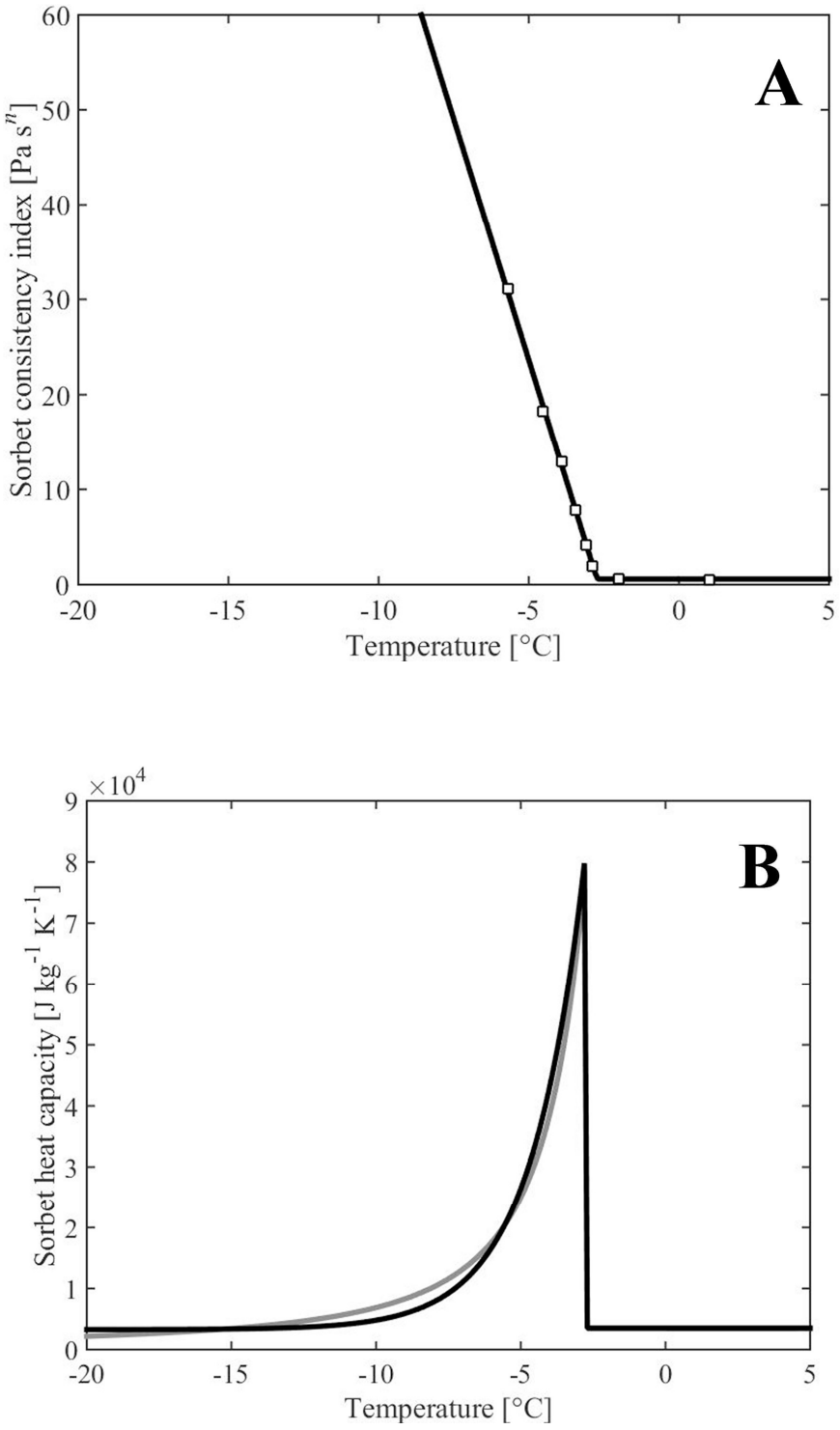

Figure 50. Sorbet physical properties as taken into account in this study : **A)** consistency index: (□) obtained experimentally by Arellano et al. (2013c) and (—) estimated using equation (6.13); **B)** heat capacity : (—) estimated as proposed by Cogné et al. (2003) and (—) estimated using equation (6.15) ; **C)** thermal conductivity: (—) estimated as proposed by Cogné et al. (2003) and (—) estimated using equation (6.16); **D)** ice mass fraction in sorbet according to temperature using equations (6.9) - (6.12)

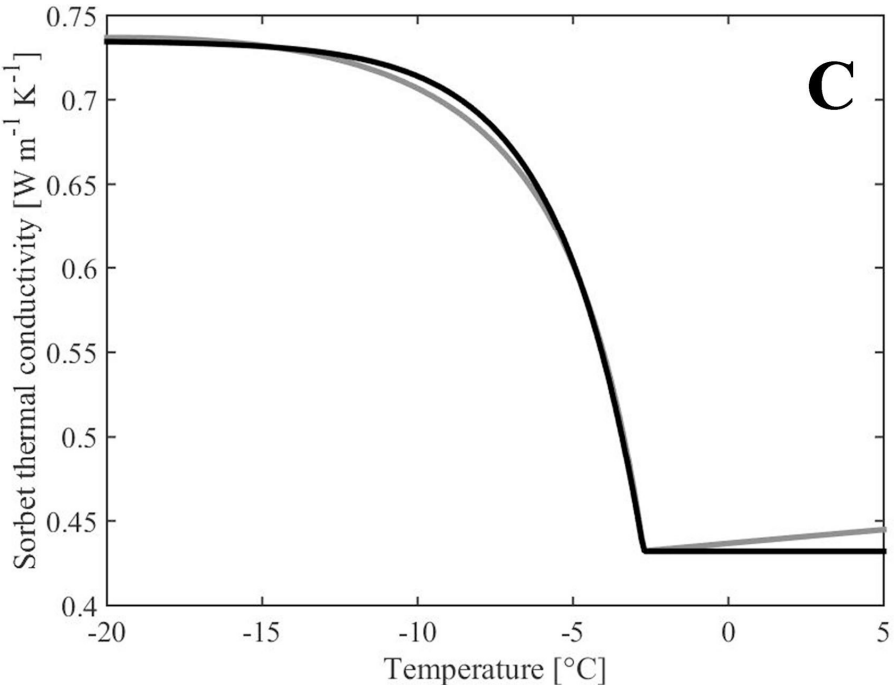

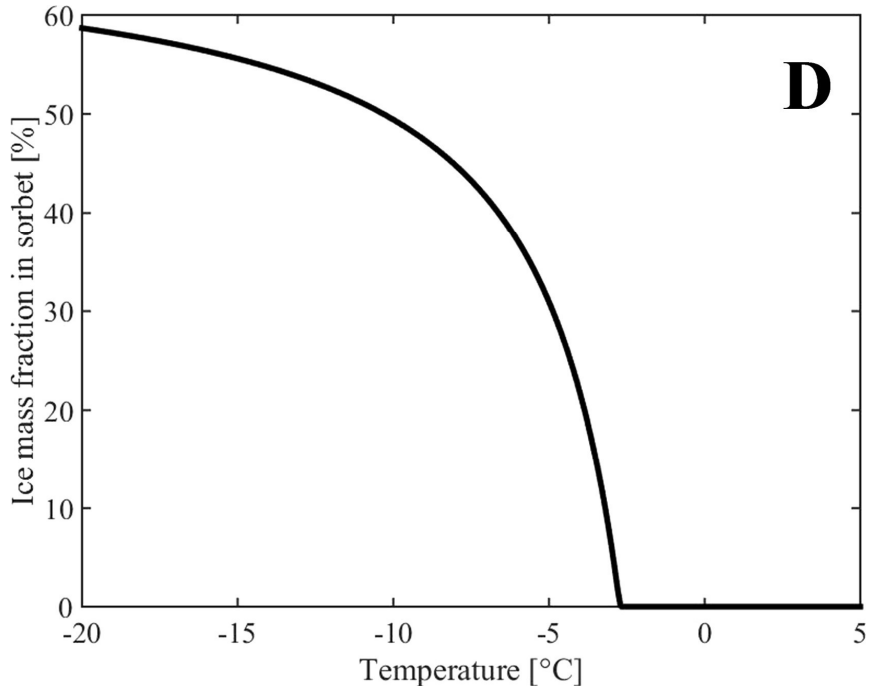

Figure 50. Continuation

6.4 Numerical model

6.4.1 Geometry

In order to avoid a computationally-intensive transient 3D simulation with moving boundaries, we adopt here the geometrical representation of the SSHE which is displayed in Figure 47A. While being quite simple, this representation allows us to conduct a steady state simulation of all the relevant phenomena occurring in the cylindrical section of the SSHE: scraped surfaces, dasher, and blades.

The inner cylinder of the SSHE under consideration contains several elements: i) the sorbet that is subjected to heat transfer and flow, ii) the internal solid elements that constitute the rotor (I.e. the dasher, the blades and their supports), and iii) the temperature sensors added to the dasher. Dasher and blades were considered for simulations given their major influence on the global performance of SSHEs; nevertheless, the blade supports and temperature sensors were not included since they have a relative small size and hence an expected negligible influence on flow profiles as well as on heat transfer mechanisms. Both headers of the exchanger contain reservoirs for the fluid entering or leaving the inner cylinder, as well as the dasher supports and the mechanical joints required. They were simplified, as shown in Figure 51 replacing them by co-axial cones of 0.01 m length connecting the inner cylinder of the SSHE to the inlet and outlet pipes. Also, in the exchanger the mix enters the bowl laterally, while the sorbet exit downwards. This was simplified by using co-axial horizontal tubes of 0.0125 m diameter, and 0.1 m long for ensuring a complete development of flow profiles.

Although the gaps between the blades and the wall of the internal cylinder have been shown to have an effect on the flow patterns inside the SSHEs with liquid flow (Dumont et al., 2000a, b), they were neglected in this work by extending the blades up to the inner wall of the internal cylinder. This was made considering that ice formation takes place mostly on the inner wall of the internal cylinder during the production of ice creams and sorbets and the action of the scraping blades on this ice could block the gap from the fluid (Cook and Hartel, 2010).

6.4.2 Mesh construction

Looking for the resolution of equations which govern the coupled phenomena, every computational domain has to be subdivided into a number of small, non-overlapping cells. The mesh was constructed using the COMSOL Multiphysics integrated builder, version 5.2. In order to account correctly for the momentum and thermal boundary layers, the mesh around the surfaces was built using four-element layer of prismatic elements, while the domain interiors were filled out with tetrahedral elements of varying minimum sizes.

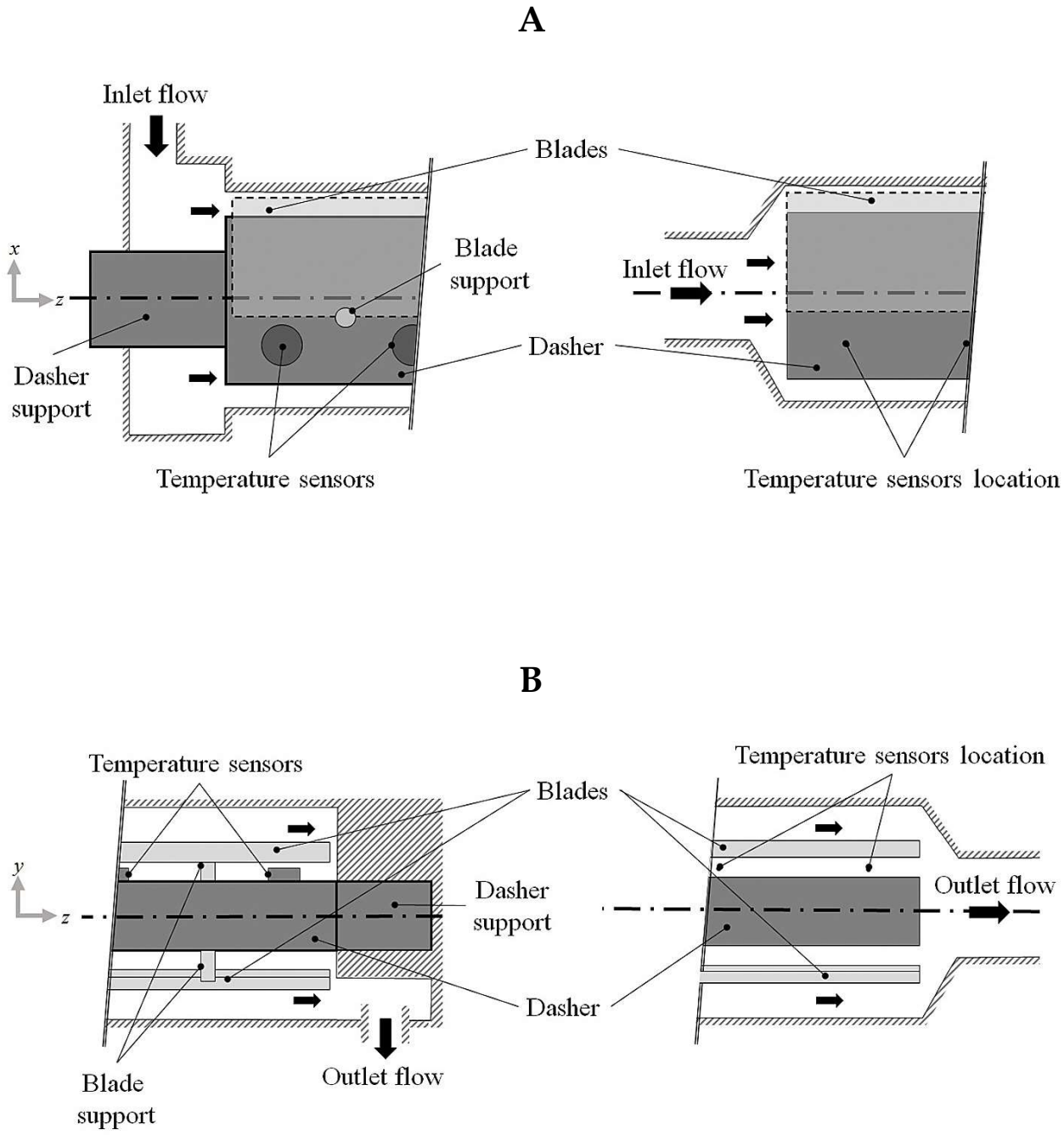

Figure 51. **A**) Actual cross-section view of the SSHE inlet bowl (left), and its representation in the numerical model (right). **B**) The same for the SSHE outlet bowl

Results achieved with the mesh constituted by 1.5×10^6 elements provide a satisfactory level of reliability in terms of the predicted profile of temperature along the SSHE axis, as indicated by a comparison with two other meshes (see section 6.5.3). Figure 52 displays this mesh around the dasher and the blades, as well as a cut view at z = 0.2 m.

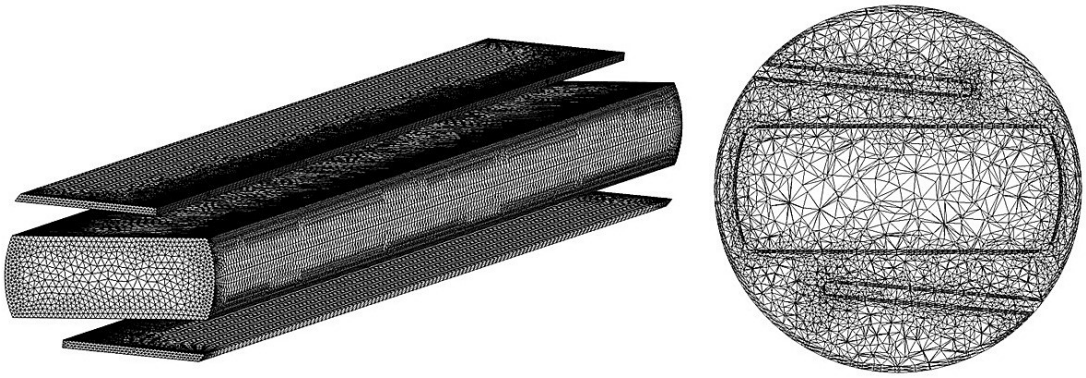

Figure 52. Mesh built for the simulations carried out in this work. Right: mesh around the solid elements (dasher and blades); left: cut view in the center of the SSHE inner cylinder.

6.4.3 Calculation strategy

The solution of the linear system resulting from the linearization of the governing equations is reached through the Parallel Sparse Direct Linear Solver (PARDISO) (Schenk and Gärtner, 2004), as implemented with the finite-elements method in the simulation package COMSOL Multiphysics, version 5.2 (Zimmerman, 2006). Satisfactory convergence of numerical solutions was reached after hundreds of iterations, looking for a relative tolerance better than 10^{-5}. Simulations were implemented in a PC station with 6 CPU at 3.50-GHz and 128-Gb RAM.

The coupled problem to be solved is challenging from different perspectives: on one hand, the product is characterized by physical properties which vary significantly with temperature; on the other hand, the product experiences a complex flow pattern, including obstructions and relatively fast rotation. The mathematical solution associated with every operating condition of interest was obtained as the result of a particular step-by-step calculation strategy. Firstly, preliminary fields for velocity and pressure were estimated at the temperature 5°C, by solving equations (6.2) and (6.3); secondly, a preliminary temperature field was estimated for that preliminary flow field by solving only equations (6.4) and (6.5); finally, assuming theses first-guesses as starting condition, the ensemble of coupled equations (6.2) – (6.5) was solved simultaneously by a direct method, iteratively, while increasing the maximal value for the sorbet consistency index, until no further increase influenced the mathematical solution.

6.5 Results and discussion

6.5.1 Analysis of flow and temperature profiles

Main features of fluid flow in the SSHE as predicted by the numerical model are displayed in Figure 53. These results were obtained under the reference operating conditions $\dot{m}_{mix}$ = 50 kg/h, T_R = -15.3°C and f_{rot} = 750 rpm. The rotation direction of the inner wall of the heat exchanger is clockwise as seen from the exit of the outlet pipe.

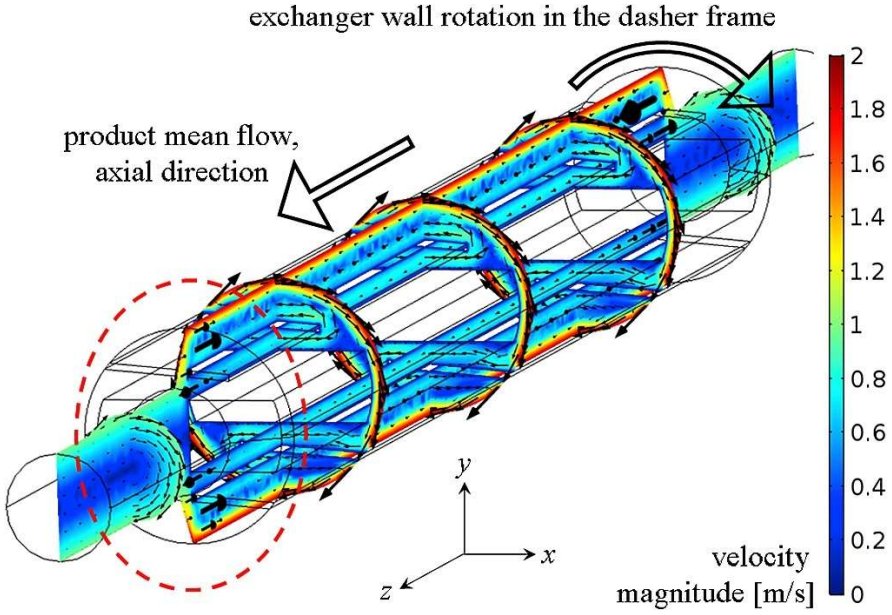

Figure 53. Velocity field in the SSHE, as predicted by the numerical model under reference operating conditions: $\dot{m}_{mix}$ = 50 kg/h, T_R = −15.3 °C and f_{rot} = 750 rpm. Velocity vectors presented in the plane YZ containing the axial direction are not in the same scale than those in the three planes XY crossing the axial direction.

Firstly, the velocity field is largely dominated by rotation: the highest velocities occur in the vicinity of the exchanger wall, and the maximal tangential velocity (1.97 m/s) is about 200 times higher than the mean axial velocity (about 0.01 m/s).

Secondly, the flow is confined between the exchanger wall, the dasher and the blades; as a consequence, changes of velocity direction are significant. The region indicated by the red ellipse in Figure 53 puts in evidence the occurrence of recirculation in the vicinity of the blades endings. Indeed, the occurrence of recirculation near the blades endings has been predicted by mathematical modeling of fluid flow in scraped surface heat exchangers (Duffy et al., 2007). Fluid parcels travelling between the dasher and the blades near the exchanger outlet are reoriented back towards the exchanger inlet, following pathways between the

blades and the wall. The reciprocal feature takes place near the exchanger inlet, where parcels coming between the dasher and the blades are reoriented back towards the exchanger outlet, between the blades and the wall. Such features are particularly important for the temperature axial distribution, because they foster mixing between fluid parcels experiencing different thermal histories. Indeed, near the exchanger inlet, colder parcels travelling between the dasher and the blades do encounter relatively warmer parcels just coming from the entrance of the inlet pipe (at 5°C), allowing a faster decrease of temperature than we might expect without such a recirculation.

Figure 54A to C displays the velocity, pressure and temperature profiles in the SSHE as predicted by the numerical model under the operating condition $\dot{m}_{mix}$ = 50 kg/h, T_R = -15.3°Cand f_{rot} = 750 rpm. In the left-hand side of Figure 54A, 8B and 8C, as well as in Figure 54D and 54E, the product flows from the left to the right, as indicated by the vector velocity in the inlet and the outlet pipes in Figure 54B.

From the rotating reference frame, the inner cylinder wall is perceived turning clockwise (right-hand side of Figure 54A, B, and C; the liquid flows from the annular space left by the dasher (**point 1**) towards the zone near the lower face of the blade (**point 2**). In this zone, the high-speed flow is blocked suddenly by the lower surface of the blade and immediately forced to change direction. This momentum accumulation yields a pressure increase in this region, whose maximum occurs where the blade encounters the wall. The region on the opposite side of the blade (**point 6**) experiences the opposite phenomena, with the pressure reaching its lowest value at the contact between the blade and the wall. These trends can be appreciated in the cross-section view of the pressure field in Figure 54B.

Therefore, from point 2, the fluid is forced to follow the lower surface of the blade (**point 3**), get around it (**point 4**) and follow the upper side of the blade (**point 5**) towards point 6. From there, the rotating wall forces the flow to change direction drastically (**point 7**) leading the fluid back to the opposite annular section (**point 1'**) where the sequence described before is repeated following the symmetry in the SSHE. It is noteworthy that the entire trajectory is carried out 12.5 times per second (for f_{rot} = 750 rpm).

The longitudinal view in the pressure profile shown in Figure 54B also indicates the axial flow direction in the SSHE. It can be observed that, inside the SSHE between the dasher and the blades (high-pressure zone, **point 9**), pressure increases from the inlet pipe towards the outlet pipe, reaching a maximum before the blades ending (z ~ 0.36 m). This forces the fluid in this zone to go back to the exchanger inlet promoting back-mixing. Between the blades and the wall (low-pressure zone, **point 10**) the opposite effect (decreasing pressure) directs the flow towards the outlet pipe. Near the blades ending (z > 0.36 m), where the pressure gradients are inversed, a recirculation zone is observed (**point 11**), as displayed in Figure 53.

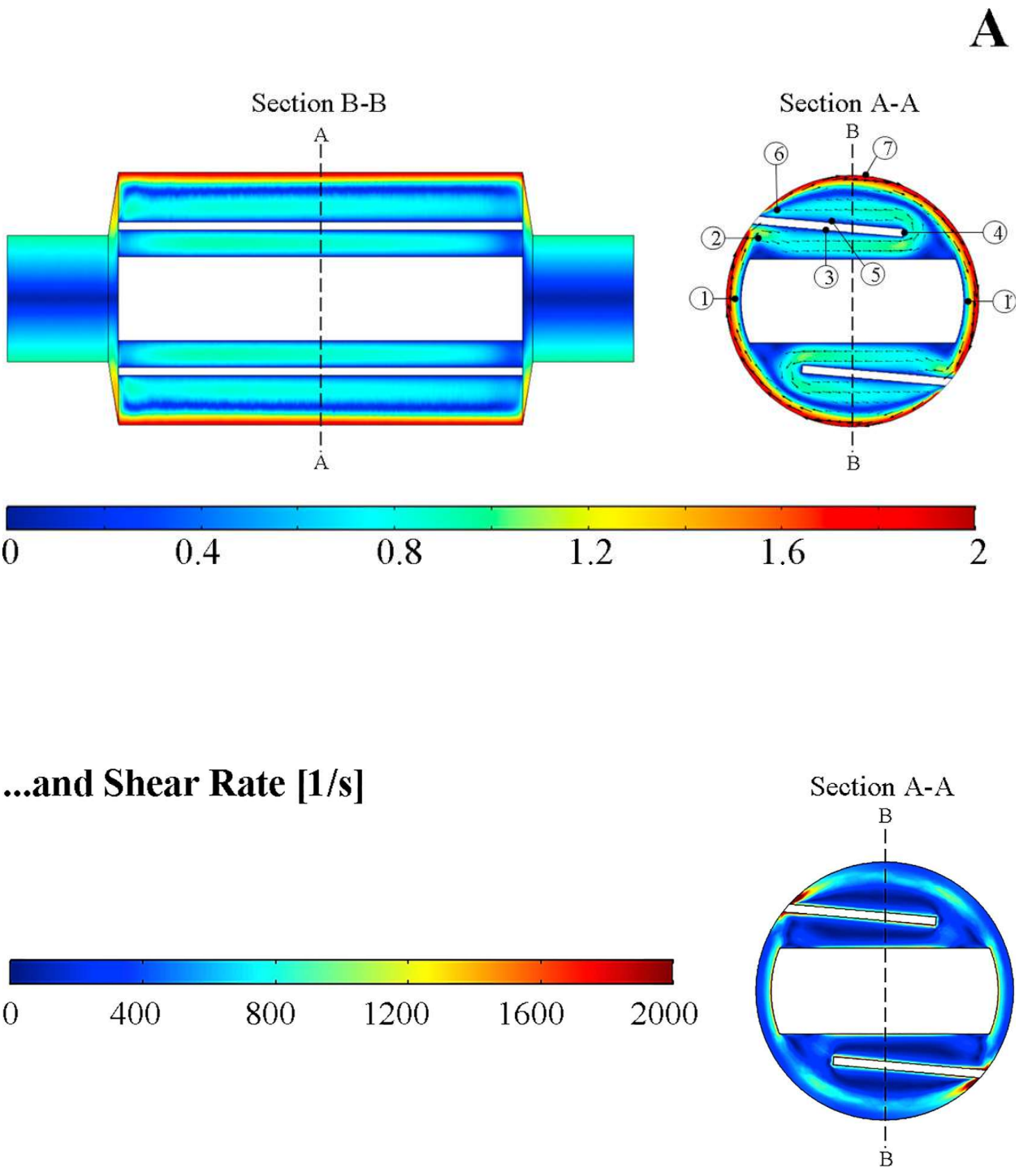

Figure 54. Views of the profiles in the SSHE as predicted by the numerical model under reference operating conditions: $\dot{m}_{mix}$ = 50 kg/h, T_R = −15.3 °C and f_{rot} = 750 rpm: **A**) velocity magnitude (top) and shear rate (bottom), **B**) pressure, **C**) temperature, **D**) enthalpy and ice fraction, and **E**) viscous dissipation rate.

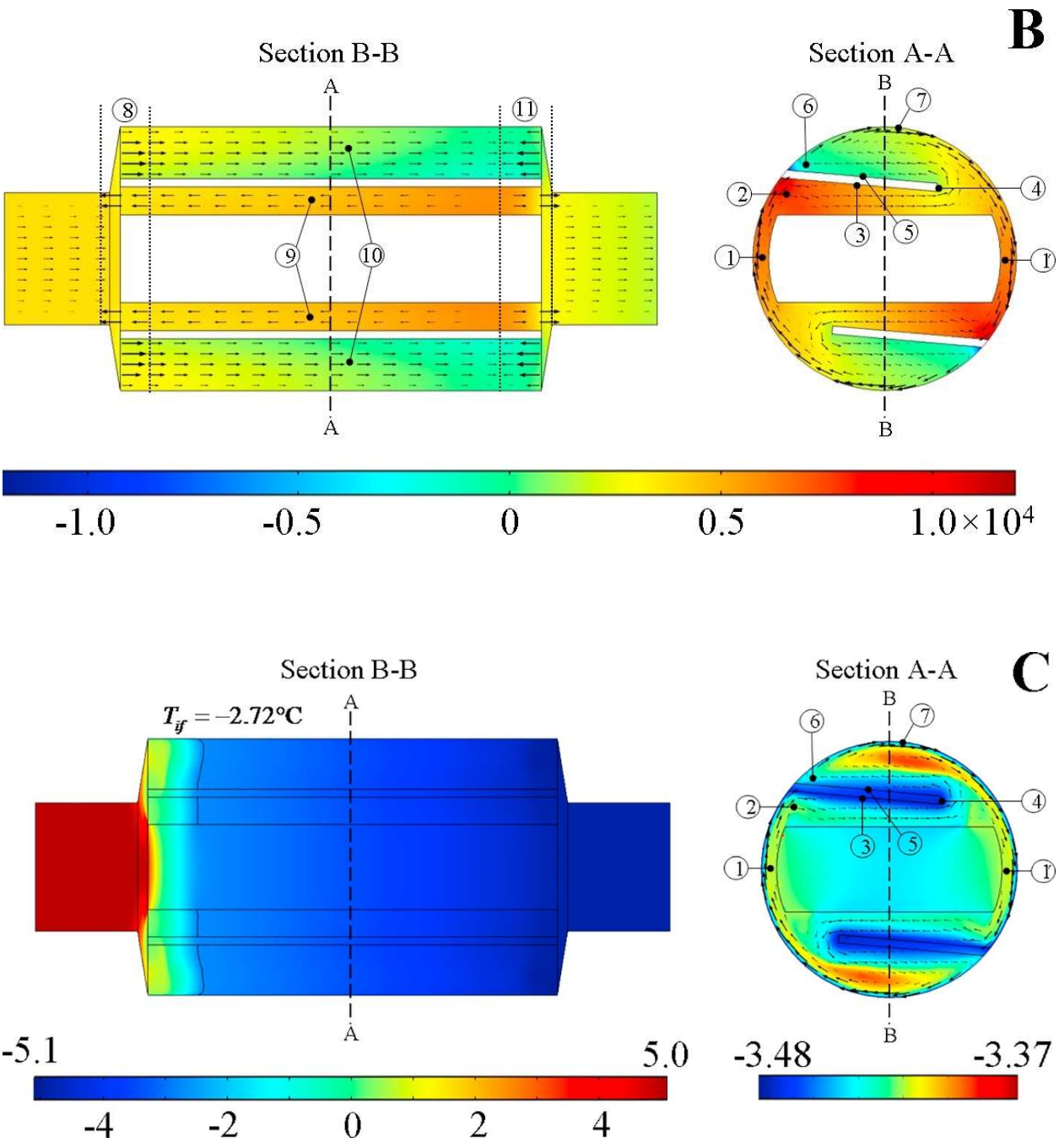

Figure 54. Continuation

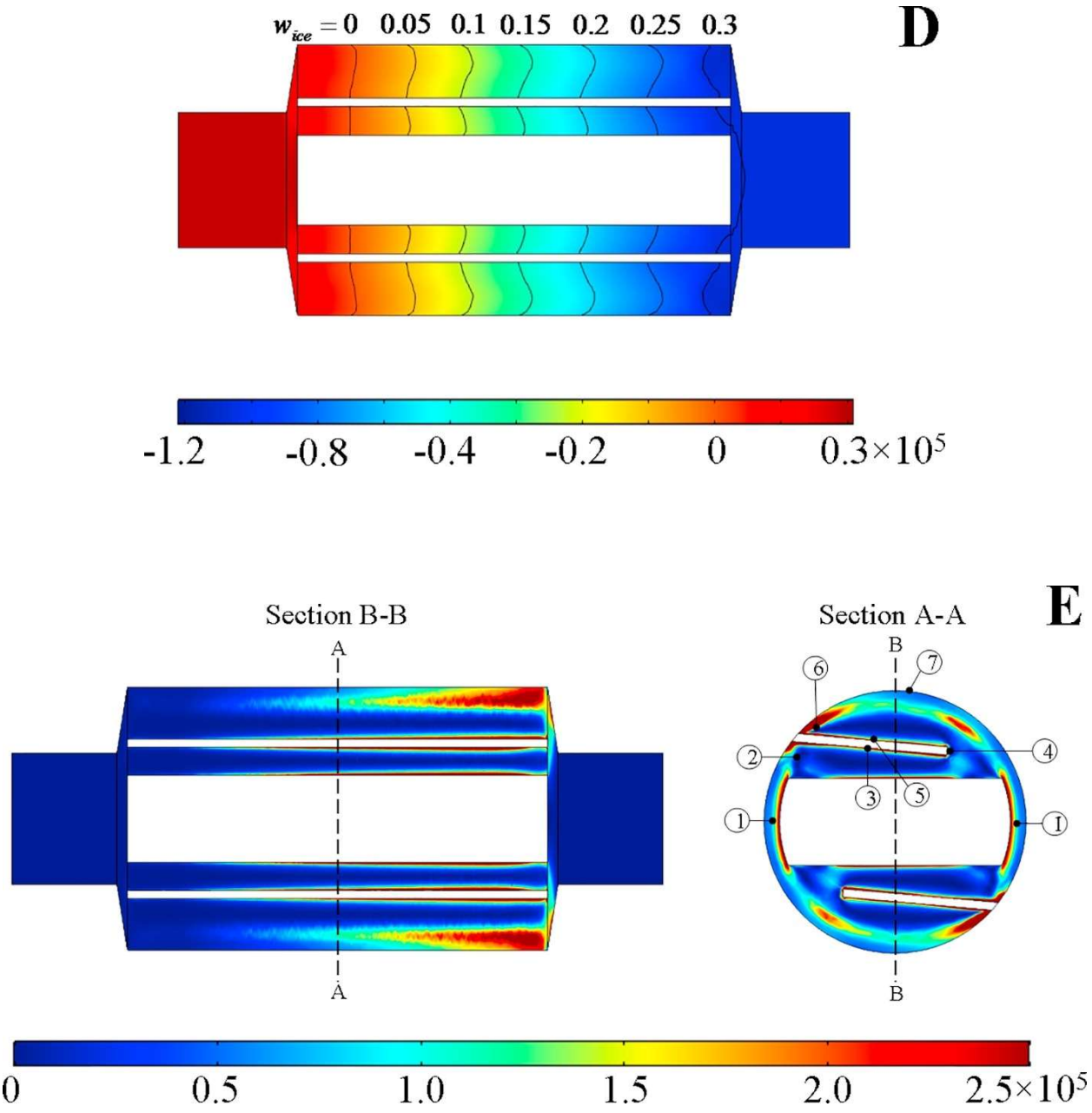

Figure 54. Continuation

The range of shear rate conditions in the SSHE is wide, actually from zero up to more than 2000 s^{-1}. On one hand, as suggested by the blue regions in the shear rate display of Figure 54A, the velocity field can exhibit quite "gentle" features (e.g. between the dasher and one blade), being associated with relatively low shear. On the other hand, shear rates are very high near the region where the blades touch the inner wall of the SSHE.

The volume-averaged value of the shear rate in the SSHE can indicate the typical shear conditions experienced by the sorbet while it undergoes progressive freezing. Considering the heat exchanger itself only, without the inlet and the outlet cylindrical pipes and bowls (see Figure 47A), the volume-averaged shear rate was about 420 s^{-1}. We are aware that such a value is near the higher limit of shear rates observed in the experiments conducted by Arellano et al. (2013c) (see section 6.3). The application of the rheological model developed by those authors is assumed to be satisfactory in most of the volume of the SSHE. Nevertheless, the lack of rheological data at high shear rate could impact the accuracy of velocity prediction in the region where the blades touch the inner wall of the SSHE.

The temperature profile in the exchanger is presented in Figure 54C. At the entrance of the inlet pipe, the temperature was assigned to 5°C, following the experimental condition in Arellano et al. (2013b). It can be observed a sharp temperature decrease in the entrance region of exchanger, down to the initial freezing temperature of the sorbet mix (-2.72°C, $w_{ice} = 0$). Such a decrease is most likely due to the inlet recirculation and the back-mixing observed between dasher and blade, which puts into contact frozen sorbet from the mid-section with the warmer fluid coming from the inlet pipe.

Once the initial freezing temperature is reached, the temperature decreases more slowly with axial coordinate. This could be explained by the higher energy required to freeze the sorbet mix once passed the initial freezing temperature, which can be better appreciated following the specific enthalpy of the sorbet presented in Figure 54D. It can be seen how inside the SSHE freezing an additional 5% of the sorbet mass required about the same amount of energy regardless of the location inside the exchanger.

Also, as a consequence of the predominant tangential component of the velocity and the fluid complex trajectory, the temperature variations in cross sections across the exchanger were found to be very small (less than 0.2°C) suggesting a strong radial mixing. The fluid cooled at the wall is carried out around the blades and mixed with the slightly warmer fluid in the zone between blades and the exchanger wall.

Globally, the cooling effect of the scraped wall is thwarted by viscous dissipation effects. The latter are the highest in the exit area, given that the lower the temperature the higher the consistency index, and so the apparent viscosity of the sorbet. Viscous dissipation profiles are shown in Figure 54E. As discussed above, the increased presence of ice because of lower temperatures increases the viscous dissipation near the end

of the SSHE. Also, viscous dissipation near the end of the SSHE. Also, viscous dissipation in caused by the friction of fluid changing direction radically (i.e. near the point 4) or friction with the solid elements in the exchanger, therefore on the dasher surface (i.e. point 1) or around the blades (i.e. points 3-6).

6.5.2 Comparison between experimental and simulated values

The experimental verification of numerical model predictions represents a complicated task in the case of coupled problems of rotating flow, heat transfer and product transformation. Model predictions of isothermal fluid flow without product transformation in SSHE have been compared with observations gathered through noninvasive techniques, like Magnetic Resonance Imaging with nonmagnetic and nonmetal exchangers (Wang et al., 1999), and Particle Image Velocimetry with exchangers with transparent walls (Crespí-Llorens et al., 2016; Stranzinger et al., 2001). These techniques cannot be applied to the SSHE here considered, whose walls are made of steel. The reliability of our modeling approach is hereafter assessed by comparing temperature predictions with in situ observations which were performed while running the SSHE. The interest on the temperature field can be justified by its determinant role on product transformation, and therefore on product rheology. Arellano et al. (2013b) have successfully employed wireless temperature sensors in order to monitor the temperature profile inside the SSHE under a variety of operating conditions; forthcoming paragraphs consider these measurements in assessing the bulk reliability of model predictions. Pressure drop measurements are unfortunately not available.

Figure 55 compares Arellano et al. (2013b)'s measurements (indicated by circles) with the temperature profile in the SSHE as predicted by the numerical model (black lines) under the operating conditions $\dot{m}_{mix}$ = 50 kg/h, T_R = -15.3°C and f_{rot} = 750 rpm. The left-most circle indicates the temperature 5°C prescribed at the entrance of the inlet pipe, upstream to the heat exchanger; the right-most circle indicates the temperature value observed at the exit of the outlet pipe, downstream to the heat exchanger. All the other four measurements correspond to positions inside the heat exchanger (see figure 2 of Arellano et al. (2013b)). The black line in displays in Figure 55A and B show temperature predictions obtained after setting to 15 W m^{-1} K^{-1} the thermal conductivity of solids and setting to 2500 W m^{-2} K^{-1} the heat transfer coefficient at the SSHE inner wall. Such a thermal conductivity is typical of stainless steel employed in food processing units, while this heat transfer coefficient value was estimated by Arellano et al. (2013a) after energy balance considerations and closure experiments conducted with the SSHE. Four results emerge from this comparison.

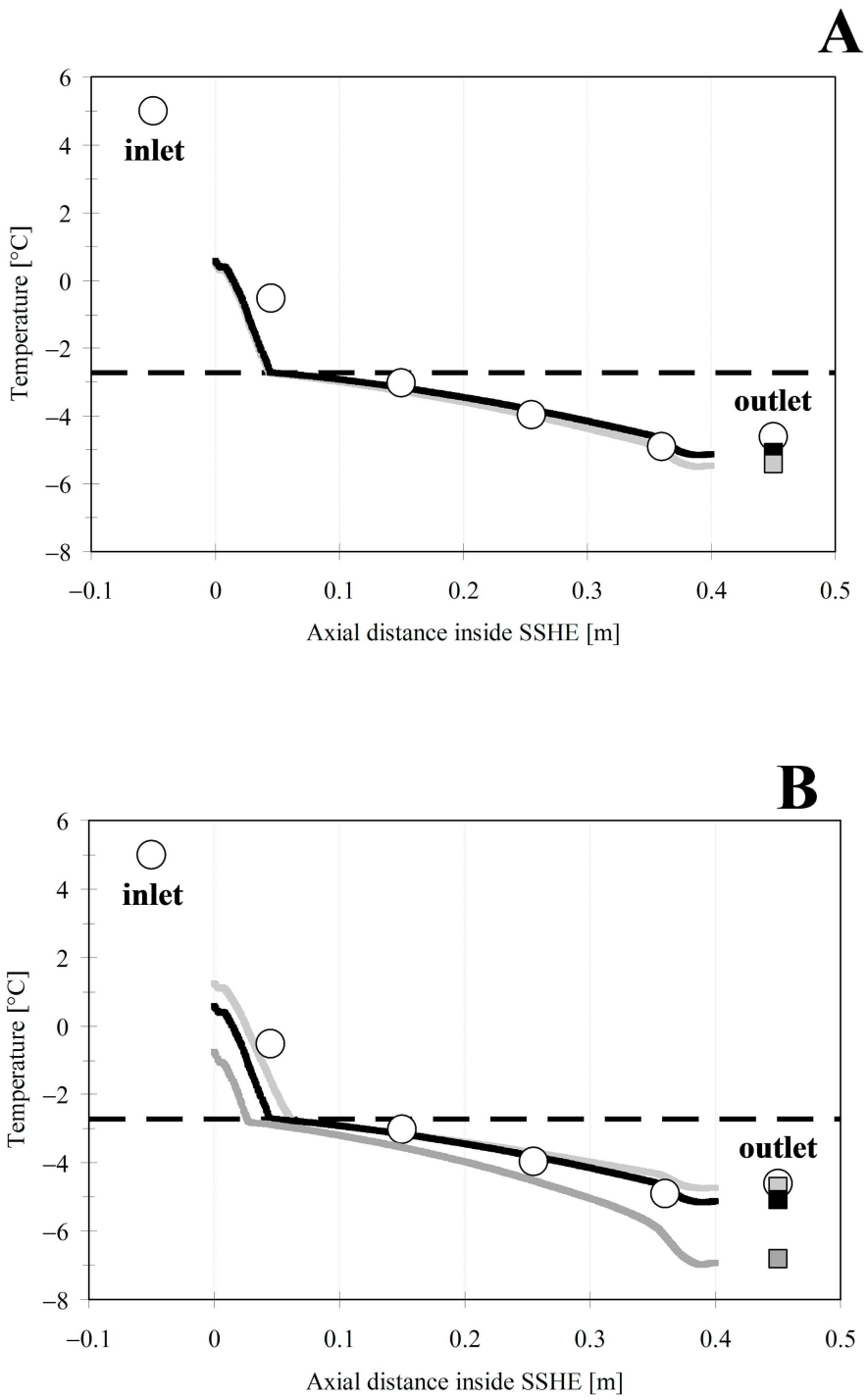

Figure 55. **A**) Measurements of temperature by Arellano et al. (2013b) at selected positions of the SSHE (circles) and temperature axial profiles predicted by the numerical model under reference operating conditions ($\dot{m}_{mix}$ = 50 kg/h, T_R = −15.3 °C and f_{rot} = 750 rpm), after setting the thermal conductivity of solids to 15 W m^{-1} K^{-1} (black line) and to zero (grey line). Squares indicate mean surface values of temperature as predicted by the numerical model at the exit of the outlet pipe. The dashed line indicates the initial freezing temperature. **B**) The same but setting the heat transfer coefficient at the SSHE inner wall to 2500 W m^{-2} K^{-1} (black line), to a value 20% larger (3000 W m^{-2} K^{-1}) (dark grey line) and to a value 20% smaller (2000 W.m^{-2} K^{-1}) (light grey line).

Firstly, the experimental temperature at the first measuring position inside the exchanger inlet (z = 0.045 m) is underestimated by the model; actually, this was the case for all the operating conditions considered in our study (see below). In the real SSHE pilot unit, as displayed in Figure 51A and B, the dasher is in contact with its support at the inlet bowl (the header), which in turn is in contact with fresh mix at higher temperature. This could lead to a non-negligible conductive heat transfer to the dasher, eventually reaching the temperature sensor. The predicted temperature profile cannot incorporate this phenomenon because the numerical model does not include the dasher supports.

Secondly, model predictions of the temperature profile follow the experimental temperature at the second, third and fourth measuring positions inside the SSHE: differences reach +/- 0.2°C, with no systematic sign. The temperature sensors are in contact with the dasher while being submerged in a liquid product which becomes colder towards the exchanger outlet.

Thirdly, the averaged value of the temperature at the exit of the outlet pipe (-5.1°C) agrees relatively well with the available measurement (-4.6°C). Such a level of agreement can be considered as satisfactory, given the sensibility of temperature predictions with respect to model parameters (see below) and the influence of phenomena potentially affecting the product temperature at the measuring position which were not included in the numerical model (like conduction through dasher supports).

Lastly, the initial freezing temperature constitutes a key value in the coupled phenomena represented by the numerical model. When temperatures decrease below -2.72°C, the sorbet thermal properties as well as its consistency coefficient experience a sharp increase (see Figure 50); as a consequence, both the fluid flow and the heat transfer are significantly affected, promoting a major decrease in the gradient of axial temperature near the dasher (see Figure 55).

Two sensitivity tests were conducted in order to evaluate the influence of key parameters on model predictions.

In building the numerical model, we have assumed a typical value for the thermal conductivity of the solid elements which were taken into account (dasher and blades). One may ask the importance of heat conduction in these solid elements on the predicted temperature. Figure 55A presents the results of a first sensitivity test: black and grey lines correspond to the temperature profiles after setting the thermal conductivity of solids to 15 W m^{-1} K^{-1} and to zero, respectively. The thermal conductivity of solids is many times greater than that for non-aerated sorbet (see Figure 50D); solid elements contribute to reduce temperature gradients within the SSHE. With no conduction in solids, the predicted temperature profile along the SSHE axis becomes slightly colder, from 0.1°C at the exchanger inlet (z = 0) up to about 0.35°C at its outlet (z = 0.4 m); the latter difference can be found also between the corresponding surface-averaged

temperatures at the exit of the outlet pipe (squares in Figure 55A). We can conclude that the influence of conduction in solids on the predicted temperature along the SSHE axis is relatively weak, because it exhibits the same order of magnitude than the difference between temperature measurements and predictions.

Figure 55B summarizes the results of a second sensitivity test with the numerical model, in order to assess the influence of the heat transfer coefficient assumed at the internal side of the SSHE inner cylinder wall. The black line displays the temperature profile obtained after setting this coefficient to 2500 W m^{-2} K^{-1}; dark-grey and light-grey lines correspond to results obtained after increasing and decreasing that value by 20%, respectively. After increasing the heat transfer coefficient, the liquid is exposed to more effective cooling while travelling in the SSHE. As a consequence, the predicted temperature profile along the SSHE axis becomes relatively colder, from -1.3°C at the exchanger inlet to -1.8°C at its outlet; hence, the initial freezing temperature is reached early (at about z = 0.025 m, see dark grey line in Figure 55B. Effects of opposite sign and smaller magnitude take place after decreasing the heat transfer coefficient. Therefore, the value 2500 W m^{-2} K^{-1} proposed by Arellano et al. (2013a) allows a reliable prediction of the product temperature.

The convective heat transfer resistance between the external side of the SSHE inner cylinder and the refrigerant fluid ($1/h_{outside}$) cannot be neglected. Indeed, such an assumption is equivalent to estimate $U = k_w/e_w \approx 7500$ W m^{-2} K^{-1} in equation (6.8). As demonstrated above, even for U = 3000 W m^{-2} K^{-1} the product temperature is largely underestimated.

In this CFD approach the heat transfer between the internal side of the wall and the product is directly calculated by the convection-conduction equation. Therefore no convective heat transfer coefficient required on this side of the SSHE inner cylinder. Nevertheless, the order of magnitude of a hypothetical coefficient can be estimated from model predictions. The averaged heat transfer coefficient between the liquid product and the internal side of the SSHE inner cylinder could be defined by

$$h_{inside} = \frac{\dot{m}\left(\hat{H}_{outlet} - \hat{H}_{inlet}\right)}{A_{wall}\left(\overline{T}_{wall} - \overline{T}\right)} \tag{6.17}$$

Where $\dot{m}$ is the product mass flow rate; $\hat{H}_{inlet}$ and $\hat{H}_{outlet}$ are specific enthalpy (J/kg) values at the SSHE inlet and outlet respectively; A_{wall} is heat exchange area, $\overline{T}_{wall}$ the averaged wall temperature, and $\overline{T}$ an averaged product temperature. The difficulty to define and to calculate such a coefficient comes from that, towards the SSHE outlet, the phase change of the product occurs under recirculation (see for instance Figure 53); the flow pattern is very far from plug flow. Therefore the logarithmic mean temperature difference between SSHE inlet and outlet cannot be applied. We choose to use the surface averaged temperature of the product in the cylindrical part of the SSHE (say, excluding the inlet and outlet bowls). In the case of reference

operating conditions ($\dot{m}_{mix}$ = 50 kg/h, T_R = -15.3°C and f_{rot} = 750 rpm), we obtained $\overline{T}_{wall}$ = -3.49°C and $\overline{T}$ = -3.43°C; the difference is very small, about 0.06°C. Similar small differences in temperature were observed at a typical cross-section of the SSHE (Figure 54C, right display): the range of temperature is about 0.1°C. These findings denote that either the radial mixing or the heat transfer between wall and product are very efficient. Equation (6.17) provides for the "internal" heat transfer coefficient (above 10^5 W m^{-2} K^{-1}) which appears too large compared to the "external" one obtained from equation (6.8): $h_{outside} = \frac{1}{1/U - e_w/k_w} \approx$ 3750 W m^{-2} K^{-1}.

At this stage it is difficult to propose a general correlation for the inside heat transfer coefficient, notably because only one product was considered. At least, products with different initial freezing point and consistency should be tested and/or simulated.

6.5.3 Sensibility to mesh refinement

The representation of the gradients of state variables in the numerical model (velocity, pressure, temperature) is expected to become progressively finer as the mesh resolution increases. Its influence on temperature predictions was evaluated by comparing results obtained with three meshes, constituted of increasing number of elements in the whole computational domain (6.5×10^5, 1.5×10^6 and 3.5×10^6 elements). These meshes were built as described above and then used for solving the problem under reference operating conditions ($\dot{m}_{mix}$ = 50 kg/h, T_R = -15.3°C and f_{rot} = 750 rpm).

Figure 56 compares Arellano et al. (2013b)'s measurements (indicated by circles) with the temperature profiles in the SSHE as predicted by the numerical model after using these three meshes. The three temperature profiles behaved similarly in the central region of the heat exchanger ($0.05 < z < 0.35$ m), with differences below 0.1°C with respect to the results achieved with the intermediate mesh (1.5×10^6 elements). After increasing the mesh resolution (3.5×10^6 elements), the predicted temperature profile became slightly warmer near the exchanger inlet ($z < 0.05$ m); as a consequence, the initial freezing temperature is reached a few millimeters later than with the intermediate mesh. Effects of opposite sign and similar magnitude take place after decreasing the mesh resolution (6.5×10^5 elements). Weaker effects can be observed, in both cases, near the exchanger outlet ($z > 0.35$ m). The whole set of temperature predictions is coherent with Arellano et al. (2013b)'s measurements.

6.5.4 Effect of rotation frequency

The influence of the dasher rotation frequency was assessed by employing the numerical model and comparing its predictions with the observations reported by Arellano et al. (2013b) at 545, 750 and 1000 rpm. The results on the line through the temperature sensors are presented in Figure 57. The simulated values are in quite good agreement with the experimental data.

It is noteworthy that inside the exchanger the experimental data were already quite similar for all frequencies, and as well, the simulated values presented the same behavior. This could be due to two opposing effects: on one hand, an increase on the rotation frequency increases the heat transfer which tends to decrease fluid temperature; on the other hand, an increase in the rotation frequency increases the viscous dissipation in the fluid leading to higher temperatures.

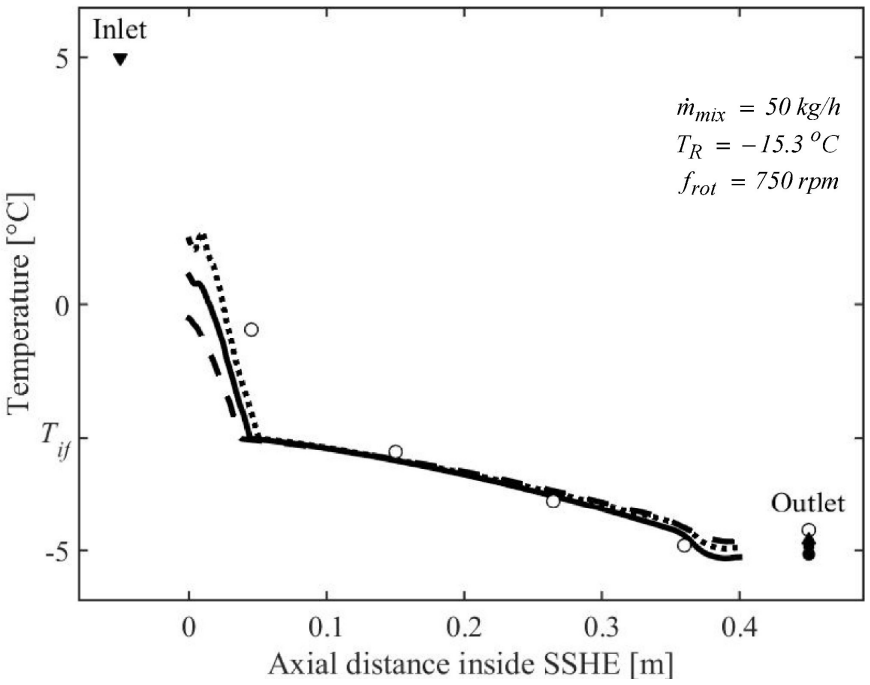

Figure 56. Measurements of temperature by Arellano et al. (2013b) at selected positions of the SSHE (circles) and temperature axial profiles predicted by the numerical model under reference operating conditions ($\dot{m}_{mix}$ = 50 kg/h, T_R = −15.3 °C and f_{rot} = 750 rpm), after using three meshes constituted by an increasing number of elements: (--) 6.5×10^5, (—) 1.5×10^6 and (▪▪▪) 3.5×10^6 elements. Corresponding values of the surface-averaged value of predicted temperatures at the exit of the outlet pipe are also indicated, for (▲) 6.5×10^5, (●) 1.5×10^6 and (■) 3.5×10^6 elements.

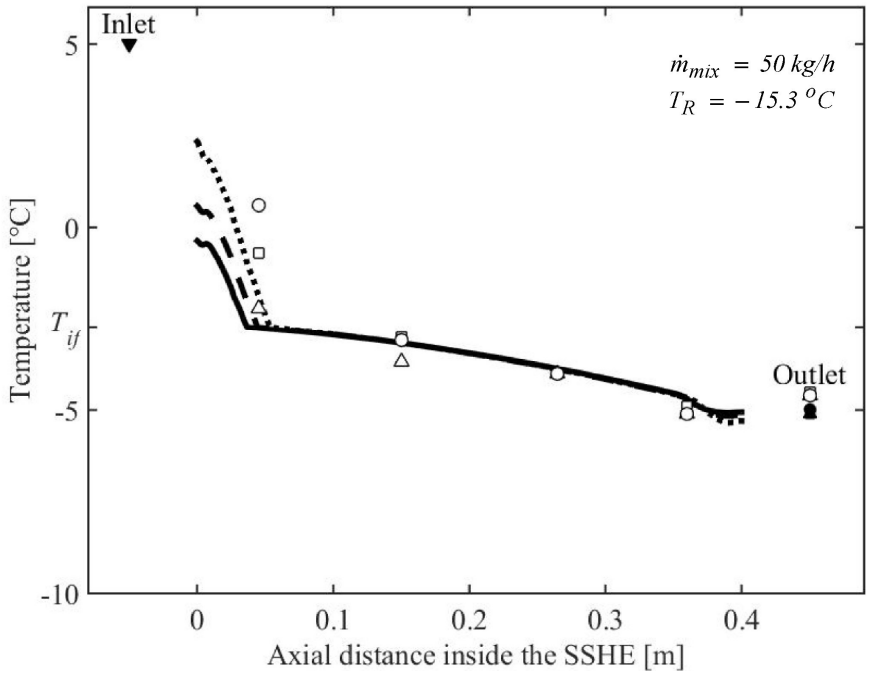

Figure 57. Effect of the dasher rotation frequency on the temperature profile along the exchanger: (▼) prescribed value at the inlet, for all the operating conditions (5 °C); measured values for (Δ) f_{rot} = 545 rpm, (□) f_{rot} = 750 rpm, and (○) f_{rot} = 1000 rpm; predicted profiles for (▪▪▪) f_{rot} = 545 rpm, (– –) f_{rot} = 750 rpm, and (—) f_{rot} = 1000 rpm; and surface-averaged values at the exit for (▲) f_{rot} = 545 rpm, (■) f_{rot} = 750 rpm, and (●) f_{rot} = 1000 rpm.

6.5.5 Effect of refrigerant temperature

The influence of the refrigerant temperature on the profiles following the sensors can be appreciated in Figure 58. The profiles for the curves at $T_R \geq$ -15.3°C show a good agreement with the experimental values while the profile for T_R = -20.1°C did not. However, the general trend of the profile is preserved; a sharp decrease in temperature is observed near the entrance of the SSHE until the initial freezing temperature of the sorbet mix, followed by a slow decrease for most of the exchanger and a small decrease near the exit of the SSHE (at about z = 0.36 m) due to the exit recirculation. Logically, the point at which the initial freezing temperature is reached is closer to the entrance for lower refrigerant temperature.

The lack of agreement at T_R = -20.1°C could be explained by the fact that for low refrigerant temperatures, the wall temperature along the SSHE could reach values lower than -6°C. As presented in Figure 50B, experimental values for sorbet consistency index are only available until this temperature. For temperatures below this point, the consistency index was extrapolated linearly in this work; however, lower temperatures in the mix would mean higher ice contents that strongly modify the apparent rheological properties of sorbet (i.e. increasing the consistency index exponentially rather than linearly). This lack of extrapolation capacity could lead to miscalculations of the velocity profile in the exchanger and

a strong under-prediction of the viscous dissipation effect in the simulations that, even if only located at the exit of the SSHE, could influence the results all over the exchanger due to the back-mixing observed.

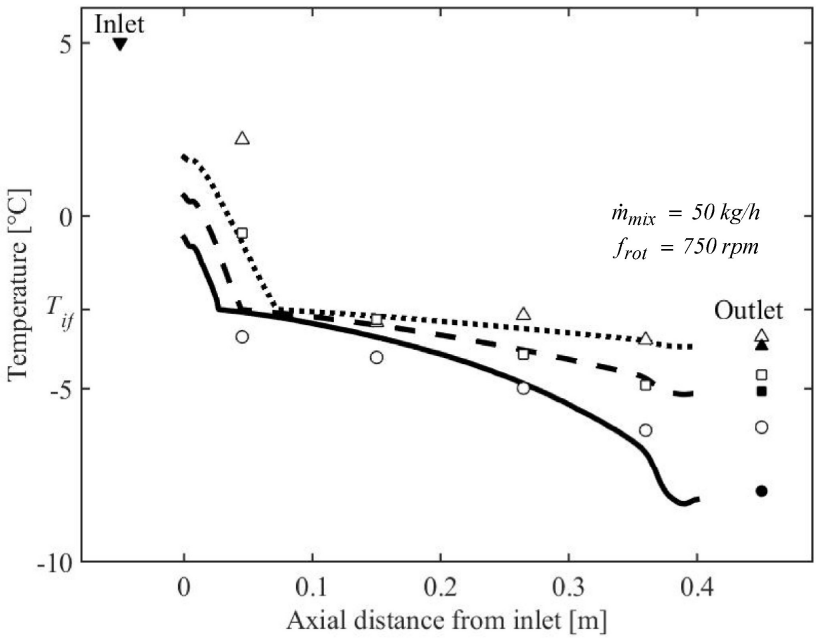

Figure 58. Effect of the refrigerant evaporation temperature on the temperature profile along the exchanger: (▼) prescribed value at the inlet, for all the operating conditions (5 °C); measured values for (Δ) = −10.3 °C, (□) = −15.3 °C, and (○) = −20.1 °C; predicted profiles for (▪▪▪) = −10.3 °C, (– –) = −15.3 °C, and (—) = −20.1 °C; and surface-averaged values at the exit for (▲) = −10.3 °C, (■) = −15.3 °C, and (●) = −20.1 °C.

6.5.6 Effect of mix flow rate

The influence of the mix flow rate was analyzed through simulations carried out at the conditions that were adopted by Arellano et al. (2013b): $\dot{m}_{mix}$ = 25, 50 and 75 kg/h. Results over the line that follows the position of the temperature sensors are shown in Figure 59. The profiles calculated at $\dot{m}_{mix}$ ≥ 50 kg/h are in good agreement with the experimental data while the profile at $\dot{m}_{mix}$ = 25 kg/h shows a good agreement until z = 0.2 m after which a strong decrease in temperature is observed. This could be explained since lower mix flow rates leads to an increase in the residence time within the exchanger, which in turn leads to fluid temperatures reaching values closer to the refrigerant temperature (the outlet temperature calculated value for this simulation was -11.1°C). As explained before, there is an uncertainty on the rheological behavior of the sorbet under such conditions; that could affect the prediction of velocity profiles and lead to underestimate the viscous dissipation effect in the exchanger.

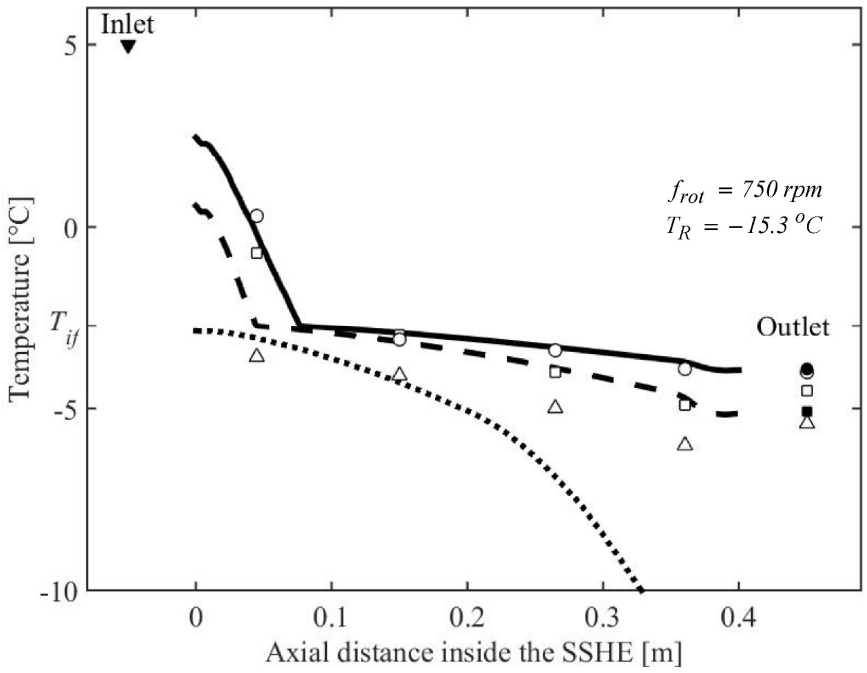

Figure 59. Effect of the mix mass flow rate on the temperature profile along the exchanger: (▼) prescribed value at the inlet, for all the operating conditions (5 °C); measured values for (Δ) $\dot{m}_{mix}$ = 25 kg/h, (□) $\dot{m}_{mix}$ = 50 kg/h, and (○) $\dot{m}_{mix}$ = 75 kg/h; predicted profiles for (▪▪▪) $\dot{m}_{mix}$ = 25 kg/h, (– –) $\dot{m}_{mix}$ = 50 kg/h, and (▬) $\dot{m}_{mix}$ = 75 kg/h; and surface-averaged values at the exit for (■) $\dot{m}_{mix}$ = 50 kg/h and (●) $\dot{m}_{mix}$ = 75 kg/h.

6.6 Conclusion and perspectives

The production of non-aerated sorbet inside a scraped surface heat exchanger was studied with the help of a 3D numerical model able to solve the coupled problem of fluid flow, heat transfer and product transformation. Fluid flow is very complex in the volume confined by the dasher, the blades and the wall of the SSHE inner cylinder. Fluid flow drives thermal convection which determines ice fraction and finally rheology evolution along the SSHE. Rheology, in turn, influences fluid flow. Model predictions compared favorably with available measurements when temperature remains in the range for which the sorbet rheology was available, indicating the global consistency of the modeling approach. Sensitivity tests allowed us to assess the influence of key model parameters. On one hand, the influence of the heat transfer coefficient at the exchanger wall is relatively high; after increasing that coefficient by 20%, the predicted temperatures near the SSHE outlet decreased by about -1.8°C. Such an increase of the heat transfer coefficient could be achieved by intensifying the heat exchange between the evaporating refrigerant and the heat exchanger cylinder. In the scope of future experimental campaigns with the pilot unit here considered, we strongly recommend the inclusion of temperature monitoring at the inner wall of the SSHE as a necessary step for a finer estimation of that coefficient. On the other hand, the influence of conduction

in solids (dasher, blades) is relatively weak: outlet temperatures decreased by 0.35°C when conduction in solids was ignored. Reducing the conduction, by using a hollow dasher for example, is therefore expected to slightly improve the SSHE performance.

Post-processing of model predictions helped us to extend the understanding of phenomena under consideration. For instance, the occurrence of recirculation near the blades endings allows backflow from the outlet region. This backflow brings cold, high ice-content, fluid near to the inlet. This explains why temperatures between the blades and the dasher in the inlet region are much lower than the value prescribed at the SSHE entrance (5°C, see for instance Figure 55). This aspect would not be predicted with a 1D model assuming plug-flow and an overall uniform heat transfer coefficient. The temperature field summarizes the strong coupling that occurs between the phenomena in the SSHE: on one hand, when the temperature decreases below the initial freezing value -2.72°C, sharp changes affects the product properties, including its rheology; on the other hand, in addition to rotation and mean axial flow, the product rheology drives the fluid motion and hence the convective flux of heat. We argue that only the fully coupled solution of this challenging problem can provide realistic predictions.

In further work, on the base on the modeling of velocity and temperature fields, CFD will be used to predict ice crystals growth and bubble fragmentation. For ice crystal growth, backflow will be also crucial because it seeds the inlet region with ice crystals, hence avoiding super-cooling. Bubble fragmentation in aerated sorbet mainly depends on shear rate, elongation rate and apparent viscosity of the surrounding fluid, which can be provided by the present work. Nevertheless, it should be kept in mind that experimental rheology data should be completed for high shear rate and ice content, because it could affect bubble fragmentation prediction. This way, 3D modeling of the coupled relevant phenomena could be really helpful for industrial applications.

Looking forward, we focus our final words on the necessity of a broader experimental dataset than the one available to the present study. Firstly, pressure drop measurements should be included, as a way to validate the model predictions of complex fluid flow occurring under heat transfer and product transformation in the SSHE. Secondly, other operating conditions and product properties should be considered, for instance the initial freezing point. Beyond the opportunity for complementary assessment of model predictions, the availability of a broad dataset is necessary to identify heat transfer correlations in SSHE during crystallization. Recent efforts have been devoted on this difficult subject (e.g. Rainieri et al. (2014); Saraceno et al. (2011)). Lastly, the product rheology must be fully characterized, as a way to improve the reliability of model predictions under particular operating conditions (low refrigerant fluid temperature, low mass flow rate). Such an enhanced characterization should include higher shear rates and ice contents.

Nomenclature

A_{wall}	heat exchange area (m)
c_p	heat capacity (J mol^{-1} K^{-1})
C , C_1 , C_2	dimensionless parameters (-)
C_p	apparent specific heat capacity (J mol^{-1} K^{-1})
e_w	wall thickness of the SSHE inner cylinder (m)
f_{rot}	frequency of rotation (rev/s)
$h_{outside}$	heat transfer coefficient, external side of SSHE inner wall (W m^{-2} K^{-1})
$\hat{H}_{inlet}$, $\hat{H}_{outlet}$	specific enthalpies at SSHE inlet and outlet (J kg^{-1})
k	thermal conductivity of product (W m^{-1} K^{-1})
k_w	thermal conductivity of stainless steel wall (W m^{-1} K^{-1})
K	consistency index (Pa s^n)
$\dot{m}$	mass flow rate (kg s^{-1})
M	molar mass (kg mol^{-1})
n	flow behavior exponent (-)
p	pressure (Pa)
$\vec{q}$	conductive heat transfer vector (W m^{-2})
$\vec{r}$	position vector
r	radial component of the position vector (m)
r_{pipe}	pipe radius (heat exchanger cylinder) (m)
R	ideal gas constant (8.314 J mol^{-1} K^{-1})
T	temperature (K)
T_R	refrigerant fluid evaporating temperature (K)
U	global heat transfer coefficient (W m^{-2} K^{-1})
$\vec{u}$	velocity vector in the Galilean frame (m s^{-1})
$\vec{v}$	velocity vector in the rotating frame (m s^{-1})
w	mass fraction (-)
w_s^*	solute mass fraction at saturation (-), see eq. (9)
x_w	water molar fraction at saturation (-)
z	axial component of the position vector (m)

Greek symbols

$\Delta h_{f,mp}$	ice-water heat of fusion (J mol^{-1}), see eq. (9)
ΔH_f	specific heat of fusion of ice (J kg^{-1}), see eq. (14)

$\vec{\Omega}_{rotor}$	angular velocity vector (rad.s^{-1})
ρ	density (kg m^{-3})
$\bar{\tau}$	viscous stress tensor (Pa)

Subscripts

0	initial
i	ice
if	initial freezing
mp	pure-water melting-point
s	solute
w	water

References

Abichandani, H., Sarma, S.C., Heldman, D.R., (1986). Hydrodynamics and heat transfer in liquid full scraped surface heat exchangers — A review. Journal of Food Process Engineering 9(2), 121-141.

Arellano, M., Benkhelifa, H., Alvarez, G., Flick, D., (2013a). Coupling population balance and residence time distribution for the ice crystallization modeling in a scraped surface heat exchanger. Chemical Engineering Science 102, 502-513.

Arellano, M., Benkhelifa, H., Alvarez, G., Flick, D., (2013b). Experimental study and modelling of the residence time distribution in a scraped surface heat exchanger during sorbet freezing. Journal of Food Engineering 117(1), 14-25.

Arellano, M., Flick, D., Benkhelifa, H., Alvarez, G., (2013c). Rheological characterisation of sorbet using pipe rheometry during the freezing process. Journal of Food Engineering 119(3), 385-394.

Baccar, M., Abid, M.S., (1997). Numerical analysis of three-dimensional flow and thermal behaviour in a scraped-surface heat exchanger. Revue Générale de Thermique 36(10), 782-790.

Baccar, M., Abid, M.S., (1999). Simulation numérique des comportements hydrodynamiques et thermiques des échangeurs racleurs opérant en régime turbulent. International Journal of Thermal Sciences 38(7), 634-644.

Błasiak, P., Pietrowicz, S., (2016). Towards a better understanding of 2D thermal-flow processes in a scraped surface heat exchanger. International Journal of Heat and Mass Transfer 98, 240-256.

Boccardi, G., Celata, G.P., Lazzarini, R., Saraceno, L., Trinchieri, R., (2010). Development of a heat transfer correlation for a Scraped-Surface Heat Exchanger. Applied Thermal Engineering 30(10), 1101-1106.

Bongers, P.M.M., (2006). A heat transfer model of a scraped surface heat exchanger for ice cream, in: Marquardt, W., Pantelides, C. (Eds.), *Computer Aided Chemical Engineering*. Elsevier, pp. 539-544.

Casenave, C., Dochain, D., Alvarez, G., Arellano, M., Benkhelifa, H., Leducq, D., (2013). Control of a nonlinear ice cream crystallization process. IFAC Proceedings Volumes 46(23), 717-722.

Casenave, C., Dochain, D., Alvarez, G., Arellano, M., Benkhelifa, H., Leducq, D., (2014). Model identification and reduction for the control of an ice cream crystallization process. Chemical Engineering Science 119, 274-287.

Cogné, C., Andrieu, J., Laurent, P., Besson, A., Nocquet, J., (2003). Experimental data and modelling of thermal properties of ice creams. Journal of Food Engineering 58(4), 331-341.

Cook, K.L.K., Hartel, R.W., (2010). Mechanisms of Ice Crystallization in Ice Cream Production. Comprehensive Reviews in Food Science and Food Safety 9(2), 213-222.

Crespí-Llorens, D., Vicente, P., Viedma, A., (2016). Flow pattern of non-Newtonian fluids in reciprocating scraped surface heat exchangers. Experimental Thermal and Fluid Science 76, 306-323.

Choi, Y., Okos, M.R., (1986). Effects of temperature and composition on the thermal properties of foods, in: Maguer, M.L., Jelen, P. (Eds.), *Food Engineering and Process Applications: Transport phenomena*, Vol. 1, Transport Phenomena ed. Elsevier Applied Science Publishers, London.

D'Addio, L., Carotenuto, C., Di Natale, F., Nigro, R., (2013). Heating and cooling of hazelnut paste in alternate blades scraped surface heat exchangers. Journal of Food Engineering 115(2), 182-189.

Dehkordi, K.S., Fazilati, M.A., Hajatzadeh, A., (2015). Surface Scraped Heat Exchanger for cooling Newtonian fluids and enhancing its heat transfer characteristics, a review and a numerical approach. Applied Thermal Engineering 87, 56-65.

Dorneanu, B., Bildea, C.S., Grievink, J., Bongers, P.M., (2009). A first-principles model for the freezing step in ice cream manufacture, in: Jacek, J., Jan, T. (Eds.), *Computer Aided Chemical Engineering*. Elsevier, pp. 171-176.

Duffy, B.R., Wilson, S.K., Lee, M.E.M., (2007). A mathematical model of fluid flow in a scraped-surface heat exchanger. Journal of Engineering Mathematics 57(4), 381-405.

Dumont, E., Fayolle, F., Legrand, J., (2000a). Electrodiffusional wall shear rate analysis in scraped surface heat exchanger. AIChE Journal 46(6), 1138-1148.

Dumont, E., Fayolle, F., Legrand, J., (2000b). Flow regimes and wall shear rates determination within a scraped surface heat exchanger. Journal of Food Engineering 45(4), 195-207.

Goff, H.D., Hartel, R.W., (2013). *Ice Cream*. Springer US.

González-Ramírez, J.E., Leducq, D., Arellano, M., Alvarez, G., (2013). Energy consumption optimization of a continuous ice cream process. Energy Conversion and Management 70, 230-238.

González Ramírez, J.E., (2012). Contribution au contrôle par la modélisation d'un procédé de cristallisation en continu. AgroParisTech, Paris, p. 151.

González Ramírez, J.E., Leducq, D., Arellano, M., Álvarez, G., (2013). Modelo de un proceso de cristalización continua de un sorbete por medio de la metodología de momentos. Revista Internacional de Métodos Numéricos para Cálculo y Diseño en Ingeniería 29(4), 215-224.

Härröd, M., (1986). Scraped surface heat exchangers. Journal of Food Process Engineering 9(1), 1-62.

Lakhdar, M.B., Cerecero, R., Alvarez, G., Guilpart, J., Flick, D., Lallemand, A., (2005). Heat transfer with freezing in a scraped surface heat exchanger. Applied Thermal Engineering 25(1), 45-60.

Lian, G., Moore, S., Heeney, L., (2006). Population balance and computational fluid dynamics modelling of ice crystallisation in a scraped surface freezer. Chemical Engineering Science 61(23), 7819-7826.

Martínez, D.S., Solano, J.P., Illán, F., Viedma, A., (2014). Analysis of heat transfer phenomena during ice slurry production in scraped surface plate heat exchangers. International Journal of Refrigeration 48, 221-232.

Qin, F., Chen, X.D., Ramachandra, S., Free, K., (2006). Heat transfer and power consumption in a scraped-surface heat exchanger while freezing aqueous solutions. Separation and Purification Technology 48(2), 150-158.

Qin, F.G.F., Chen, X.D., Russell, A.B., (2003). Heat transfer at the subcooled-scraped surface with/without phase change. AIChE Journal 49(8), 1947-1955.

Rainieri, S., Bozzoli, F., Cattani, L., Vocale, P., (2014). Parameter estimation applied to the heat transfer characterisation of Scraped Surface Heat Exchangers for food applications. Journal of Food Engineering 125, 147-156.

Rao, C.S., Hartel, R.W., (2006). Scraped Surface Heat Exchangers. Critical Reviews in Food Science and Nutrition 46(3), 207-219.

Reiser, P., Birch, G.G., Mathlouthi, M., (2012). Physical properties, in: Mathlouthi, M., Reiser, P. (Eds.), *Sucrose: Properties and Applications*. Springer-Science, pp. 186 - 223.

Saraceno, L., Boccardi, G., Celata, G.P., Lazzarini, R., Trinchieri, R., (2011). Development of two heat transfer correlations for a scraped surface heat exchanger in an ice-cream machine. Applied Thermal Engineering 31(17–18), 4106-4112.

Schenk, O., Gärtner, K., (2004). Solving unsymmetric sparse systems of linear equations with PARDISO. Future Generation Computer Systems 20(3), 475-487.

Skelland, A.H.P., (1958). Correlation of scraped-film heat transfer in the votator. Chemical Engineering Science 7(3), 166-175.

Stranzinger, M., Feigl, K., Windhab, E., (2001). Non-Newtonian flow behaviour in narrow annular gap reactors. Chemical Engineering Science 56(11), 3347-3363.

Trommelen, A.M., Beek, W.J., Van De Westelaken, H.C., (1971). A mechanism for heat transfer in a Votator-type scraped-surface heat exchanger. Chemical Engineering Science 26(12), 1987-2001.

Wang, W.E.I., Walton, J.H., McCarthy, K.L., (1999). Flow profiles of power law fluids in scraped surface heat exchanger geometry using MRI. Journal of Food Process Engineering 22(1), 11-27.

Wang, W.E.I., Walton, J.H., McCarthy, K.L., (2000). Mixing in scraped surface heat exchanger geometry using MRI. Journal of Food Process Engineering 23(6), 403-418.

Yataghene, M., Fayolle, F., Legrand, J., (2009). Experimental and numerical analysis of heat transfer including viscous dissipation in a scraped surface heat exchanger. Chemical Engineering and Processing: Process Intensification 48(10), 1447-1458.

Yataghene, M., Francine, F., Jack, L., (2011). Flow patterns analysis using experimental PIV technique inside scraped surface heat exchanger in continuous flow condition. Applied Thermal Engineering 31(14–15), 2855-2868.

Yataghene, M., Legrand, J., (2013). A 3D-CFD model thermal analysis within a scraped surface heat exchanger. Computers & Fluids 71, 380-399.

Yataghene, M., Pruvost, J., Fayolle, F., Legrand, J., (2008). CFD analysis of the flow pattern and local shear rate in a scraped surface heat exchanger. Chemical Engineering and Processing: Process Intensification 47(9–10), 1550-1561.

Zimmerman, W.B.J., (2006). *Multiphysics Modeling with Finite Element Methods*.

7. Prediction of bubble fragmentation during sorbet production in a scraped surface heat exchanger

Presented at the International Conference on Food and Biosystems engineering (FABE) June 14- 16TH 2017 in Rhodes island, Greece

Abstract

Complex phenomena occur during production of sorbet in a scraped surface heat exchanger: fluid flow, heat transfer, phase change (ice crystallization), rheological modification and fragmentation of air bubbles. In a previous work, all these coupled phenomena except bubble fragmentation were simulated through a computational fluid dynamics (CFD) model. The objective of the present work is to predict the bubble break-up. Locally, the critical radius for bubble break-up can be estimated as a function of the shear rate, the extension rate, the apparent viscosity of the 'continuous' phase, the viscosity of the gas and the surface tension, by using correlations based on the capillary number. The continuous phase surrounding the bubbles is in fact constituted by a concentrated liquid and ice crystals; its non-Newtonian rheology sharply depends on the ice mass fraction, which in turn depends on temperature. The CFD simulation allowed analyzing all the parameters influencing the critical radius. It appears that the smallest bubbles are generated a) near the contact between the blades and the scraped surface where the highest shear rate is reached, and b) in the coldest region (near to the outlet) where the continuous phase has the maximum apparent viscosity. The order of magnitude of the largest bubbles predicted by CFD corresponds to the observed values.

Keywords

Crystallization, air bubbles, fragmentation, scraped surface heat exchanger, sorbet

7.1 Introduction

Fragmentation of air bubbles inside the Scraped Surface Heat Exchanger (SSHE) of a sorbet freezer determines the texture of the final product. The air is most often introduced at the inlet of the SSHE together with the mix by a simple T-shaped tube and gives origin to large bubbles (radius around 1 mm). The fragmentation of these large bubbles is due to the local flow strength: shear rate and/or extension rate. For

highly viscous flow, the deformation and break-up of a bubble is governed by the ratio of the viscous forces acting to deform the bubble and the interfacial forces acting to restore the spherical shape (Risso, 2000). This dimensionless ratio is the capillary number:

$$Ca = \frac{\mu\dot{\gamma}}{\sigma} r \tag{7.1}$$

where μ is the viscosity of the medium surrounding the bubble, $\dot{\gamma}$ the shear rate, σ the surface tension and r the bubble radius. If the capillary number decreases below a critical value Ca_c, the bubble breaks-up. This critical value depends on the viscosity ratio $p = \mu_G/\mu$ (where μ_G is the gas viscosity) and on the dispersive mixing index, which is defined as ratio of elongation flow to shear flow:

$$\lambda = \frac{|\mathbf{D}|}{|\mathbf{D}| + |\mathbf{\Omega}|} \tag{7.2}$$

where $\mathbf{D}$ and $\mathbf{\Omega}$ are the rate of deformation and the vorticity tensors. The value of λ varies from 0 for pure rotation to 0.5 for simple shear and to 1 for pure elongation. Elongation is more efficient for bubble break-up than shear. Combining the influence of viscosity ratio proposed by Acrivos and Lo (1978) and the influence of elongation/shear ratio proposed by Vyakaranam and Kokini (2012), the critical capillary number can be expressed as:

$$Ca_c = 0.145\lambda^{-1.555} p^{-1/6} \tag{7.3}$$

Therefore, it can be assumed that if a fluid parcel containing a bubble of radius r travels in a region of large flow strength, the bubble will break-up if its radius is greater than

$$r_c = Ca_c \frac{\sigma}{\mu\dot{\gamma}} \tag{7.4}$$

where Ca_c, μ, σ and $\dot{\gamma}$ depend on the local flow characteristics, temperature and composition.

In fact, the break-up needs a certain time to be achieved; Bigio et al. (1998) proposed the following correlation for the break-up time

$$\tau = \frac{26p + 25}{\dot{\gamma}} \qquad \text{for} \quad 0.03 < p < 3 \tag{7.5}$$

The objective of the present work is to estimate the fragmentation of the bubbles inside the SSHE of a sorbet freezer, on the base of this literature knowledge and by 3D CFD simulation using Comsol 5.2.

7.2 Modelling approach

The modeling approach here proposed should be applicable to any SSHE sorbet freezer. We consider here the production of a commercial lemon sorbet (14.6% sucrose, 8% fructose, 3% lemon juice concentrate, 0.5% stabilizer) in the pilot scale freezer (WCB ® model MF50) described by Arellano et al. (2013). The SSHE of this freezer mainly consist in a refrigerated cylinder (40 cm long, 5 cm in diameter) in which a dasher with two blades is rotating at 750 rpm. The main elements of this SSHE (cylinder, dasher, blades) were represented in the numerical model whereas the inlet and outlet bowls were simplified in order to allow steady state simulation without moving geometry (Figure 60). The flow was calculated in the frame rotating with the blades; in this frame the cylindrical heat exchange surface is rotating (sliding wall). The considered flow rate was of 50 kg/h and the refrigerant evaporation temperature was -15.3 °C.

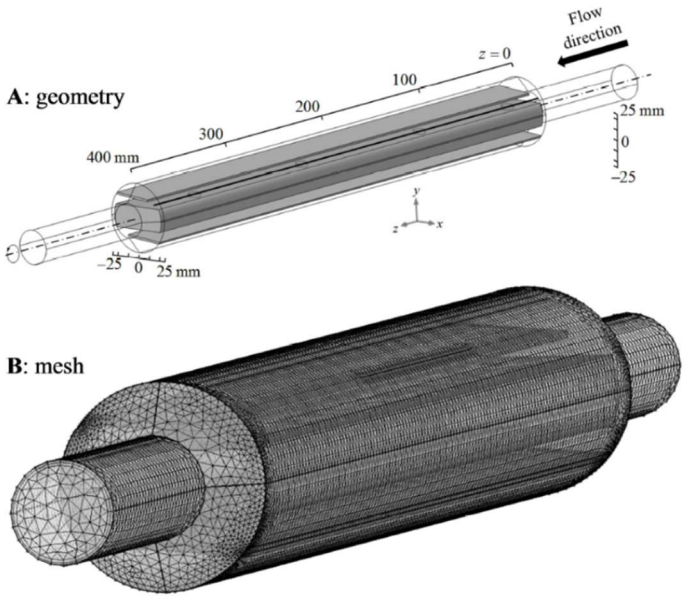

Figure 60. **A**: Sketch of the SSHE, putting in evidence the dasher and the blades. **B**: Mesh taken into account in solving the coupled problem of fluid flow and heat transfer; it is constituted of about 1.5 × 10^6 prismatic and tetrahedral elements.

The Navier-Stokes equations coupled with the conduction-convection energy equation were solved with the following properties (Hernández-Parra et al., 2018):

$$C_p\left[\mathrm{J\ kg^{-1}\ K^{-1}}\right] = 3500 \text{ for } T \geq T_{if} \quad \text{or} \quad 3266 + 7.95\times10^4 \exp\left(0.543\left(T - T_{if}\right)\right) \text{ for } T < T_{if} \quad (7.6)$$

$$K\left[\mathrm{W\,m^{-1}\,K^{-1}}\right] = 0.432 \text{ for } T \geq T_{if} \text{ or } 0.432 + 0.303\left(1 - \exp\left(0.367\left(T - T_{if}\right)\right)\right) \text{ for } T < T_{if} \quad (7.7)$$

$$\mu\left[\mathrm{Pa\,s}\right] = K\dot{\gamma}^{0.5} \text{ with } K = 0.5839 \text{ for } T \geq T_{if} \quad \text{or} \quad 0.5839 + 10.16\left(T_{if} - T\right) \text{ for } T < T_{if} \quad (7.8)$$

This denotes that

- the apparent heat capacity sharply increases (by a factor of 25) when the temperature decreases below the initial freezing point T_{if} = -2.72 °C in order to take into account the latent heat of fusion;
- the thermal conductivity increases below T_{if} because conductivity is higher for ice than for water
- both the mix and the sorbet are shear-thinning with a consistency K rising drastically when the ice content increases (i.e. T_{if} - T increases).

The ice fraction w_i is related to the temperature by the solute mass balance (equation (7.9)) and the liquidus curve. The latter which relates the solute mass fraction at saturation $w_{s.sat}$ to the temperature was experimentally characterized for the mix and fitted with a semi-empirical function.

$$\left(1 - w_i\right) w_{s,sat}\left(T\right) = w_{s,0} \quad (7.9)$$

Where $w_{s,0}$ is the solute fraction in the (non-frozen) mix.

From CFD simulation, the velocity and temperature fields can be obtained, as well as derived variables such as ice fraction w_i, consistency K, shear rate $\dot{\gamma} = |\mathbf{D}|$, vorticity magnitude $|\mathbf{\Omega}|$ and apparent viscosity μ. This way, at any location, it is possible to estimate the critical capillary number Ca_c and finally the critical radius of the bubbles r_c. The surface tension of the commercial mix was measured for different temperatures and concentrations: it ranged from 0.04 to 0.06 N m^{-1}; a constant value of 0.05 N m^{-1} was assumed in simulation.

If we follow the trajectory of a fluid parcel, we can theoretically plot the evolution of the critical radius as described schematically in Figure 61. In the inlet duct, shear is relatively low so that r_c is large, then the trajectory may enter a high shear region and r_c becomes small; finally, the fluid parcel follows, for example, intermediate flow strength regions before leaving the SSHE. Initially the fluid parcel contains bubbles of radius $r = r_0$. When the critical radius becomes smaller than the bubbles radius ($r < r_c$) the latter begins to decrease. If in the high flow strength zone (i.e. low r_c zone) the time needed for a bubble to break is very short ($\tau \approx 0$), the radius of the bubble should follow about the same evolution than r_c. When the fluid parcels leaves the high flow strength region (i.e. when r_c increases), if no coalescence occurs, the bubble radius remains small; equal to the lowest encountered value of r_c.

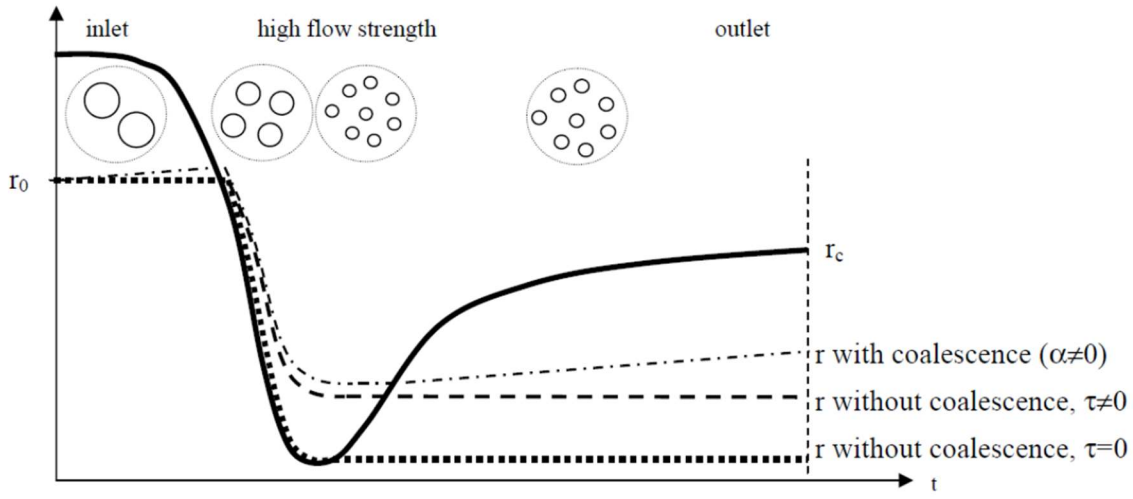

Figure 61. Schematic bubble fragmentation along one trajectory.

If the break-up time τ cannot be neglected, the bubble radius will not decrease down to the lowest value of r_c. Additionally, in case of coalescence, the bubble radius should increase at the end of the trajectory. This behavior can be modeled by following equation:

$$\frac{Dr}{Dt} = \frac{\partial r}{\partial t} + \mathbf{v} \cdot \nabla r = \frac{\min\left(r_c - r, \alpha r\right)}{\tau} \quad \alpha = 0 \text{ without coalescence} \tag{7.10}$$

This partial derivative equation was solved (additionally to flow and energy transfer) to predict the bubble radius inside the SSHE.

In fact, in a representative elementary volume at a given location, there are bubbles of different sizes. A population balance approach would be necessary to predict the bubble size distribution at any position. Equation (7.9) represents only a first approach in which *r* holds for the largest bubble size.

7.3 Results and discussion

Figure 62a shows the velocity field. It can be observed that flow is dominated by the rotation of the blades: the maximal tangential velocity is about 200 times higher than the mean axial velocity. The fluid is flowing around the blades with high velocity gradients near to the contact between blade and cylinder.

Figure 62b presents the temperature and the ice fraction. The temperature decreases rapidly to the initial freezing value T_{if} = -2.72 °C, then the ice fraction increases gradually with a small decrease of temperature. Temperature is quite homogeneous in the cross section at the middle of the SSHE (z = 0.2 m), reflecting the high radial mixing effect of the rotating blades.

Figure 62c shows the consistency K. It increases by a factor 50 along the SSHE. The higher the value of K, the higher is the apparent viscosity. Therefore, small critical radius values are expected near to the exit. In this region the fragmentation should be the highest.

Figure 63 and Figure 64 present the shear rate $\dot{\gamma} = |\mathbf{D}|$, vorticity magnitude $|\mathbf{\Omega}|$, elongation/shear ratio λ, apparent viscosity μ, critical capillary number Ca_c and critical bubble radius r_c respectively at the middle (z = 0.2m) and near the SSHE's outlet (z = 0.39 m).

The flow characteristics: $\dot{\gamma}$, $|\mathbf{\Omega}|$ and λ, are similar in the two cross sections, with high flow strength zones near the blade/cylinder contact. The apparent viscosity is higher near to the exit because the ice fraction is higher. The critical capillary number is the lowest (value near to 1) where the elongation/shear ratio λ is the highest (elongational flow). The lowest values of critical bubble radius are located near to the blade/cylinder contact where the flow strength is the highest, and in the cross-section near to the outlet where the consistency is the highest. In this zone a high fragmentation rate is expected.

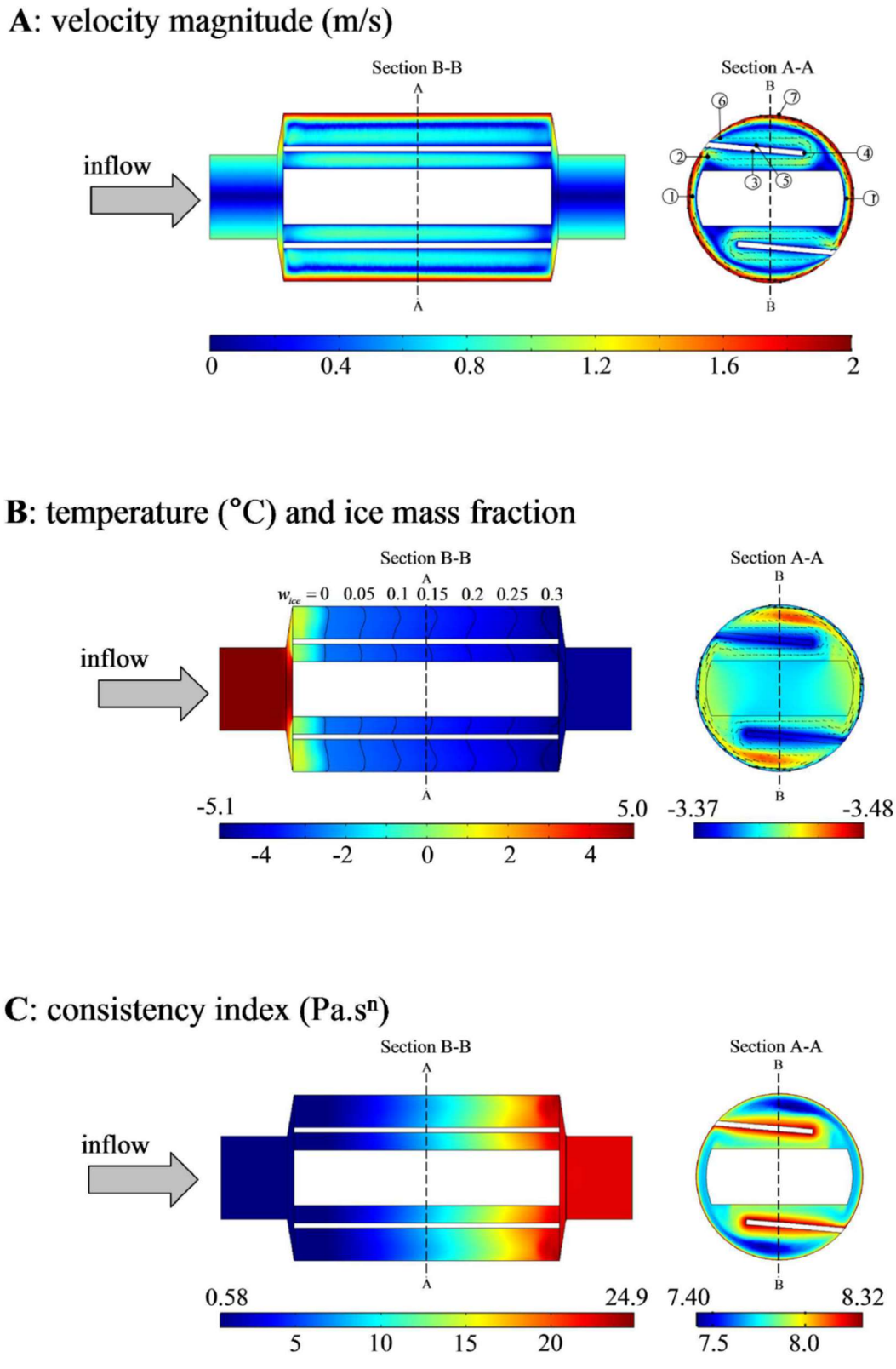

Figure 62. Numerical model predictions along the SSHE and in the middle cross-section.

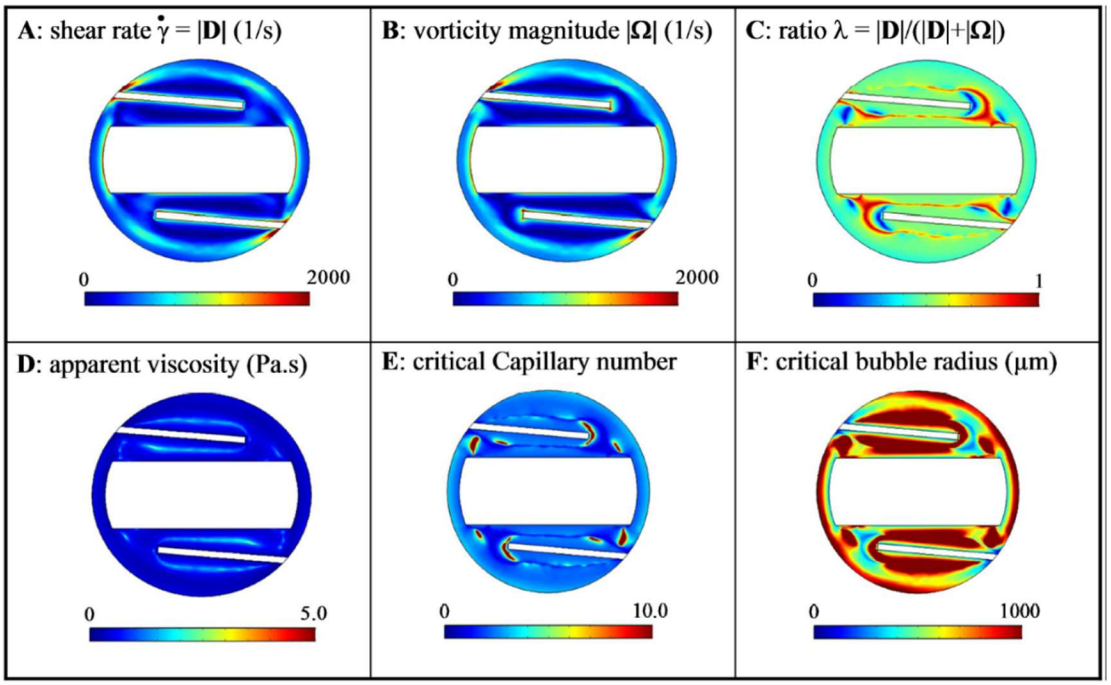

Figure 63. Model prediction at z = 0.2 m

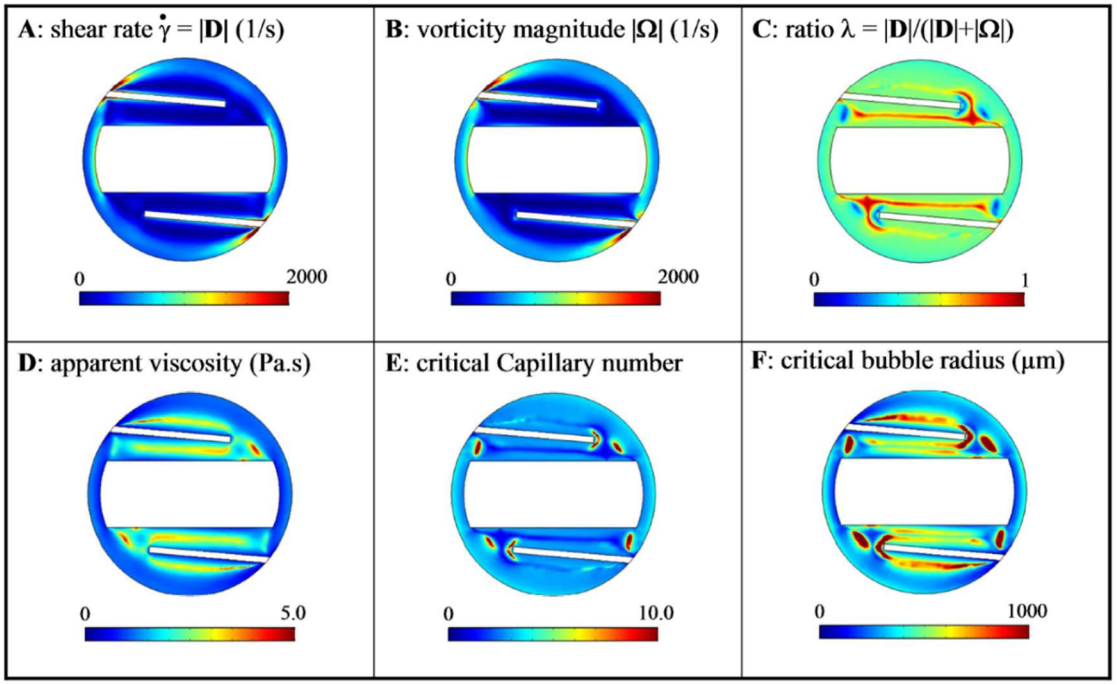

Figure 64. Model prediction at z = 0.39 m

Figure 65 shows a view of the bubble radius in three cross-sections (z = 0.01, 0.2, and 0.39 m) and in the vertical plane along the SSHE, with a constant break-up time of τ = 1 ms. In dark red appear the zones were the bubble radius is higher than 200 µm (at the inlet a value of 1 mm was assumed). The regions were the bubbles are the smallest appear in dark blue (near the exit, near the blade/cylinder contact). At the exit there is a blend of fluid parcels which experienced different shear/elongation and temperature histories. The surface-averaged value at outlet is of 48 µm (for τ = 1 ms).

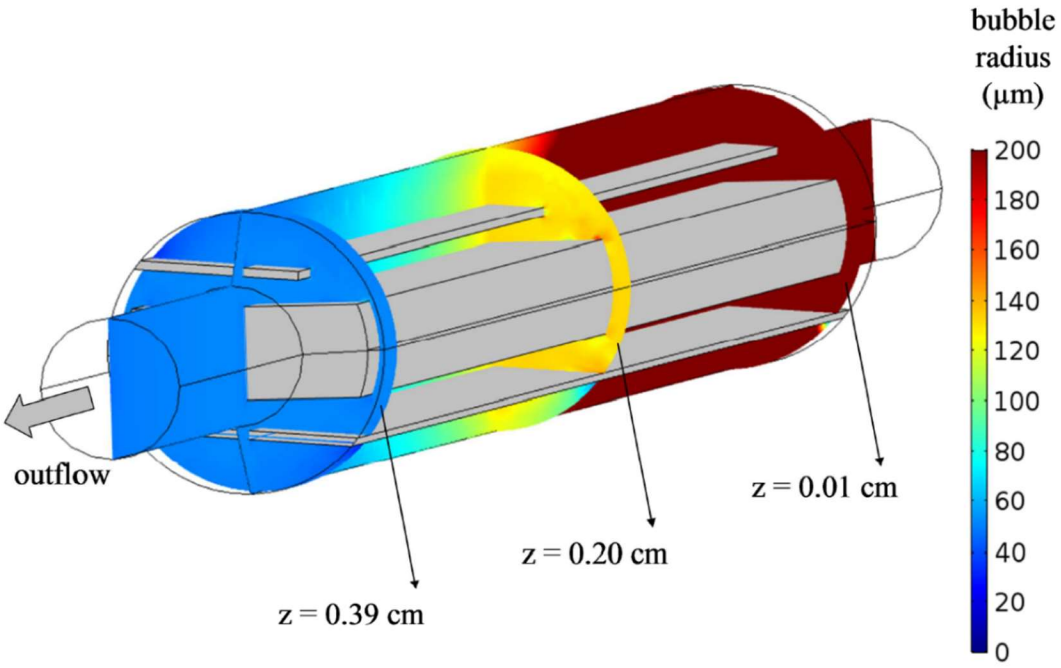

Figure 65. Model predictions of the bubble radius in three cross-sections (z = 0.01, 0.2, and 0.39 m) and in the vertical plane along the SSHE for τ = 1 ms. Bubble radius was set to be 1000 µm at the inlet. All the values above 200 µm are displayed in dark red.

The influence of the break-up time t on the outlet bubble size is presented in Figure 66. Logically, the smaller the break-up time, the smaller is the outlet bubble radius. It seems that for small values of τ, the bubble radius tends toward about 40 µm. When applying a coalescence parameter $\alpha = 10^{-4}$ (and with τ = 1 ms), the outlet bubble radius is of course larger: 80 µm. Simulation was also conducted with the break-up time given by equation (7.5), without coalescence, the outlet radius was then of 115 µm. But equation (7.5) is not strictly applicable in our case because the viscosity ratio is lower than 0.03.

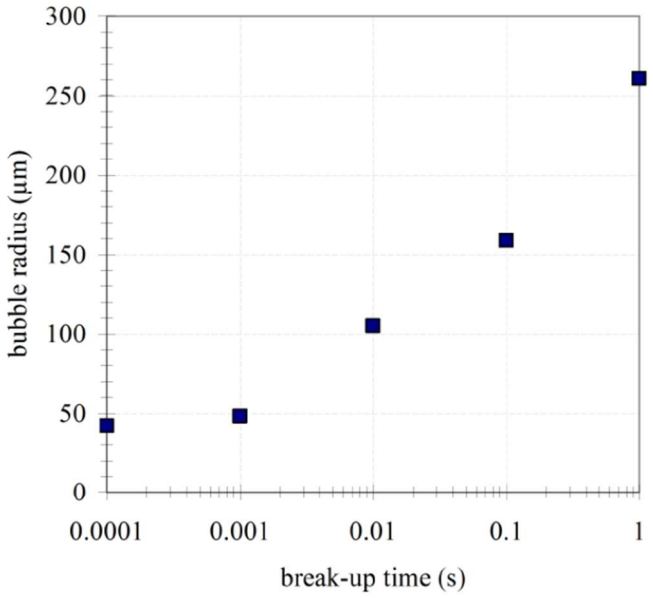

Figure 66. Surface-averaged value at the SSHE's outlet of the bubble radius while neglecting coalescence effects.

In similar conditions, under a very low air injection rate, the largest bubbles observed by microscopy in refrigerated samples taken at the outlet of the SSHE had a diameter of about 50 µm. The pressure inside the SSHE was of 5 bars. Thus, it can be assumed that the bubble volume increased by a factor 5 during the decompression. Consequently, the largest bubbles inside the SSHE should have a diameter of about $50/5^{1/3}$ ≈ 30 µm. This is of the same order of magnitude, but significantly smaller than model prediction.

This difference can be explained by the several reasons:

- the medium surrounding the bubbles is not a homogeneous fluid, but it is itself a two-phase medium (concentrated sucrose solution and ice crystals);
- the medium surrounding the bubbles does not exhibit a Newtonian behavior;
- fluid parcels move rapidly from strong to weak flow strength regions (or from elongational to shear regions)
- This was not the case for the correlation used in the model. The presence of ice crystals of about same size as the bubbles (~20µm) can notably explain additional bubble fragmentation.

7.4 Conclusion

The developed model is a first approach able to highlight the local mechanisms of bubble fragmentation and to estimate the order of magnitude of the largest bubbles. Additional work is necessary to obtain accurate/quantitative prediction of bubbles sizes, and a population balance approach should be developed to estimate the bubble size distribution. However, the present model could already provide the trends of bubble fragmentation modifications, including at local scale, when changes in operation condition or in blade geometry are envisaged.

Nomenclature

Ca	Capillary number (-)
Cp	specific heat capacity (J kg^{-1} K^{-1})
D	rate of deformation tensor (s^{-1})
K	thermal conductivity (W m^{-1} K^{-1})
w	mass fraction (-)
z	position in the heat exchanger length (m)

Greek letters

$\dot{\gamma}$	shear rate (s^{-1})
λ	dispersive mixing index (-)
μ	dynamic viscosity (Pa s)
σ	surface tension (N m^{-1})
τ	break-up time (s)
Ω	vorticity tensors (s^{-1})

Subscripts

0	non frozen
cr	critical
G	gas
i	ice
if	initial freezing
s	solute
sat	saturation

Abbreviations

CFD	computational fluid dynamics
SSHE	scraped surface heat exchanger

References

Acrivos, A., Lo, T.S., (1978). Deformation and breakup of a single slender drop in an extensional flow. Journal of Fluid Mechanics 86(4), 641-672.

Arellano, M., Benkhelifa, H., Alvarez, G., Flick, D., (2013). Experimental study and modelling of the residence time distribution in a scraped surface heat exchanger during sorbet freezing. Journal of Food Engineering 117(1), 14-25.

Bigio, D.I., Marks, C.R., Calabrese, R.V., (1998). Predicting drop breakup in complex flows from model flow experiments. International Polymer Processing 13(2), 192-198.

Hernández-Parra, O.D., Plana-Fattori, A., Alvarez, G., Ndoye, F.-T., Benkhelifa, H., Flick, D., (2018). Modeling flow and heat transfer in a scraped surface heat exchanger during the production of sorbet. Journal of Food Engineering 221, 54-69.

Risso, F., (2000). Mechanisms of deformation and breakup of drops and bubbles. Multiphase Science and Technology 12(1), 1-50.

Vyakaranam, K.V., Kokini, J.L., (2012). Prediction of air bubble dispersion in a viscous fluid in a twin-screw continuous mixer using FEM simulations of dispersive mixing. Chemical Engineering Science 84, 303-314.

CONCLUSIONS ET PERSPECTIVES

8. Conclusions et perspectives

Cette thèse s'inscrit dans la continuité des travaux déjà menés au sein de l'unité GPAN sur la caractérisation expérimentale et numérique des couplages hydrodynamique-thermique-transformation au cours de la fabrication de sorbet dans un échangeur de chaleur à surface raclée (ECSR): thèses successives de Rosalia Cerecero, J. E. González et Marcela Arellano. Ces études ne portaient que sur la cristallisation de sorbets non aéré. L'objet principal de cette étude était d'étudier le couplage entre cristallisation et foisonnement.

Le procédé de fabrication d'un sorbet comprend plusieurs opérations unitaires. En général, après le mélange des différents ingrédients qui forment un mix, celui-ci est pasteurisé, homogénéisé puis refroidi pour maturation pendant plusieurs heures. Après maturation, le mix est introduit, avec de l'air, dans un ECSR où il est alors congelé et foisonné. A la sortie de l'ECSR (à une température comprise entre -4 et -6°C), le produit formé est stocké à basse température (environ -23°C) pour durcissement.

Le cœur du procédé réside dans l'ECSR, seul endroit où se forment de nouveaux cristaux et où les bulles d'air sont introduites et fragmentées. Les cristaux de glace se forment sur la surface d'échange. Le rotor muni de lames racleuses, permet en tournant rapidement de détacher de manière continue les cristaux de glace formés à la paroi et de fragmenter les bulles d'air. Par ce procédé se forme un produit avec une microstructure particulière composée d'une phase liquide (eau, sucre…) cryo-concentrée de viscosité élevée, de cristaux de glace et de bulles d'air. Cette microstructure dépend fortement des conditions opératoires du procédé.

Le foisonnement est effectué dans l'optique d'assurer la stabilité du produit et de lui conférer des propriétés texturales et sensorielles particulières telle que l'onctuosité. Ces propriétés techno-fonctionnelles ainsi que la stabilité du produit final sont grandement liées à la formation des structures au niveau microscopique : la taille et l'état de dispersion des cristaux de glace mais aussi des bulles d'air au sein du produit à la sortie du freezer. Cette dispersion est elle-même conditionnée par différents paramètres liés à la physico-chimie ou aux conditions opératoires.

Ce travail a permis d'estimer les effets de l'introduction d'air sur les processus de cristallisation et de foisonnement. Une approche combinée expérimentation et modélisation a été mise en œuvre pour mener à bien cet objectif, selon 3 axes :

1. Mise au point d'une technique de granulométrie discriminante permettant de distinguer les distributions de tailles de bulles et de cristaux dans un même échantillon. Cette technique permet de caractériser l'influence des conditions opératoires (débit de mix, vitesse de raclage, température d'évaporation et fraction d'air) sur la dispersion des bulles d'air et la taille des cristaux dans le sorbet foisonné (un travail sur l'influence de la formulation est en cours au laboratoire).
2. Etude de la distribution de temps de séjour dans l'ECSR et de la relation entre température de sortie et température d'évaporation du fluide frigorigène en condition de foisonnement pour déterminer l'influence de la fraction d'air incorporée sur les écoulements et les transferts au sein de l'équipement.
3. Modélisation du couplage écoulement, transferts thermiques et cristallisation afin de prédire l'effet des conditions opératoires sur les champs de vitesse au sein d'un ECSR et d'en déduire les conditions de cisaillement et d'élongation subies par les bulles d'air le long de leur parcours dans l'échangeur.

Du côté des écoulements, avec les résultats obtenus dans cette thèse on a pu constater que le débit de mix, le débit d'air et moins fortement la température du réfrigérant influencent la distribution de temps de séjour dans l'ECSR. Pourtant, qualitativement les résultats des DTS normalisés sont raisonnablement proches indiquant qu'il n'y a pas un changement de régime d'écoulement dans les conditions étudiés. En résumé :

- Un volume de liquide stagnant ou presque stagnant a été identifié dans l'ECSR sans circulation d'air. Ce résultat est en accord avec les résultats rapportés par M. Arellano. Il a été attribué au fait d'avoir une couche près de la paroi d'échange de chaleur où la fraction de glace est plus élevée et la température plus basse entrainant une viscosité apparente beaucoup plus grande que vers le rotor.
- Un volume de gaz stagnant ou a plus basse vitesse de circulation que le liquide dans l'ECSR a été mis en évidence quand l'air est introduit. Ceci pourrait s'expliquer par l'action de forces centrifuges exercées sur le liquide, le poussant vers l'extérieur et déplaçant les bulles vers le rotor.
- En conséquence, le temps de séjour moyen ainsi que le temps de séjour minimum diminuent avec une augmentation du débit d'air du fait qu'un plus grand débit d'air force le liquide à circuler dans un volume plus petit et donc à plus grande vitesse axiale.

- À débits d'air plus grands la dispersion axiale semble s'accroître ; probablement en raison d'une différence plus importante de viscosité apparente entre la couche proche de la paroi d'échange et le centre.
- À plus basse température du réfrigérant, les temps de séjour moyen et minimum diminuent et le volume de gaz stagnant augmente. Cela est attribué au même effet que celui décrit précédemment en termes de la viscosité apparente.

Du point de vue des transferts thermiques, la modélisation s'est présentée comme un outil efficace en complément de l'expérimentation pour étudier l'importance des mécanismes de transferts de chaleur dans le système. En résumé nous avons trouvé que :

- La température de sortie est étroitement liée aux propriétés physiques, notamment la rhéologie du sorbet. Une caractérisation précise y compris à forte concentration en glace s'avère nécessaire. Cela permettrait sans doute d'approcher les résultats simulés des modèles de données expérimentales.
- La température de sortie s'est montrée limitée à des valeurs entre -3 et -7°C du fait de l'importance de la dissipation visqueuse.
- La modélisation de l'écoulement dans l'ECSR a permis d'identifier des zones de recirculation à l'entrée comme à la sortie de l'échangeur qui peuvent influencer la dispersion axiale, l'efficacité des transferts de chaleur et la dynamique de fragmentation ou de coalescence des bulles.

Du point de vu de la cristallisation, ce travail a permis de conclure que :

- Une diminution de la température du réfrigérant dans le freezer favorise l'obtention des cristaux plus petits sans ou avec l'introduction d'air. Cet effet a été aussi observé dans la production des crèmes glacés. Il est principalement attribué au fait qu'une température de paroi basse favorise la nucléation des cristaux plus petits à la paroi d'échange.
- La distribution de tailles des cristaux est sensible à la présence d'air. Cet effet est probablement dû au fait que les bulles d'air limitent l'efficacité du transfert de chaleur limitant la croissance des cristaux.
- La granulométrie des cristaux est principalement influencée par la température du réfrigérant. En conséquence, il est recommandé d'étendre la plage des températures de réfrigérant étudiée. Il faut remarquer qu'au niveau industriel, la température d'évaporation du réfrigérant peut descendre jusqu'à -30°C.

Du point de vue du foisonnement on peut retenir de ce travail que :

- La technique de microscopie à basse température ne permet pas seulement d'obtenir les distributions de taille des bulles de manière répétable mais elle permet aussi de le faire en même temps que la détermination de la distribution de tailles des cristaux. La technique mise au point permet l'observation de la microstructure des sorbets foisonnés dans des conditions proches de celle rencontrées à la sortie de l'ECSR.
- Une diminution de la température du réfrigérant a comme effet une réduction des diamètres des bulles. Cette tendance est probablement due à une viscosité plus élevée, ce qui accroît la contrainte de cisaillement et favorise la rupture des bulles ; en même temps qu'elle défavorise la probabilité de coalescence dans l'échangeur.
- L'effet du débit d'air sur le foisonnement n'est pas significatif qu'à fortes débits. Ceci pourrait être lié au fait que lorsque le volume d'air stagnant augmente, le volume de liquide se réduit, entrainant un cisaillement plus fort et une rupture plus efficace des bulles.
- Dans cette thèse nous avons développé un modèle qui permet d'obtenir une idée des mécanismes locaux de fragmentation des bulles et de prédire l'ordre de grandeur de la taille des plus grandes bulles dans les sorbets foisonnés. En revanche, une approche par bilan de population est recommandée pour compléter l'information sur la distribution de tailles des bulles.

REFERENCES BIBLIOGRAPHIQUES

9. Références bibliographiques

Abichandani, H., Sarma, S.C., Heldman, D.R., (1986). Hydrodynamics and Heat Transfer in Thin Film Scraped Surface Heat Exchangers — A Review. *Journal of Food Process Engineering* 9(2), 143-172.

Acrivos, A., Lo, T.S., (1978). Deformation and breakup of a single slender drop in an extensional flow. *Journal of Fluid Mechanics* 86(04), 641-672.

Aguilera, J.M., Lillford, P.J., (2008). *Food Materials Science. Principles and Practice*. Springer.

Alcairo, E.R., Zuritz, C.A., (1990). Residence time distributions of spherical particles suspended in non-Newtonian flow in a scraped-surface heat exchanger. *Transactions of the American Society of Agricultural Engineers* 33(5), 1621-1628.

Alhamdan, A., Sastry, S., (1997). Residence time distribution of food and simulated particles in a holding tube. *Journal of Food Engineering* 34(3), 271-292.

Arellano, M., Benkhelifa, H., Alvarez, G., Flick, D., (2013a). Coupling population balance and residence time distribution for the ice crystallization modeling in a scraped surface heat exchanger. *Chemical Engineering Science* 102, 502-513.

Arellano, M., Benkhelifa, H., Alvarez, G., Flick, D., (2013b). Experimental study and modelling of the residence time distribution in a scraped surface heat exchanger during sorbet freezing. *Journal of Food Engineering* 117(1), 14-25.

Arellano, M., Benkhelifa, H., Flick, D., Alvarez, G., (2012a). Online capillary rheometry of commercial sorbet, 16th IUFoST World Congress of Food Science and Technology, Foz do Iguaçu - Brazil.

Arellano, M., Benkhelifa, H., Flick, D., Alvarez, G., (2012b). Online ice crystal size measurements during sorbet freezing by means of the focused beam reflectance measurement (FBRM) technology. Influence of operating conditions. *Journal of Food Engineering* 113(2), 351-359.

Arellano, M., Flick, D., Benkhelifa, H., Alvarez, G., (2013c). Rheological characterisation of sorbet using pipe rheometry during the freezing process. *Journal of Food Engineering* 119(3), 385-394.

Azizi, F., Al Taweel, A.M., (2007). Population balance simulation of gas–liquid contacting. *Chemical Engineering Science* 62(24), 7436-7445.

Baccar, M., Abid, M.S., (1997). Numerical analysis of three-dimensional flow and thermal behaviour in a scraped-surface heat exchanger. *Revue Générale de Thermique* 36(10), 782-790.

Baccar, M., Abid, M.S., (1999). Simulation numérique des comportements hydrodynamiques et thermiques des échangeurs racleurs opérant en régime turbulent. *International Journal of Thermal Sciences* 38(7), 634-644.

Balerin, C., Aymard, P., Ducept, F., Vaslin, S., Cuvelier, G., (2007). Effect of formulation and processing factors on the properties of liquid food foams. *Journal of Food Engineering* 78(3), 802-809.

Barigou, M., Douaire, M., (2013). 9 - X-ray micro-computed tomography for resolving food microstructures, in: Morris, V.J., Groves, K. (Eds.), *Food Microstructures*. Woodhead Publishing, pp. 246-272.

Belhamri, R., Fayolle, F., Flick, D. (2009). Simplified flow pattern model in SSHE during crystallization process.

Benezech, T., Maingonnat, J.F., (1989). Etude de la distribution des temps de séjour dans des échangeurs à surface raclée traitant des fluides non-Newtoniens. *Entropie* 151, 37 - 46.

Benezech, T., Maingonnat, J.F., (1993). Study of residence-time distribution of non-Newtonian fluids in scraped-surface heat exchangers. *International Chemical Engineering* 33(2), 215-225.

Bentley, B.J., Leal, L.G., (1986). A computer-controlled four-roll mill for investigations of particle and drop dynamics in two-dimensional linear shear flows. *Journal of Fluid Mechanics* 167, 219-240.

Bigio, D.I., Marks, C.R., Calabrese, R.V., (1998). Predicting drop breakup in complex flows from model flow experiments. *International Polymer Processing* 13(2), 192-198.

Błasiak, P., Pietrowicz, S., (2016). Towards a better understanding of 2D thermal-flow processes in a scraped surface heat exchanger. *International Journal of Heat and Mass Transfer* 98, 240-256.

Boccardi, G., Celata, G.P., Lazzarini, R., Saraceno, L., Trinchieri, R., (2010). Development of a heat transfer correlation for a Scraped-Surface Heat Exchanger. *Applied Thermal Engineering* 30(10), 1101-1106.

Bolliger, S., Wildmoser, H., Goff, H.D., Tharp, B.W., (2000). Relationships between ice cream mix viscoelasticity and ice crystal growth in ice cream. *International Dairy Journal* 10(11), 791-797.

Bongers, P.M.M., (2006). A heat transfer model of a scraped surface heat exchanger for ice cream, in: Marquardt, W., Pantelides, C. (Eds.), *Computer Aided Chemical Engineering*. Elsevier, pp. 539-544.

Caillet, A., Cogné, C., Andrieu, J., Laurent, P., Rivoire, A., (2003). Characterization of ice cream structure by direct optical microscopy. Influence of freezing parameters. *LWT - Food Science and Technology* 36(8), 743-749.

Campbell, G.M., Mougeot, E., (1999). Creation and characterisation of aerated food products. *Trends in Food Science & Technology* 10(9), 283-296.

Cantat, I., Cohen-Addad, S., Elias, F., Graner, F., Höhler, R., Pitois, O., Rouyer, F., Saint-Jalmes, A., (2013). *Foams: Structure and Dynamics*. Oxford University Press.

Casenave, C., Dochain, D., Alvarez, G., Arellano, M., Benkhelifa, H., Leducq, D., (2013). Control of a nonlinear ice cream crystallization process. IFAC Proceedings Volumes 46(23), 717-722.

Casenave, C., Dochain, D., Alvarez, G., Arellano, M., Benkhelifa, H., Leducq, D., (2014). Model identification and reduction for the control of an ice cream crystallization process. *Chemical Engineering Science* 119, 274-287.

Cogné, C., Andrieu, J., Laurent, P., Besson, A., Nocquet, J., (2003). Experimental data and modelling of thermal properties of ice creams. *Journal of Food Engineering* 58(4), 331-341.

Cook, K.L.K., Hartel, R.W., (2010). Mechanisms of Ice Crystallization in Ice Cream Production. *Comprehensive Reviews in Food Science and Food Safety* 9(2), 213-222.

Cook, K.L.K., Hartel, R.W., (2011). Effect of freezing temperature and warming rate on dendrite break-up when freezing ice cream mix. *International Dairy Journal* 21(6), 447-453.

Costa, C.B.B., Maciel, M.R.W., Filho, R.M., (2007). Considerations on the crystallization modeling: Population balance solution. *Computers & Chemical Engineering* 31(3), 206-218.

Crespí-Llorens, D., Vicente, P., Viedma, A., (2016). Flow pattern of non-Newtonian fluids in reciprocating scraped surface heat exchangers. *Experimental Thermal and Fluid Science* 76, 306-323.

Chang, Y., Hartel, R.W., (2002a). Development of air cells in a batch ice cream freezer. *Journal of Food Engineering* 55(1), 71-78.

Chang, Y., Hartel, R.W., (2002b). Measurement of air cell distributions in dairy foams. *International Dairy Journal* 12(5), 463-472.

Chang, Y., Hartel, R.W., (2002c). Stability of air cells in ice cream during hardening and storage. *Journal of Food Engineering* 55(1), 59-70.

Chen, C.R., Ramaswamy, H.S., (2000). A neuro-computing approach for modeling of residence time distribution (RTD) of carrot cubes in a vertical scraped surface heat exchanger (SSHE). *Food Research International* 33(7), 549-556.

Cheng, J., Carreau, P.J., (1994). Aerated mixing of viscoelastic fluids with helical ribbons impellers. *Chemical Engineering Science* 49(12), 1965-1972.

Chhabra, R.P., Richardson, J.F., (2011). *Non-Newtonian Flow and Applied Rheology: Engineering Applications.* Elsevier Science.

Choi, Y., Okos, M.R., (1986). Effects of temperature and composition on the thermal properties of foods, in: Maguer, M.L., Jelen, P. (Eds.), *Food Engineering and Process Applications: Transport phenomena, Vol. 1, Transport Phenomena* ed. Elsevier Applied Science Publishers, London.

D'Addio, L., Carotenuto, C., Di Natale, F., Nigro, R., (2013). Heating and cooling of hazelnut paste in alternate blades scraped surface heat exchangers. *Journal of Food Engineering* 115(2), 182-189.

Danckwerts, P.V., (1953). Continuous flow systems: Distribution of residence times. *Chemical Engineering Science* 2(1), 1-13.

Dehkordi, K.S., Fazilati, M.A., Hajatzadeh, A., (2015). Surface Scraped Heat Exchanger for cooling Newtonian fluids and enhancing its heat transfer characteristics, a review and a numerical approach. *Applied Thermal Engineering* 87, 56-65.

Djelveh, G., Bacati, O., Gros, J.B., (1994). Mechanical aspects of gas dispersion in continuous foaming food processes using scraped surface heat exchangers. *Journal of Food Engineering* 23(2), 213-223.

Djéridi, H., Favé, J.F., Billard, J.Y., Fruman, D.H., (1999). Bubble capture and migration in Couette-Taylor flow. *Experiments in Fluids* 26(3), 233-239.

Djéridi, H., Gabillet, C., Billard, J.-Y., (2002). Écoulement de Couette Taylor diphasique. *Comptes Rendus Mécanique* 330(2), 113-119.

Donhowe, D.P., Hartel, R.W., Bradley Jr, R.L., (1991a). Determination of Ice Crystal Size Distributions in Frozen Desserts. *Journal of Dairy Science* 74(10), 3334-3344.

Donhowe, D.P., Hartel, R.W., Bradley, R.L., Jr., (1991b). Determination of Ice Crystal Size Distributions in Frozen Desserts. *Journal of Dairy Science* 74(10), 3334-3344.

Dorneanu, B., Bildea, C.S., Grievink, J., Bongers, P.M., (2009). A first-principles model for the freezing step in ice cream manufacture, in: Jacek, J., Jan, T. (Eds.), *Computer Aided Chemical Engineering*. Elsevier, pp. 171-176.

Drewett, E.M., Hartel, R.W., (2007). Ice crystallization in a scraped surface freezer. *Journal of Food Engineering* 78(3), 1060-1066.

Druzinec, D., Salzig, D., Kraume, M., Czermak, P., (2015). Micro-bubble aeration in turbulent stirred bioreactors: Coalescence behavior in Pluronic F68 containing cell culture media. *Chemical Engineering Science* 126, 160-168.

Duffy, B.R., Wilson, S.K., Lee, M.E.M., (2007). A mathematical model of fluid flow in a scraped-surface heat exchanger. *Journal of Engineering Mathematics* 57(4), 381-405.

Dumont, E., Fayolle, F., Legrand, J., (2000a). Electrodiffusional wall shear rate analysis in scraped surface heat exchanger. *AIChE Journal* 46(6), 1138-1148.

Dumont, E., Fayolle, F., Legrand, J., (2000b). Flow regimes and wall shear rates determination within a scraped surface heat exchanger. *Journal of Food Engineering* 45(4), 195-207.

Eisner, M.D., Wildmoser, H., Windhab, E.J., (2005). Air cell microstructuring in a high viscous ice cream matrix. *Colloids and Surfaces A: Physicochemical and Engineering Aspects* 263(1–3), 390-399.

Ekambara, K., Joshi, J.B., (2004). Axial mixing in laminar pipe flows. *Chemical Engineering Science* 59(18), 3929-3944.

Faydi, E., Andrieu, J., Laurent, P., (2001). Experimental study and modelling of the ice crystal morphology of model standard ice cream. Part I: Direct characterization method and experimental data. *Journal of Food Engineering* 48(4), 283-291.

Fayolle, F., Belhamri, R., Flick, D., (2013). Residence time distribution measurements and simulation of the flow pattern in a scraped surface heat exchanger during crystallisation of ice cream. *Journal of Food Engineering* 116(2), 390-397.

Fayolle, F., Mabit, J., Legrand, J., (2005). Determination of heterogeneities in a scraped surface heat exchanger using electrochemical sensors. *Journal of Applied Electrochemistry* 35(5), 487-498.

Fénot, M., Bertin, Y., Dorignac, E., Lalizel, G., (2011). A review of heat transfer between concentric rotating cylinders with or without axial flow. *International Journal of Thermal Sciences* 50(7), 1138-1155.

Fillaudeau, L., Le-Nguyen, K., André, C., (2009). Influence of flow regime and thermal power on residence time distribution in tubular Joule Effect Heaters. *Journal of Food Engineering* 95(3), 489-498.

Flores, A.A., Goff, H.D., (1999). Ice Crystal Size Distributions in Dynamically Frozen Model Solutions and Ice Cream as Affected by Stabilizers. *Journal of Dairy Science* 82(7), 1399-1407.

Fogler, H.S., (1999). *Elements of Chemical Reaction Engineering*. Prentice Hall PTR.

Fradette, L., Li, H.-Z., Choplin, L., Tanguy, P., (2006). Gas/liquid dispersions with a SMX static mixer in the laminar regime. *Chemical Engineering Science* 61(11), 3506-3518.

Fu, X.Y., Ishii, M., (2003). Two-group interfacial area transport in vertical air–water flow: I. Mechanistic model. *Nuclear Engineering and Design* 219(2), 143-168.

Germain, J.C., Aguilera, J.M., (2014). Multi-scale properties of protein-stabilized foams. *Food Structure* 1(1), 55-70.

Goff, H.D., Hartel, R., (2013a). Freezing and Refrigeration, *Ice Cream*. Springer US, pp. 193-248.

Goff, H.D., Hartel, R.W., (2013b). *Ice Cream*. Springer US.

Goff, H.D., Verespej, E., Smith, A.K., (1999). A study of fat and air structures in ice cream. *International Dairy Journal* 9(11), 817-829.

González-Ramírez, J.E., (2012). Contribution au contrôle par la modélisation d'un procédé de cristallisation en continu. AgroParisTech, Paris – France.

González-Ramírez, J.E., Leducq, D., Arellano, M., Alvarez, G., (2013). Energy consumption optimization of a continuous ice cream process. *Energy Conversion and Management* 70, 230-238.

González Ramírez, J.E., Leducq, D., Arellano, M., Álvarez, G., (2013). Modelo de un proceso de cristalización continua de un sorbete por medio de la metodología de momentos. *Revista Internacional de Métodos Numéricos para Cálculo y Diseño en Ingeniería* 29(4), 215-224.

Grace, H.P., (1982). Dispersion phenomena in high viscosity inmiscible fluid systems and application of static mixers as dispersion devices in such systems. *Chemical Engineering Communications* 14(3-6), 225-277.

Green, D., Perry, R., (2007). *Perry's Chemical Engineers' Handbook*, Eighth Edition. McGraw-Hill Education.

Groeneweg, F., van Dieren, F., Agterof, W.G.M., (1994). Droplet break-up in a stirred water-in-oil emulsion in the presence of emulsifiers. *Colloids and Surfaces A: Physicochemical and Engineering Aspects* 91(0), 207-214.

Haddad Amamou, A., Benkhelifa, H., Alvarez, G., Flick, D., (2010). Study of crystal size evolution by focused-beam reflectance measurement during the freezing of sucrose/water solutions in a scraped-surface heat exchanger. *Process Biochemistry* 45(11), 1821-1825.

Ham, J.H., Platzer, B., (2004). Semi-Empirical Equations for the Residence Time Distributions in Disperse Systems – Part 1: Continuous Phase. *Chemical Engineering & Technology* 27(11), 1172-1178.

Härröd, M., (1986). Scraped surface heat exchangers - a literature survey of flow patterns, mixing effects, residence time distribution, heat transfer and power requirements. *Journal of Food Process Engineering* 9(1), 1-62.

Hernández-Parra, O.D., Plana-Fattori, A., Alvarez, G., Ndoye, F.-T., Benkhelifa, H., Flick, D., (2018). Modeling flow and heat transfer in a scraped surface heat exchanger during the production of sorbet. *Journal of Food Engineering* 221, 54-69.

Hernandez, O., Ndoye, F., Benkhelifa, H., Flick, D., Alvarez, G., (2015). A discriminating microscopy technique for the measurement of ice crystals and air bubbles size distribution in sorbets, 24ième Congrès International du Froid ICR 2015, Yokohama, Japan, p. 8 p.

Hinch, E.J., Acrivos, A., (1980). Long slender drops in a simple shear flow. *Journal of Fluid Mechanics* 98(02), 305-328.

Hinze, J.O., (1955). Fundamentals of the hydrodynamic mechanism of splitting in dispersion processes. *AIChE Journal* 1(3), 289-295.

Hubacz, R., (2015). Classification of flow regimes in gas-liquid horizontal Couette-Taylor flow using dimensionless criteria. *Journal of Hydrodynamics, Ser. B* 27(5), 773-781.

Hubacz, R., Wroński, S., (2004). Horizontal Couette–Taylor flow in a two-phase gas–liquid system: flow patterns. *Experimental Thermal and Fluid Science* 28(5), 457-466.

Indrawati, L., Wang, Z., Narsimhan, G., Gonzalez, J., (2008). Effect of processing parameters on foam formation using a continuous system with a mechanical whipper. *Journal of Food Engineering* 88(1), 65-74.

Inoue, K., Ochi, H., Taketsuka, M., Saito, H., Sakurai, K., Ichihashi, N., Iwatsuki, K., Kokubo, S., (2008). Modeling of the Effect of Freezer Conditions on the Principal Constituent Parameters of Ice Cream by Using Response Surface Methodology. *Journal of Dairy Science* 91(5), 1722-1732.

Ji, L., Wu, B., Chen, K., Zhu, J., (2010). Experimental study and modeling of residence time distribution in impinging stream reactor with GDB model. *Journal of Industrial and Engineering Chemistry* 16(4), 646-650.

Keshav, T.R., Somaraju, P., Kalyan, K., Saroha, A.K., Nigam, K.D.P., (2008). Liquid phase residence time distribution for gas–liquid flow in Kenics static mixer. *Chemical Engineering and Processing: Process Intensification* 47(12), 2275-2280.

Kruglyakov, P.M., Karakashev, S.I., Nguyen, A.V., Vilkova, N.G., (2008). Foam drainage. *Current Opinion in Colloid & Interface Science* 13(3), 163-170.

Labbafi, M., Thakur, R.K., Vial, C., Djelveh, G., (2007). Development of an on-line optical method for assessment of the bubble size and morphology in aerated food products. *Food Chemistry* 102(2), 454-465.

Lagarias, J.C., Reeds, J.A., Wright, M.H., Wright, P.E., (1998). Convergence Properties of the Nelder--Mead Simplex Method in Low Dimensions. *SIAM Journal on Optimization* 9(1), 112-147.

Lakhdar, M.B., Cerecero, R., Alvarez, G., Guilpart, J., Flick, D., Lallemand, A., (2005). Heat transfer with freezing in a scraped surface heat exchanger. *Applied Thermal Engineering* 25(1), 45-60.

Lee, J.H., Singh, R.K., (1993). Residence time distribution characteristics of particle flow in a vertical scraped surface heat exchanger. *Journal of Food Engineering* 18(4), 413-424.

Levenspiel, O., (1999). *Chemical Reaction Engineering* (3rd ed). John Wiley & Sons, New York.

Lian, G., Moore, S., Heeney, L., (2006). Population balance and computational fluid dynamics modelling of ice crystallisation in a scraped surface freezer. *Chemical Engineering Science* 61(23), 7819-7826.

Liao, Y., Lucas, D., (2009). A literature review of theoretical models for drop and bubble breakup in turbulent dispersions. *Chemical Engineering Science* 64(15), 3389-3406.

Mabit, J., Fayolle, F., Legrand, J., (2003). Shear rates investigation in a scraped surface heat exchanger. *Chemical Engineering Science* 58(20), 4667-4679.

Madhuranthakam, C.M.R., Pan, Q., Rempel, G.L., (2009). Residence time distribution and liquid holdup in Kenics® KMX static mixer with hydrogenated nitrile butadiene rubber solution and hydrogen gas system. *Chemical Engineering Science* 64(14), 3320-3328.

Martínez, D.S., Solano, J.P., Illán, F., Viedma, A., (2014). Analysis of heat transfer phenomena during ice slurry production in scraped surface plate heat exchangers. *International Journal of Refrigeration* 48, 221-232.

Mary, G., Mezdour, S., Delaplace, G., Lauhon, R., Cuvelier, G., Ducept, F., (2013). Modelling of the continuous foaming operation by dimensional analysis. *Chemical Engineering Research and Design* 91(12), 2579-2586.

Metzner, A.B., Otto, R.E., (1957). Agitation of non-Newtonian fluids. *AIChE Journal* 3(1), 3-10.

Middleton, J.C., (1997). Gas-liquid dispersion and mixing, in: Harnby, N., Edwards, M.F., Nienow, A.W. (Eds.), *Mixing in the Process Industries*. Butterworth-Heinemann, Oxford, pp. 322-363.

Miller-Livney, T., Hartel, R.W., (1997). Ice Recrystallization in Ice Cream: Interactions Between Sweeteners and Stabilizers. *Journal of Dairy Science* 80(3), 447-456.

Müller-Fischer, N., Tobler, P., Dressler, M., Fischer, P., Windhab, E., (2008). Single bubble deformation and breakup in simple shear flow. *Experiments in Fluids* 45(5), 917-926.

Müller-Fischer, N., Windhab, E.J., (2005). Influence of process parameters on microstructure of food foam whipped in a rotor–stator device within a wide static pressure range. *Colloids and Surfaces A: Physicochemical and Engineering Aspects* 263(1–3), 353-362.

Nagy, Z.K., Fevotte, G., Kramer, H., Simon, L.L., (2013). Recent advances in the monitoring, modelling and control of crystallization systems. *Chemical Engineering Research and Design* 91(10), 1903-1922.

Narsimhan, G., (2010). Analysis of creaming and formation of foam layer in aerated liquid. *Journal of Colloid and Interface Science* 345(2), 566-572.

Nauman, E.B., Nigam, A., (2004). On Axial Diffusion in Laminar-Flow Reactors. *Industrial & Engineering Chemistry Research* 44(14), 5031-5035.

Ndoye, F.T., Alvarez, G., (2015). Characterization of ice recrystallization in ice cream during storage using the focused beam reflectance measurement. *Journal of Food Engineering* 148, 24-34.

Ndoye, F.T., Erabit, N., Alvarez, G., Flick, D., (2012). Influence of whey protein aggregation on the residence time distribution in a tubular heat exchanger and a helical holding tube during heat treatment process. *Journal of Food Engineering* 112(3), 158-167.

Oriol, J., Leclerc, J.P., Jallut, C., Tochon, P., Clement, P., (2008). Characterization of the two-phase flow regimes and liquid dispersion in horizontal and vertical tubes by using coloured tracer and non-intrusive optical detector. *Chemical Engineering Science* 63(1), 24-34.

Qin, F., Chen, X.D., Ramachandra, S., Free, K., (2006). Heat transfer and power consumption in a scraped-surface heat exchanger while freezing aqueous solutions. *Separation and Purification Technology* 48(2), 150-158.

Qin, F.G.F., Chen, X.D., Russell, A.B., (2003). Heat transfer at the subcooled-scraped surface with/without phase change. *AIChE Journal* 49(8), 1947-1955.

Rainieri, S., Bozzoli, F., Cattani, L., Vocale, P., (2014). Parameter estimation applied to the heat transfer characterisation of Scraped Surface Heat Exchangers for food applications. *Journal of Food Engineering* 125, 147-156.

Ramaswamy, H.S., Abdelrahim, K.A., Marcotte, M., Clavier, P., (1995a). Residence time distribution (RTD) characteristics of meat and carrot cubes in starch solutions in a vertical scraped surface heat exchanger (SSHE). *Food Research International* 28(4), 331-342.

Ramaswamy, H.S., Abdelrahim, K.A., Simpson, B.K., Smith, J.P., (1995b). Residence time distribution (RTD) in aseptic processing of particulate foods: a review. *Food Research International* 28(3), 291-310.

Ramkrishna, D., (2000). *Population Balances: Theory and Applications to Particulate Systems in Engineering*. Elsevier Science.

Rao, C.S., Hartel, R.W., (2006). Scraped Surface Heat Exchangers. *Critical Reviews in Food Science and Nutrition* 46(3), 207-219.

Regand, A., Goff, H.D., (2003). Structure and ice recrystallization in frozen stabilized ice cream model systems. *Food Hydrocolloids* 17(1), 95-102.

Reiser, P., Birch, G.G., Mathlouthi, M., (2012). Physical properties, in: Mathlouthi, M., Reiser, P. (Eds.), *Sucrose: Properties and Applications*. Springer-Science, pp. 186 - 223.

Risso, F., (2000). Mechanisms of deformation and breakup of drops and bubbles. *Multiphase Science and Technology* 12(1), 1-50.

Russell, A.B., Burmester, S.S.H., Winch, P.J., (1997). Characterization of Shear Thinning Flow Within a Scraped Surface Heat Exchanger. *Food and Bioproducts Processing* 75(3), 191-197.

Russell, A.B., Cheney, P.E., Wantling, S.D., (1999). Influence of freezing conditions on ice crystallisation in ice cream. *Journal of Food Engineering* 39(2), 179-191.

Saraceno, L., Boccardi, G., Celata, G.P., Lazzarini, R., Trinchieri, R., (2011). Development of two heat transfer correlations for a scraped surface heat exchanger in an ice-cream machine. *Applied Thermal Engineering* 31(17–18), 4106-4112.

Sattar, M.A., Naser, J., Brooks, G., (2013). Numerical simulation of creaming and foam formation in aerated liquid with population balance modeling. *Chemical Engineering Science* 94(0), 69-78.

Saxena, A.K., Nigam, K.D.P., Schumpe, A., Deckwer, W.D., (1996). Liquid phase residence time distribution for two phase flow in coiled tubes. *The Canadian Journal of Chemical Engineering* 74(6), 861-866.

Scanlon, M.G., Campbell, G.M., Pyle, D.L., Chemists, A.A.o.C., (2008). *Bubbles in Food 2: Novelty, Health and Luxury*. Egan Press [for the American Association of Cereal Chemists].

Schenk, O., Gärtner, K., (2004). Solving unsymmetric sparse systems of linear equations with PARDISO. *Future Generation Computer Systems* 20(3), 475-487.

Sharma, L., Nigam, K.D.P., Roy, S., (2017). Axial dispersion in single and multiphase flows in coiled geometries: Radioactive particle tracking experiments. *Chemical Engineering Science* 157, 116-126.

Shiomi, Y., Kutsuna, H., Akagawa, K., Ozawa, M., (1993). Two-phase flow in an annulus with a rotating inner cylinder (flow pattern in bubbly flow region). *Nuclear Engineering and Design* 141(1–2), 27-34.

Shiomi, Y., Kutsuna, H., Akagawa, K., Ozawa, M., (1995). Bubble and Particle Behavior in Taylor- and Spiral-Vortex Flows, in: Serizawa, A., Fukano, T., Bataille, J. (Eds.), *Multiphase Flow* 1995. Elsevier, Amsterdam, pp. 17-26.

Simoneau, C., McCarthy, M.J., German, J.B., (1993). Magnetic resonance imaging and spectroscopy for food systems. *Food Research International* 26(5), 387-398.

Skelland, A.H.P., (1958). Correlation of scraped-film heat transfer in the votator. *Chemical Engineering Science* 7(3), 166-175.

Sofjan, R.P., Hartel, R.W., (2004). Effects of overrun on structural and physical characteristics of ice cream. *International Dairy Journal* 14(3), 255-262.

Stewart, P.S., Davis, S.H., Hilgenfeldt, S., (2013). Viscous Rayleigh–Taylor instability in aqueous foams. *Colloids and Surfaces A: Physicochemical and Engineering Aspects* 436, 898-905.

Stranzinger, M., Feigl, K., Windhab, E., (2001). Non-Newtonian flow behaviour in narrow annular gap reactors. *Chemical Engineering Science* 56(11), 3347-3363.

Taylor, G.I., (1934). The Formation of Emulsions in Definable Fields of Flow. *Proceedings of the Royal Society of London*. Series A 146(858), 501-523.

Tester, J.W., Modell, M., (1997). *Thermodynamics and Its Applications*. Prentice Hall PTR.

Thakur, R.K., Vial, C., Djelveh, G., (2003a). Foaming of Commercial Grade Food Products in a Continuous Stirred Column. *Chemical Engineering Research and Design* 81(9), 1083-1089.

Thakur, R.K., Vial, C., Djelveh, G., (2003b). Influence of operating conditions and impeller design on the continuous manufacturing of food foams. *Journal of Food Engineering* 60(1), 9-20.

Thakur, R.K., Vial, C., Djelveh, G., (2005). Combined effects of process parameters and composition on foaming of dairy emulsions at low temperature in an agitated column. *Journal of Food Engineering* 68(3), 335-347.

Thijert, M.P.G., Oyevaar, M.H., Kuper, W.J., Westerterp, K.R., (1992). Residence time distribution of the gas phase in a mechanically agitated gas-liquid reactor. *Chemical Engineering Science* 47(13–14), 3339-3346.

Torres, A.P., Oliveira, F.A.R., (1998). Residence time distribution studies in continuous thermal processing of liquid foods: a review. *Journal of Food Engineering* 36(1), 1-30.

Trommelen, A.M., Beek, W.J., (1971). Flow phenomena in a scraped-surface heat exchanger ("Votator"-type). *Chemical Engineering Science* 26(11), 1933-1942.

Trommelen, A.M., Beek, W.J., Van De Westelaken, H.C., (1971). A mechanism for heat transfer in a Votator-type scraped-surface heat exchanger. *Chemical Engineering Science* 26(12), 1987-2001.

Vedantam, S., Joshi, J.B., (2006). Annular Centrifugal Contactors—A Review. *Chemical Engineering Research and Design* 84(7), 522-542.

Villermaux, J., (1993). *Génie de la réaction chimique - Conception et fonctionnement des réacteurs* (2nde ed). Tec & Doc - Lavoisier, Paris.

Vyakaranam, K.V., Kokini, J.L., (2012). Prediction of air bubble dispersion in a viscous fluid in a twin-screw continuous mixer using FEM simulations of dispersive mixing. *Chemical Engineering Science* 84(0), 303-314.

Wang, W.E.I., Walton, J.H., McCarthy, K.L., (1999). Flow profiles of power law fluids in scraped surface heat exchanger geometry using MRI. *Journal of Food Process Engineering* 22(1), 11-27.

Wang, W.E.I., Walton, J.H., McCarthy, K.L., (2000). Mixing in scraped surface heat exchanger geometry using MRI. *Journal of Food Process Engineering* 23(6), 403-418.

Wen, C.Y., Fan, L.T., (1975). *Models for flow systems and chemical reactors*. Marcel Dekker.

Xu, W., Nikolov, A., Wasan, D.T., Gonsalves, A., Borwankar, R.P., (2003). Foam film rheology and thickness stability of foam-based food products. *Colloids and Surfaces A: Physicochemical and Engineering Aspects* 214(1–3), 13-21.

Yang, H.-H., Manas-Zloczower, I., (1992). 3D Flow field analysis of a Banbury mixer, in: Moldenaers, P., Keunings, R. (Eds.), *Theoretical and Applied Rheology*. Elsevier, Amsterdam, pp. 408-410.

Yataghene, M., Fayolle, F., Legrand, J., (2009). Experimental and numerical analysis of heat transfer including viscous dissipation in a scraped surface heat exchanger. *Chemical Engineering and Processing: Process Intensification* 48(10), 1447-1458.

Yataghene, M., Francine, F., Jack, L., (2011). Flow patterns analysis using experimental PIV technique inside scraped surface heat exchanger in continuous flow condition. *Applied Thermal Engineering* 31(14–15), 2855-2868.

Yataghene, M., Legrand, J., (2013). A 3D-CFD model thermal analysis within a scraped surface heat exchanger. *Computers & Fluids* 71, 380-399.

Yataghene, M., Pruvost, J., Fayolle, F., Legrand, J., (2008). CFD analysis of the flow pattern and local shear rate in a scraped surface heat exchanger. *Chemical Engineering and Processing: Process Intensification* 47(9–10), 1550-1561.

Yeoh, G.H., Cheung, C.P., Tu, J., (2014). Population Balance Approach—A Generic Framework, in: Yeoh, G.H., Cheung, C.P., Tu, J. (Eds.), *Multiphase Flow Analysis Using Population Balance Modeling*. Butterworth-Heinemann, Oxford, pp. 69-90.

Yuan, Y., Han, M., Wang, D., Jin, Y., (2004). Liquid phase residence time distribution for a two-phase countercurrent flow in a packed column with a novel internal. *Chemical Engineering and Processing: Process Intensification* 43(12), 1469-1474.

Zhang, T., Wang, T., Wang, J., (2005). Mathematical modeling of the residence time distribution in loop reactors. *Chemical Engineering and Processing: Process Intensification* 44(11), 1221-1227.

Zimmerman, W.B.J., (2006). *Multiphysics Modeling with Finite Element Methods*. World Scientific, Singapore.

Title : Coupling crystallization-foaming within a scraped surface heat exchanger during sorbet production

Keywords : Water crystallization; Ice crystal size distribution; Bubble size distribution; Scraped surface heat exchanger; Residence time distribution; Computational fluid dynamics

Abstract :

During sorbet production, a crucial step is the initial freezing in a scraped surface heat exchanger (SSHE), whose main goals is to generate small ice crystals (by crystallization) and air bubbles (by foaming) to obtain a product with a smooth texture. The crystallization-foaming coupling undertake diverse interactions which lead to a modification of the product in terms of flow, mixing, phase change, heat transfers and rheology, which in turn, can affect the crystallization mechanisms and therefore the size distributions.

The objective of this thesis is to provide a better knowledge of the mechanisms involved during crystallization and simultaneous foaming in an SSHE and their impact on the structural and textural properties of the final product. This thesis made possible a better understanding the phenomena induced by the foaming on the crystallization processes during the manufacture of sorbet in an SSHE, thanks to a combined approach of experimentation and modeling.

The study of the influence of the operating conditions of the freezing process on the size distributions of ice crystals and air bubbles was carried out through the development of a discriminatory granulometry technique using a refrigerated glove box. It demonstrated the strong coupling between the mechanisms of crystallization and foaming.

The overall characterization of the flows within the SSHE was made through an experimental and numerical study of the residence time distribution (RTD) during the simultaneous process of crystallization and foaming. In particular, the RTD revealed the presence of an almost stagnant air pocket inside the heat exchanger.

A 3D digital flow model was developed to study the thermal transfer flow coupling in the absence of air. It made it possible to highlight recirculation zones which can influence the transfers and the dynamics of air bubble formation.

Another model based on local air bubble fragmentation mechanisms has been developed using a CFD approach. It allows, as a first approach, to identify the zones of formation of the first air bubbles and to predict the order of magnitude of the size of the largest air bubbles.

Titre : Couplage cristallisation-foisonnement au sein d'un échangeur de chaleur à surface raclée lors de la production de sorbet

Mots-clés : Cristallisation de l'eau ; Distribution de la taille de cristaux de glace ; Distribution de la taille des bulles ; Echangeur de chaleur à surface raclée ; Distribution des temps de séjour ; Modèle numérique d'écoulement

Résumé :

Lors de la fabrication de sorbet, une étape cruciale est la congélation initiale dans un échangeur de chaleur à surface raclée (ECSR), où l'on cherche à générer des petits cristaux de glace (par cristallisation) et des bulles d'air (par foisonnement) afin d'obtenir un produit avec une texture lisse. Le couplage cristallisation-foisonnement met en œuvre diverses interactions qui entrainent une modification du produit en termes d'écoulement, de mélange, de changement de phase, de transferts thermiques et de rhéologie, pouvant affecter les mécanismes de cristallisation et donc les distributions de tailles.

L'objectif de ce travail de thèse est d'apporter une meilleure connaissance des mécanismes mis en jeu lors de la cristallisation et du foisonnement simultané dans un ECSR et de leur incidence sur les propriétés structurales et texturales du produit final. Cette thèse a permis de mieux appréhender les phénomènes induits par le foisonnement sur les processus de cristallisation lors de la fabrication de sorbet dans un ECSR, grâce à une approche combinée d'expérimentations et de modélisation.

L'étude de l'influence des conditions opératoires du procédé de congélation sur les distributions des tailles de cristaux de glace et de bulles d'air a été réalisée à travers la mise au point d'une technique de granulométrie discriminatoire à l'aide d'une boîte à gants réfrigérée. Elle a mis en évidence le fort couplage entre les mécanismes de cristallisation et de foisonnement.

La caractérisation globale des écoulements au sein de l'ECSR s'est faite grâce à une étude expérimentale et numérique de la distribution des temps de séjour (DTS) pendant le processus simultané de cristallisation et de foisonnement. La DTS a notamment révélée la présence d'une poche d'air quasi- stagnante à l'intérieur de l'échangeur.

Un modèle numérique d'écoulement en 3D a été développé pour étudier le couplage écoulement transfert thermique en absence d'air. Il a permis de mettre en évidence des zones de recirculation qui peuvent influer sur les transferts et la dynamique de formation des bulles d'air.

Un autre modèle basé sur les mécanismes locaux de fragmentation des bulles d'air a été développé grâce à une approche CFD. Il permet, en première approche, d'identifier les zones de formation des premières bulles d'air et de prédire l'ordre de grandeur de la taille des bulles d'air les plus larges.